A QUANTITATIVE STUDY OF THE WELDABILITY OF INCONEL 718 USING GLEEBLE AND VARESTRAINT TEST METHODS

A Thesis

presented to

the Faculty of California Polytechnic State University,

San Luis Obispo

In Partial Fulfillment

of the Requirements for the Degree

Master of Science in Engineering with Specializations in Materials Engineering

by

Sean Quigley

September 2011

COMMITTEE MEMBERSHIP

TITLE:	A quantitative study of the weldability of Inconel 718 using Gleeble and Varestraint test methods
AUTHOR:	Sean Quigley
DATE SUBMITTED:	September 2011
COMMITTEE CHAIR:	Dr. Trevor Harding, PhD
COMMITTEE MEMBER:	Dr. Dan Walsh, PhD
COMMITTEE MEMBER:	Dr. David Crockett, PhD

ABSTRACT

A quantitative study of the weldability of Inconel 718 using Gleeble and Varestraint test methods

Sean Quigely

Nickel super alloy Inconel 718 was tested and compared to Haynes 230 using Gleeble and Varestraint mechanical test methods. Hot cracking susceptibility was examined in either alloy using a sub-scale Varestraint test method at 5 augmented strain levels: 0.25%, 05.%, 1%, 2%, and 4%. Maximum crack length, total crack length, and number of cracks were measured for each strain level. Gleeble hot ductility on-heating and on-cooling tests were performed on both alloys. Inconel 718 was tested on-heating at target temperatures of 1600˚F, 2000˚F, 2100˚F, 2200˚F, and on cooling at 1600˚F, 1700˚F, 1800˚F, 1900˚F, and 2100˚F. Haynes 230 was tested on-heating at target temperatures of 2050 ˚F, 2200 ˚F, 2240 ˚F, 2330 ˚F, and on-cooling at 1800 ˚F, 1900 ˚F, 1990 ˚F, 2040 ˚F, 2090 ˚F, 2100 ˚F, 2140 ˚F, and 2190 ˚F. Ductility in Gleeble samples was measured in a reduction of surface area. A nil-strength temperature was established for either alloy. The nil-strength temperature was 2251˚F and 2411˚F, for Inconel 718 and Haynes 230, respectively. The nil ductility temperature <5% R/A) was 2188˚F for Inconel 718 and 2341˚F for Haynes 230. Ductility recovery temperature occurred at 1924˚F for Inconel 718 and 2147˚F for Haynes 230. The brittle temperature range was determined to be 326˚F for Inconel 718 and 228˚F for Haynes 230. Varestraint testing revealed that Inconel 718 had a lower threshold strain for crack initiation than Haynes 230 (0.5% vs 1%), and a higher number of cracks, as well as a larger maximum crack length, at every strain level. These results show a greater tendency for liquation cracks to form in Inconel 718 than in Haynes 230.

Keywords: Weldability, Inconel 718, Haynes 230, Gleeble, Varestraint, liquation cracking, crack susceptibility, SEM, microscopy, ductility, fracture, cracking.

TABLE OF CONTENTS

LIST OF TABLES

LIST OF FIGURES

1.0 Introduction

1.1 Background

1.1.1 History of Superalloys

Superalloys were introduced shortly after World War II. The term was initially coined to describe a group of alloys developed specifically for use in high temperature applications such as turbochargers and aircraft turbine engines that required high performance at elevated temperatures. Prior to their introduction, internal combustion piston engines were the primary power source for aircraft. In the early 1940s the German Messerschmitt Me-262 marked one of the earliest uses of a turbine engine, but this design remained limited to small jet fighters. With a lack of suitable materials, larger aircraft were unable to utilize the newer technology. It would take another decade of research and development before bigger turbine designs would become feasible, mainly due to the development of suitable superalloys[1]. Since that time, the range of applications for superalloys has continued to expand into other gas turbine applications, rocket engines, nuclear power generation, and chemical and petroleum drilling and processing[2]. The superalloys ability to withstand creep during extended exposure to high temperatures (>650˚C) and during constant thermal cycling, coupled with their natural resistance to corrosion, high strength-to-weight ratio, and good ductility make them excellent candidates for the above applications.

1.1.2 Structure and Composition

Superalloys typically consist of some combination of Fe, Ni, Co, and Cr as the main alloying elements, with lesser amounts of W, Mo, Ta, Nb, Ti, and Al[3]. Nickel based alloys make up one of the most important families of superalloys. These alloys achieve their high strength primarily through solid solution or precipitation strengthening, with the latter process being much more effective. Alloying elements in Ni based systems are

typically Cr (10-20 %wt), Al and Ti (up to 8 %wt combined total), and Co (5-10 %wt). Lesser amounts of B, Zr, C, Mo, W, Ta, Hf, and Nb are also often included[4]. These elements partition to different phases and thus can be found at different locations in the microstructure. Their size, electronegativity and volume relative to the nickel rich matrix are key to explaining this phenomenon.

These elements can be categorized into four basic classes based on their effect: gamma (γ) forming, some gamma prime (γ') forming, some carbide forming, and those that segregate preferentially to grain boundaries. Gamma (γ) forming elements tend to partition to the γ matrix, while γ' forming elements partition to the γ' precipitates. The nature of each element is dictated by its atomic diameter relative to the bulk Ni matrix. Co, Cr, Mo, W and Fe are considered γ formers, with an atomic diameter which differs from Ni by 3-13%. Al, Ti, Nb, Ta, and Hf are considered γ' formers, differing in diameter by 6-18%. Cr, Mo, W, Nb, Ta, and Ti can also form carbides, while B, C and Zr segregate strongly to the grain boundary, differing in size by 21-27%. Alloying elements are added for specific reasons (Tbl I). Mo and W go into solid solution to add strength to the matrix, Cr is used to enhance high temperature oxidation resistance, and Al and Ti are added to form the γ'-phase for precipitation hardening[5].

Table I: Elemental Effects in Nickel-based Superalloys[6]

Element	Effect
Nickel	High temperature strength, stability
Cobalt	High temperature strength
Chromium	Oxidation resistance
Molybdenum	High temperature strength
Tungsten	High temperature strength
Iron	Reduces cost
Silicon	Oxidation and sulfidation resistance
Carbon	High temperature strength and grain size control
Boron	High temperature creep strength
Manganese	Oxidation resistance
Lanthanum	Oxidation resistance
Ytrium	Oxidation resistance
Aluminum	Deoxidation (0.2–0.3%), gamma prime formation (0.6–2%)
Titanium	Gamma prime formation (2–3%)

The bulk matrix in most nickel based superalloys is made up of the γ-phase, a face centered cubic (FCC) nickel based austenitic phase containing high percentages of solid solution elements, mainly Co, Cr, Mo, and W. The γ'-phase makes up the primary strengthening phase, consisting of $Ni_3(Al,Ti)$. The combination of similar lattice parameters of the matrix and precipitate and good chemical compatibility results in homogenous precipitation of the γ' and adds to long term stability. Additionally, the high ductility of the γ' phase helps add to the overall strength of the alloy without adversely effecting fracture toughness. The ability to maintain strength and resist creep deformation at high temperatures is largely due to the γ' phase[7]. Total amount of γ' present in the material is dependent on temperature and chemical composition (Figure 1).

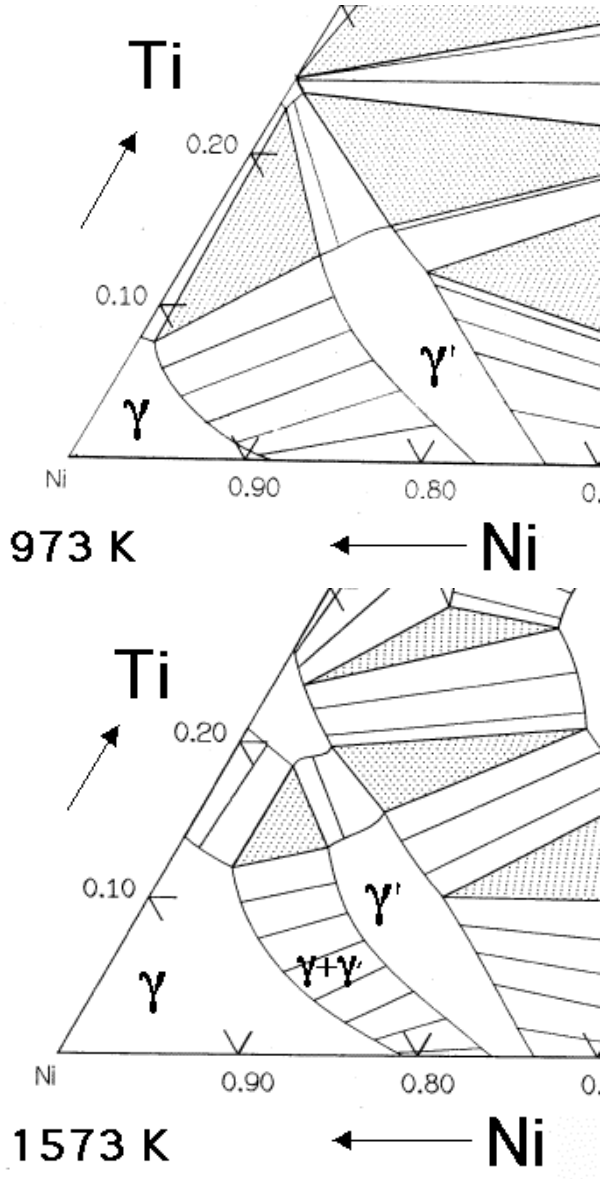

Figure 1: Ternary Ni-Al-Ti phase diagrams at two temperatures. The percentage of γ' decreases as temperature increases[8].

The existence of carbides within the bulk matrix can be attributed to the presence of low levels of carbon, at 0.05-0.2%, reacting with Ti, Ta and Hf, Mo, and Nb, forming TiC, TaC, HfC, MoC and NbC. Carbides aid in the strengthening of the alloy in several ways. If properly formed, "they make the grain boundary stronger, prevent or retard the grain boundary sliding, and permit stress relaxation," and "can tie up certain elements that

would otherwise cause phase instability during service."[9] High temperatures experienced during heat treatment or service can lead to the formation of the secondary $M_{23}C_6$ and M_6C carbides. As MC carbides decompose, yielding carbon, the following reactions can take place:

$$MC + \gamma \rightarrow M_{23}C_6 + \gamma' \quad \text{(Eq. 1)}$$

or

$$(Ti,Mo)C + (Ni,Cr,Al,Ti) \rightarrow Cr_{21}Mo_2C_6 + Ni_3(Al,Ti) \quad \text{(Eq. 2)}$$

and

$$MC + \gamma \rightarrow M_6C + \gamma' \quad \text{(Eq. 3)}$$

or

$$(Ti,Mo)C + (Ni,Co,Al,Ti) \rightarrow Mo_3(Ni,Co)_3C + Ni_3(Al,Ti) \quad \text{(Eq. 4)}$$

These secondary carbides typically form along grain boundaries[10]. In alloys where composition has not been closely controlled, brittle and undesirable topologically close-packed (TPC) sigma (σ), mu (μ) and laves phases can precipitate during heat treatment or service. They generally appear as thin linear plates, nucleating on grain boundary particles. They are detrimental to mechanical properties in several ways. The physical hardness and plate-like morphology of σ makes it a location susceptible for crack initiation and propagation, leading to low-temperature brittle failure. The formation of σ also draws refractory metal elements from the γ matrix, lessening the effect of solution strengthening, and lowering high temperature rupture strength. The presence of the μ phase has not been determined to have as severe an effect[11]. The presence of the laves phase will be discussed more thoroughly later in this paper.

The similarities in the lattice parameters of γ and γ' phases play an important role in the high temperature strength of nickel based superalloys. As mentioned, the γ phase has an FCC structure with random ordering of the compositional atoms. The γ' phase

differs, consisting of a primitive cubic lattice structure, with nickel atoms at the face centers, and aluminum or titanium atoms at the cube corners (Figure 2).

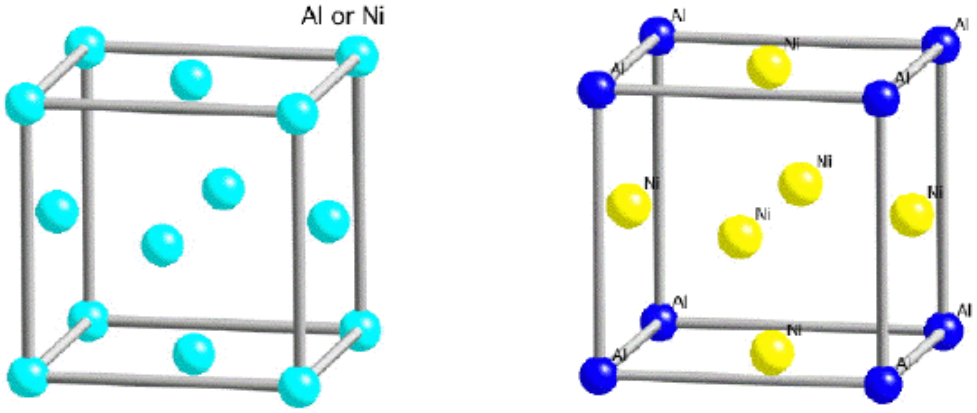

Figure 2: FCC lattice structure of the γ phase (left) and γ' phase (right) [12].

Because of similar sizing and structure, the γ' phase precipitates into the γ matrix in a cube-cube orientation. This means that the cell edges of the γ' phase are parallel to the γ phase cell edges. Due to the close match of lattice parameters, the γ' phase precipitates are coherent with the γ matrix. Despite their coherency, it is difficult for dislocations in the γ matrix to slip through the γ' precipitates[13]. This difficulty, manifested as an increase in strength, is caused by the ordering of its crystal structure. In the γ phase, the Burgers vector of a dislocation is a/2<1 1 0>, which prevents altering of the lattice structure due to slip. In the γ' phase, the Burgers vector of a dislocation is a<1 1 0> (Figure 3). A dislocation originating in the γ phase and moving along the a/2<1 1 0> direction into the γ' phase will disrupt the order of the γ' crystal structure, resulting in an anti-phase domain boundary. The passage of a second dislocation will restore the order. Thus, dislocations can only penetrate into the γ' phase in pairs, called "superdislocations." The requirement of superdislocations makes it more difficult for movement into the γ' phase to occur, a key characteristic in resisting creep deformation[14]. Dislocation movement is inhibited by the presence of the γ' precipitates,

which act as barriers. When a dislocation encounters a precipitate, it will wrap around, rather than pass through (Figure 4). The presence of γ' precipitates are what provides such high strength and creep deformation resistance at elevated temperatures. Only at temperatures beyond 600C is any significant loss of strengths noticed. When temperatures do reach this limit, there is enough thermal energy for dislocations to surpass any precipitates or carbides.

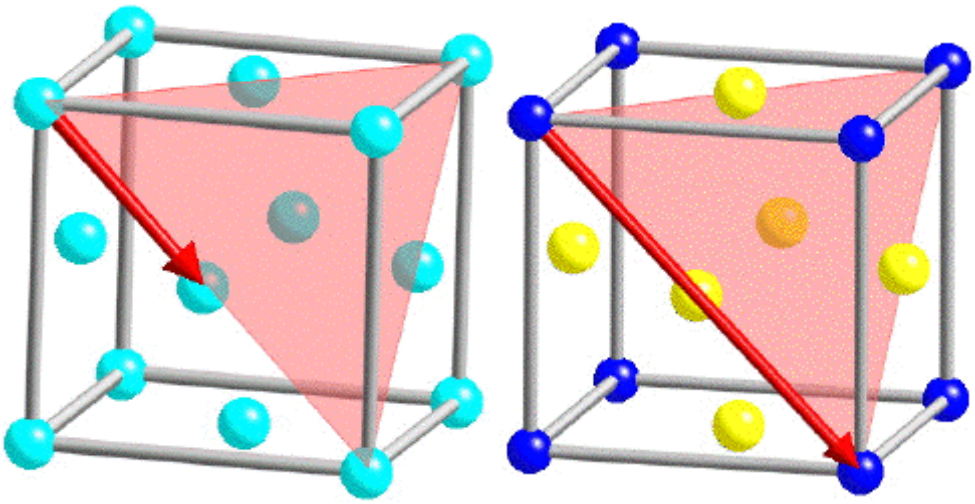

Figure 3: Lattice vectors along the <1 1 0> directions in γ (left) and γ' (right) crystal structures. Atoms are randomly oriented in the γ phase, while Nickel atoms are located at the face centers of the γ' phase[15].

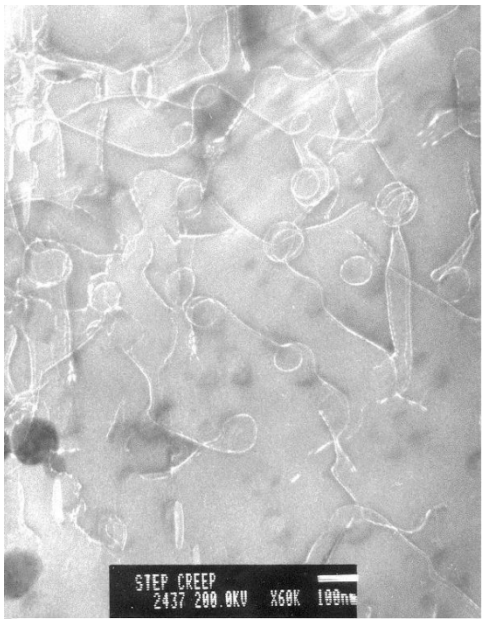

Figure 4: TEM image of C263 alloy after a 2.5 day creep test at 800˚C, at a stress of 160 MPa. Dislocations are looped around γ' precipitates, impeding movement[16].

In nickel alloys containing sufficient amounts of niobium or vanadium, like Inconel 718, another phase can exist: the gamma double prime (γ'') phase. These precipitates typically take disc form, in contrast to the spherical or cuboidal form of γ'. The composition is either Ni_3Nb or Ni_3V, with a body-centered tetragonal lattice and ordered arrangement of atoms (Figure 5: Body centered tetragonal lattice structure of the γ'' phase. The arrangement of Nickel and Niobum atoms are ordered.). This phase adds to the strength to the alloy through coherency hardening and order hardening[4]. Both the γ' and γ'' phases are the metastable counterparts of two other stable phases. Upon sufficient exposure to elevated temperatures (>1110 ^{0}F for γ', >1200 ^{0}F for γ''), γ' and γ'' will transform to the stable hexagonal close packed (HCP) Ni_3Ti eta (η) phase and the orthorhombic Ni_3Nb delta (δ) phase, respectively. Neither stable phase is considered desirable; their development leads to a reduction of strength at elevated temperatures[17].

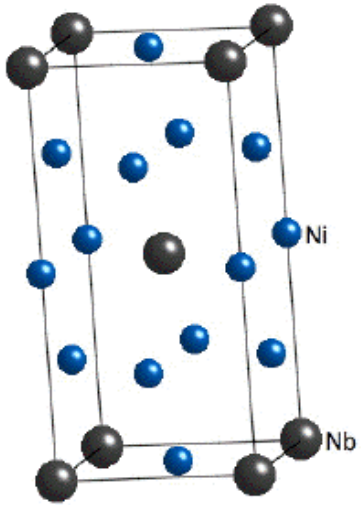

Figure 5: Body centered tetragonal lattice structure of the γ'' phase. The arrangement of Nickel and Niobum atoms are ordered[18].

1.1.3 The Weld HAZ

The weld region in Ni based alloys can be visualized as four consecutive regions: the composite zone, the unmixed zone, the partially melted zone (PMZ), and the "true" heat affected zone (Figure 6). The composite region exists within the weld pool, where any added filler metal has been diluted by the melted base metal. The unmixed zone exists at the boundary of the weld pool, where the base metal has melted, but has not been mechanically mixed with the weld pool, and maintains a composition similar to the base metal, but sometimes with a different solidification sub-structure. The partially melted zone typically extends one or two grains into the HAZ, relative to the fusion boundary of the weld pool, and is characterized by liquation initiating along grain boundaries. The true heat affected zone is between the partially melted zone and the unaffected base metal where changes to the base metal occur by solid state transformation[19].

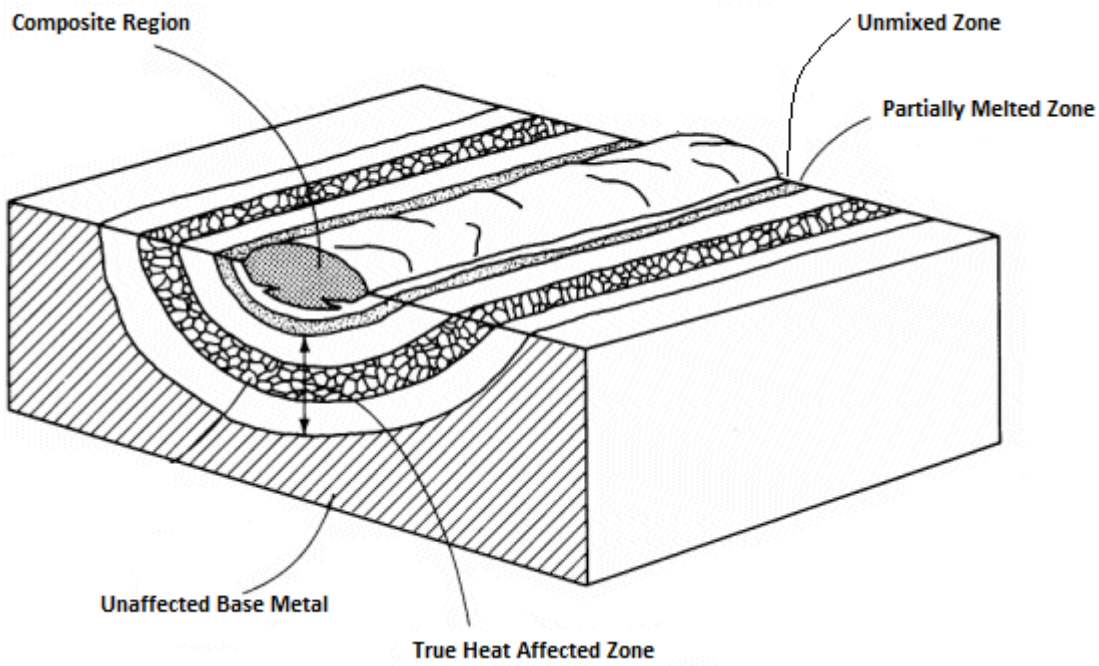

Figure 6: Weld Zones[20]

The unmixed zone and the composite zone are at temperatures in excess of the effective liquidus temperature (T_L) of the alloy. In the PMZ temperatures between T_L and the effective solidus temperature (T_S) are recorded. The "true" heat affected zone experiences temperatures below the effective T_S, and thus has no liquid present, but still undergoes solid state reactions such as precipitate coarsening, precipitate dissolution and grain growth or refinement. Note that because segregation is always present in industrial materials, the effective T_S is depressed below the equilibrium T_S. In addition, reactions such as constitutional liquation may occur because of the dynamic nature of the weld thermal cycle and extend the PMZ.

1.1.4 Hot Cracking Issues

One of the most troublesome issues with nickel-based superalloys is their tendency to suffer from a phenomenon generally referred to as hot cracking. Hot cracking can occur at elevated temperatures during service use, during the welding

process, or as a result of post weld heat treatment (PWHT) processes. Hot cracking can occur both in the solid state (subsolidus cracking), and above the liquation temperature (supersolidus cracking). Supersolidus cracking that occurs in the weld pool during solidification is appropriately referred to as solidification cracking. Supersolidus cracking that occurs in the HAZ during the welding process is typically referred to as liquation cracking, or sometimes more specifically as grain boundary liquation cracking, as these cracks form intergranularly. Subsolidus cracking that occurs in the weld pool, HAZ or parent metal during PWHT is referred to as strain age cracking. Cracks that develop in the solid state, at elevated temperatures, are referred to as ductility dip cracks, and are a result of a high level of restraint, and "ductility exhaustion" along grain boundaries.[21] This cracking typically occurs in multipass weld metals.

Solidification cracks can develop in the newly formed weld pool as thermal contraction of the solidifying metal introduces tensile stresses, and a high fraction of solid (fs>0.9) prevents the flow of liquid metal to backfill interdendritic regions. Liquation cracking in the HAZ is a result of the constitutional liquation of grain boundary phases, such as primary MC and M_6C carbides, and Laves phases, or matrix phases, such as Ni_3Al and Ni_3Nb, and thermally induced strain introduced through the welding process. During rapid heating these grain boundary phases are unable to fully dissolve into the surrounding matrix, and a liquid state, low melting point eutectic results. A more generalized illustration of this process is offered in Figure 6. For a simple two phase system of α+β, of composition C, with an increased solubility of β into α as temperature increases, β would normally enter into solution as temperatures rise under equilibrium conditions. But if temperatures are rapidly increased beyond the solidus point of β, diffusion cannot occur fast enough and a liquid phase develops around the β phases[9] (Figure 7). If the two-phase system undergoes equilibrium heating, β will enter into

solution at the temperature dictated by its concentration, and no localized melting will transpire.

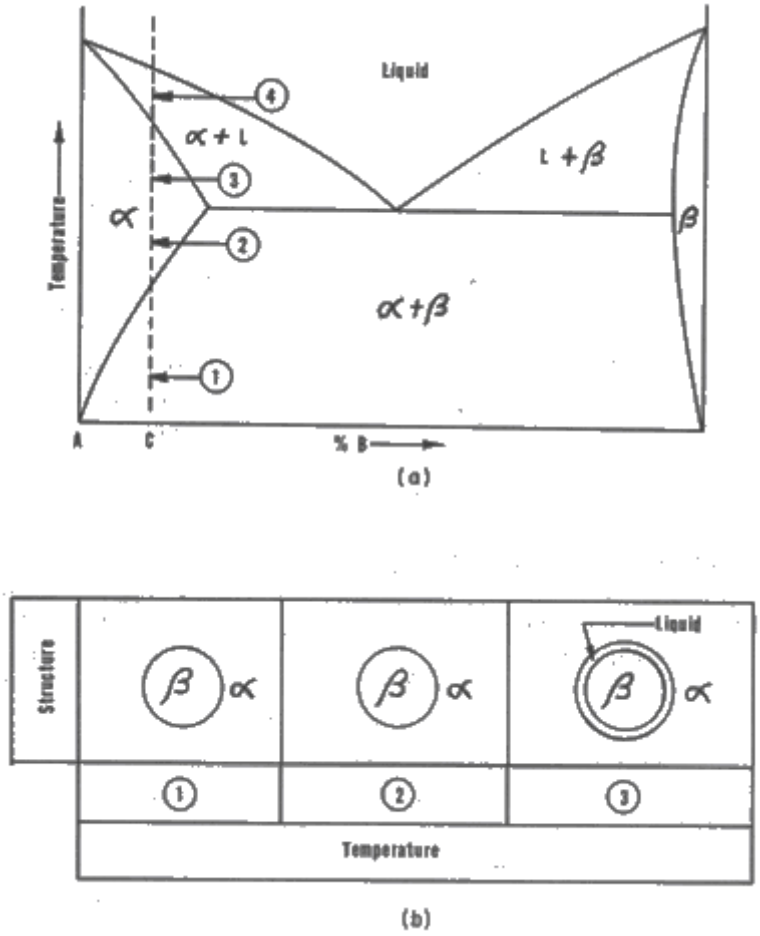

Figure 7: Phase diagram of two phase system (a) and existing structures during rapid heating (b). At temperature 2, β still exists as a solid. Rapid heating from temperature to temperature 3 does not allow sufficient time for the diffusing of β into α, and liquation results.

In terms of precipitates within the matrix, this results in a liquid film between the matrix and the precipitate. Migrating grain boundaries can intersect these liquated precipitates within the matrix, both introducing liquid along the grain boundary, and pinning them in place. In alloys containing grain boundary precipitates, the constitutional liquation process provides the necessary conditions for the development of intergranular liquid

films[22]. This usually occurs outside of the fusion zone in the grain coarsened region of the HAZ. Grain coarsening decreases the grain boundary area per unit volume, subsequently increasing the amount of segregation along the grain boundaries. The presence of the impurity elements sulfur, phosphorus and boron can further contribute to the issue by suppressing the eutectic melting temperature[23]. Liquation cracking will result when strain levels exceed the cohesion limit of the liquid films present along grain boundaries[24]. Chadwick, *et al*[25]. calculated that for a grain boundary containing liquid film of thickness *h*, the tensile stress required to overcome the surface tension γ_L, was:

$$\sigma = 2\gamma_L/h \qquad \text{(Eq. 5)}$$

An increase in liquid film thickness therefore results in a decrease in required tensile stress to cause decohesion at the solid-liquid interface. This problem can be worsened by the occurrence of liquid film migration (LFM). Constitutional liquation along the grain boundaries produces a metastable intergranular liquid, which considerably lowers the non-equilibrium solid-liquid interfacial energy[26]. This allows for wetting and penetration of the nearby grain-boundaries by the liquid film, referred to as LFM, which increases the local range over which decohesion may result. Table II contains data for the stress required to overcome the surface tension of pure Fe, Ni, Co and Cr at varying film thicknesses.

Table II - Required Stress to Overcome Liquid Surface Tension of Pure Alloying Metals at Varying Liquid Film Thicknesses

Metal	Surface Tension (J/m2)	Tensile Stress at 0.1 um (PSI)	Tensile Stress at 1 um (PSI)	Tensile Stress at 10 um (PSI)
Fe	0.269	780.30	78.03	7.80
Ni	0.306	887.63	88.76	8.88
Co	0.289	838.32	83.83	8.38
Cr	0.230	667.17	66.72	6.67

1.1.5 Effects of Alloying Elements on Hot Cracking

Various alloying elements can specifically influence the tendency to form inter granular liquids that lead to liquation cracking. The presence of Nb and Ti can increase the susceptibility to cracking due to their propensity to form Nb and/or Ti liquid films along the grain boundaries below the bulk melting temperature, while additions of Al can further suppress melting points[27]. In one recent study of Inconel 738, constitutional liquation of MC carbides, boride, sulphocarbide, eutectic and coarse γ' precipitates all contributed to cracking in the HAZ[28]. Subsolidus cracking, in general, is considered more detrimental than supersolidus cracking because it both broadens the effective melting range of the alloy, and introduces a non-equilibrium liquid film that can alter the reaction kinetics during further heating[29]. Strain age cracking is an issue that is especially problematic in γ' precipitation strengthened superalloys. The high heat introduced into the weld pool and surrounding HAZ during welding can cause precipitates to enter back into solution, while cooling of the weld pool introduces solidification strains, resulting in a weakened region of metal. If the residual stresses in the solidified weld pool or HAZ are above the yield strength, cracks can develop. A PWHT can both promote the reformation of strengthening precipitates, and relieve the residual stresses. The issue becomes the temperature and rate at which either process

occurs. The stress relieving temperature is often higher than the range for precipitation. The precipitation strengthening process begins during the process of heating to the stress relief temperature. The precipitates simultaneously strengthen the matrix and add to the strain that must be accommodated by the matrix. Once the precipitates form, and the high creep strength and low creep ductility of the alloy are restored, stress relief ceases, as creep and plastic deformation are prevented[30,31, 32].

1.2 Alloys of Study

1.2.1 Primary Alloy: Inconel 718

Inconel 718 (INCO 718), developed by International Nickel Corporation in the 1950s[33], is one of the most popular and highly utilized nickel-based superalloys, frequently chosen for its broad temperature range of service (-253˚C to 704˚C), excellent corrosion resistance, high temperature stability, creep resistance, machinability and weldability[34]. INCO 718 differs from many other nickel-based superalloys in its main source of strengthening in its age hardened form. It's high strength is largely a product of the formation of $Ni_3(Nb,Ti)$ γ'', rather than $Ni_3(Al,Ti)$ γ', with γ' acting as a secondary age hardening phase. INCO 718 can be obtained in aged, solution annealed tempered, cold worked, and cold worked and aged form. With such desirable properties, it finds a large number of applications, including gas turbine components, cryogenic storage tanks, jet engines, pump bodies and parts, rocket motors and thrust reversers, nuclear fuel element spacers, hot extrusion tooling, high strength bolting, and down hole shafting[35]. Its composition can be found in Table III.

Table III– Complete composition of Inconel 718[12]

Limiting Chemical Composition[a], %	
Nickel (plus Cobalt)	50.00-55.00
Chromium	17.00-21.00
Iron	Balance*
Niobium (plus Tantalum)	4.75-5.50
Molybdenum	2.80-3.30
Titanium	0.65-1.15
Aluminum	0.20-0.80
Cobalt	1.00 max.
Carbon	0.08 max.
Manganese	0.35 max.
Silicon	0.35 max.
Phosphorus	0.015 max.
Sulfur	0.015 max.
Boron	0.006 max.
Copper	0.30 max.

[a]Conforms to AMS specifications

*Reference to the 'balance' of a composition does not guarantee this is exclusively of the element mentioned but that it predominates and others are present only in minimal quantities.

A primary goal in the development of INCO 718 was to reduce the issue of strain age cracking during the PWHT process. This was achieved through the addition of Niobium, which causes the formation of γ'' precipitates. These have much slower precipitation kinetics than γ' precipitates, allowing time for the PWHT to proceed through the precipitation range into the stress relief temperature range before γ'' precipitates form, thus relieving the residual stresses introduced through the weld process. Other age-hardenable alloys of the same strength class (Rene' 41, M252, Astroloy), that existed at the time of INCO 718's design, were all hardened by γ', $Ni_3(Al,Ti)$ precipitates. Compared to INCO 718, their age hardening responses are all more rapid (Figure 8)[36], hindering the stress relief process. The presence of these internal stresses in the HAZ

is, as stated previously, a partial factor in the formation liquation cracks along grain boundaries in the grain coarsened region[37].

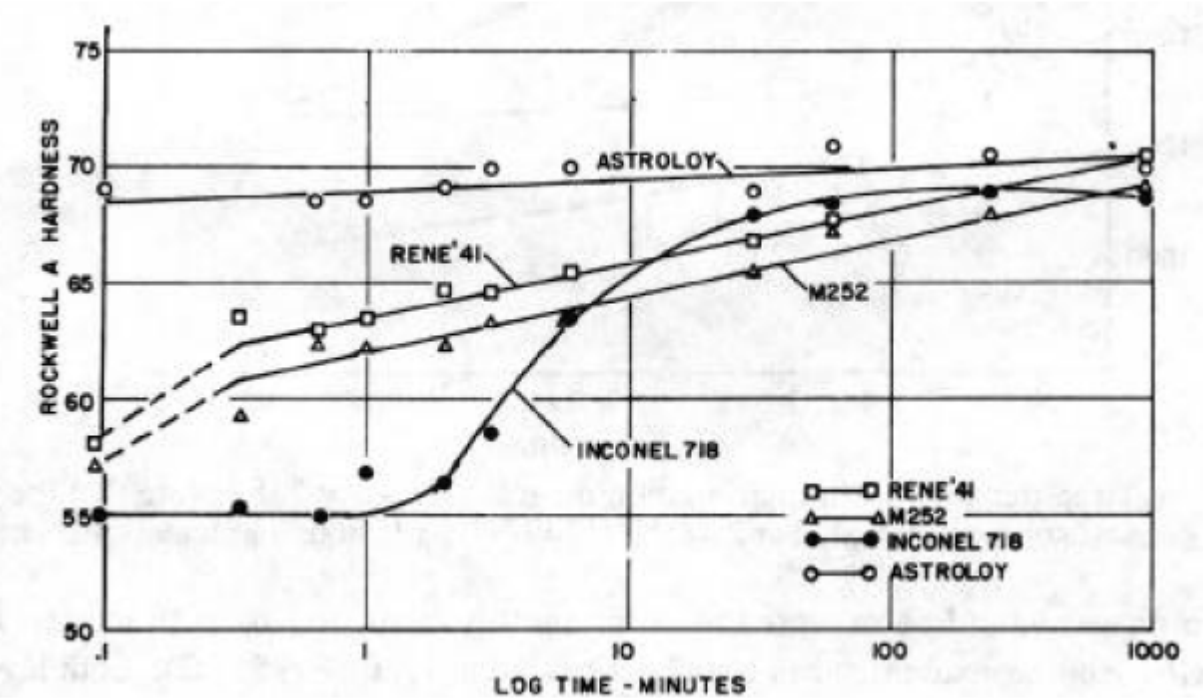

Figure 8: Age hardening response curves for Rene' 41, INCO 718, M252, and Astroloy. INCO 718 has a notably slower response time than any of the other three alloys, which allows time for the process of stress relief[38].

INCO 718's original development was in wrought form, but greater use for large components such as rocket engines, compressors and turbine blades has led to it being produced in cast form, which requires less welding. The cast form appears to be more susceptible to HAZ cracking, possibly due to an increase in Laves clusters, solute-enriched regions, and large grain size. Laves clusters consist of a mix of Laves phase ($[Fe,Ni,Cr]_2$, [Nb,Mo,Ti]), δ-phase (Ni_3Nb), γ', γ'', and NbC[39].

While the use of Nb as an alloying element in INCO 718 was successful in combating strain age cracking issues during PWHT, it unfortunately negatively influenced the tendency to form liquation and solidification cracks during the welding

process, largely due to the formation of NbC, Laves phase, and δ-phases along grain boundaries. These phases have a lower melting point than the bulk γ matrix, and rapid heating can cause them to constitutionally liquate, introducing liquid along the grain boundaries. Of these three phases, Laves appears to be the most detrimental. Isothermal liquation tests have revealed a lower initiation point for liquation of Laves than for NbC, by approximately 55^0F[40]. Additionally, its presence lowers both strength and tensile ductility of the bulk material in three distinct ways: "depleting the matrix of principal alloying elements required for hardening, introducing a weak-zone microstructure between the Laves phase and the matrix interface, and acting as a preferential site for easy crack initiation and propagation because of its inherent brittle nature.[41]" Laves phase forms easily during the welding process due to the microsegregation of its compositional elements, Nb, Mo and Ti, because of non-equilibrium solidification conditions. Microsegregation takes place when solute-rich liquid at the solid-liquid interface solidifies between already formed dendrites. Laves phase already present in cast forms of the metal can further contribute to weldability issues by increasing the potential for liquation cracks to form in the HAZ[42]. Segregation in castings is difficult to remedy, because the segregation patterns and scale preclude effective homogenization of substitutional elements at feasible temperatures, as solution heat treating will increase homogeneity throughout the matrix, but will do little to alter the elemental makeup along the grain boundaries that leads to low-melting phases during the weld thermal cycle[43].

Research suggests that the issue of liquation cracking is not simply limited to the constitutional liquation of Laves phase and NbC. Although making up a small weight percent of the alloy, boron, carbon, sulfur and phosphorus levels have been shown to play a critical role in liquation and solidification crack susceptibility, if present in sufficient

amounts at susceptible locations (sulfur greater than 0.008 %wt, phosphorous > 0.025 %wt, boron > 0.010 %wt). Boron is used to maintain stress-rupture ductility and hot malleability during the production process, and is kept at levels below 0.006 %wt. Amounts in the range of 0.001-0.003 %wt have typically been acceptable in maintaining formability while not increasing liquation cracking susceptibility[44]. Chen *et al*[45]*.* found that the melting and resolidification temperatures of boron-segregated grain boundaries can be 180^0F to 360^0F lower than those that experience constitutional liquation of NbC and Laves phases. An increase in boron content from 0.0011 %wt to 0.004 %wt led to an increase in total and maximum liquation crack lengths on spot welded Varestraint test samples. Other theories propose that boron increases liquation cracking susceptibility through increased wetting of the grain boundaries, not simply melting temperature depression[46]. Studies of carbon and sulfur content have shown similar effects on liquation cracking susceptibility. Increases in carbon content from 0.02 to 0.06%wt have been shown to result in a 70% increase in volume fraction of NbC, which can significantly increase liquation cracking through constitutional liquation[47]. Similar to the presence of boron along grain boundaries, sulfur can contribute to the formation of low-melting Ni-Ni_3S_2 films along grain boundaries, further depressing melting and solidification temperatures[48].

Grain size can also influence liquation cracking susceptibility in INCO 718. Grain size can be influenced by the production method, pre-weld heat treatments, or the weld process itself. In general, larger grains are more susceptible to liquation cracking. The time-temperature-transformation (T-T-T-) diagram in Figure 9 depicts the temperature at which the alloying phases enter into solution, for a solution annealed sample of INCO 718.

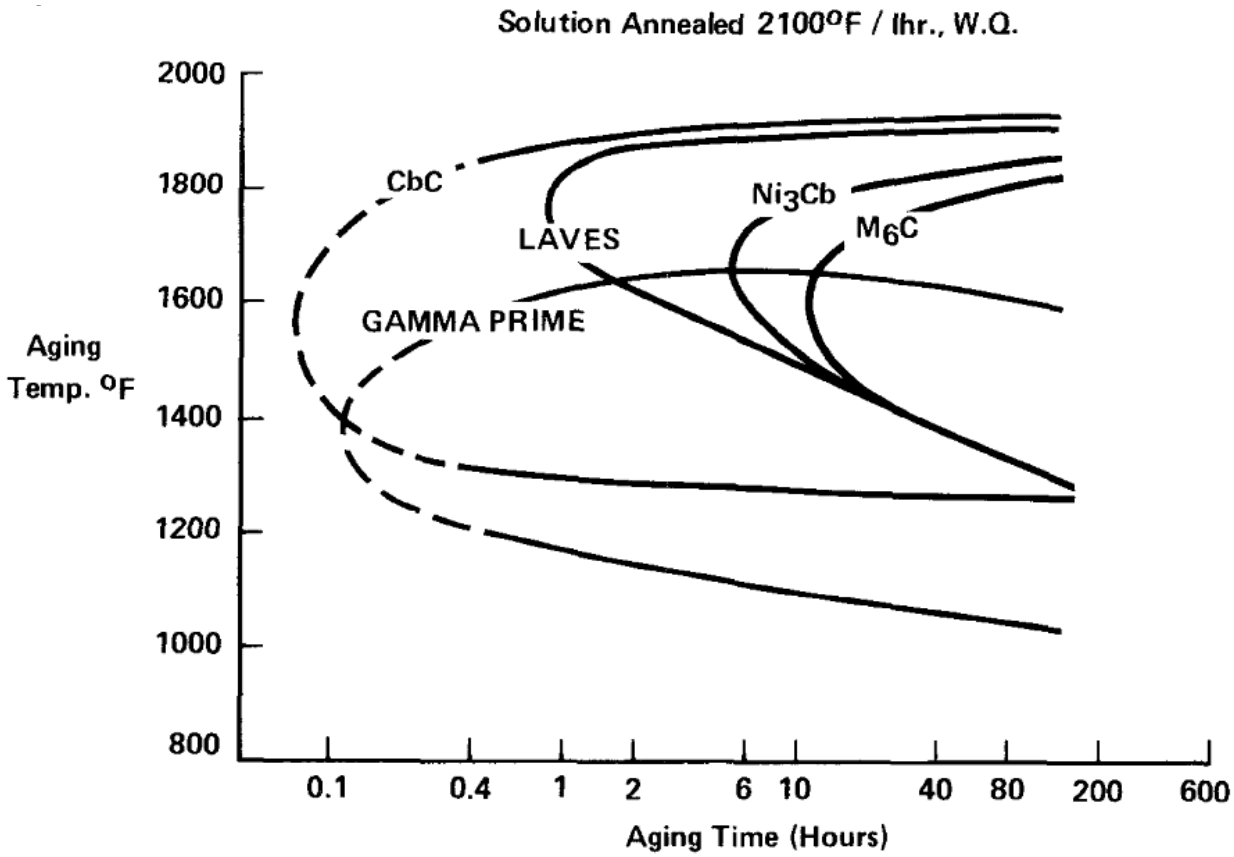

Figure 9: T-T-T diagram of solution annealed and water quenched INCO 718. All alloying phases enter solution by 1950 ^{0}F. Note: Niobium is referred to in this diagram as *Columbium* (Cb).

All phases enter solution by 1950 ^{0}F. Once in solution, they no longer act to pin grain boundaries, and as a result grain growth typically begins to can occur at temperatures above 1900 ^{0}F. The region of the HAZ nearest to the weldpool frequently experiences temperatures above 1900 ^{0}F, and thus, grain growth results in this region. Some theories[49,50,51] propose that during the period of grain growth that occurs in the HAZ during welding, migrating grain boundaries "sweep up" solute and impurity atoms, leading to enhanced grain boundary segregation. Presence of these segregates lower the melting temperature along the grain boundaries, and susceptibility to liquation cracking increases. High-temperature annealing treatments or hot-rolling production methods can also produce large grain sizes throughout the entire base metal, further

increasing the risk for liquation cracking. Maintaining a fine grain size requires that hot-working processes be kept below 1950 ^{0}F, where alloying phases reenter solution, and above 1750 ^{0}F, where recrystallization begins[52]. Smaller grain size in the base metal prior to welding has been shown to reduce liquation cracking through the reduced presence of laves clusters along grain boundaries, and an increased grain boundary area per unit volume. A fine grained microstructure provides a greater total interfacial area than a course grained microstructure, and reduces the concentration difference between the bulk and interface, and thus reduces the lineal fraction of the laves clusters. The net effect of smaller grains is then an increase in grain boundary liquation temperatures[53].

1.2.2 Comparison Alloy: Haynes 230

Haynes 230®, the comparison alloy that will be used in this study, is another nickel-based superalloy that derives its strength primarily through solid-solution strengthening. Haynes 230® (Table III) was developed in the 1980s by Haynes International, partially as a result of the need for lower cobalt-containing superalloys. It has found extensive use in aerospace and industrial gas turbine applications, because it exhibits good resistance to high-temperature oxidation and nitridation, and thermal and low-cycle fatigue. The use of Cr as an alloying element provides oxidation resistance through the formation of a protective oxide surface film, while Cr and W act as the solid-solution strengthening agents. Solid solutioning is achieved through the preferential partitioning of Cr and W to the γ matrix, which has two key effects. First, the presence of Cr and W reduces the matrix solubility of the precipitation-strengthening elements Al, Ti and Nb. And second, Cr and W expand the lattice parameter of the γ austenite. This expansion increases the degree of mismatch with coherent strengthening precipitates, and reduces stacking fault energy, thus impeding cross-slip at elevated temperatures[54].

The presence of W also leads to the formation of tungsten-carbides, further enhancing the strength properties. Haynes 230® has high thermally stability because it does not form many of the deleterious phases, such as laves, μ, σ and Ni_3Nb, that other nickel-based superalloys tend to form, while its good low-cycle fatigue life comes from the minimal effect of aging relative to other heat resistant alloys[55]. Haynes 230® is generally considered readily weldable with gas-tungsten arc welding (GTAW), gas-metal arc welding (GMAW), shielded medal arc welding (SMAW), and resistance welding techniques, with no requirement for pre or post weld heat treatment processes[56]. However, solidification and liquation cracking have been reported during the welding process. Solidification cracking is attributed to the segregation of Cr and W to solidification boundaries and the resulting solidification temperature depression, while liquation cracking is thought to be a product of constitutional liquation and grain boundary wetting due to the presence of boron[57]. Haynes 230 also has a comparable thermal diffusivity to INCO 718 at temperatures within the range experienced during testing. At 1800 ^{o}F, Hanyes 230 has a thermal diffusivity of $44.4x10^{-3}$ cm^2/sec, as listed by the manufacturer,[58] while INCO 718 is calculated to be $74.80x10^{-3}$ cm^2/sec based on published data[59]. This amounts to a difference of less than 13%. For these reasons, it will serve as a suitable comparison alloy for INCO 718.

Table IV – Complete Composition of Haynes 230®

Chemistry: Weight %

Ni[a]	Co	Cr	Mo	W	Fe	Si	Mn	C	Al	B	La
57	5*	22	2	14	3*	0.4	0.5	0.10	0.3	0.015*	0.02

[a] As Balance *Maximum

1.3 Testing Equipment

Gleeble® thermomechanical simulations and longitudinal Varestraint (VARiable RESTRAINT) testing are two common, frequently used methods of evaluating alloys weldability. Both were used in this study.

1.3.1 Gleeble® Test Apparatus

The first Gleeble® test apparatus was originally designed and built by Dr. Warren Savage, Dr. Ernest Nippes, and Dr. Hugo Ferguson, at Rensselaer Polytechnic Institute. In 1957 they founded Dynamic Systems, Inc., the company which now produces and sells Gleeble® test apparatuses worldwide. They were successful in building the first ever machine that could simulate welding processes in a lab setting, with precise control over thermal conditions. This provided a much more effective way of evaluating microstructural evolution and development in the heat affected zone (HAZ) of a weld[60]. The Gleeble® achieves this by fixing machined samples, typically in rod form, between two water-cooled copper grips, while applying a low voltage, high amperage current. Thermocouples attached directly to the sample continuously monitor temperature, creating a closed-loop system, and providing a means to constantly adjust current flow to create a controlled thermal profile(Figure 10, Figure 11).

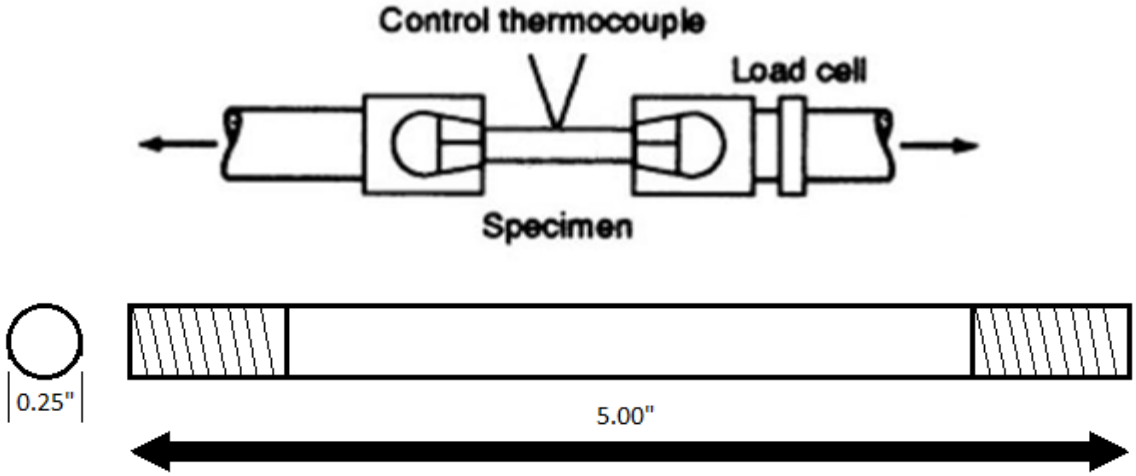

Figure 10: Schematic of the Gleeble® jaw setup, and a typical sample with dimensions noted. The threaded ends of a sample screw into the Gleeble® jaws during test set up.

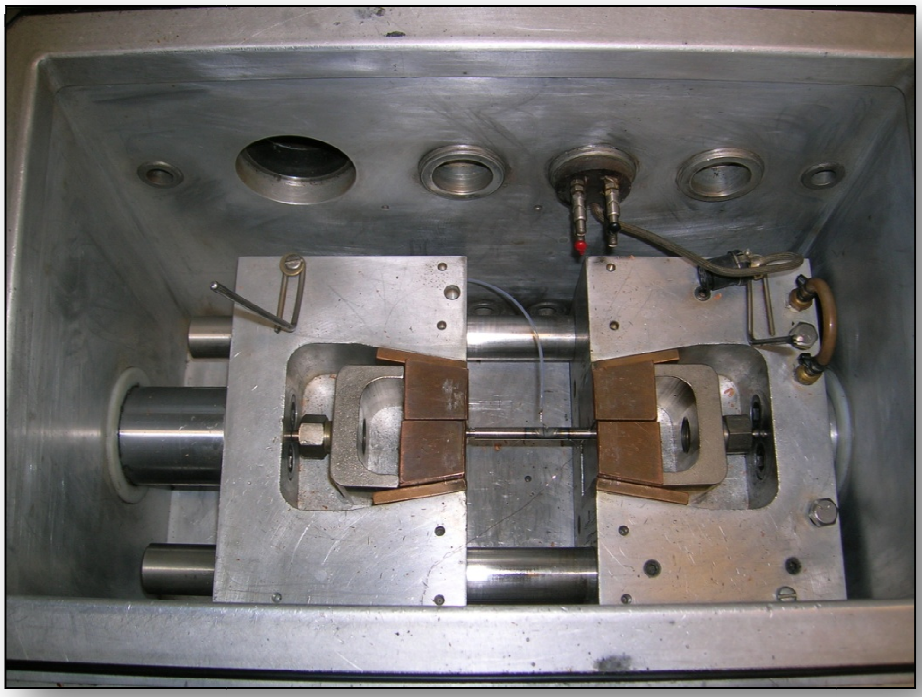

Figure 11: Gleeble® test chamber. The test sample is fixed into place between the water-cooled jaws. Attached thermocouples monitor temperatures.

Peak temperature and heating and cooling rates can both be closely monitored and adjusted. By controlling these parameters, duplication of thermal cycles experienced by regions of the HAZ can be produced on a larger physical scale than in an actual weld. Microstructural evolution as it would occur in the HAZ becomes easier to observe through post-testing optical microscopy of sectioned samples. Fracture surfaces can be examined through scanning electron microscopy to provide supplementary information on the nature of the failure. Additionally, the machines ability to apply a tensile or compressive load during testing alloys for an even greater range of experimentation. Ultimate tensile strength and ductility of an alloy can be measured as a function of temperature. The machine's data acquisition system automatically records a load profile while the sample is being elongated or compressed. Load can be constant, variable, or a combination of the two. Samples can be subject to a specified load, or tested to failure using a dynamic load. By utilizing these features, hot ductility testing can be performed. The hot ductility test is different from all other weldability tests. This approach characterizes the hot ductility and hot strength of a metal during welding and correlates this information to hot cracking susceptibility. In this test, samples are fractured by rapidly pulling them to failure at predetermined temperatures in either the on-heating or on-cooling parts of a simulated welding thermal cycle (Figure 12).

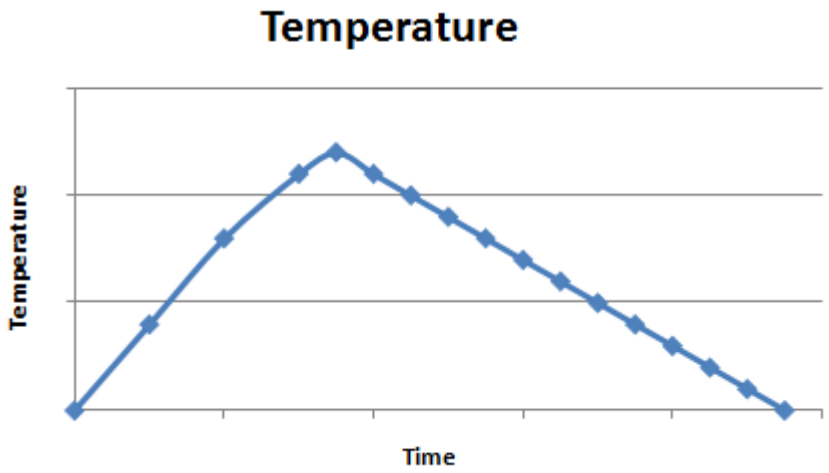

Figure 12: Schematic representation of a thermal cycle, with boxes indicating test temperatures

Ductility is measured as reduction in cross sectional area. Through these tests, three important characteristic temperatures for an alloy can be established: the nil-strength temperature (NST,) the nil-ductility temperature (NDT), and the ductility recovery temperature (DRT) (Fig X). The NST is defined as the temperature on heating where the strength of the alloy drops to zero. The NDT is the temperature on heating where the ductility of the alloy drops to zero. The DRT is the temperature during cooling from a peak temperature (T_p) above the NDT, where ductility has been restored to an arbitrary limit (often >5%)[61].

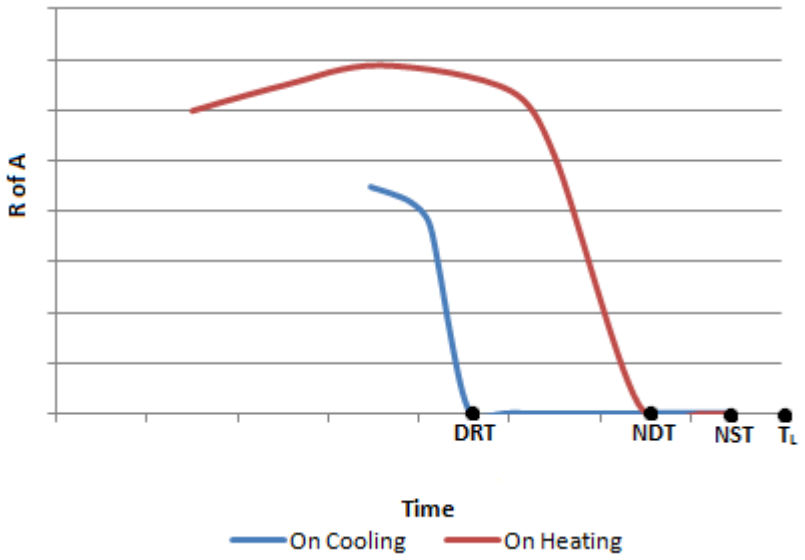

Figure 13: Typical hot ductility curves, with DRT, NDT, NST and T_L indicated

Exact determination of these two temperatures can be difficult, as it requires a high number of samples to do so. With a finite level of samples available, some estimation or interpolation technique must be used to determine these temperatures. Other valuable criteria can be gathered from hot ductility curves, including the rate of ductility recovery, the rate of strength recovery, the nil-ductility range (NDR), and the brittle temperature range (BTR). The NDR is the range of temperature during cooling from a temperature near melting at which observable ductility remains below the determined arbitrary limit[62] while the BTR is the temperature range between T_p and the DRT. The rate of ductility recovery is helpful in establishing an alloy's sensitivity to cracking. A more rapid ductility recovery would suggest resistance to cracking, whereas less rapid rate of ductility recovery may be an indicator of crack susceptibility. Similarly, for alloys with comparable ductility recovery rates, but different strength recovery rates, the alloy with a slower strength recovery rate would be more susceptible to cracking. Alloys with large nil-ductility ranges and brittle temperature ranges are typically more crack sensitive.

1.3.2 Varestraint testing

Varestraint testing is a simple method of determining an alloy's susceptibility to solidification and liquation cracking. It was developed in the 1960s at Rensselar Polytechnic Institute, and first introduced by W.F. Savage and C. D. Lundin. It was developed to satisfy the six "ideal test criteria" for hot cracking, as defined by Krammer, *et al,*[63] which are:

1. Ability to show a direct correlation with actual fabrication and service behavior.
2. Reproducibility of results with freedom from variation due to the human element.
3. Sensitivity to small changes in a test variable.
4. Ability to show the effects of several welding variables.
5. Economical preparation of specimens and running of test.
6. Applicability to all welding processes.

Through the use of an actual welding process, simple sample preparation, and the ability to apply a repeatable and known strain to samples, the Varestraint succeeded in fulfilling each criteria. Several variations of the original design have since been developed, including the subscale longitudinal Varestraint test, which was used in this study (Figure 15). The full scale test setup, developed by Savage and Lundin, utilized a cantilever design to fix samples in place. The pneumatic ram in this set up acted at one end of the sample, forcing the sample to conform to radiused die placed mid-sample. A sub-scale test method was developed to utilize smaller samples, making testing more economic, allowing for larger sample sizes and greater statistical significance for groups of testing. A typical sub-scale sample is shown in Figure 14, and a schematic of the sub-scale test

apparatus is show in Figure 15. During testing, an autonomous GTAW weld is produced, starting at the left end, and proceeding from left to right. At a predetermined location, the trailing arc trips the pneumatic ram, and the sample is forced to conform to the surface of a radiused die block. By doing so, liquation cracks are created in the weld HAZ.

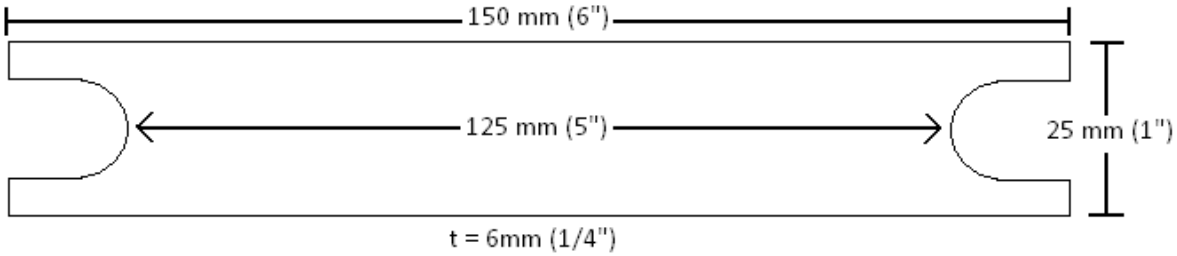

Figure 14: Varestraint Coupon, with dimensions noted.

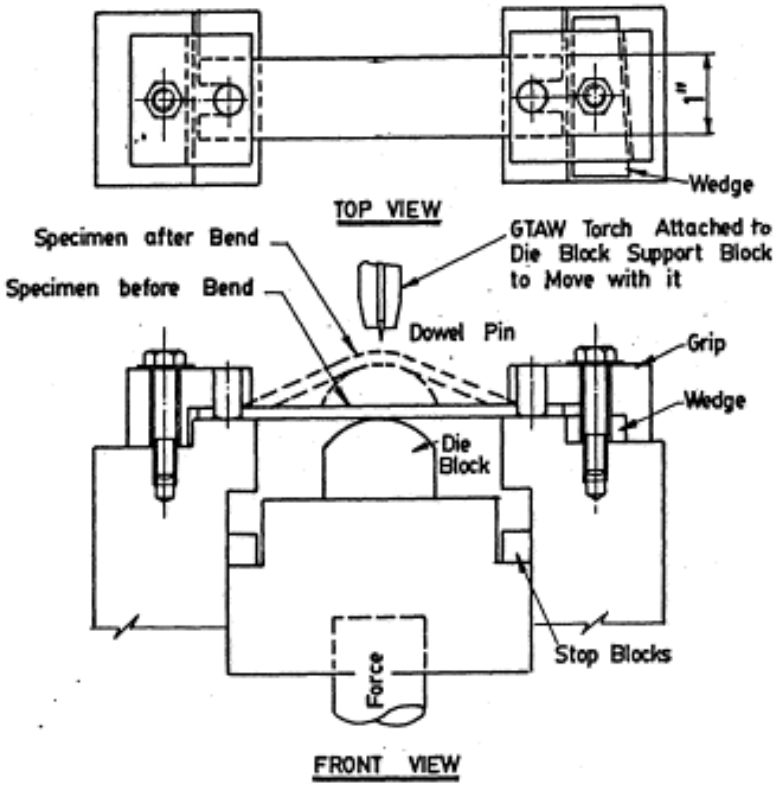

Figure 15: Schematic view of the longitudinal Varestraint test apparatus[64]

The augmented tangential strain induced in the coupon is approximated by

$$\varepsilon_t = t/2R \qquad \text{(Eq. 6)}$$

where t is the coupon thickness, and R is the radius of the die block. Consistency in the arc-gap is controlled either manually, through adjustment of the weld head height over the sample and monitoring of the current and voltage, or, in newer machines, through an automated process. The introduction of increasing levels of strain will eventually lead to the formation of cracks inside the solidifying weld pool, in the HAZ, or both. Cracks typically form radially along the trailing edge of the weld pool and in the HAZ. The advantage of this test method is that it created cracks at the surface, where maximum strain is produced, rather than internally, allowing for easier observation and analysis[65]. Post testing analysis is then done on each sample. Typically, the following data are collected for a Varestraint test: the number of cracks, the maximum crack length, and the total crack length, as a function of augmented strain. The lowest augmented strain level that produces cracking for a given set of weld parameters provides a quantitative cracking sensitivity index referred to as cracking threshold strain, or simply threshold strain. Changes in the threshold strain due to alterations in the welding process or parameters also provide a quantitative method of comparing welding procedures. Second, the maximum crack length for a given set of welding parameters and an augmented strain level provides a useful qualitative index for cracking sensitivity. Cracks normally extend into the HAZ in a direction perpendicular to the weld pool, and act as an indicator of the physical width of the HAZ and associated temperature range, for a given augmented strain level, in which cracking remains problematic. Finally, total combined crack length in the weld pool and in the HAZ for a given set of weld procedures and strain level can be the most useful qualitative measure of solidification

and liquation cracking, respectively. Varestraint testing is extremely useful in comparing crack sensitivity between alloys, as cracks can be generated in even the most crack-insensitive materials when exposed to a suitable level of augmented strain[66].

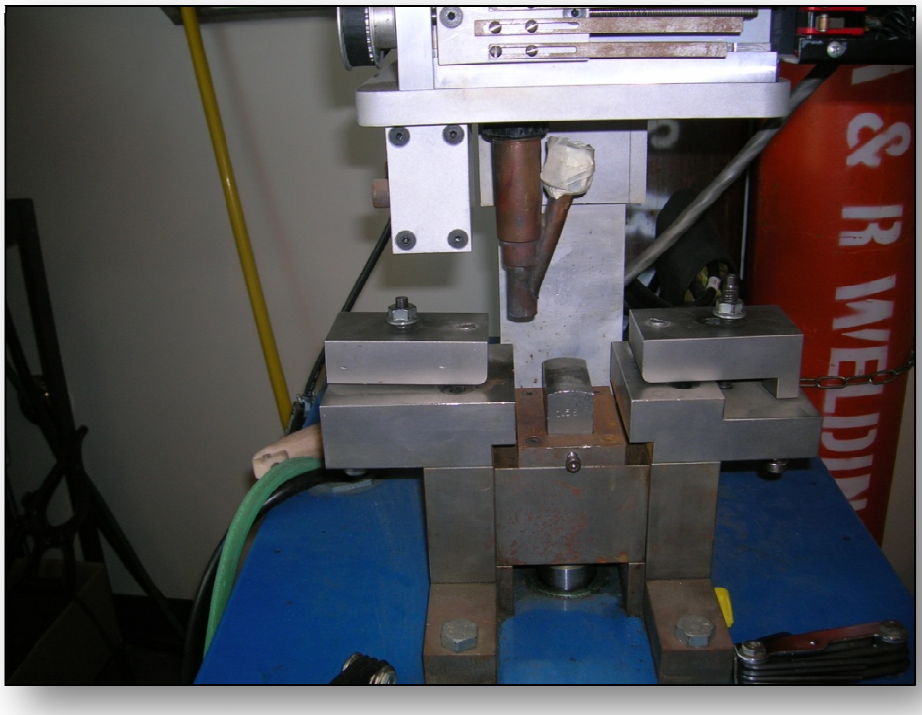

Figure 16: Varestraint test apparatus. Samples are fixed into either clamp, above the ram head. The TIG weld head travels from left to right, along the sample surface.

1.4 Broader Impacts

1.4.1 Economic benefits

As new designs look to utilize superalloys in innovative ways, research is often needed to provide greater understanding of the materials available. One such area of research is in determining *weldability.* The American Welding Society (AWS) defines weldabilty as "*the capacity of a material to be welded under the imposed fabrication conditions into a specific, suitably designed structure and to perform satisfactorily in the intended service.*[67]" Weldability is a critical portion of development of commercial use

super-alloys.[68] Weldability tests exist in a number of different forms, all of which can provide some base level of comparison between materials. Newly developed alloys' uses are limited until such testing is completed. United Technologies is reliant on such work to qualify a suitable super-alloy for use in the current design of their next generation jet engine[69].

A quantifiable study on the weldability of INCO 718 has the potential to benefit not only United Technologies, but the greater materials and manufacturing community in a number of ways. Although similar studies have been performed on INCO 718 before, this project can still yield valuable data. Results of weldability studies can vary from alloy to alloy, and even from heat to heat of a single alloy. The effects of slight changes in major and minor alloying elements within the limits defined by the alloy type can produce significant differences in overall crack susceptibility, critical temperature range of susceptibility, and strain levels that will induce cracking. Generating new data in a method familiar to the industries that rely on such studies will help to further the understanding of INCO 718, while providing qualitative and quantitative values specific to a heat United Technologies looks to utilize in future designs. INCO 718 is most widely used superalloy in the world[70] accounting for approximately 35% of all superalloy production[71], yet it is still limited to in-use temperatures of approximately 1200 ^{0}F, due to the instability of its main strengthening phase γ''[72]. Understanding the high-temperature instability of this alloy, and the mechanisms that control it, are critical in improving upon its design and increasing the number of suitable applications. Each new heat of the alloy produced must be tested to determine its high temperature limits, and these tests must be done in a way that allows for direct comparison to previous results.

Since the introduction of turbine engines in aircraft, dating back to the 1940s, materials capability has been the limiting factor on performance[73]. The peak temperature a turbine blade material can withstand are a critical parameter in determining the maximum efficiency an engine can achieve. Additionally, cost efficient commercial application of nickel-based superalloys has been severely limited by the difficulty in joining them through conventional welding techniques during the manufacturing process, and during repair[74]. An increased capacity to weld newly developed heats of INCO 718 could lead to decreased manufacturing costs, and broader adoption throughout turbine designs. Improvements to INCO 718's high-temperature properties could lead to the use of higher turbine inlet temperatures (TIT) in gas-turbine engines, a key factor in increasing system efficiency. Because the net work output of a gas turbine engine is directly related to power output per unit mass flow of fuel, increasing the gas turbine inlet temperature is one effective method of increasing power output for a given mass flow of fuel[75]. Higher temperatures call for more strict design constraints, and thus the selection of components that will withstand the environment. An increase in efficiency of gas-turbine engines provides an economic improvement for a number of industries ranging from domestic power production to aerospace and commercial air travel. This could lead to decrease in energy costs and cheaper travel. Increased efficiency also opens up the possibility for gas-turbine engines to replace more dated technologies in other industries, such as the high-emission two-stroke diesel engines used in almost all large container ships, tankers, and bulk carriers. Cost of international shipping of bulk goods could experience a reduction, while lessoning environmental impact in terms of sulfur oxides, nitrogen oxides, carbon monoxide, hydrocarbons, and particulate matter emissions[76]. Similar financial and environmental

gains could be extracted from any industry reliant on gas-turbine engines as an energy or propulsion source.

1.4.2 Environmental benefits

The world's energy needs depend on the effective use of turbine-systems, specifically steam, to provide power. Currently, 80% of the world's energy is produced by processes that utilize steam turbines, with the potential for those numbers to climb even higher[77]. Growing interest in nuclear energy means the continued demand for efficient steam turbine systems. The benefits are again both economic and environmental in improving and maximizing these systems. Energy demands continue to grow, while the concern over the environmental impacts of increased energy production remains at the forefront of current global issues. With "current goals of the U.S. Department of Energy's Advanced Power Systems Initiatives include[ing] power generation from coal at 60% efficiency, which would require steam temperatures of up to 760℃[78]," clearly advances in materials properties will be required. These properties include ductility and strength loss at elevated temperatures and crack susceptibility during the production process and while in use. The availability of suitable materials will play a critical role in the advancement of energy production. The value of improving our understanding of current and newly developed super-alloys that could be utilized in energy production extends world-wide.

1.4.3 Stakeholders

A number of key stakeholders exist in this project. Most directly is the United Technologies materials and processing group. The alloy system being tested was specifically selected by the materials and processing group as a potential candidate for future use. With applications for use already in mind, United Technologies will be

awaiting the results of this study. They will be expecting well developed conclusions, clear supporting data, and documentation of the test methods utilized in examining the microstructural evolution, hot ductility dip and crack susceptibility of the selected alloy. Beyond the explicit benefits relating to United Technologies lie the benefits to the greater materials community. Any individual, group, company or organization looking to utilize this alloy system for high temperature applications could gain from this research. By using standard and frequently used test methods to obtain and analyze reproducible results, and clearly supporting any conclusions drawn from these results, a strong basis from which others can build off of will be provided. Finally, the Cal Poly Materials Engineering Department has a vested interest in the success of this project. The project exists as both an internal method of evaluation, and a tool to showcase the department's ability to produce successful young engineers. The department's needs are unique from others, and are based more on meeting deadlines, documenting all research, developing clear test methods, effectively communicating with project supporters, and producing a final written report of all work completed.

1.4.4 Design Constraints

The scope of this project was limited by several factors. Results were based on the two previously mentioned methods of weldability testing: Gleeble® thermomechanical simulation and Varestraint testing. The combination of Gleeble® and Varestraint testing can provide valuable results, but are not entirely indicative of in-use properties of tested alloys. They instead provide a method of comparison between alloys or alloy groups. Results will require application-specific analysis by any end user looking to benefit from this research. Economics and manufacturability also play a deciding factor in the scope of this project. Levels of testing were limited by sample size. Costs of bulk metal for many nickel-based superalloys are currently high. Added to that

is the time and energy needed to prepare coupons for testing, in the form of round bars for Gleeble® testing, and flat stock for Varestraint testing.

Nickel-based alloys are commonly categorized as hard-to-machine materials. A combination of low thermal conductivity, tendency to strain-harden, and inclusion of hard carbides and intermetallic phases makes ordinary machining tools inadequate. Even carbide bits require extremely low cutting speeds (compared to steel or aluminum). Ranges of specialty machining tools and machining processes have been developed specifically for the machining of nickel-based superalloys. These tools are typically made from cutting ceramics or polycrystalline cubic boron nitride (PCBN), and rely on high hardness and resistance to thermal wear. Costs of these tools are higher than normal machining equipment, but do allow for higher feed rates than even those attained by carbide bits. The high cost of bulk material and machining processes combined with a test plan that utilizes destructive methods leads to a high overall cost of testing, and an effective limitation on the number of coupons available[79].

2.0 Methods and Materials

Mechanical testing was divided into two categories: Gleeble® testing and Varestraint testing. Gleeble® testing was performed to determine the reduction in on heating and on cooling ductility and strength as a function of test temperature, and to determine the characteristic temperatures discussed previously: NDT, NST, and DRT. Varestraint testing was performed to evaluate liquation crack susceptibility due to strain, during welding.

2.1 Gleeble® Hot Ductility Testing

Hot ductility tests were performed using a Gleeble® HAZ 1000 thermomechanical simulator. All tests were performed under an Argon atmosphere. Standard specimens were 6.35mm (0.25in.) in diameter and 113mm (4.5 in.) long. A free span of 25mm (1in.) was used in each test. Two thermocouple wires made of Platinum and Platinum Rhodium were percussion welded at the center point of each sample and used to both control and record temperature. The first test performed was the Nil strength test (NST), done to determine the temperature at which a samples strength drops essentially to zero. A slow heating temperature profile was chosen, with a peak temperature set at 2300˚F for the INCO 718 samples, and 2500 ˚F for the Haynes 230 samples. The loaded test sample was subjected to a constant 20 lb load during heating. The lowest temperature at which it failed due to the presence of sufficient liquid film buildup along grain boundaries was determined to be the Nil strength temperature (2251 ˚F for INCO 718, 2411 ˚F for Haynes 230). This value provided the upper limit of testing temperatures for either alloy and defined a peak temperature for subsequent thermal cycling. On-heating tests were done by heating the samples to the proscribed peak temperature following the program shown in Table V. Once the target temperature was reached, samples were pulled to failure at a stroke rate of 5cm/sec. (2 in./sec). The on-

cooling tests were performed by heating the samples to the target peak temperature following the program shown in Table V, and cooling to the test temperature at a rate of 60^0 C per second. Once the test temperature was reached, on-cooling samples were pulled to failure at a stroke rate of 5cm/sec. (2 in./sec). The rapid stroke rate was employed to reduce the sample temperature change during testing. Sample ductility is presented as percent reduction – in – area (%R/A) at fracture. The sample diameter at fracture was measured using veneer calipers and a digital stereoscope. The conditions for the hot ductility test are summarized in Table V.

Table V: Hot Ductility test Conditions

Conditions	
Atmosphere	Ar
Free Span	25mm
Stroke Rate	5 cm/sec
Heating Rate	Program
Cooling Rate	60 deg C/sec
Hold time at test T	0.01 sec

The Gleeble® system automatically records the temperature profile that was followed as well as the load at failure. From the temperature profile peak temperature and temperature at failure can be determined. A total of nine Gleeble® tests were performed for INCO 718: four on heating, and five on cooling, at target temperatures of 1600˚F, 2000˚F, 2100˚F, 2200˚F, and 1600˚F, 1700˚F, 1800˚F, 1900˚F, and 2100˚F, respectively. On-cooling tests used a peak temperature of 2250˚F before cooling to the target temperature. A total of fifteen tests were performed for Hanyes 230: four on-heating, and eleven on-cooling, at target temperatures of 2050 ˚F, 2200 ˚F, 2240 ˚F, 2330 ˚F, and 1800 ˚F, 1900 ˚F, 1990 ˚F, 2040 ˚F, 2090 ˚F, 2100 ˚F, 2140 ˚F, and 2190 ˚F, respectively. On-cooling tests used a peak target temperature of 2375 ˚F.

2.2 Varestraint Testing

Varestraint testing was performed using a Varestraint Moving Torch test apparatus, Model LT 1100, paired with a Miller Dynasty 300SD power source. Test samples were 5.25 in x 1.0 in flat stock of INCO 718, with a thickness of 0.125 in. Samples were tested at each of five different levels of augmented strain: 0.25%, 0.5%, 1%, 2%, and 4%. Tests were triply replicated for INCO 718 and doubly replicated for Haynes 230. Movement of the TIG weld head over the sample, and activation of the pneumatic ram during testing was automated. Height of the TIG weld head above the sample was manually controlled to maintain an arc voltage of 10 volts during welding. For each test it was adjusted at the beginning of the pass in order to achieve a voltage and current rating as near to 10 volts and 98 amps as possible. Movement of the weld head and flow of the shielding gas argon was manually stopped after the ram engaged, with a two second delay between stopping motion and the start of a 15 second delay in extinguishing gas flow. This ensured the weld pool was still protected while in liquid form, and prevented oxidation issues. Each sample was quenched in water after being removed from the Varestraint, and set aside for later analysis.

2.3 Analysis methods

2.3.1 Gleeble® samples

Gleeble® samples were analyzed using Scanning Electron Microscopy (SEM), and optical microscopy. Due to the destructive nature of preparing the optical microscopy samples, SEM was performed first. The goal of SEM was to observe and record the fracture surfaces created during failure. Samples were prepared by first sectioning them down to a shorter length that would fit within the SEM chamber. After sectioning, samples were cleaned ultrasonically in an alcohol bath, and mounted on the appropriate hardware for placement in the SEM. Surfaces were imaged at a variety of

magnifications, with attention being paid to significant or interesting features. Optical microscopy samples were prepared using one side of the original sample, thus preserving the other for potential future SEM analysis. Samples were sectioned in half longitudinally using a TechCut4 diamond saw, and mounted in Bakelite. They were then wet sanded, before being polished. A Texmet hard polishing pad was used with a 6 micron solution, while a Microcloth polishing cloth was used at the 3 micron level. Samples were then etched using a solution of 1M HCl + 3% H_2O_2, at a ratio of 65:35. Microstructures were then observed and recorded.

2.3.2 Varestraint Samples

Varestraint samples were analyzed by counting the flaws present in each sample, using a digital stereoscope and accompanying software. Images of the flaws were captured, and using the digital imaging software, length was measured on the captured images. The software was calibrated each time it was used, employing a stage micrometer. The length of the flaw was defined as the linear distance between the crack tip and the fusion line, projected in a direction perpendicular to the fusion line. Results for each flaw on each sample were recorded and saved.

3.0 Results

3.1 Gleeble® Testing results

In this study, both INCO 718 and Haynes 230 were investigated. The on-heating and on-cooling strengths of each material are listed in Table V and

Table VI. The data is graphically represented in Figure 17 and Figure 18 respectively. The on-heating and on-cooling ductility for each alloy is presented in tables S and T. The on-heating and on-cooling ductility curves are shown in Figure 19 and Figure 20.

The NST for the INCO 718 was measured as 2251 ^{o}F and that of the Haynes 230 as 2420 ^{o}F. The on-heating ductility of the 718 decreased rapidly above 2000 ^{o}F and approached zero at 2200 ^{o}F. On cooling from the NST, the ductility of this alloy did not recover significantly until a temperature below 1930 ^{o}F was reached. Thus for this material the NDT was 2188 ^{o}F and the DRT was 1924 ^{o}F, using 5% reduction in area as the arbitrary ductility recovery point, and linear extrapolation to indentify the temperature.

The behavior of the Haynes 230 material was similar. The on-heating ductility of the 230 decreased rapidly above 2200 ^{o}F and approached zero at 2340 ^{o}F. On cooling from the NST, the ductility of this alloy did not recover significantly until a temperature below 2100 ^{o}F was reached. Thus for this material the NDT was 2341 ^{o}F and the DRT was 2147^{o}F using 5% reduction in area as the arbitrary ductility recovery point, and linear extrapolation to identify the temperature. Moreover, the ratio of the ductility recovered on-cooling to the ductility measured on-heating at a given temperature was

lower for the Haynes 230. The Haynes 230 also exhibits a ductility dip below 2150 °F on-cooling.

Table VI– Load and Strength at failure, INCO 718

Heat cycle	Target Temperature at Failure (F)	Target Peak Temperature (F)	Actual Peak Temperature (F)	Actual Temperature at Failure (F)	Load at Failure (lbs)	Strength (psi)
On-heating	1600	1600	1577	1577	4836	98518
On-heating	2000	2000	1987	1987	2227	45368
On-heating	2100	2100	2073	2073	2080	42373
On-heating	2200	2200	2188	2188	925	18844
On-cooling	1600	2250	2251	1626	3906	79572
On-cooling	1700	2250	2225	1690	3687	75111
On-cooling	1800	2250	2244	1870	3064	62419
On-cooling	1900	2250	2230	1930	1733	35304
On-cooling	2100	2250	2246	2130	635	12936
Nil-Strength	Nil Strength	Nil Strength	2251	2251	20	407
Nil-Strength	Nil Strength	Nil Strength	2273	2273	20	407

Table VII – Load and Strength at Failure, Haynes 230

Heat cycle	Target Temperature at Failure (F)	Target Peak Temperature (F)	Actual Peak Temperature (F)	Actual Temperature at Failure (F)	Load at Failure (lbs)	Strength (psi)
On-heating	2050	2050	2058	2058	2705	55134
On-heating	2200	2200	2200	2200	2036	41498
On-heating	2240	2240	2249	2249	1829	37279
On-heating	2330	2330	2341	2341	1343	27373
On-cooling	2190	2375	2390	2202	1321	26925
On-cooling	2140	2375	2153	2153	1218	24825
On-cooling	2100	2375	2390	2112	2437	49671
On-cooling	2090	2375	2385	2090	2529	51546
On-cooling	2040	2375	2387	2046	2712	55276
On-cooling	1990	2375	2388	1995	2878	58660
On-cooling	1900	2375	2402	1914	3279	66833

On-cooling	1800	2375	2395	1810	3711	75638
Nil-Strength	Nil-Strength	Nil-Strength	2419	2419	20	408
Nil-Strength	Nil-Strength	Nil-Strength	2441	2419	20	408
Nil-Strength	Nil-Strength	Nil-Strength	2411	2419	20	408

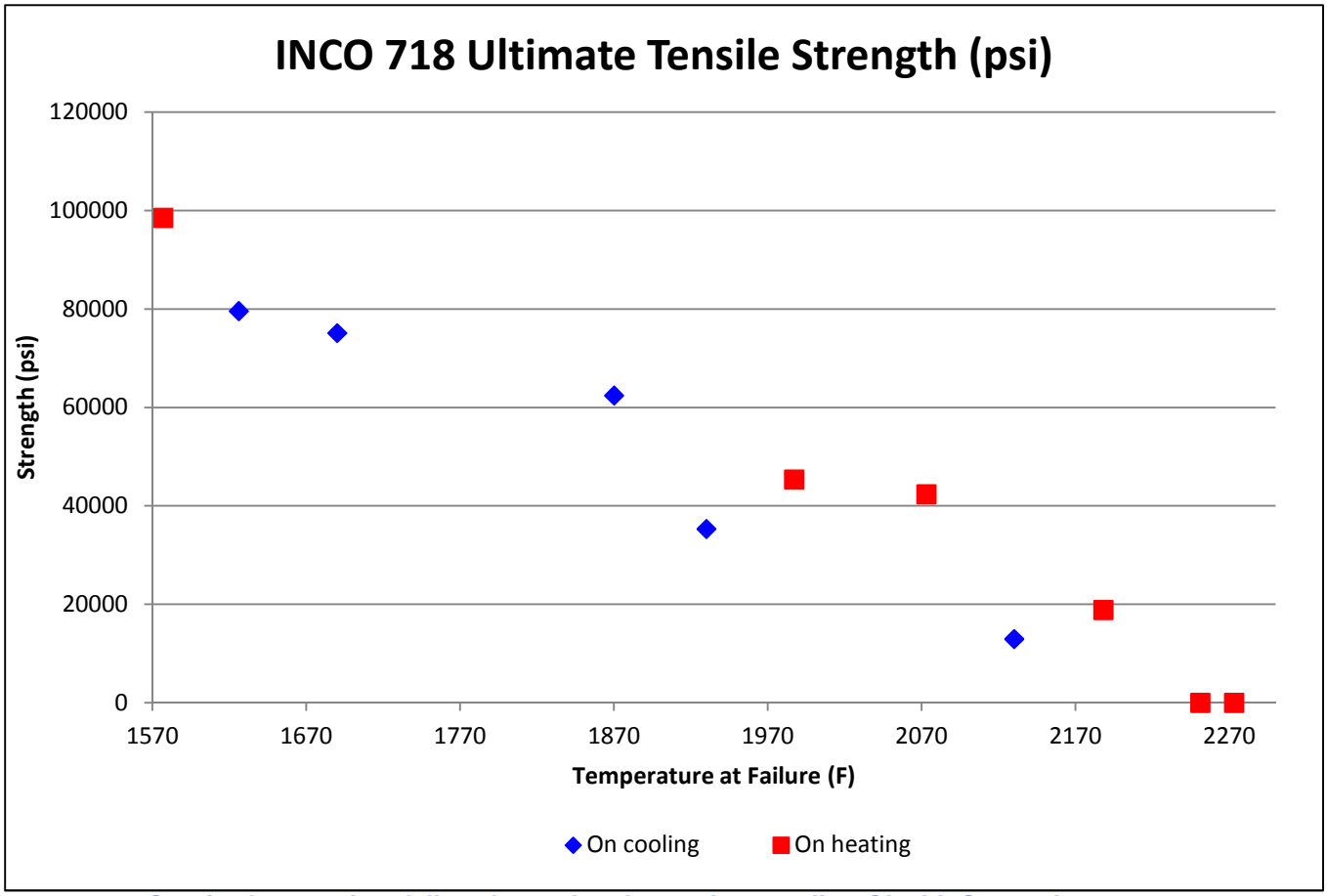

Figure 17: Graph of strength at failure for on-heating and on-cooling Gleeble® samples, INCO 718.

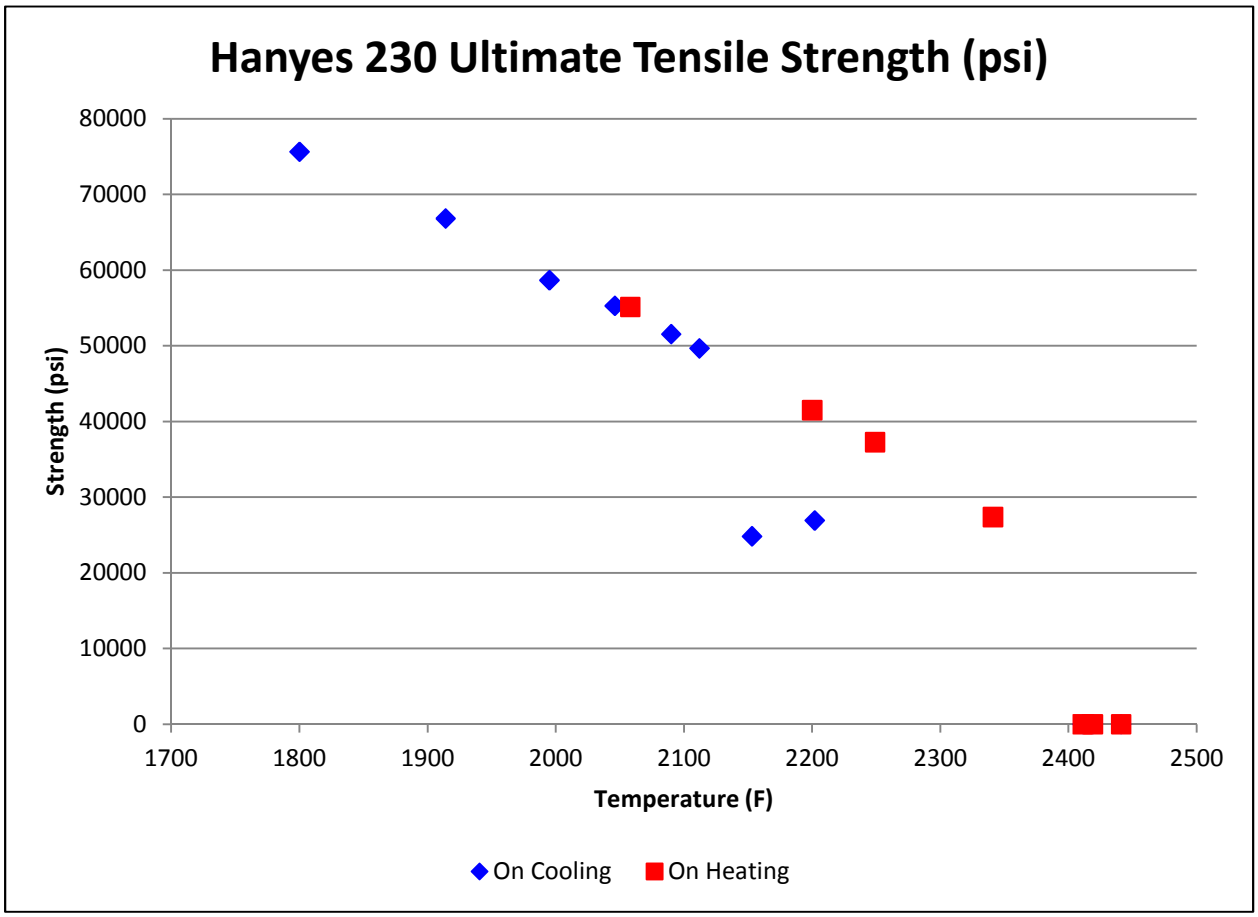

Figure 18: Graph of strength at failure for on-heating and on-cooling Gleeble® samples, Haynes 230

Table VIII – Percent reduction in cross-sectional area, INCO 718

Heat cycle	Target Temperature at Failure (F)	Target Peak Temperature (F)	Actual Peak Temperature (F)	Actual Temperature (F)	Reduction in Area (%)
On-heating	1600	1600	1577	1577	71
On-heating	2000	2000	1987	1987	66
On-heating	2100	2100	2073	2073	57
On-heating	2200	2200	2188	2188	1
On-cooling	1600	2250	2251	1626	61
On-cooling	1700	2250	2225	1690	54
On-cooling	1800	2250	2244	1870	54
On-cooling	1900	2250	2230	1930	0
On-cooling	2100	2250	2246	2130	0
Nil-Strength	Nil-Strength	Nil-Strength	2251	2273	0
Nil-Strength	Nil-Strength	Nil-Strength	2273	2249	0

Table IX – Percent Reduction in cross-sectional area, Haynes 230

Heat cycle	Target Temperature at Failure (F)	Target Peak Temperature (F)	Actual Peak Temperature (F)	Actual Temperature at Failure (F)	Reduction in Area (%)
On-heating	2050	2050	2058	2058	69
On-heating			2200	2200	64
On-heating	2240	2240	2249	2249	51
On-heating	2330	2330	2341	2341	2
On-cooling	2190	2375	2390	2202	2
On-cooling	2140	2375	2153	2153	1
On-cooling	2100	2375	2390	2112	37
On-cooling	2090	2375	2381	2090	42
On-cooling	2040	2375	2387	2046	45
On-cooling	1990	2375	2388	1995	29
On-cooling	1900	2375	2402	1914	22
On-cooling	1800	2375	2395	1810	37
Nil-Strength	Nil-Strength	Nil-Strength	2419	2419	0
Nil-Strength	Nil-Strength	Nil-Strength	2441	2419	0
Nil-Strength	Nil-Strength	Nil-Strength	2411	2419	0

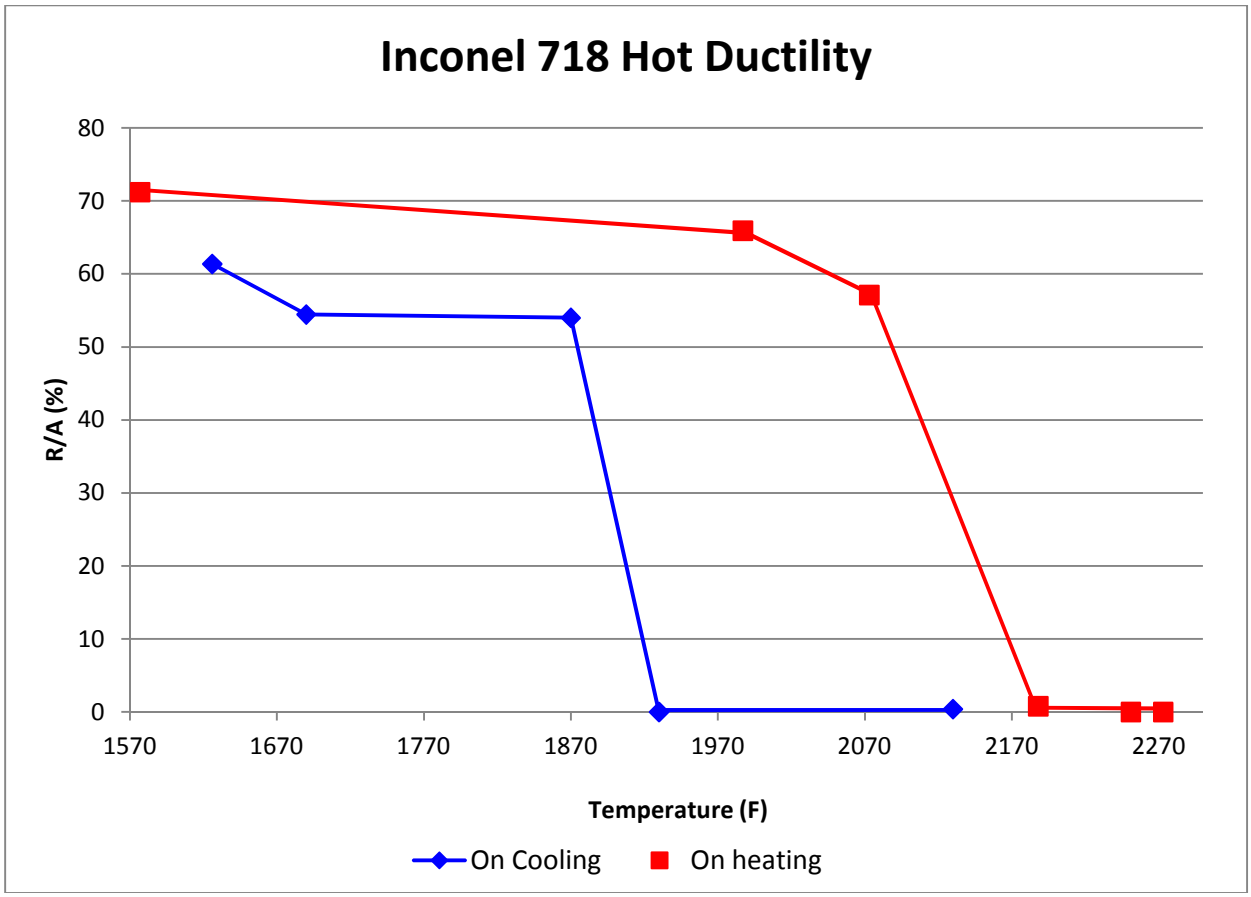

Figure 19: Percent reduction in cross-sectional area as a measure of hot ductility for on-heating and on-cooling Gleeble® samples, INCO 718

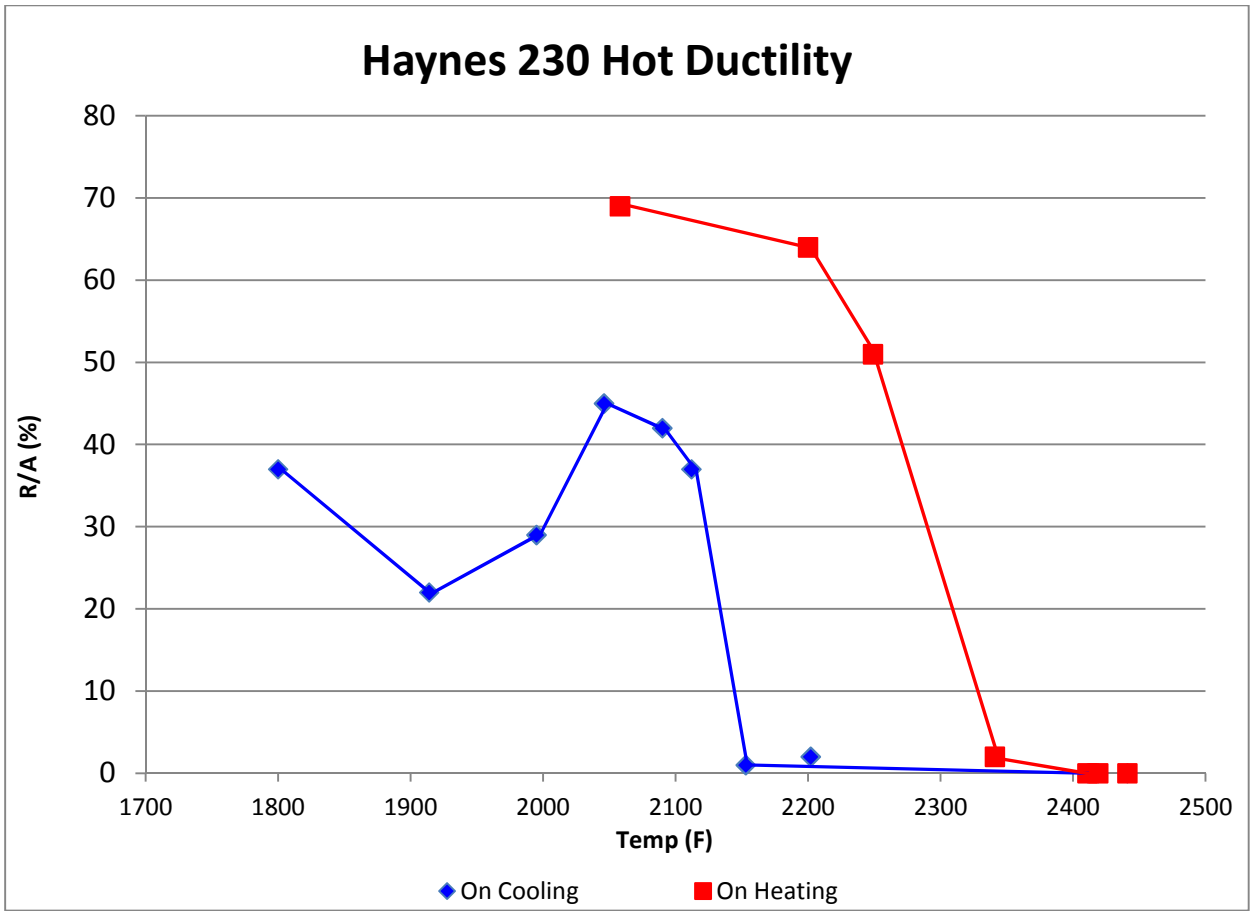

Figure 20**:** Ductility measured as a percent reduction in area, as a function of temperature for on-heating and on-cooling hot ductility tests.

3.2 Varestraint Testing results

Varestraint testing results differed significantly between INCO 718 and Haynes 230. The threshold and saturation limits for MCL (

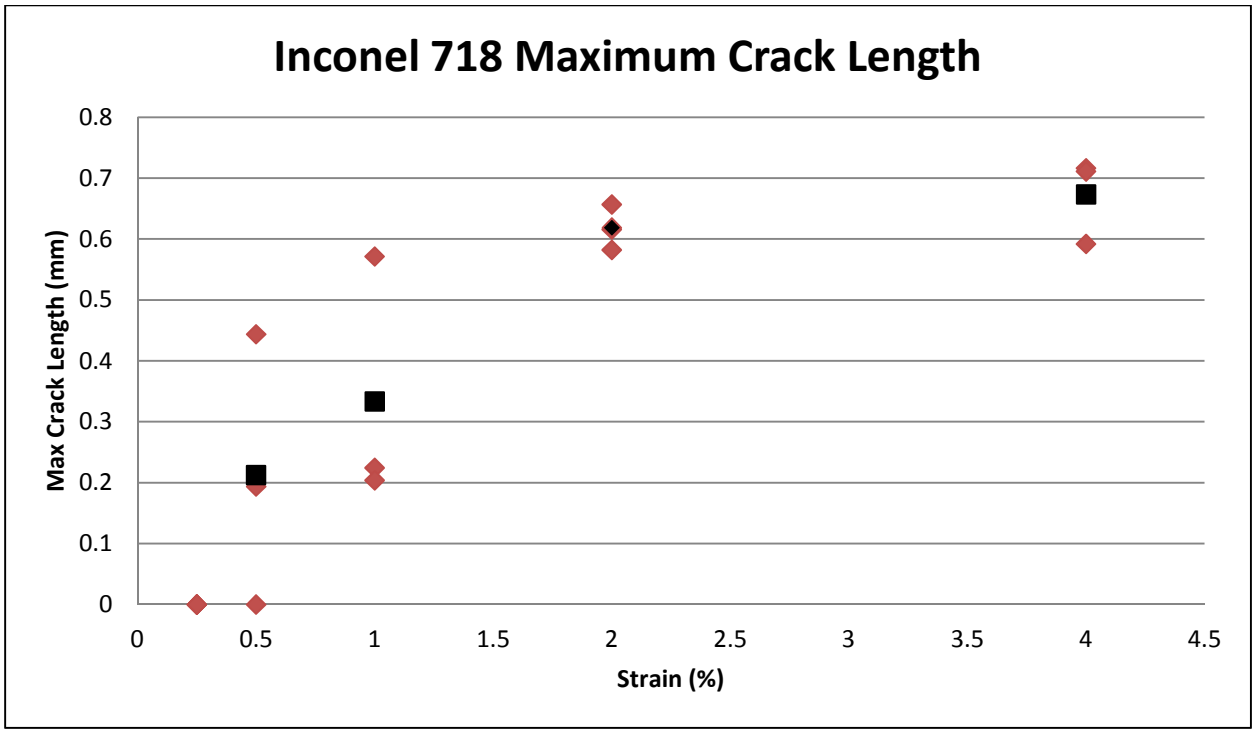

Figure 21,

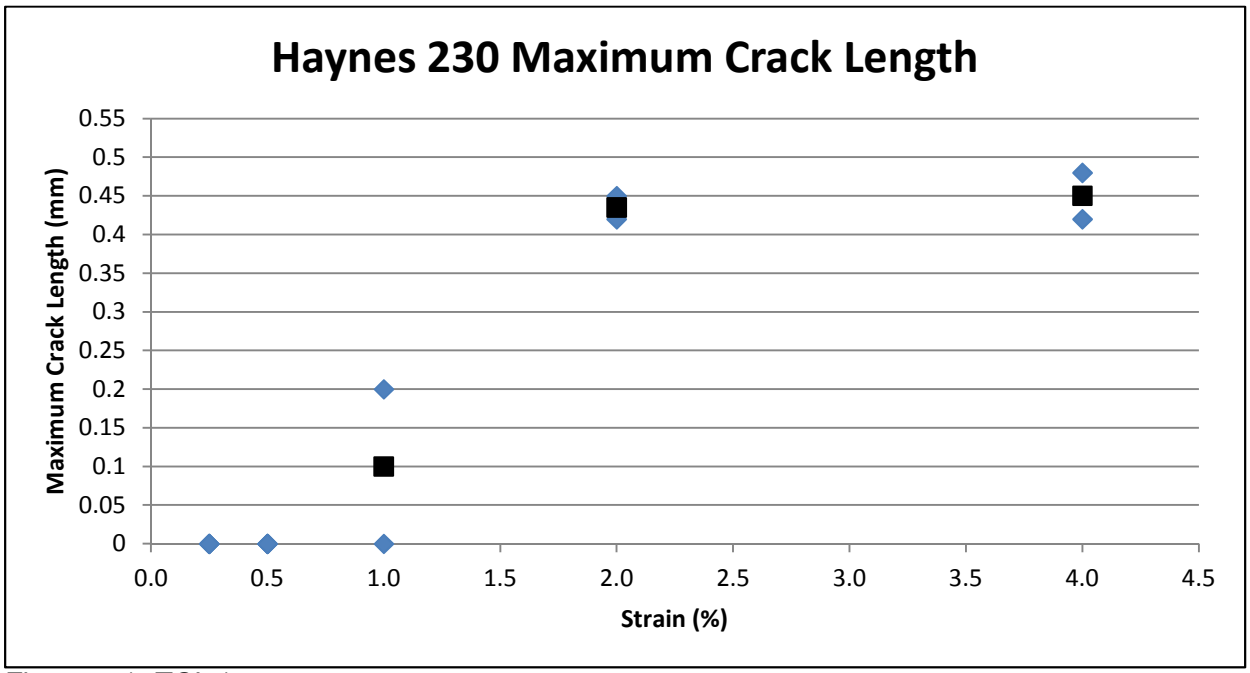

Figure 22), TCL (

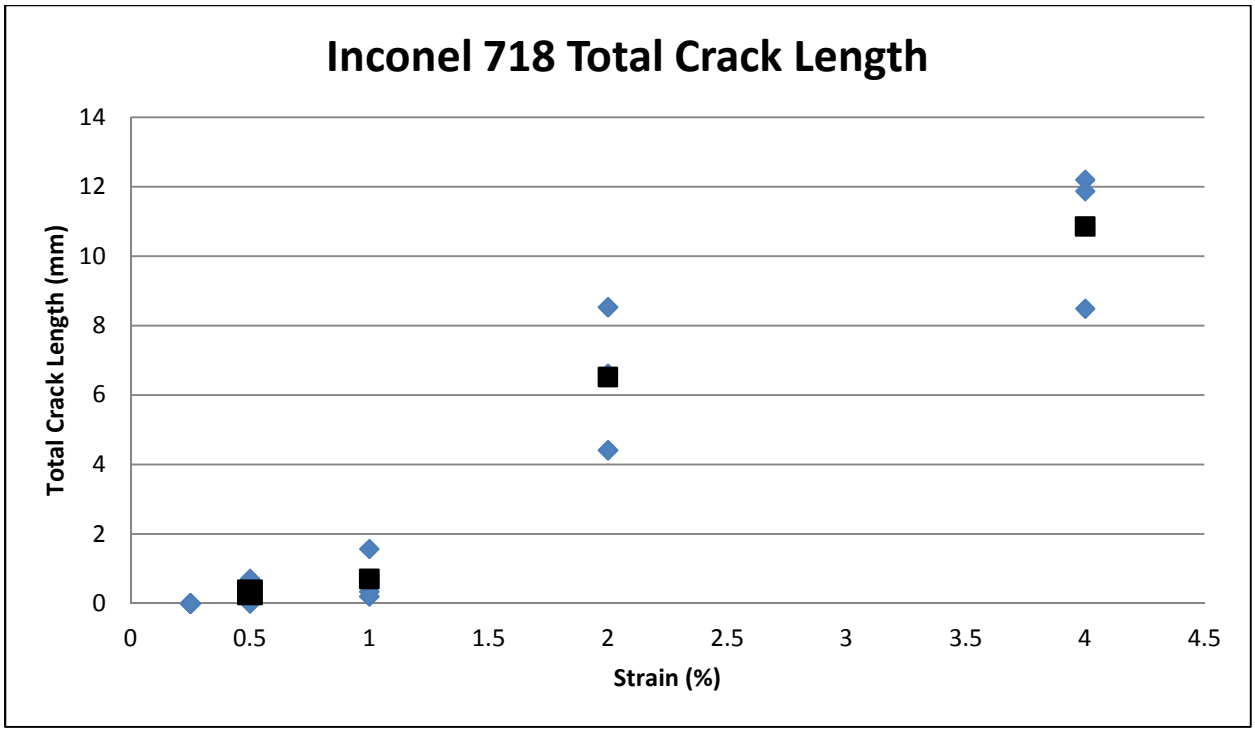

Figure 23,

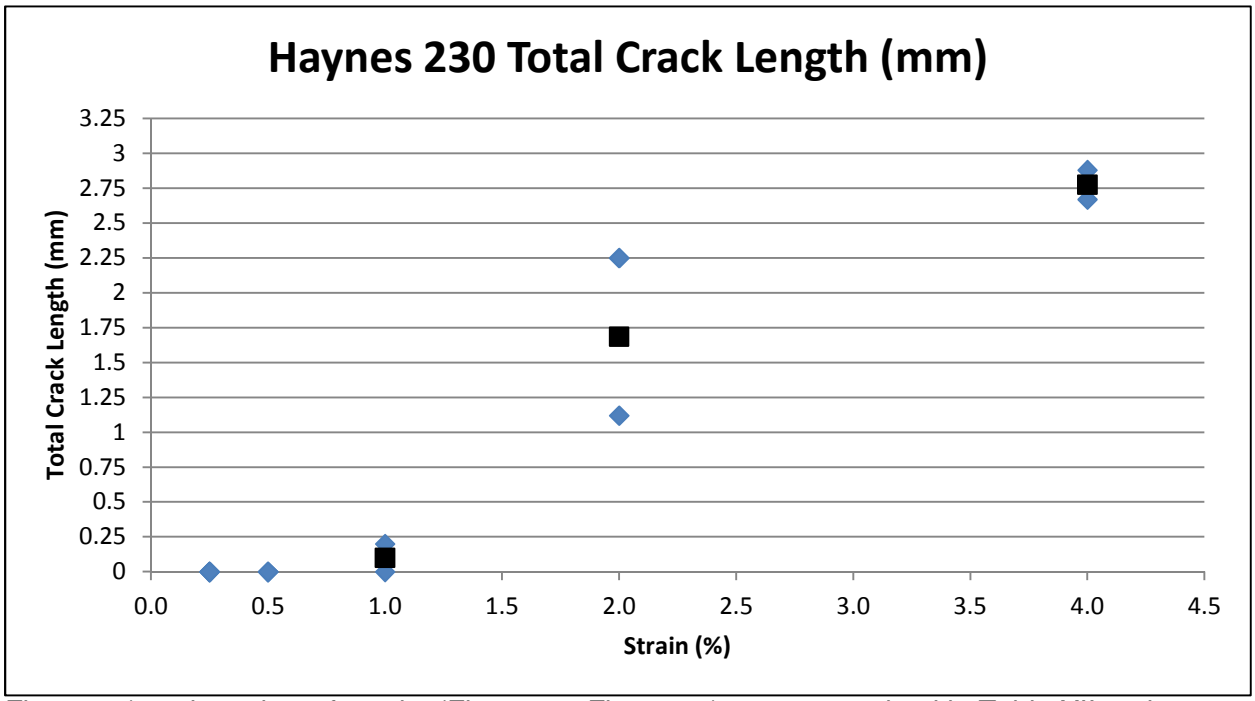

Figure 24) and number of cracks (Figure 25, Figure 26) are summarized in Table XII and Table XIII. Threshold strain for crack initiation was lower for INCO 718 than for Haynes 230, at 0.5% versus 1%. Both alloys saw an apparent MCL saturation strain at 4% (

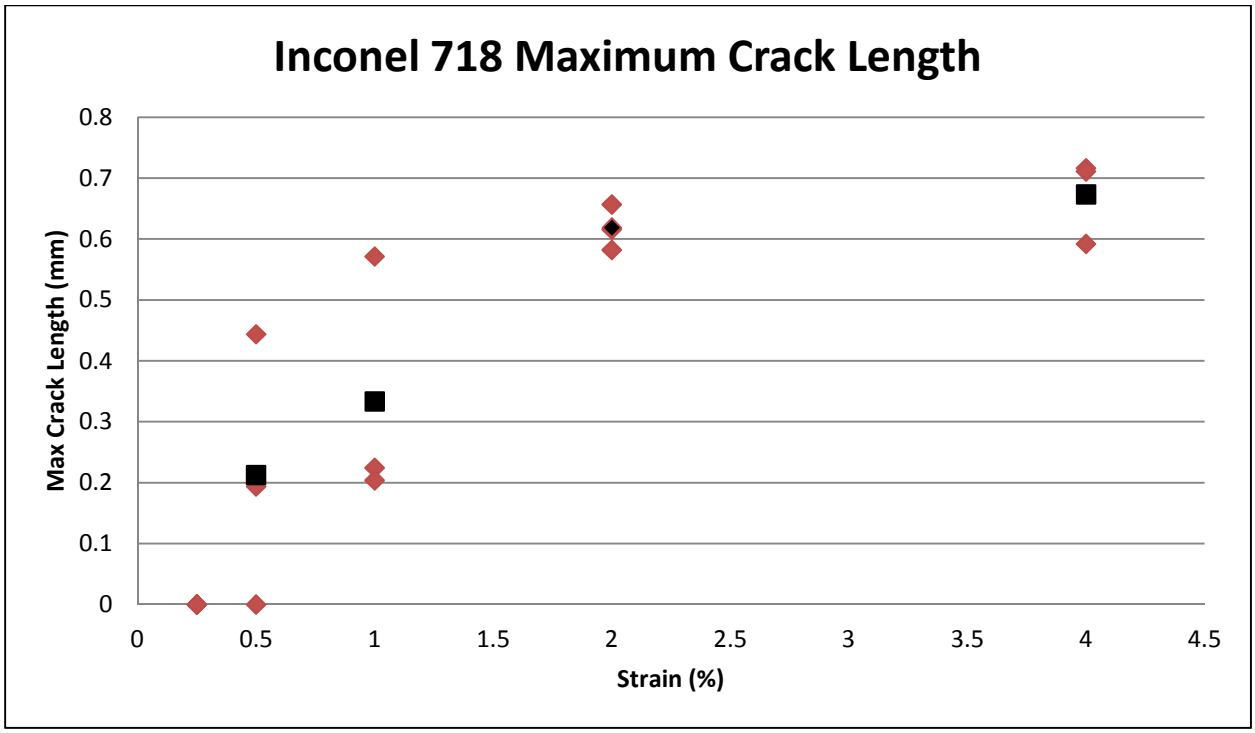

Figure 21,

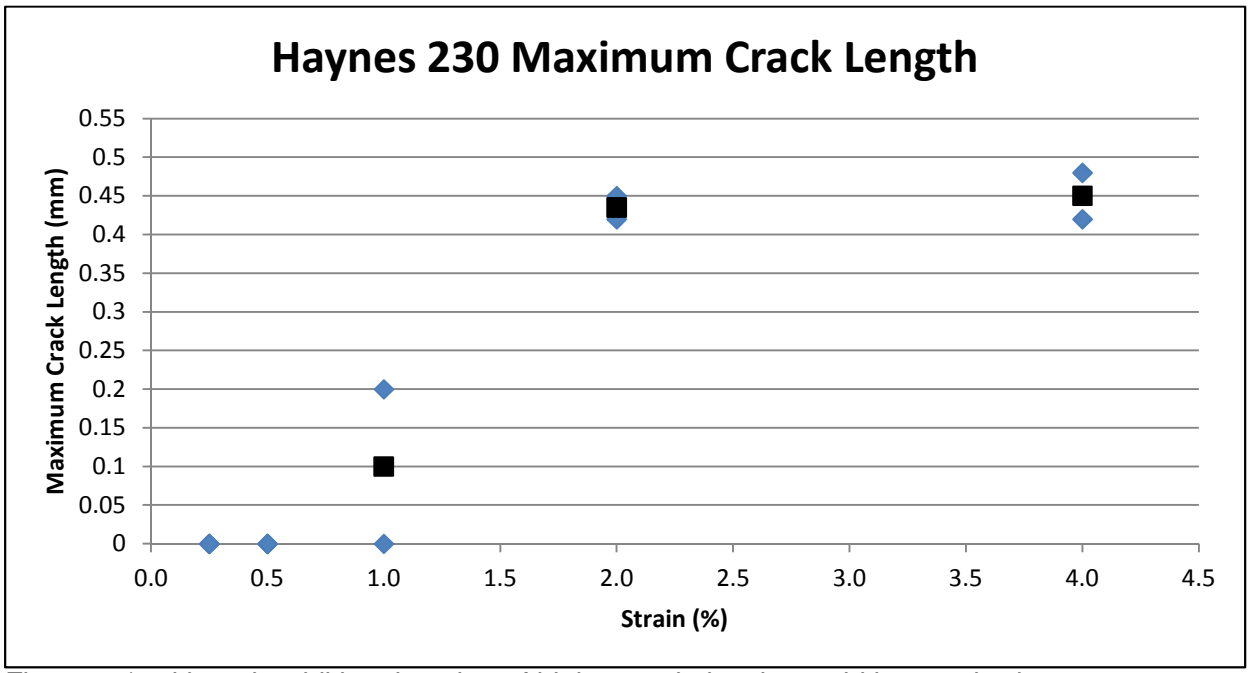

Figure 22), although additional testing of higher strain levels would be required to definitively establish this limit. Saturation strain levels for TCL and number of cracks was not possible to determine based on the strain levels tested. A quantitative analysis of MCL, TCL and number of cracks further illustrates the differences between INCO 718

and Haynes 230. INCO 718 had a higher average MCL, TCL and number of cracks at every strain level tested at which cracks were formed (Table XII, Table XIII). In other words, more cracks formed, and extended further into the base metal in INCO 718 at every strain level including and above the threshold strain.

Table X– Threshold and Saturation Strains for Inconel 718

Criteria	Threshold Strain (%)	Saturation Strain (%)
Maximum Crack Length	0.5	4
Total Crack Length	0.5	Undetermined
Number of Cracks	0.5	Undetermined

Table XI – Threshold and Saturation Strains for Haynes 230

Criteria	Threshold Strain (%)	Saturation Strain (%)
Maximum Crack Length	1	4
Total Crack Length	1	Undetermined
Number of Cracks	1	Undetermined

Table XII – Inconel 718 Complete flaw count from Varestraint testing at five different strain levels

Sample #	Augmented Strain (%)	Max Crack Length (mm)	Total Crack Length (mm)	Number of Cracks
9	0.25	0	0	0
2	0.25	0	0	0
15	0.25	0	0	0
AVG	0.25	0	0	0
4	0.5	0	0	0
11	0.5	0.44	0.71	2
13	0.5	0.19	0.32	2
AVG	0.5	0.21	0.34	1.3
6	1	0.57	1.57	6
7	1	0.23	0.34	2
17	1	0.20	0.20	1
AVG	1	0.33	0.71	3
5	2	0.58	6.61	17
10	2	0.66	8.53	19
14	2	0.62	4.41	14
AVG	2	0.62	6.52	16.7
1	4	0.72	12.20	29
8	4	0.59	11.87	25
16	4	0.71	8.49	25
AVG	4	0.67	10.86	26.3

Table XIII: Haynes 230 Complete flaw count from Varestraint testing at five different strain levels

Sample #	Augmented Strain (%)	Max Crack Length (mm)	Total Crack Length (mm)	Number of Cracks
6	0.25	0	0	0
12	0.25	0	0	0
AVG	0.25	0	0	0
7	0.5	0	0	0
14	0.5	0	0	0
AVG	0.5	0	0	0
1	1	0.2	0.2	1
15	1	0	0	0
AVG	1	0.1	0.1	0.5
13	2	0.42	1.12	4
5	2	0.45	2.25	7
AVG	2	0.435	1.685	5.5
11	4	0.48	2.88	9
4	4	0.42	2.67	7
AVG	4	0.45	2.775	8

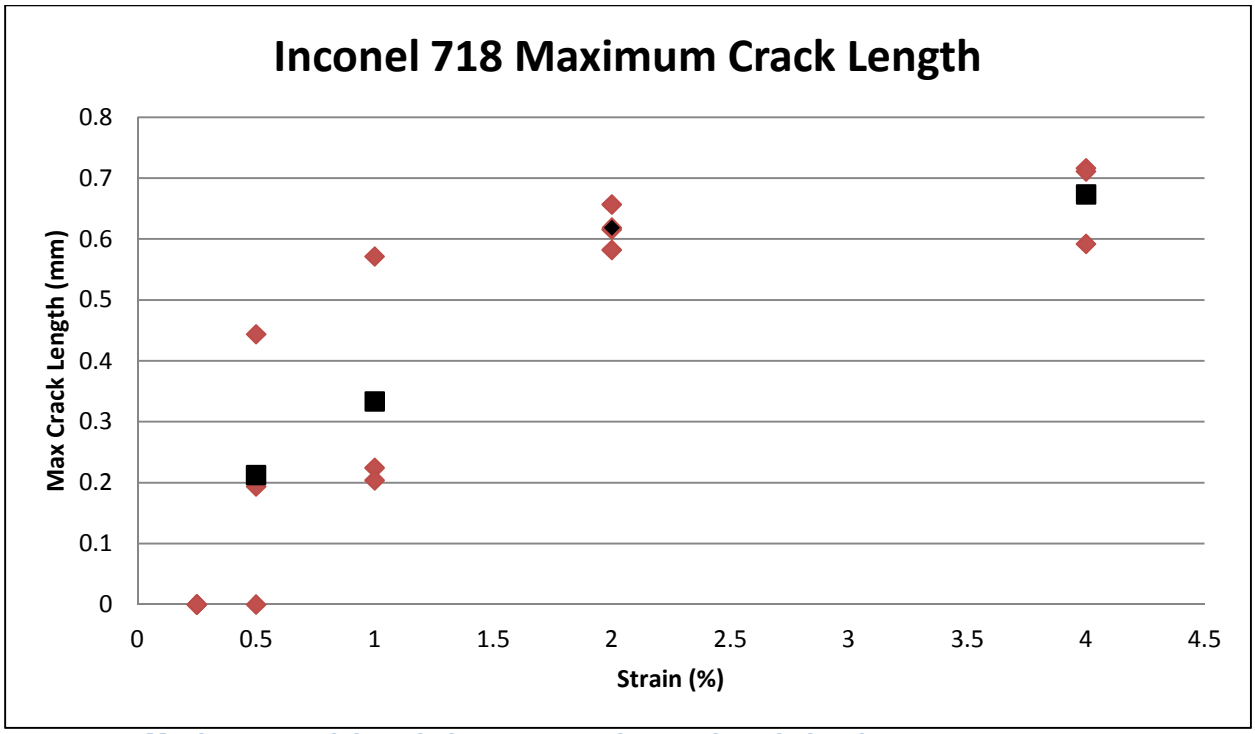

Figure 21: Maximum crack length, in mm, at each tested strain level. Black square markers indicate averages.

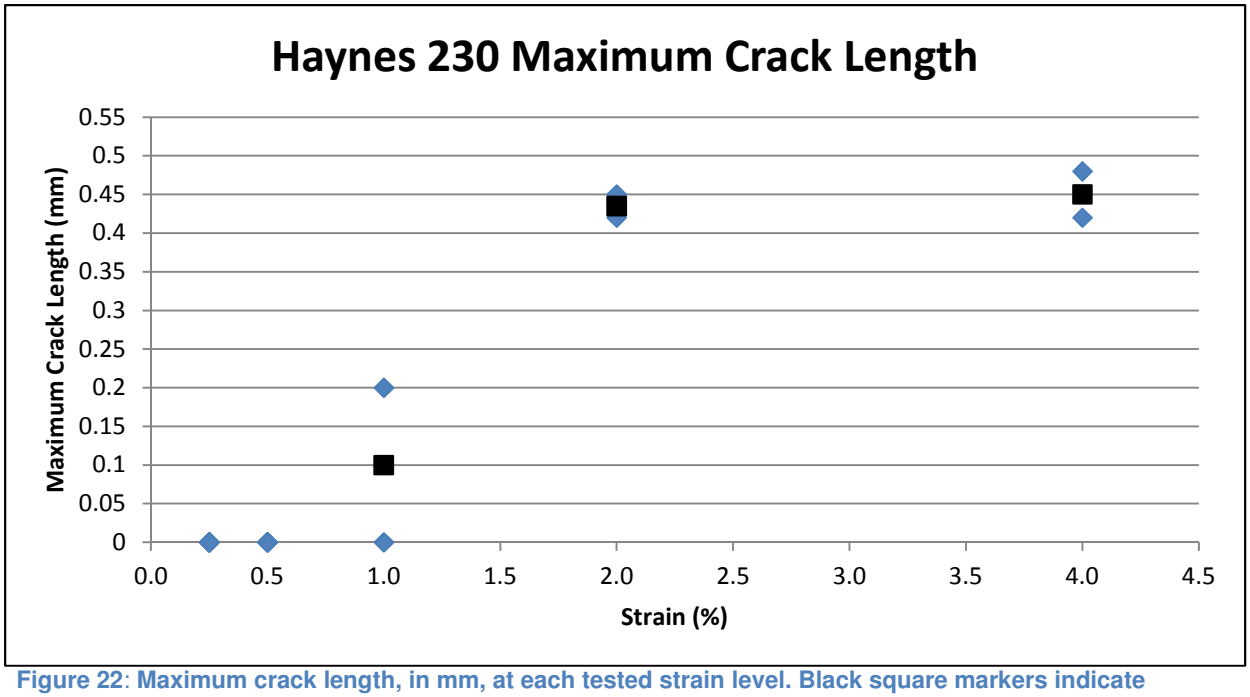

Figure 22: Maximum crack length, in mm, at each tested strain level. Black square markers indicate averages.

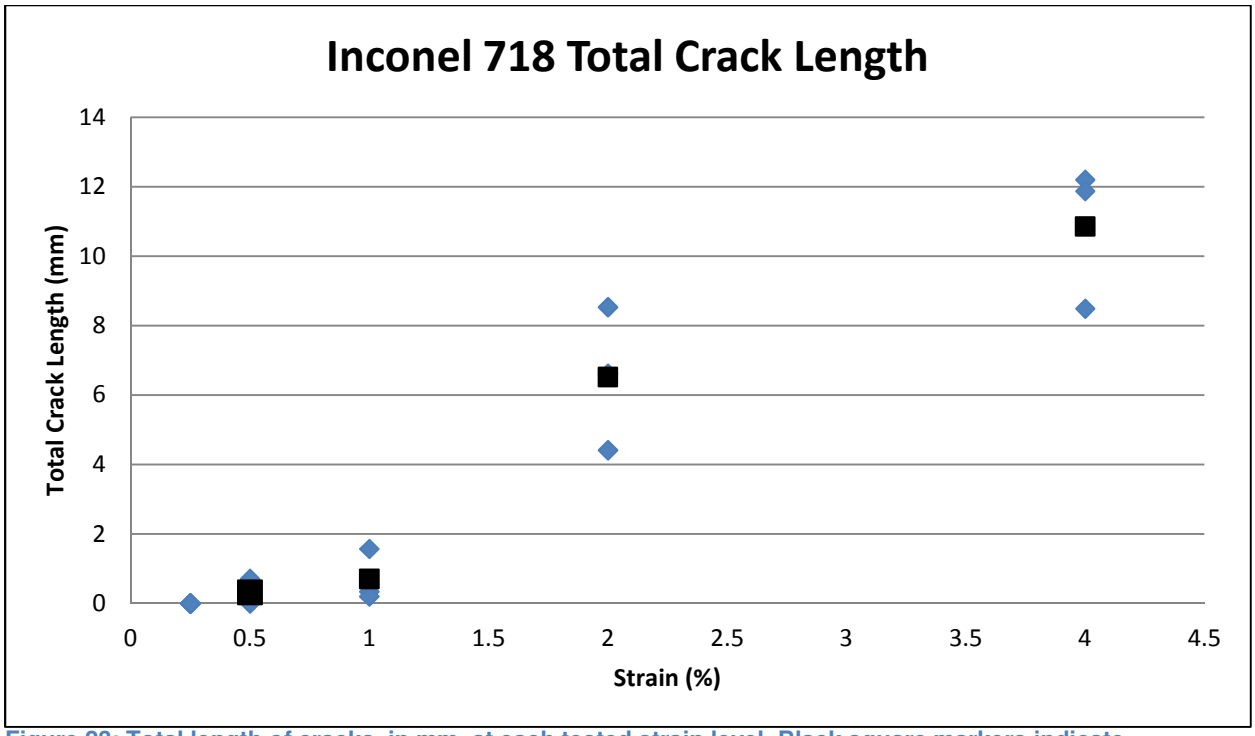

Figure 23: Total length of cracks, in mm, at each tested strain level. Black square markers indicate averages.

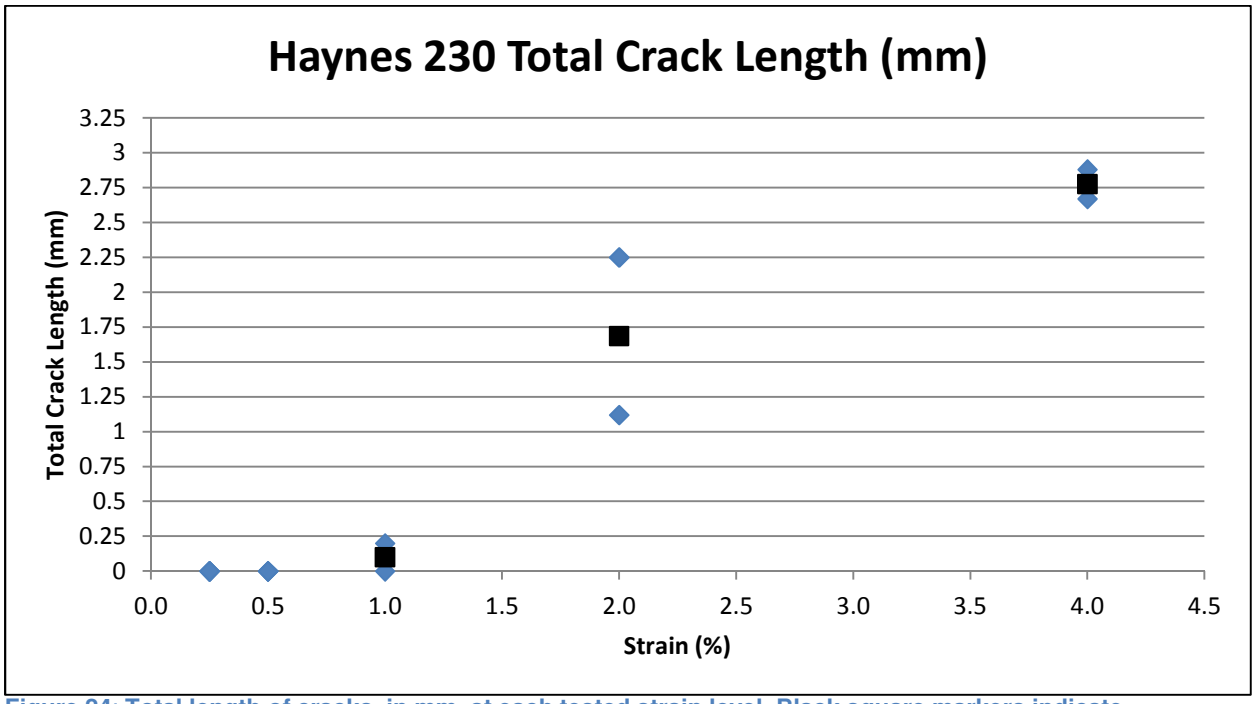

Figure 24: Total length of cracks, in mm, at each tested strain level. Black square markers indicate averages.

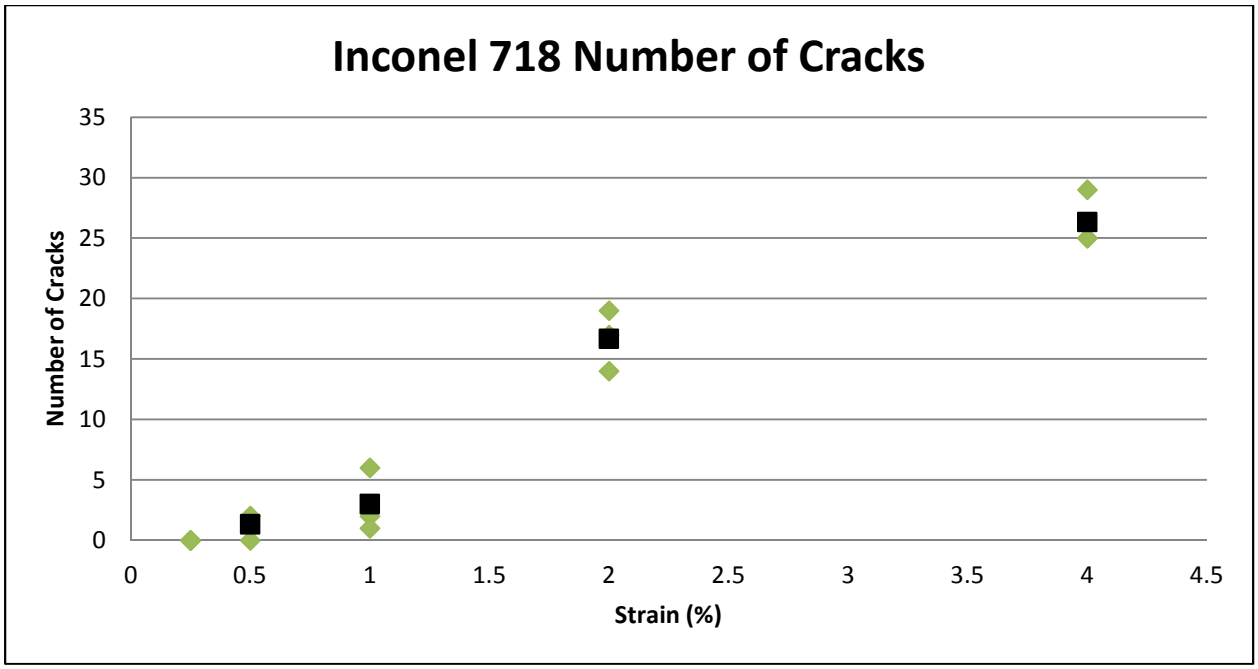

Figure 25: Total number of flaws, at each tested train level. Black square markers indicate averages.

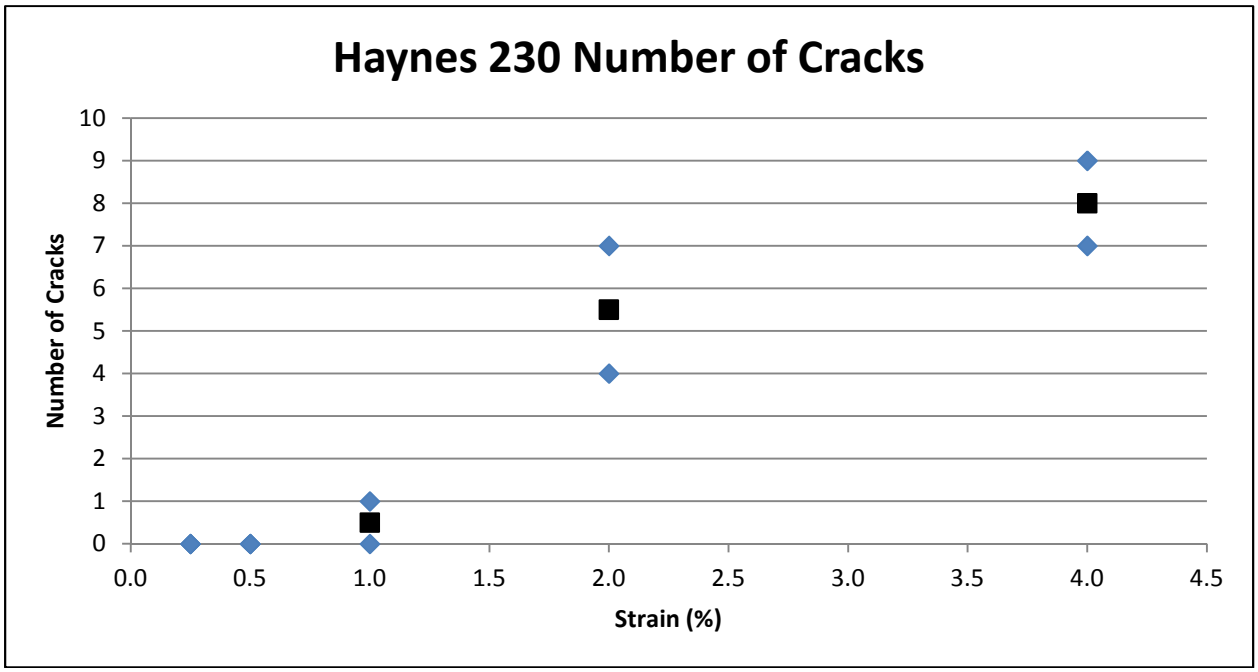

Figure 26: Total number of flaws, at each tested train level. Black square markers indicate averages.

3.3 Gleeble® Fracture Surfaces: SEM Images

SEM images were first taken of the fracture surfaces created during the nil-strength tests. This provided an idea of what fully liquated grain boundaries looked like upon failure and cooling for either alloy. Features were similar for both alloys. Visible features appear rounded, and smooth, indicative of liquid grain boundary films present at failure. As expected, there are no apparent signs of ductile rupture, which agrees with the zero percent reduction in area results for both alloys. The Haynes 230 samples showed possible signs of where constitutional liquation had occurred, appearing as spherical indentations of roughly 10-20 um diameter. An interesting feature was noted in one of the INCO 718 nil-strength samples. A secondary crack formed just behind the fracture surface, where temperatures were expected to be below the nil-strength temperature (Fig X). The crack had a distinctly different appearance than the fracture surface, with grain surfaces more visible, and edges more sharp and defined.

3.3.1 Inconel 718 Images

The images captured of the INCO 718 NST sample are displayed below in Figures A-D. All of the images indicate a large volume of liquid presence at failure, with the exception of Figure D. Figure D is an image of a secondary crack that formed just behind the fracture surface, where temperatures were lower. The effects of failure occurring at a lower temperature are clear, as its appearance lacks the wavy, liquated appearance of Figures A-C. Instead, the surface of the crack is very jagged, with individual grains visible, and undistorted by the larger volume of liquid that was present along the primary fracture surface.

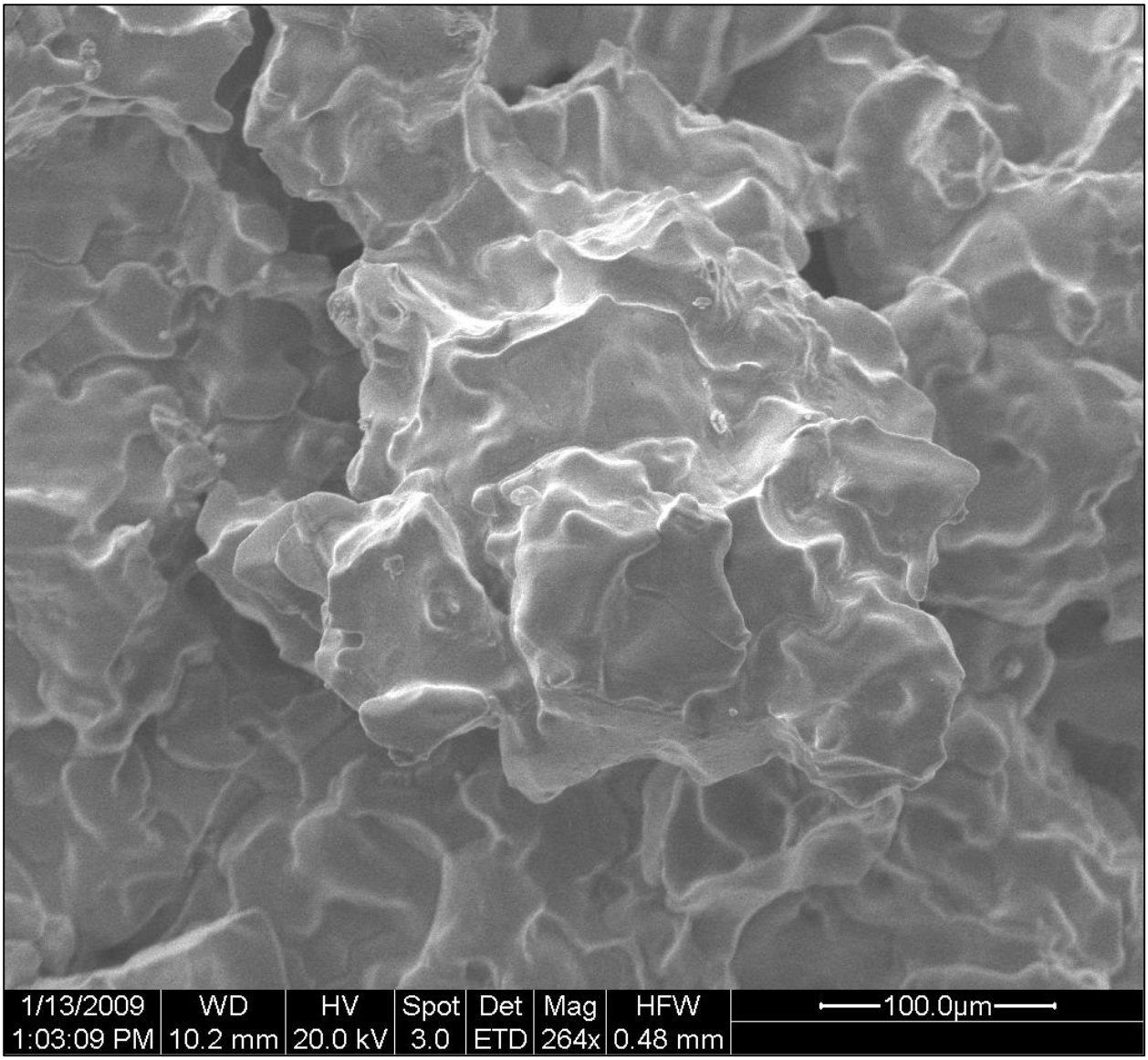

Figure 27: Inconel 718 Nil strength Gleeble® sample fracture surface. Edges are rounded, smooth, and globular, all indicators of liquid film presence upon failure.

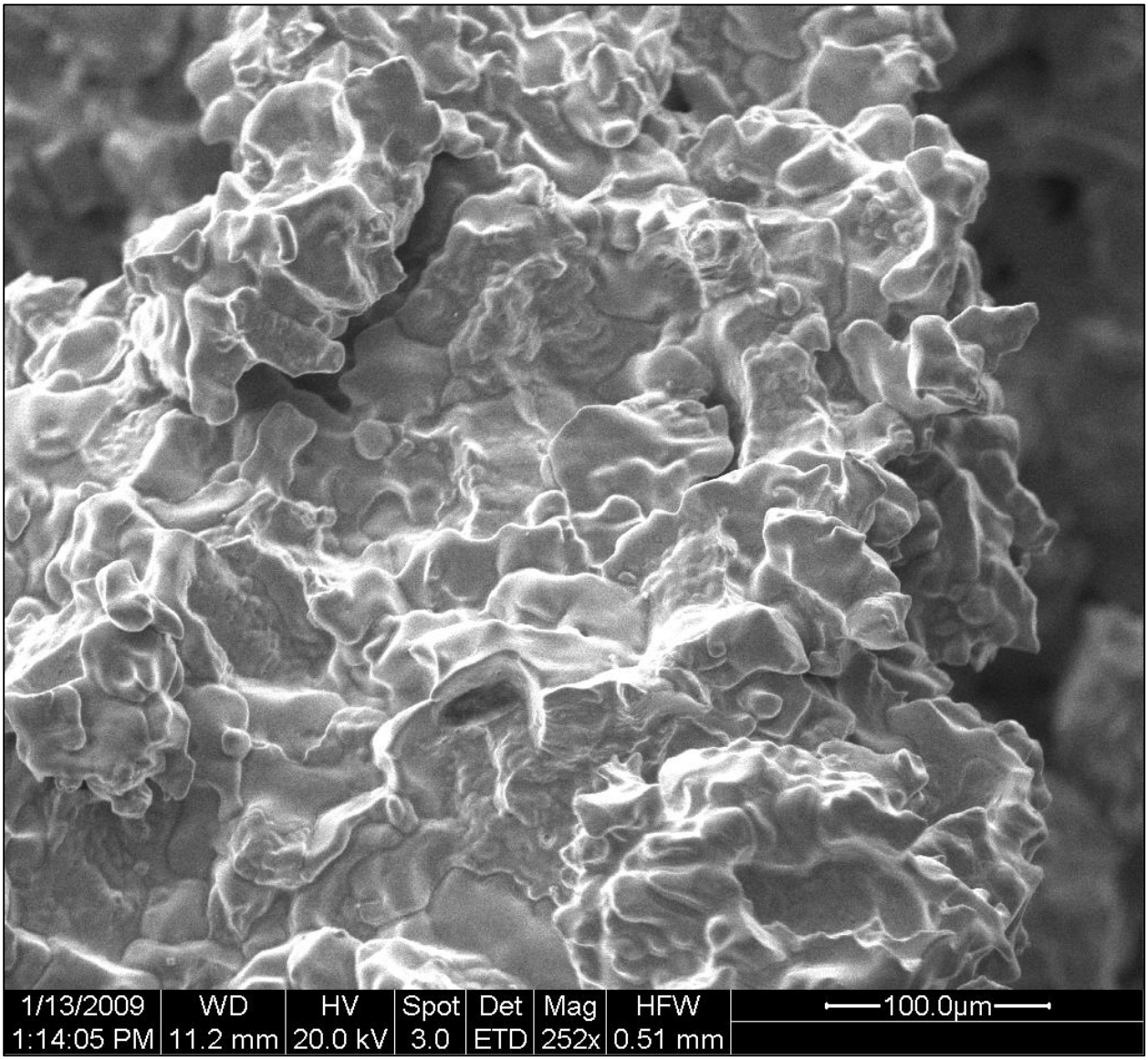

Figure 28: Inconel 718 Nil strength fracture surface. Distinct grain boundary surfaces are not visible.

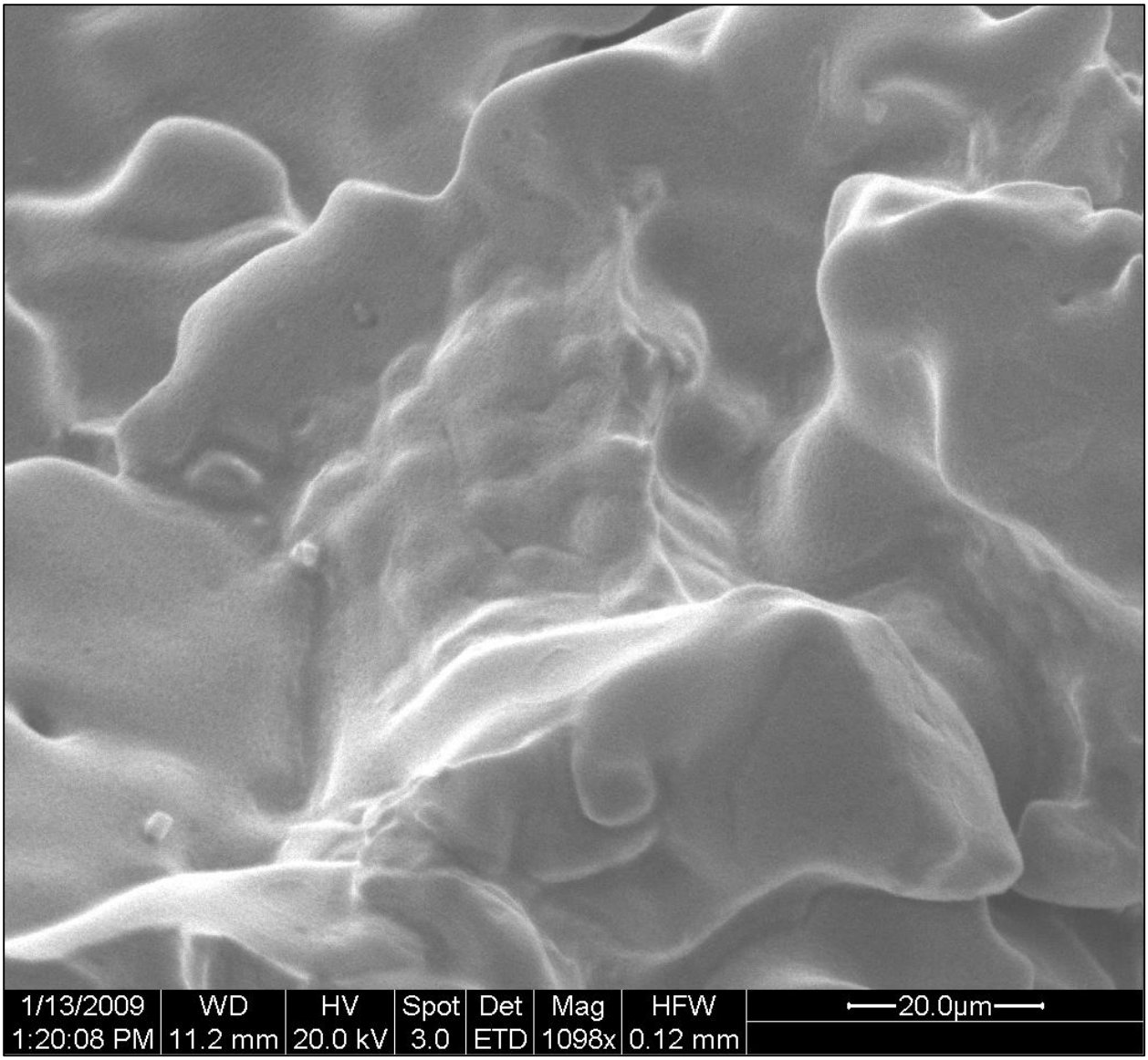

Figure 29: Inconel 718 nil-strength fracture surface. The lack of flat grain boundary surfaces and sharp edges is distinct.

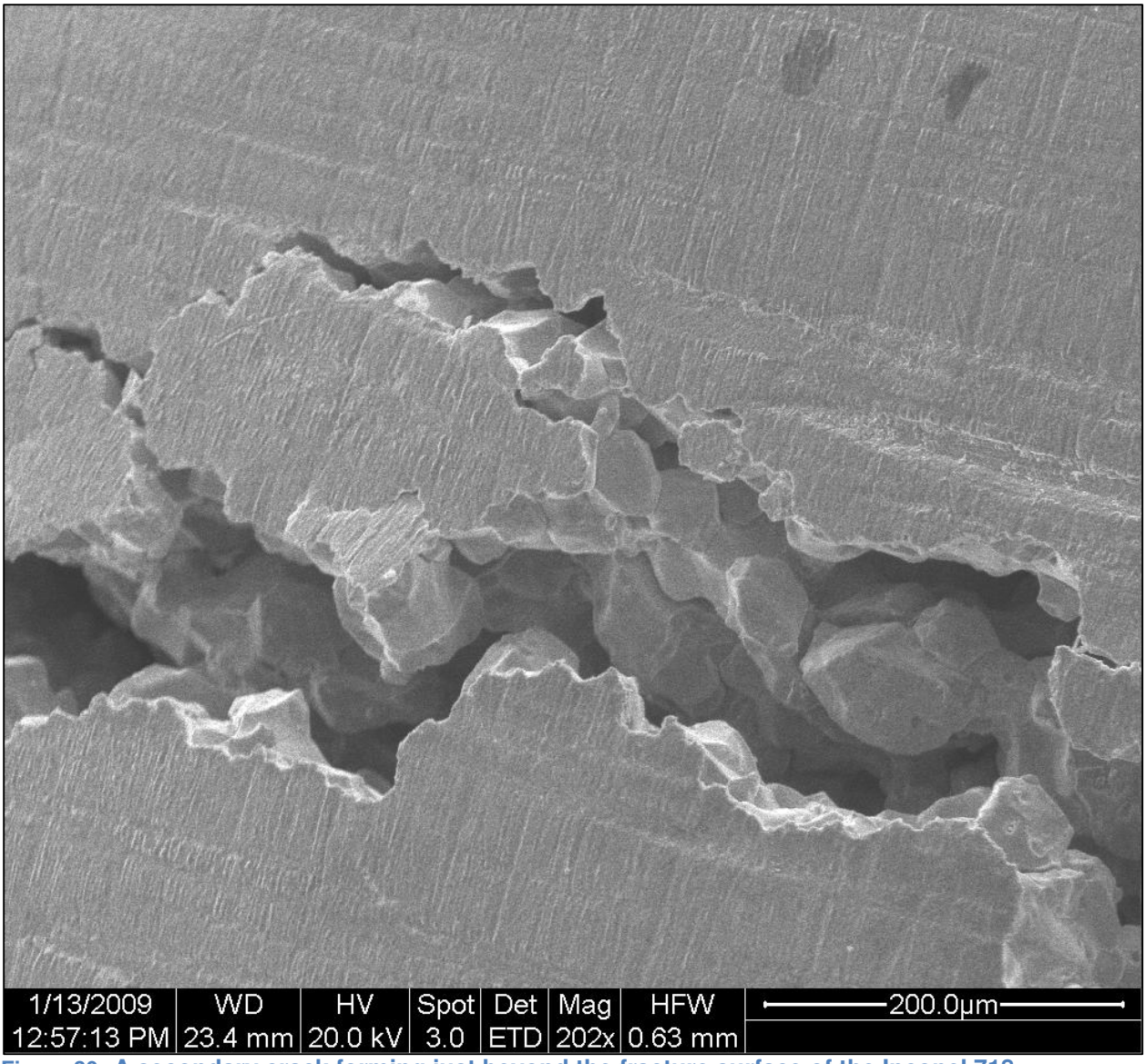

Figure 30: A secondary crack forming just beyond the fracture surface of the Inconel 718 nil-strength sample has a different appearance. Grain surfaces can be seen, with sharp corners and flat edges clearly evident. Temperatures in this region are lower than at the fracture surface.

SEM images taken of the on-heating, 2188˚F sample appeared similar in nature to the secondary crack that formed in the Nil-strength sample. Fracture surfaces are sharp and flat, with grain boundaries clearly visible. Some signs of constitutional liquation appear to be present. Individual grains are approximately 20-50 um in diameter.

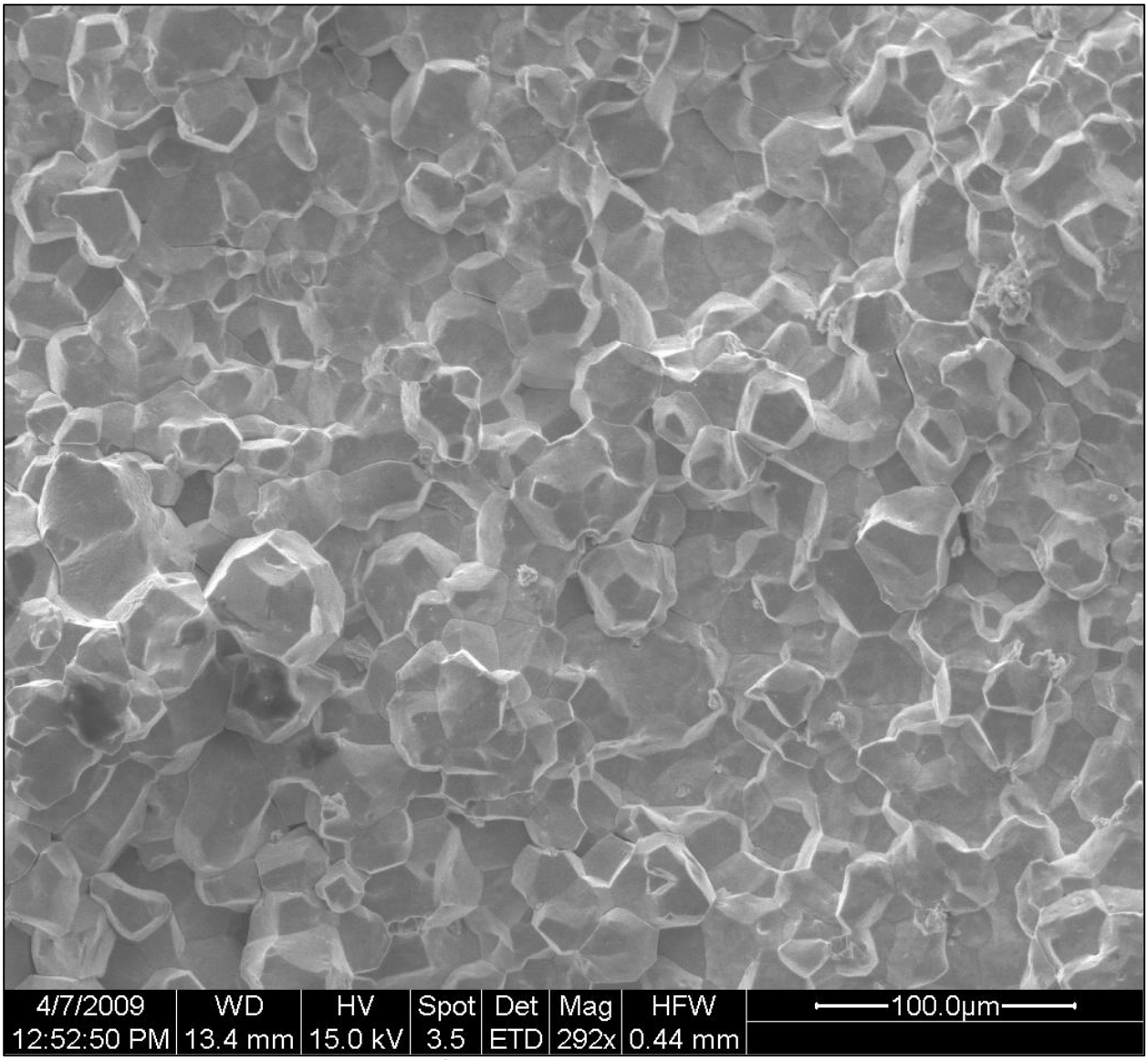

Figure 31: Inconel 718 On-heating 2188˚F fracture surface. Flat grain boundary surfaces and sharp edges are clearly visible.

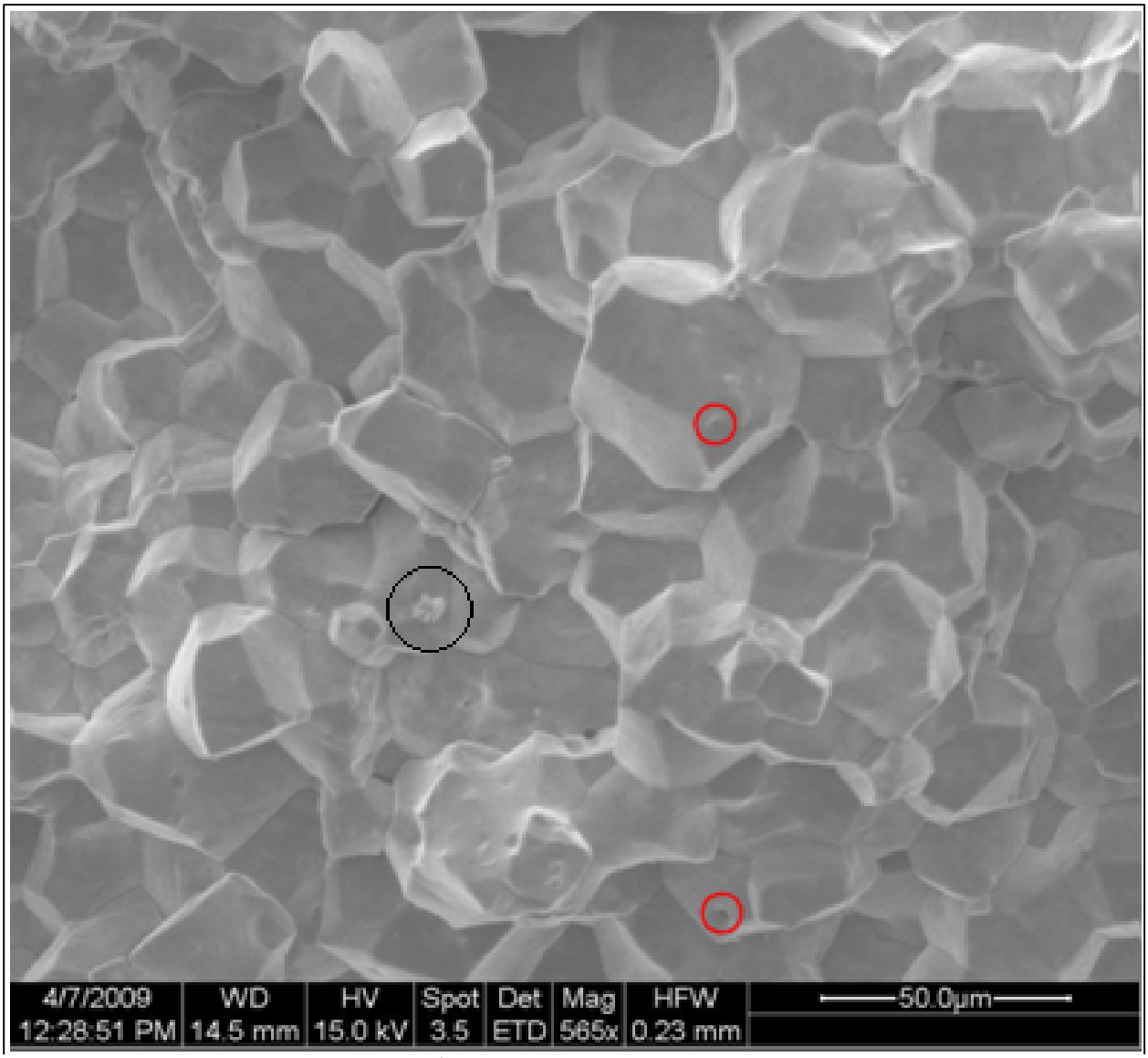

Figure 32: Inconel 718 on-heating 2188˚F fracture surface. Red circles indicate possible areas where constitutional liquation has occurred. The black circle highlights a carbide located along a grain boundary.

SEM images of the next lowest on-heating temperature, 2073 ˚F, had a significantly different appearance. Individual grain surfaces can no longer be distinguished. Surfaces appear rough and porous, an indicator of ductile rupture through microvoid coalescence.

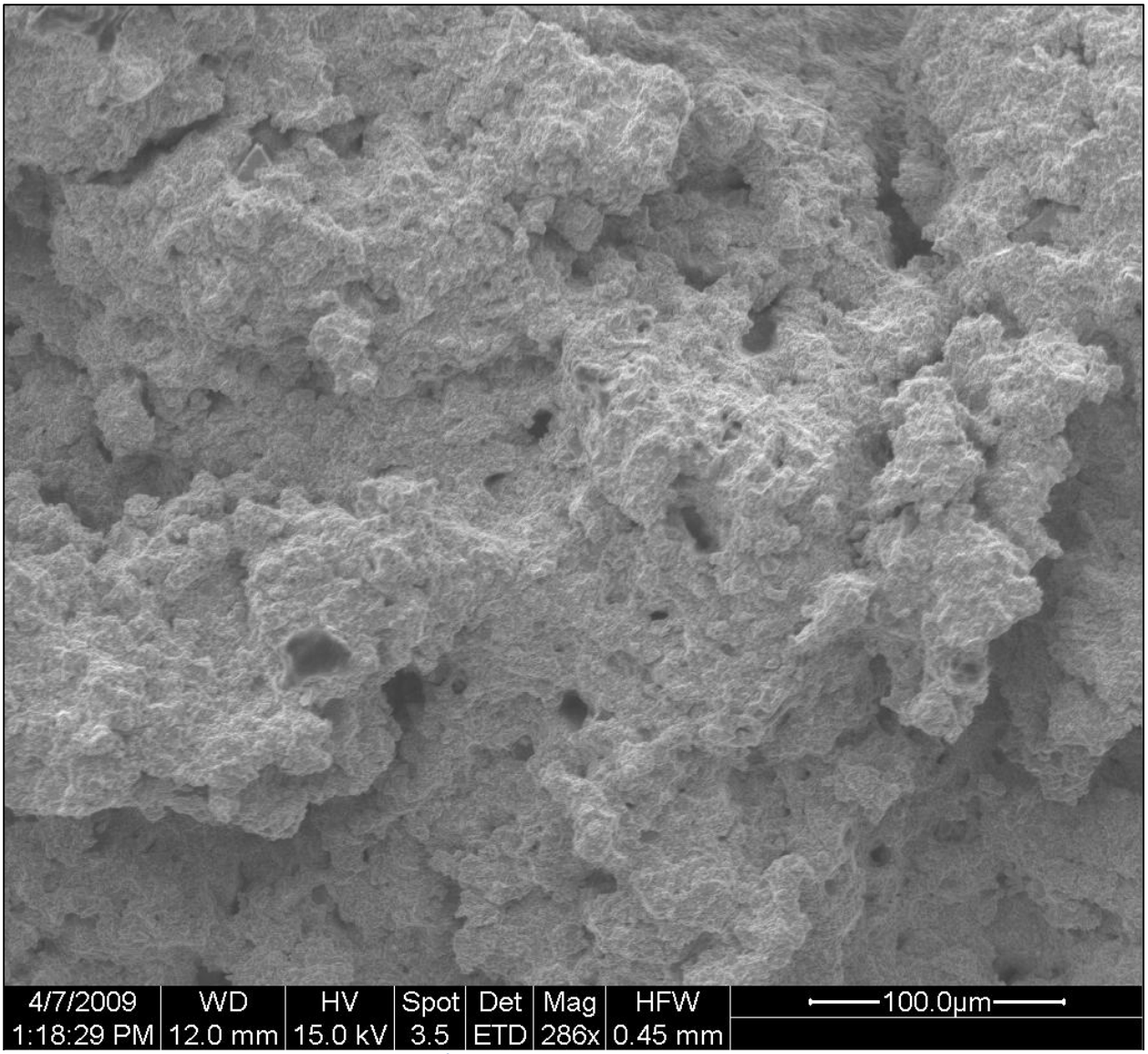

Figure 33: Inconel 718 on-heating 2073 ˚F fracture surface. Appearance is noticeable different from Fig 17, the 2188 ˚F fracture surface, captured at a similar magnification.

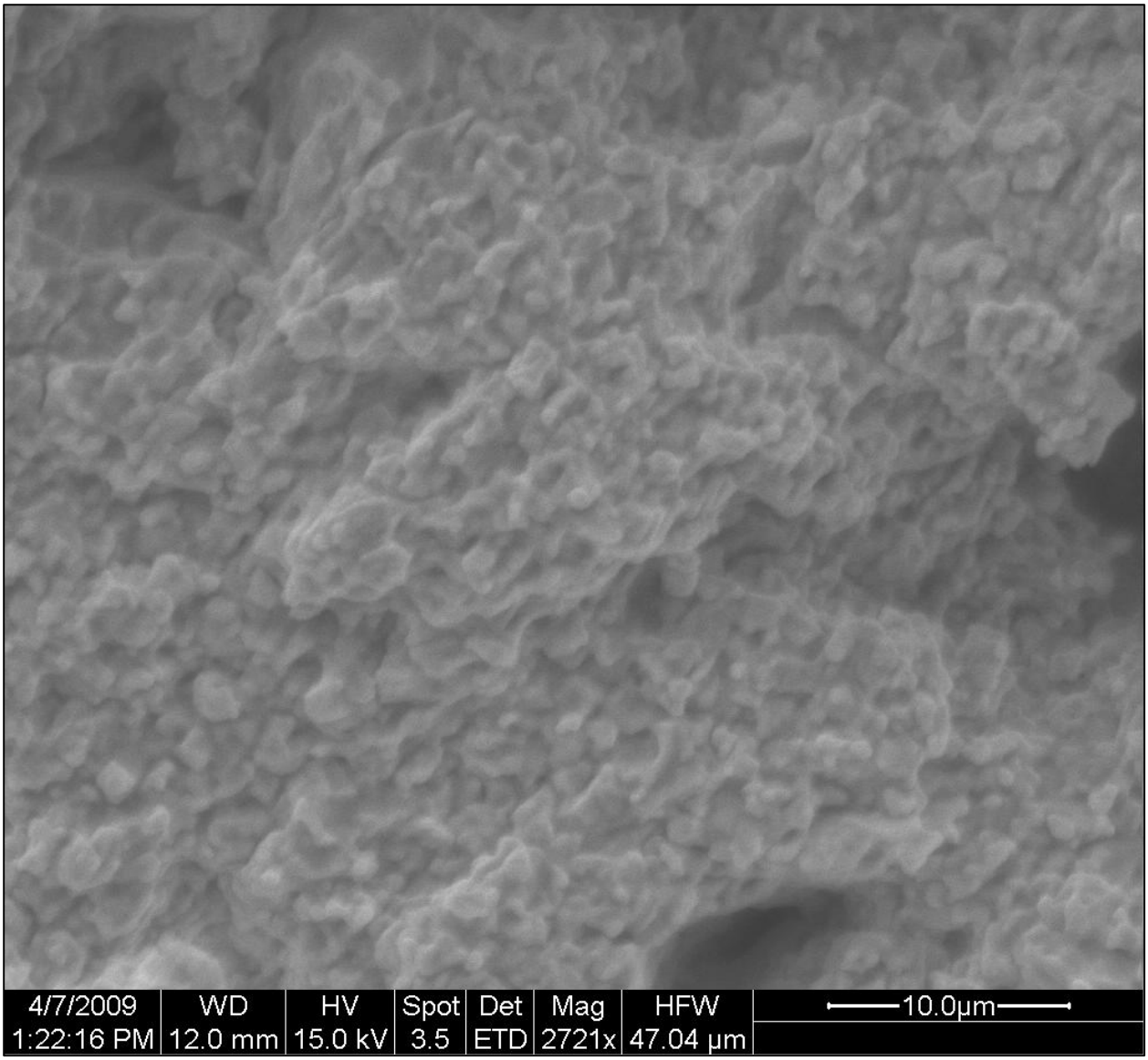

Figure 34: Inconel 718 On-heating 2073˚F fracture surface. Even at higher magnification, surfaces still appear rough and undefined, with individual features less than 5 um in size.

In looking at the highest temperature on-cooling sample, 2130˚F, we see a return to a form resembling the on-heating 2188˚F sample. Surfaces are not as smooth and flat as the on-heating 2188 ^{o}F sample, but the shape of individual grain boundaries has returned, perhaps indicating a greater volume of liquid film along grain boundaries at the time of failure.

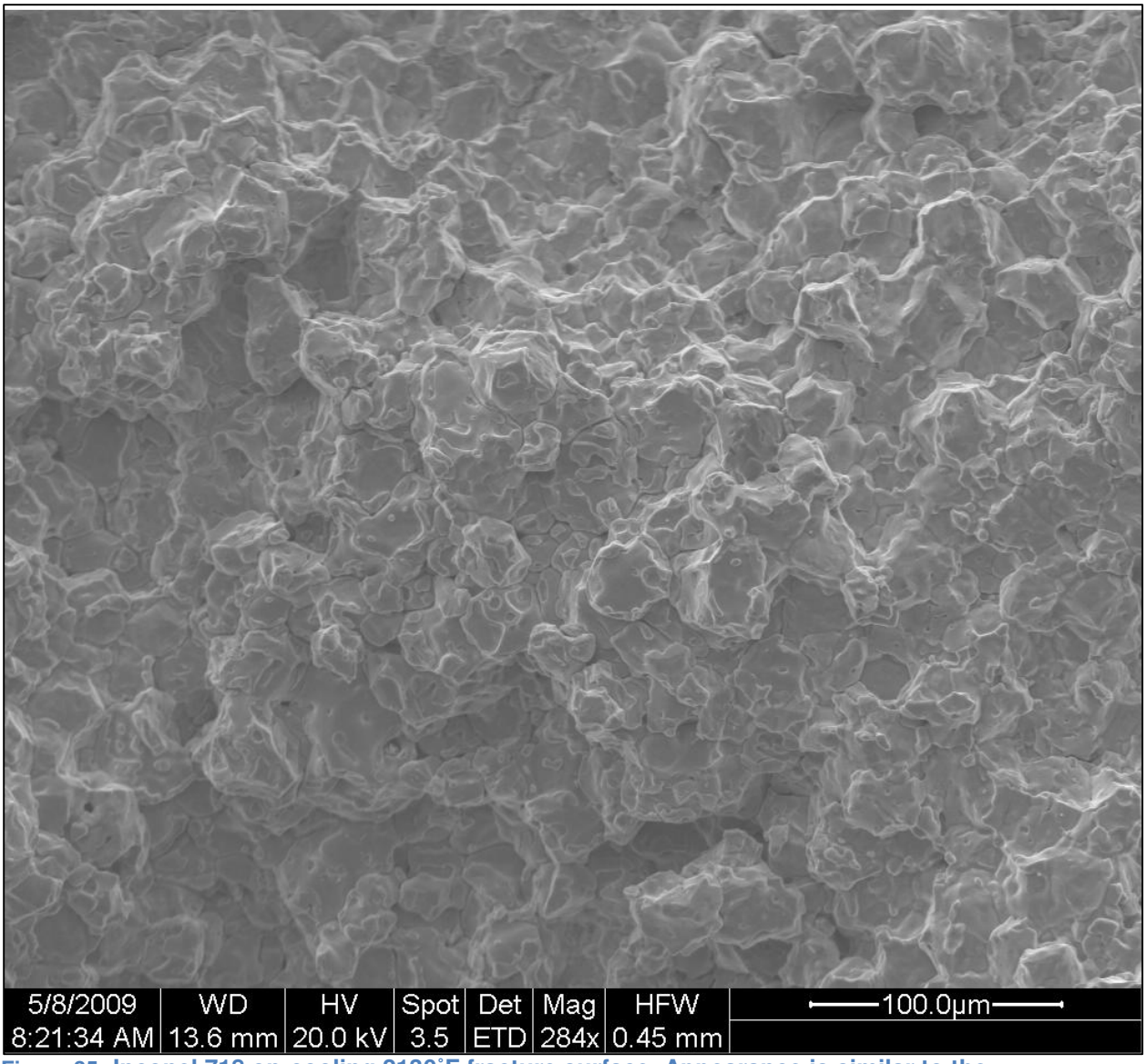

Figure 35: Inconel 718 on-cooling 2130˚F fracture surface. Appearance is similar to the highest temp on-heating sample, 2188˚F.

The next highest temperature on-cooling test, 1930˚F, varies in appearance from the nearest temperature on-heating sample, 1987˚F. The on-cooling surface is less rough, grains are more defined, and features are larger, again suggesting the presence of a greater volume of liquid films along grain boundaries at the time of failure, and failure occurring intergranularly rather than transgranularly.

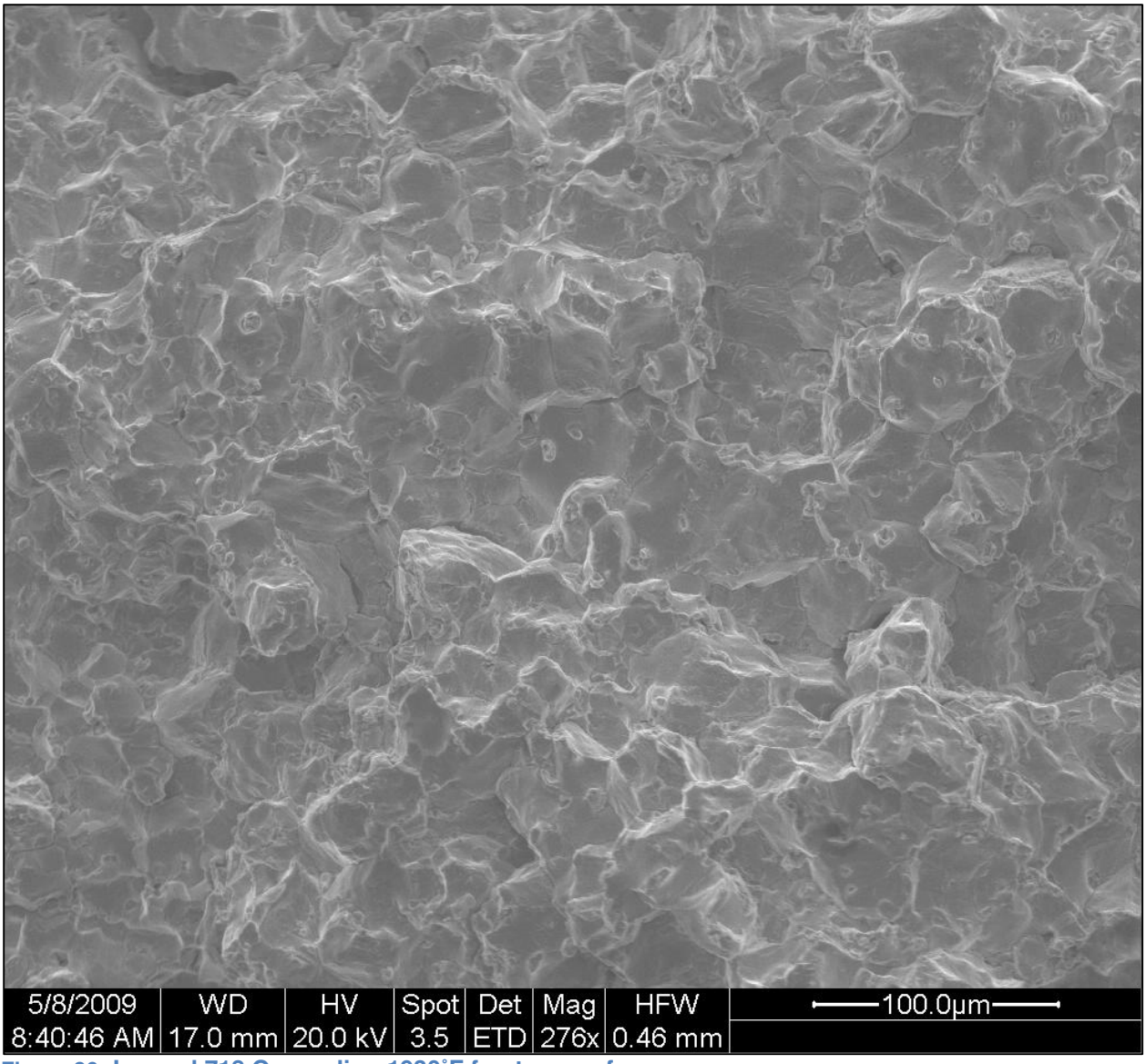

Figure 36: Inconel 718 On-cooling 1930˚F fracture surface.

The fracture surface of the on-cooling 1870˚F sample shows a return to more ductile fracture, with surfaces again appearing rough, and signs of ductile rupture present again.

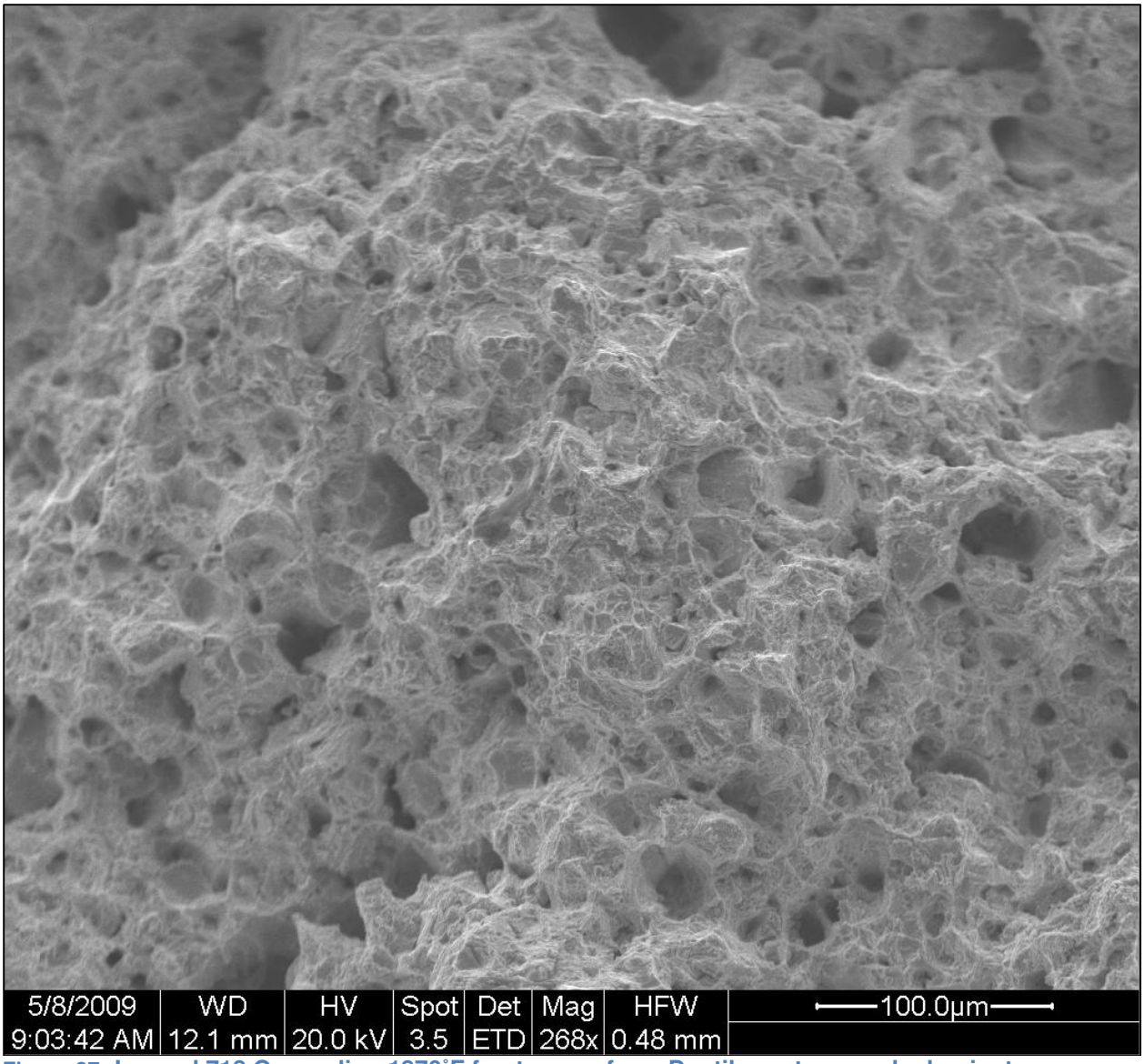

Figure 37: Inconel 718 On-cooling 1870˚F fracture surface. Ductile rupture mode dominates.

3.3.2 Haynes 230 Images

SEM examination of the fracture of the Haynes 230 nil-strength sample shows that a significant volume of liquid present at the time of failure. Features are rounded and smooth, and sites where constitutional liquation of a secondary phase has occurred visible. These precipitatse are probably carbides, a major constituent of the alloy. Although the general shape of grains can be detected, surfaces are softened by the

presence of copius liquid at the time of fracture, and any sharp corners, lines, ridges, or grain boundary edges are lacking. There are no signs of plastic deformation having occurred anywhere on the surface.

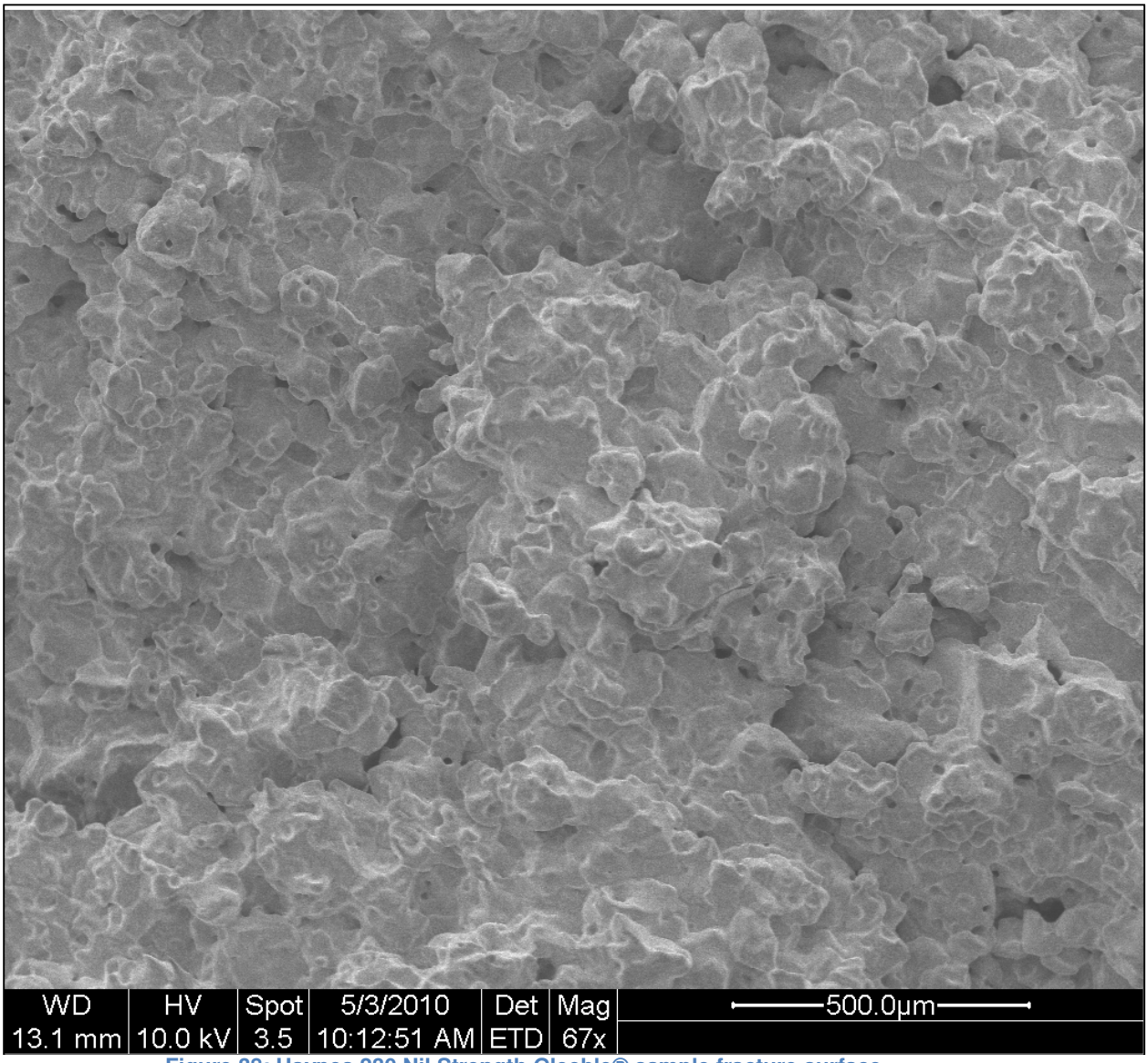

Figure 38: Haynes 230 Nil Strength Gleeble® sample fracture surface.

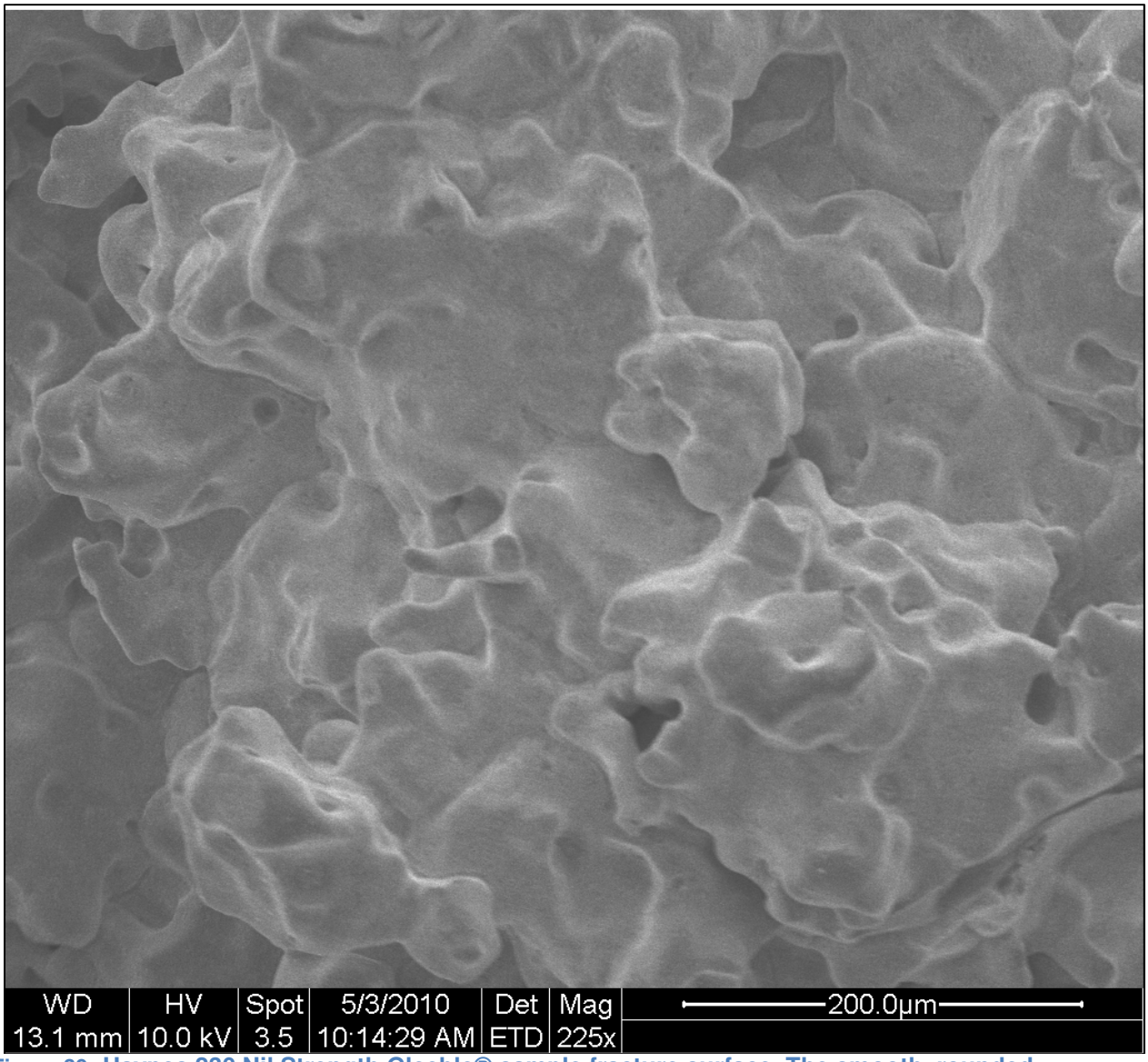

Figure 39: Haynes 230 Nil Strength Gleeble® sample fracture surface. The smooth, rounded and globular appearance is noted here as well.

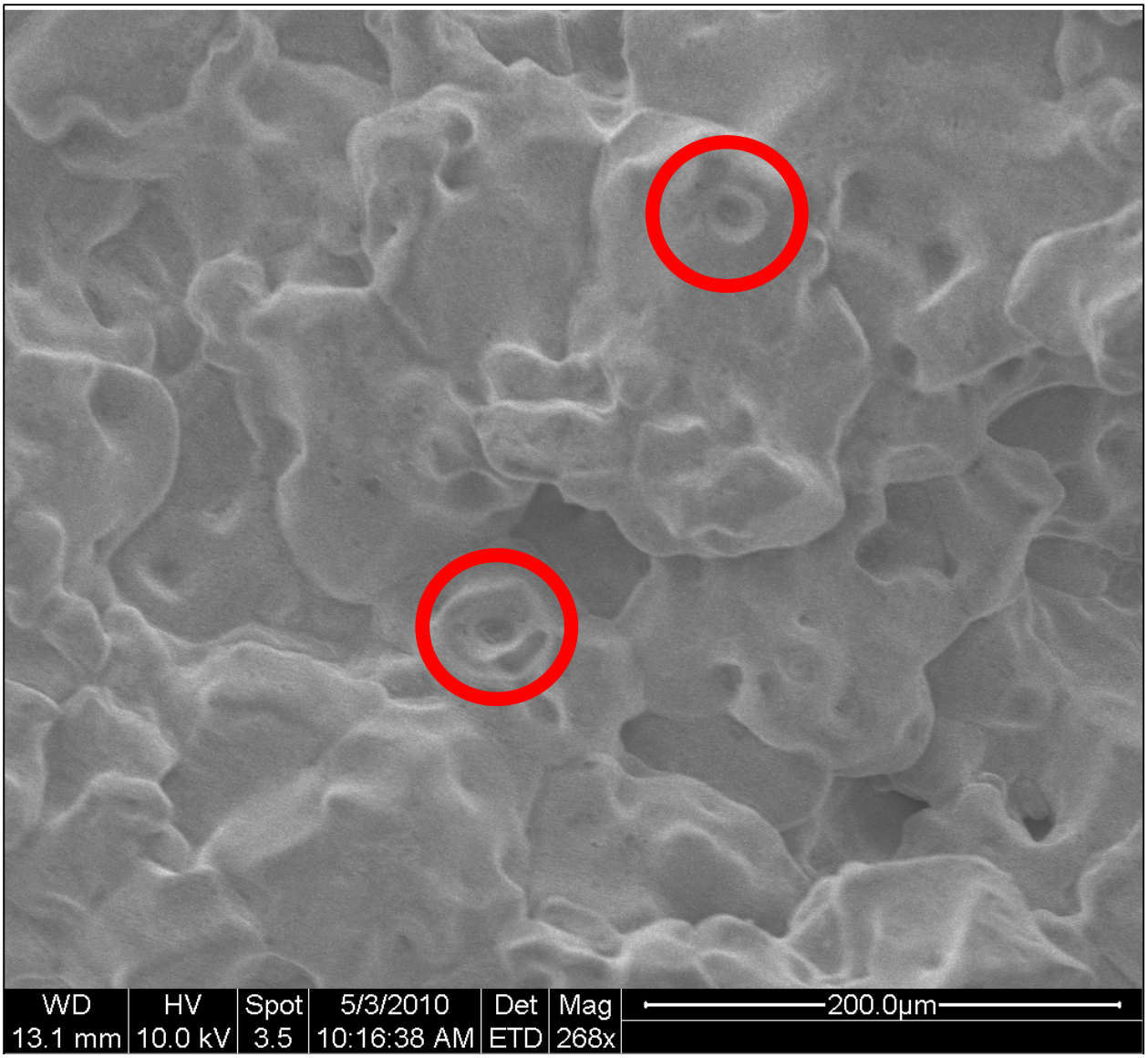

Figure 40: Haynes 230 Nil Strength Gleeble® sample fracture surface. Dimple like features suggest locations of constitutional liquation.

The sample tested on-heating at 2249^{0}F has a fracture surface with a considerably different appearance than the nil strength sample. Ductility remains high at this test temperature (45% R/A), and the fracture surface reflects a ductile form of failure. Individual grains and grain boundaries are difficult to distinguish, as the result of transgranular failure. Precipitates, probably carbides, can be seen throughout the fracture surface. The finely textured appearance of nearly all surfaces is likely

caused by oxidation to the sample immediately following testing. The combination of high temperature and strain drives dynamic recovery and recrystallization at this temperature, and is an energy absorption mechanism which which allows greater plastic deformation to occur. Large individual grains are difficult to identify both due to transgranular failure having occurred, and smaller grains having recrystallized where plastic deformation occurred during failure.

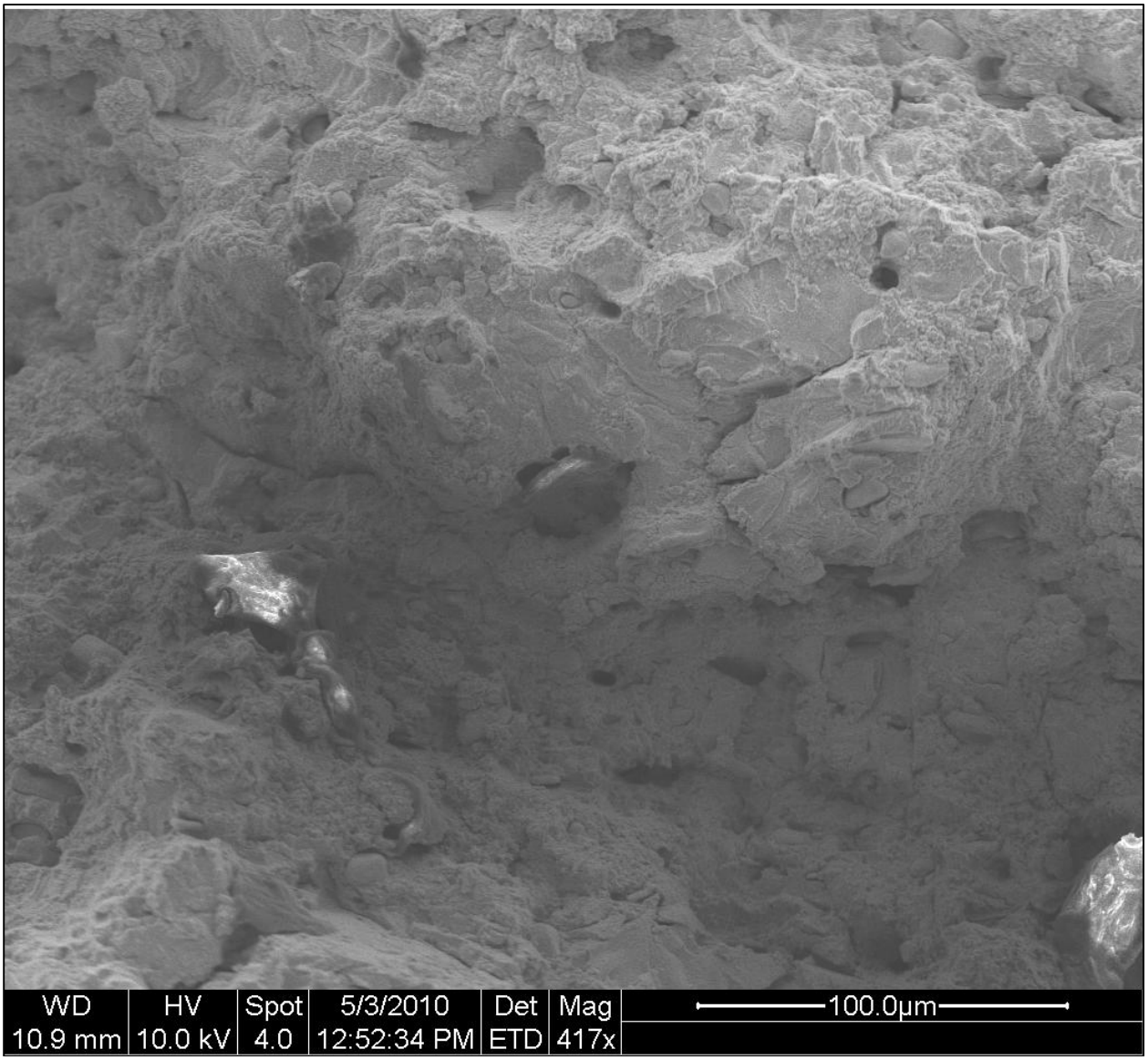

Figure 41: Haynes 230 On Heating 2249 sample fracture surface.

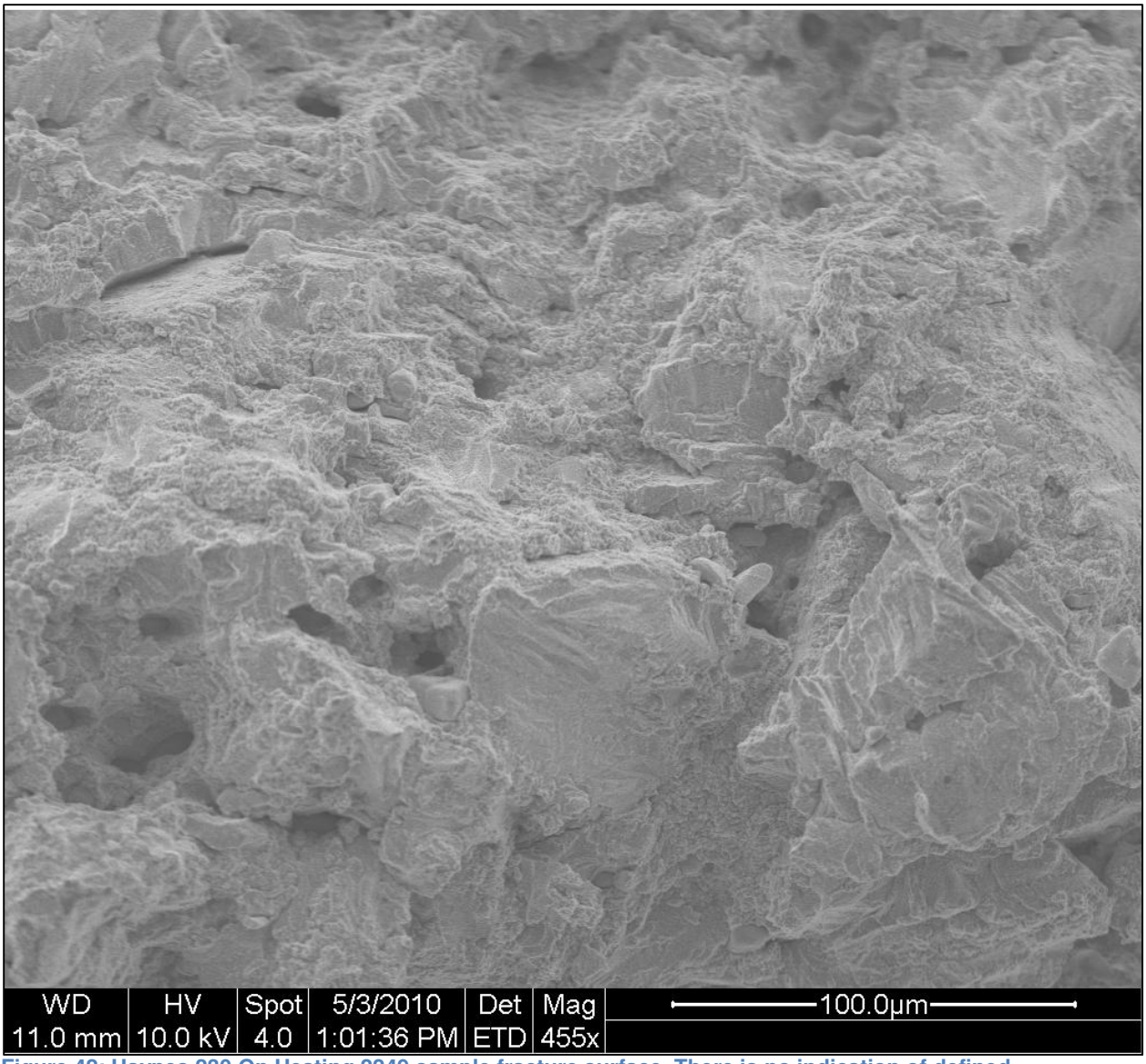

Figure 42: Haynes 230 On Heating 2249 sample fracture surface. There is no indication of defined grain boundaries.

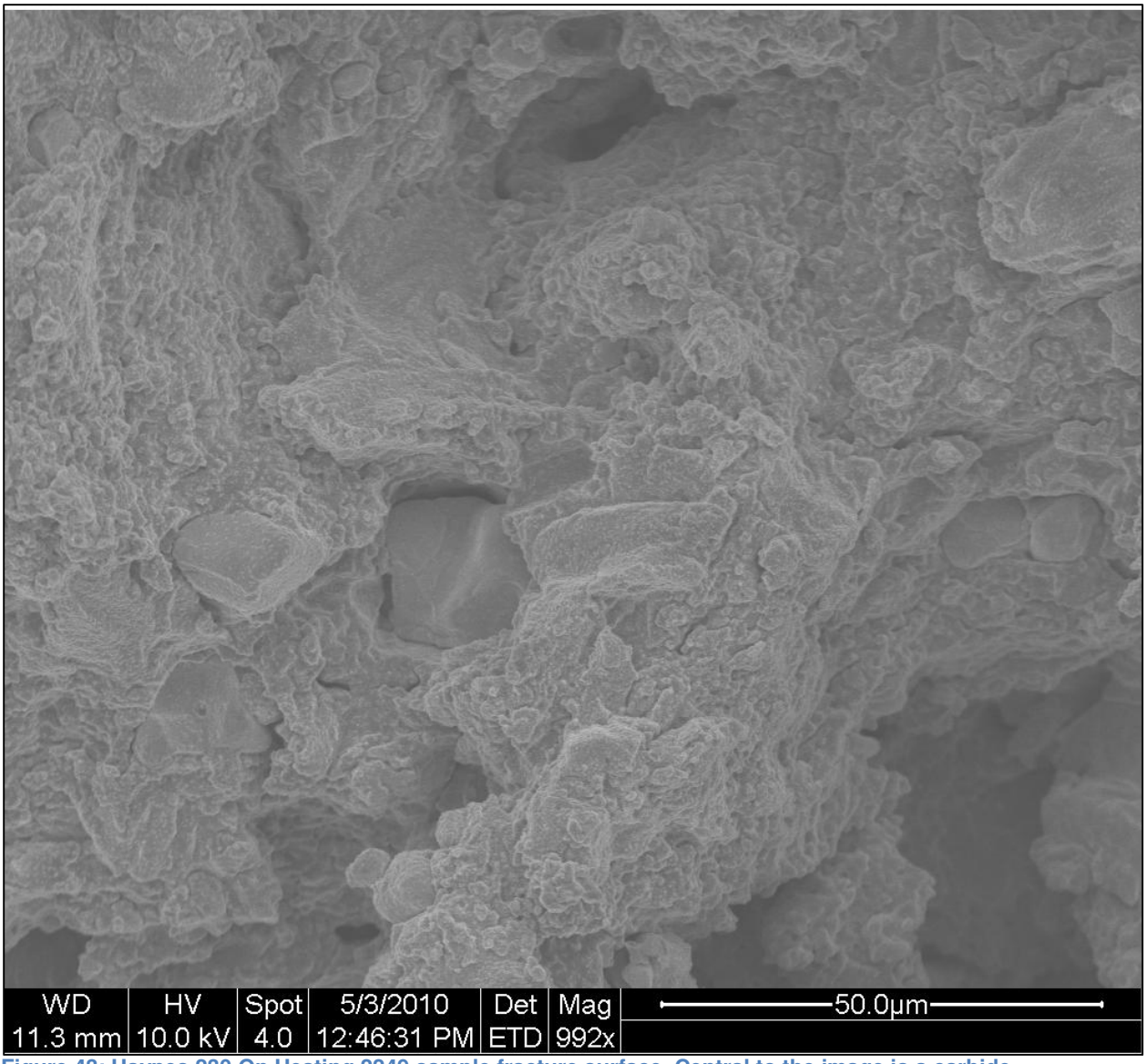

Figure 43: Haynes 230 On Heating 2249 sample fracture surface. Central to the image is a carbide embedded within the matrix.

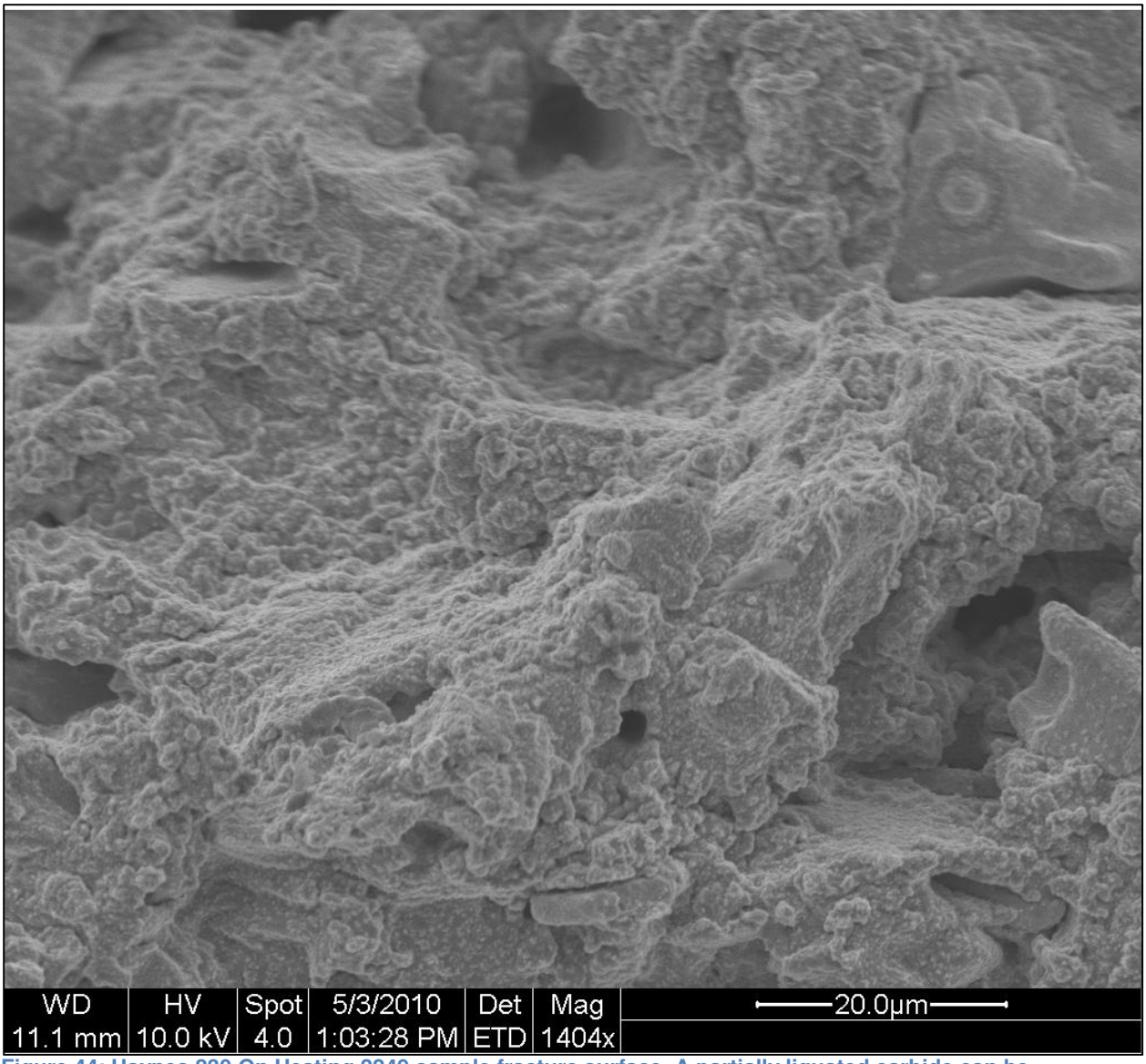

Figure 44: Haynes 230 On Heating 2249 sample fracture surface. A partially liquated carbide can be seen in the upper right corner of the image.

The on-heating sample tested at the highest temperature, 2341 ^{o}F, clearly shows an intergranular fracture. The appearance of the fracture surface is similar to the 718 sample tested on-heating at the point where its ductility plummeted to low levels. Individual grains can now be distinguished, and grain boundaries have the same flat shaping, with sharp edges and corners. The formation of secondary cracks along grain boundaries is clear. Signs of plastic deformation are lacking. Grain boundaries

look largely undisturbed. Secondary cracking along grain boundaries is clearly evident. There are no visible signs of dynamic recrystallization having taken place during failure because no plastic deformation took place.

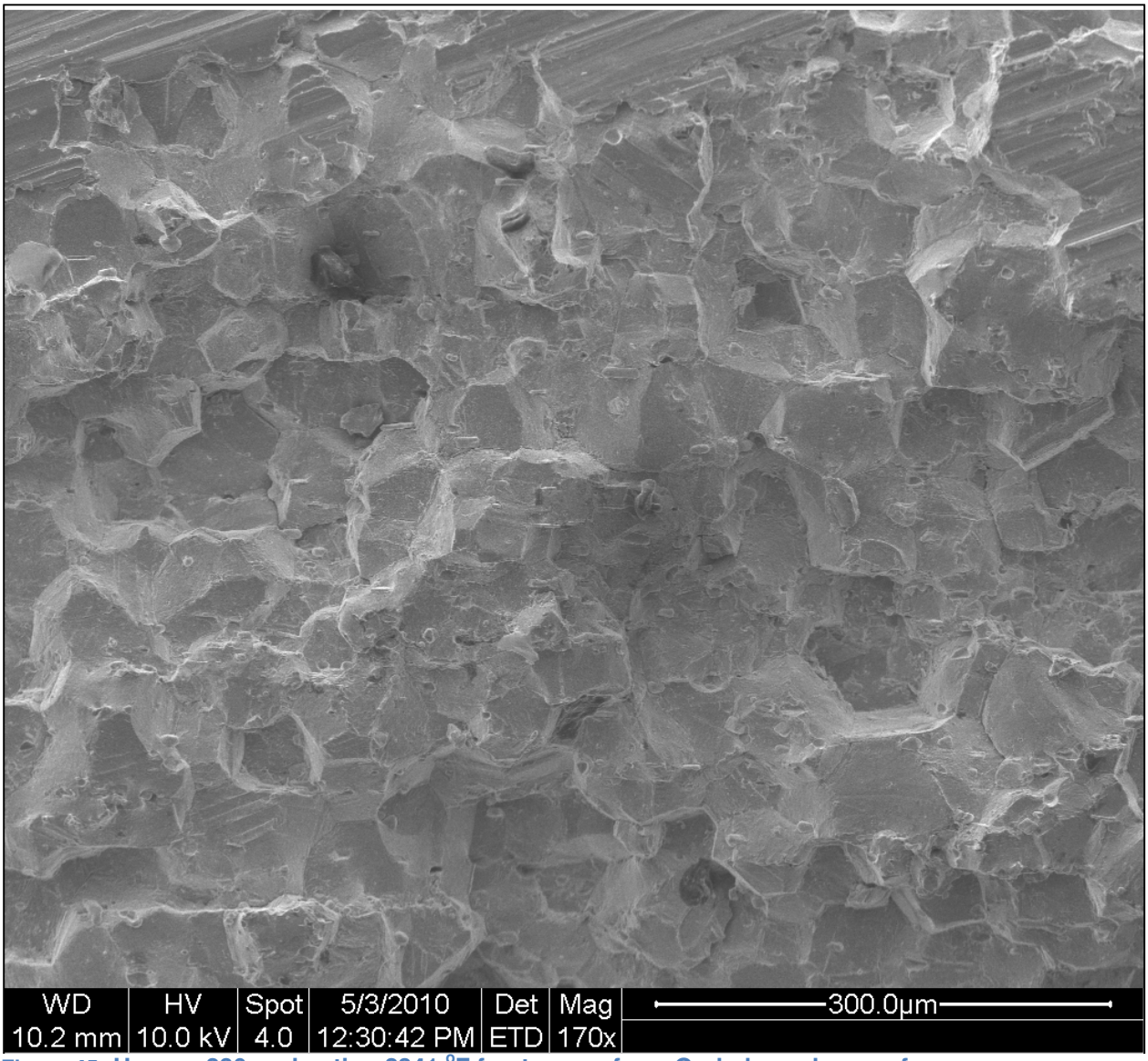

Figure 45: Haynes 230 on-heating 2341 ^{o}F fracture surface. Grain boundary surfaces are clearly defined.

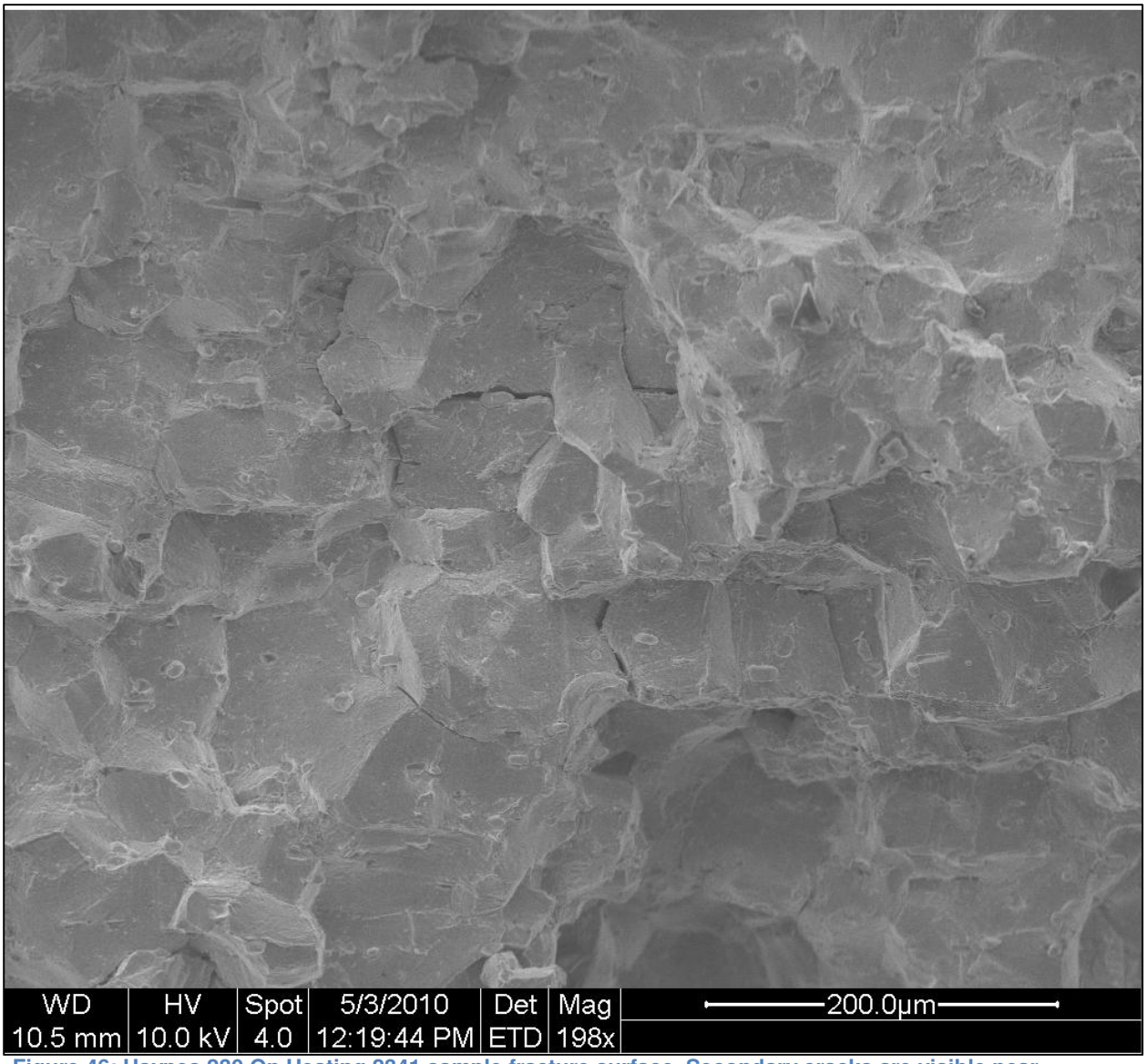

Figure 46: Haynes 230 On Heating 2341 sample fracture surface. Secondary cracks are visible near the center of the image.

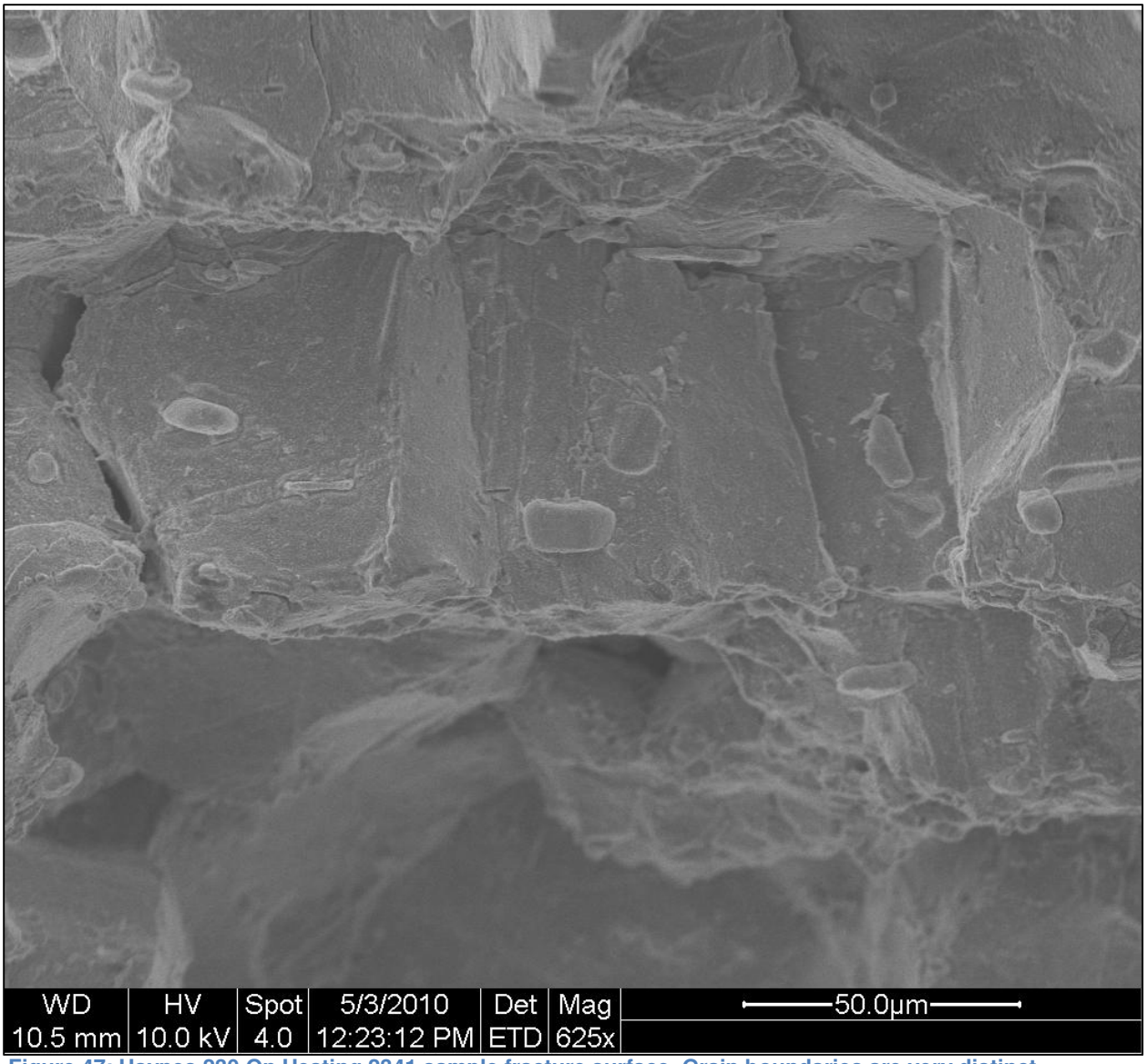

Figure 47: Haynes 230 On Heating 2341 sample fracture surface. Grain boundaries are very distinct.

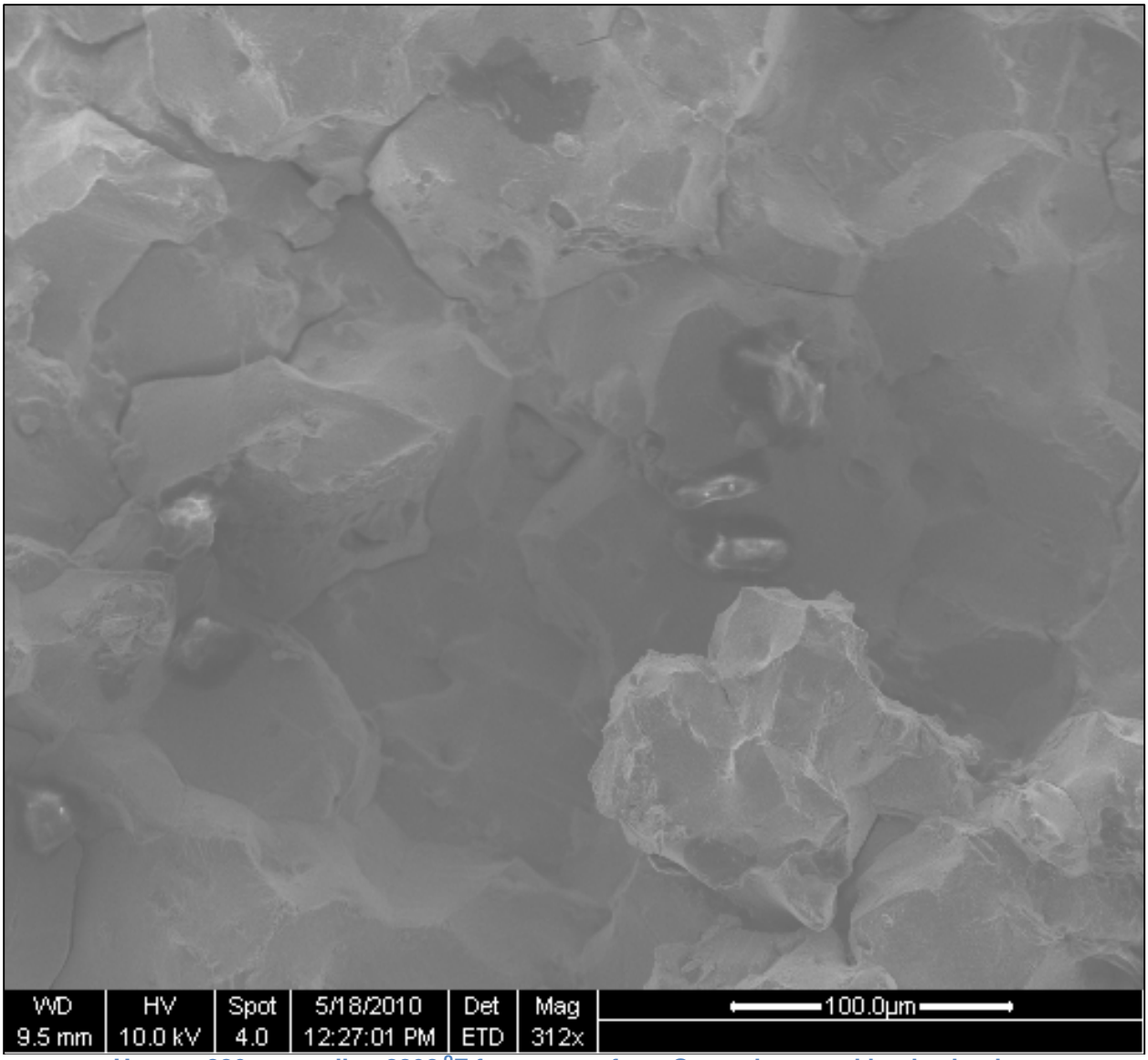

Figure 48: Haynes 230 on-cooling 2202 °F fracture surface. Secondary cracking is clearly visible throughout the image.

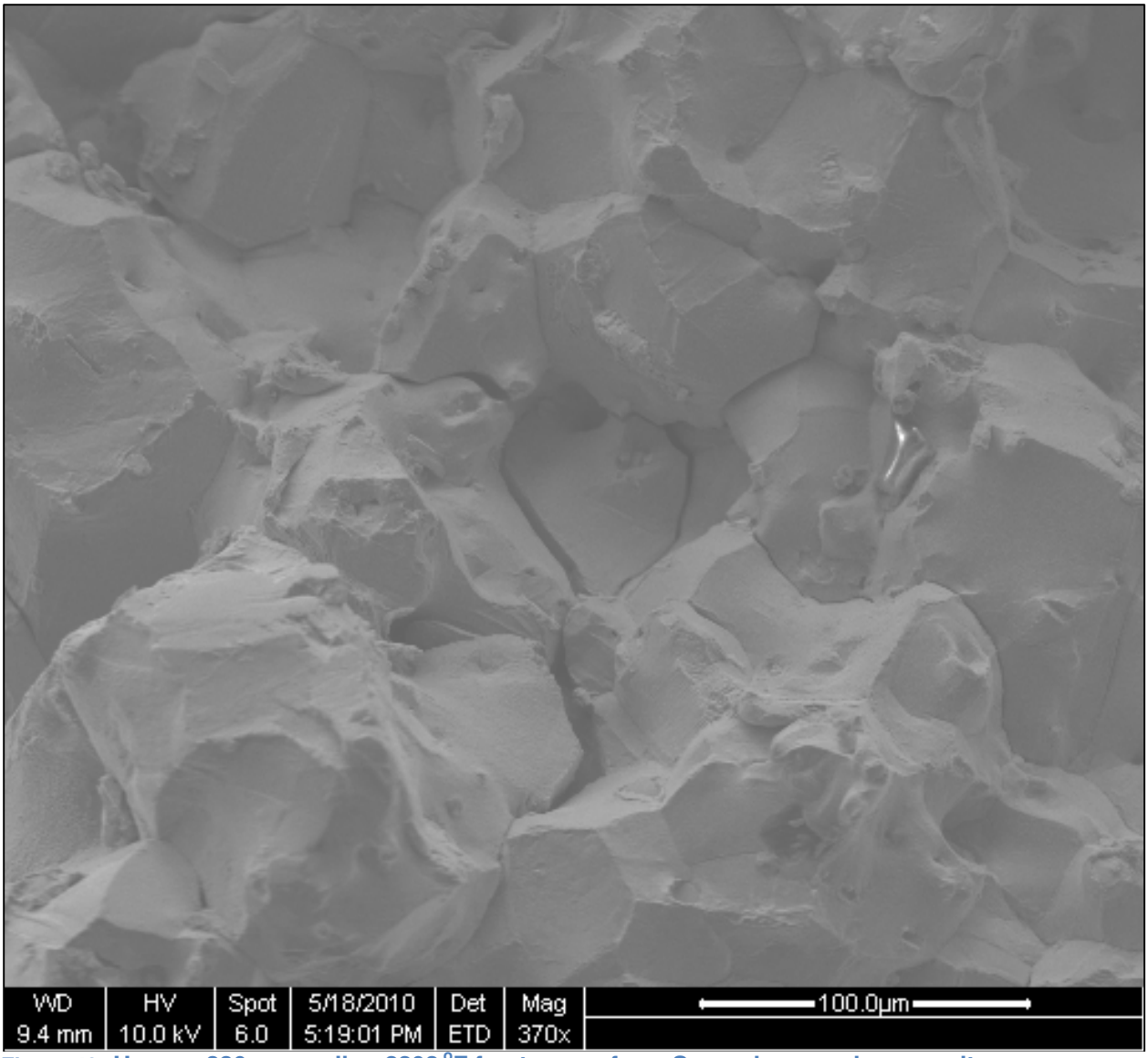

Figure 49: Haynes 230 on-cooling 2202 °F fracture surface. Secondary cracks are quite clear, and grain boundary surfaces are largely undeformed.

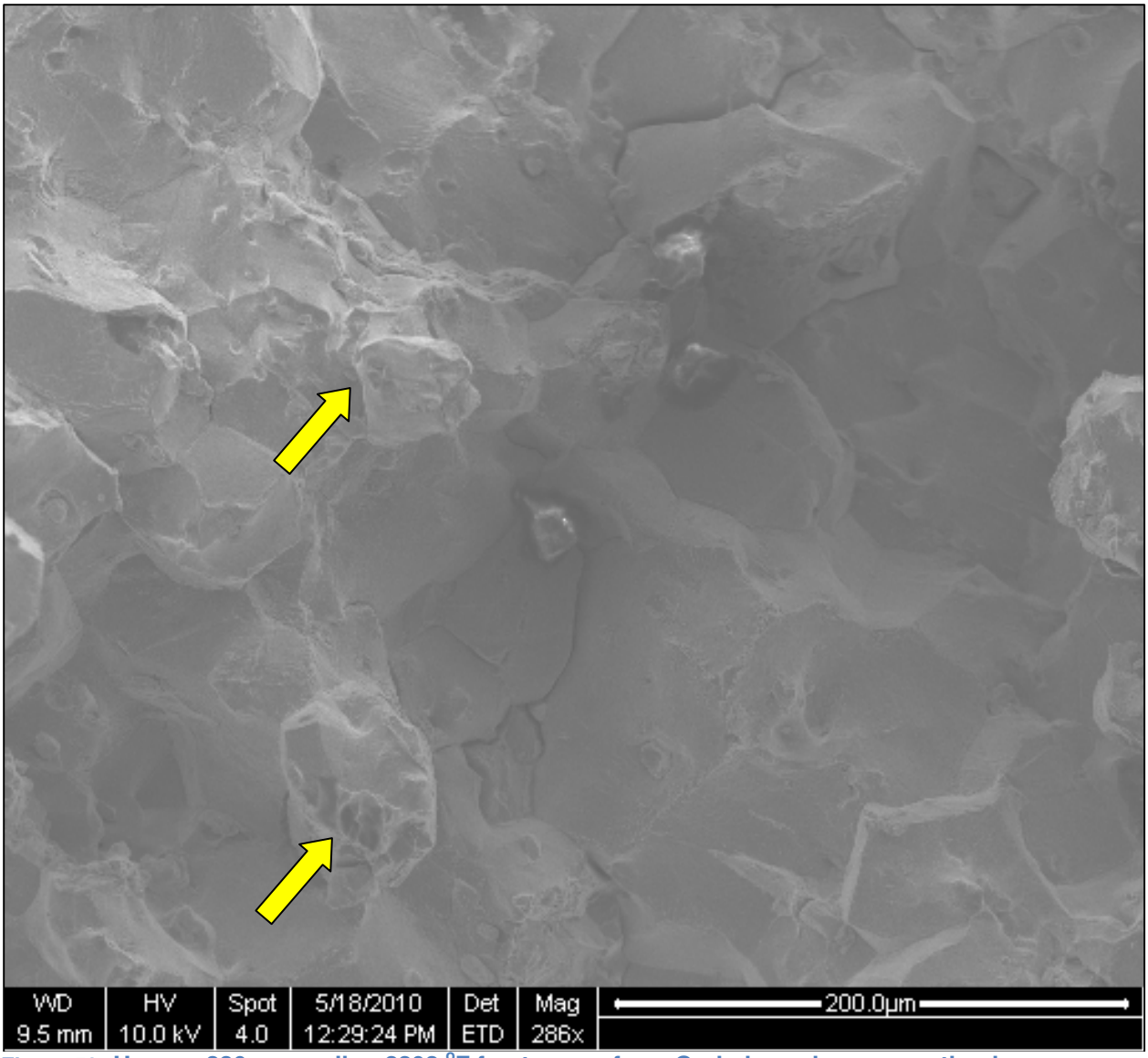

Figure 50: Haynes 230 on-cooling 2202 °F fracture surface. Grain boundary separation is again visible, along with a carbide located directly along a grain boundary (image center). Some localized regions of plastic deformation are present throughout the image (arrows).

The fracture surface of the on-cooling sample tested at 2153 °F, appeared similar to the sample tested at 2200 °F, with secondary cracks visible, and localized regions of plastic deformation. Ductility was still low (1%) at this temperature. Grain boundaries are still clearly visible in many cases, although not as well preserved or as universally outlined as in the 2200 °F sample. In Figures 206-210, regions of plastic

deformation can be seen along grain boundary edges. The appearance suggests that some liquid was present along grain boundaries at the time of fracture, but isolated regions had solidified, forming intact solid bridges at these sites. These small regions contributed to the minimal ductility that was detected as they plastically deformed during failure. The textured appearance of these bridged areas indicates dynamic recrystallization having occurred during failure.

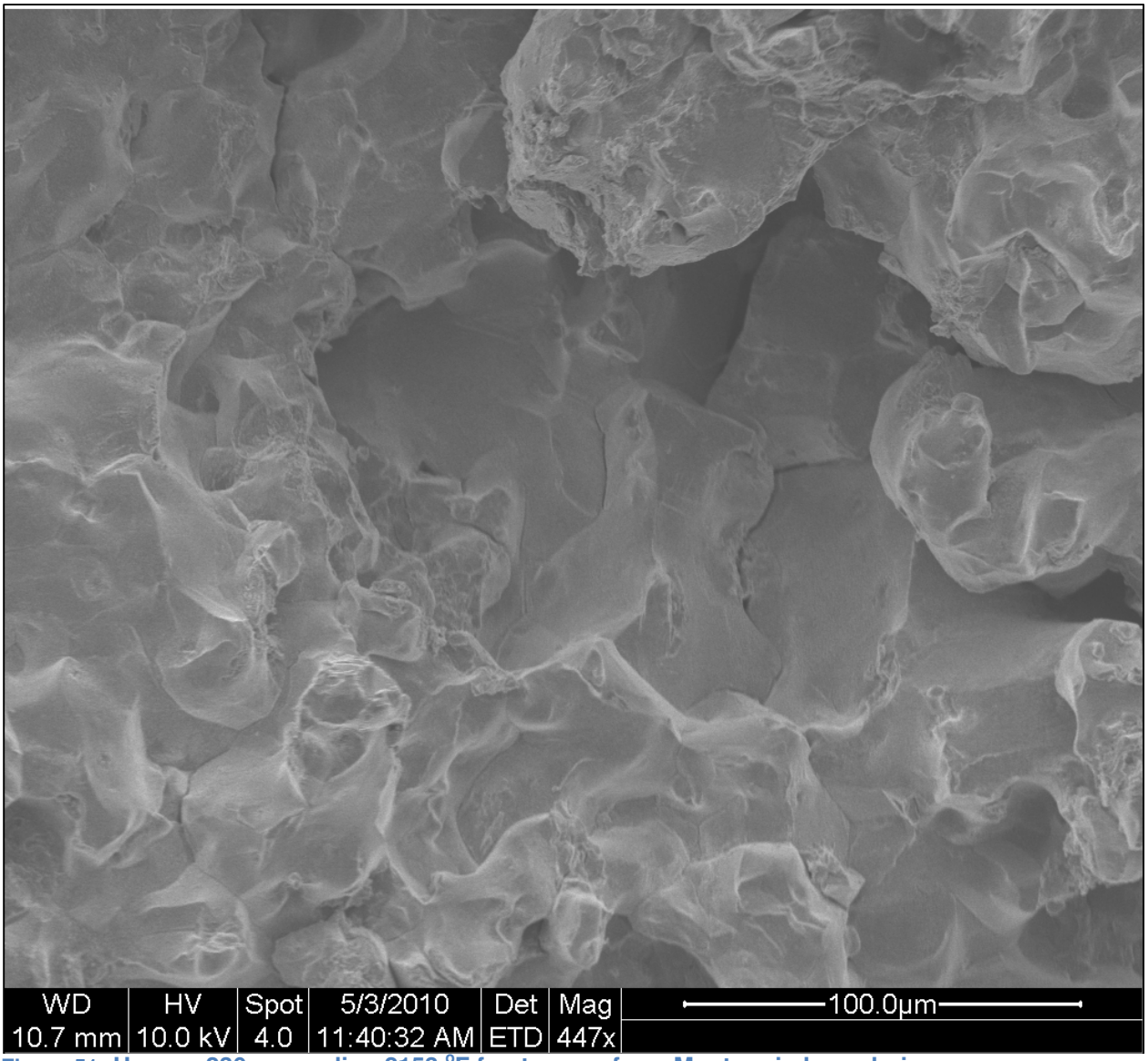

Figure 51: Haynes 230 on-cooling 2153 °F fracture surface. Most grain boundaries are smooth and undeformed.

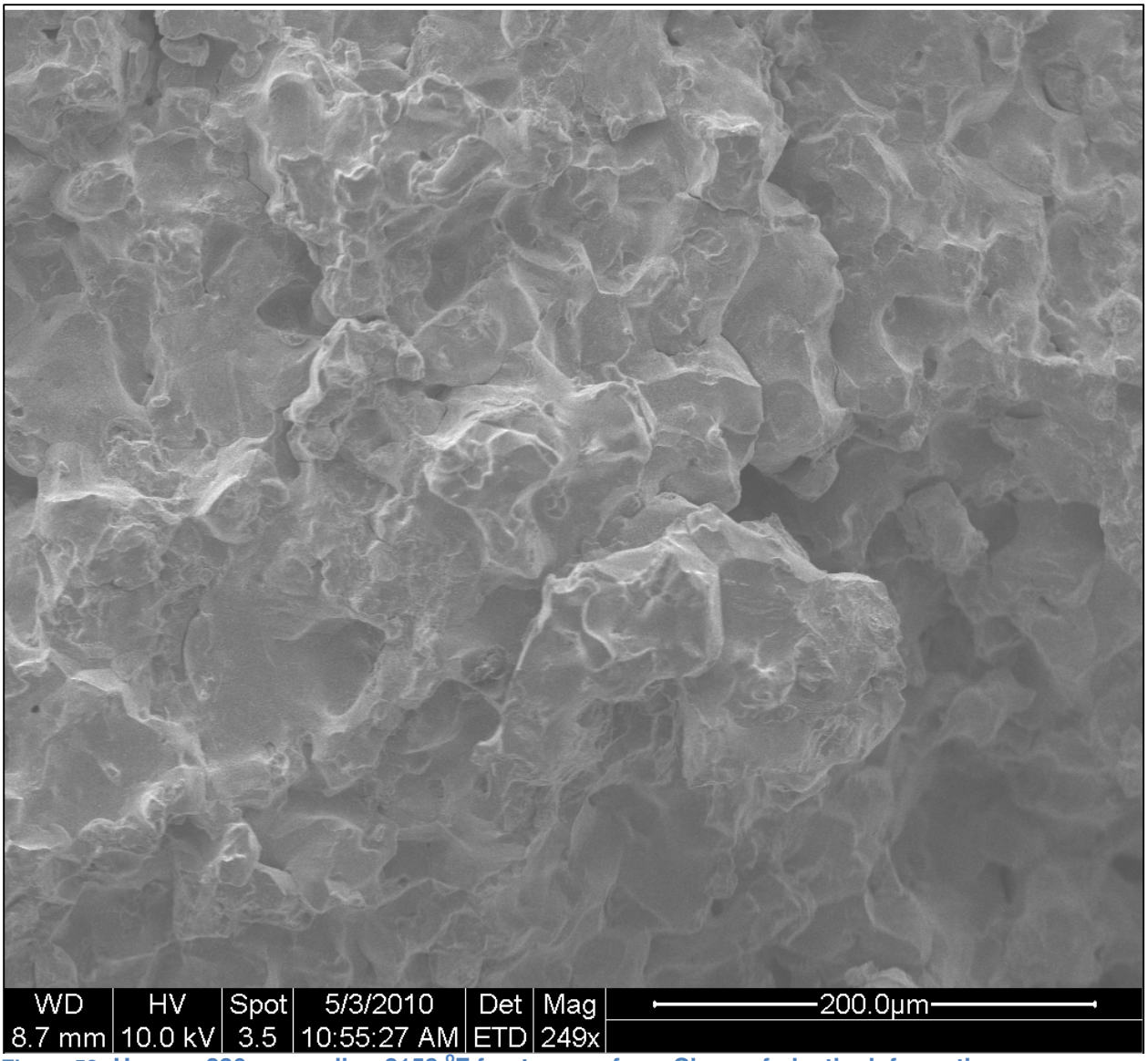

Figure 52: Haynes 230 on-cooling 2153 °F fracture surface. Signs of plastic deformation are limited but visible, differing in appearance from the smooth grain boundary surfaces.

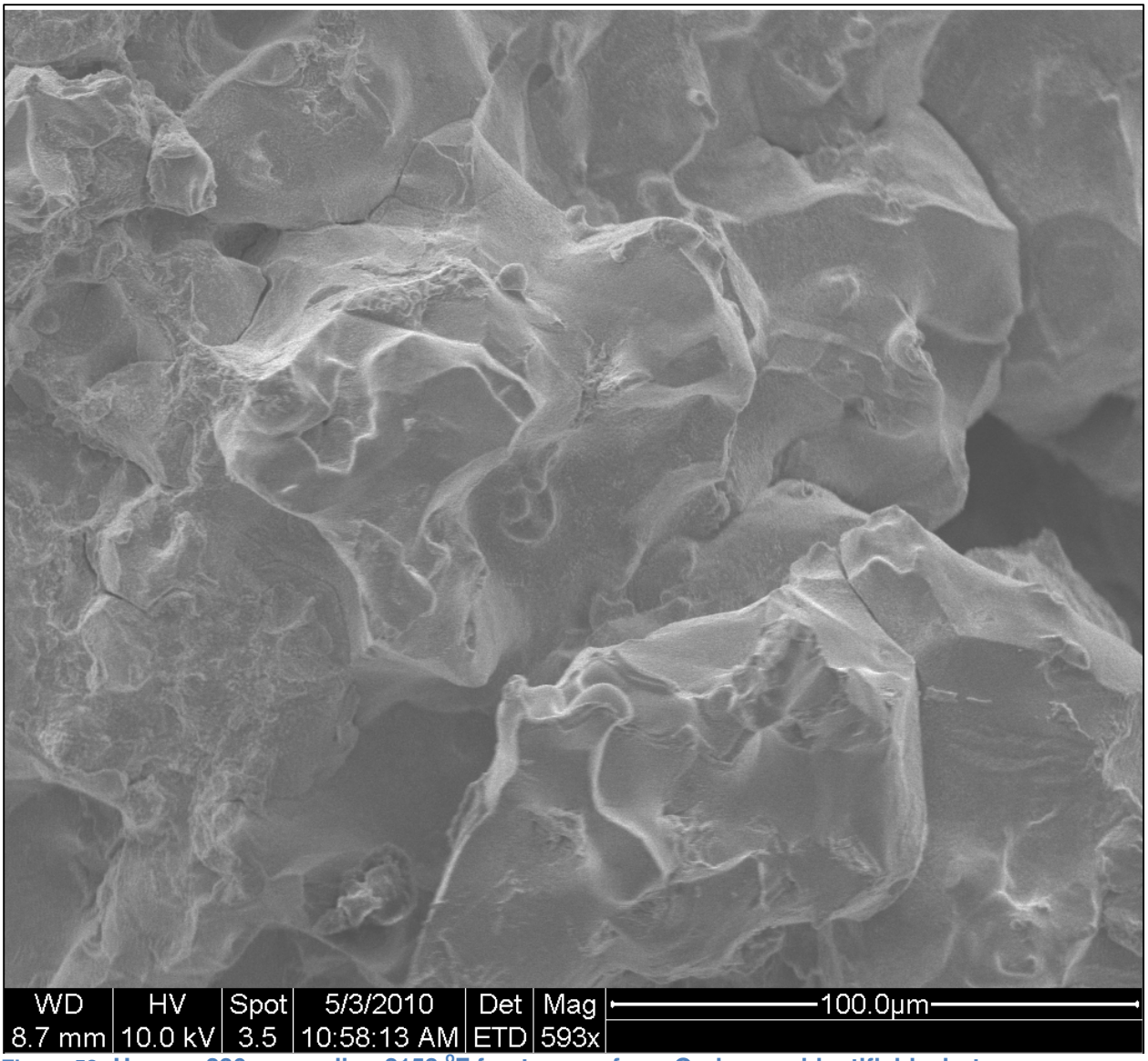

Figure 53: Haynes 230 on-cooling 2153 °F fracture surface. Grains are identifiable, but regions of plastic deformation are visible, appearing more textured than the majority of surfaces in the image.

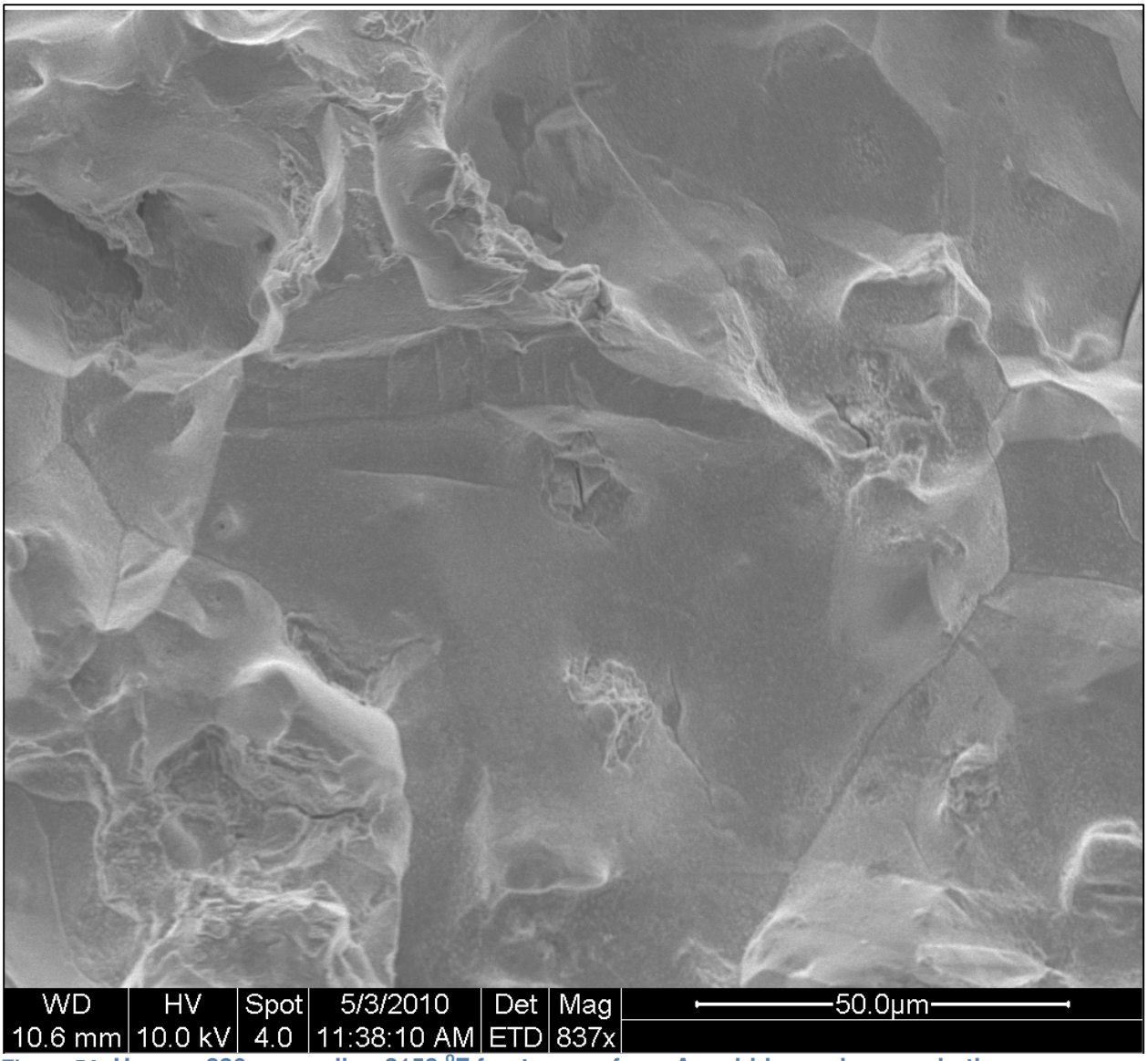

Figure 54: Haynes 230 on-cooling 2153 °F fracture surface. A carbide can be seen in the middle of the image.

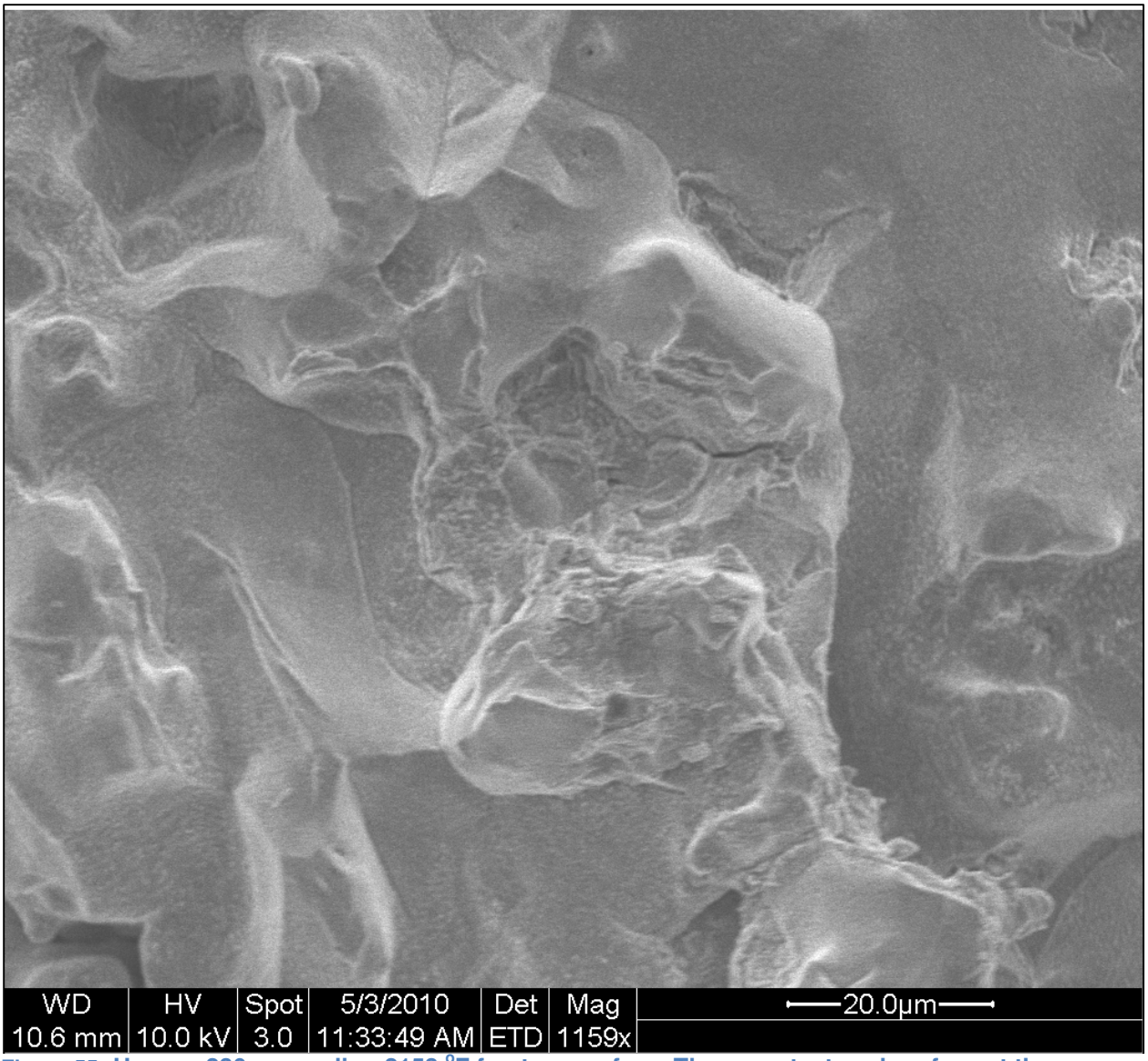

Figure 55: Haynes 230 on-cooling 2153 °F fracture surface. The more textured surface at the image center indicates localized plastic deformation resulting from the failure process.

The fracture surface images of the Haynes 230 samples tested on-cooling at 2046 °F show obvious signs of a return to ductile failure, which agrees with the 45% R/A. No grain boundaries are evident on the fracture surface. The surface appears as a combination of ductile cup and cone failure, and larger ductile tears. Grain boundary films present at the peak temperature have completely solidified, but the temperature is high enough to drive the dynamic recrystallization process. As large grains tear

and plastically flow during failure, new smaller grains nucleate in the highly stressed material. Nucleation of these recrystallized grains is typically heterogeneous and can occur along pre-existing grain boundaries, effectively making the original grains difficult to identify after failure. The large void displayed in Figure 59 has the appearance of having been formed through a tearing process. The combination of its lineal nature, and inward projects of material perpendicular to the length of the void contribute to this appearance. These peaks of material are the result of a ductile flow of material as the void opened, thinning the material as it deformed, until complete separation occurred.

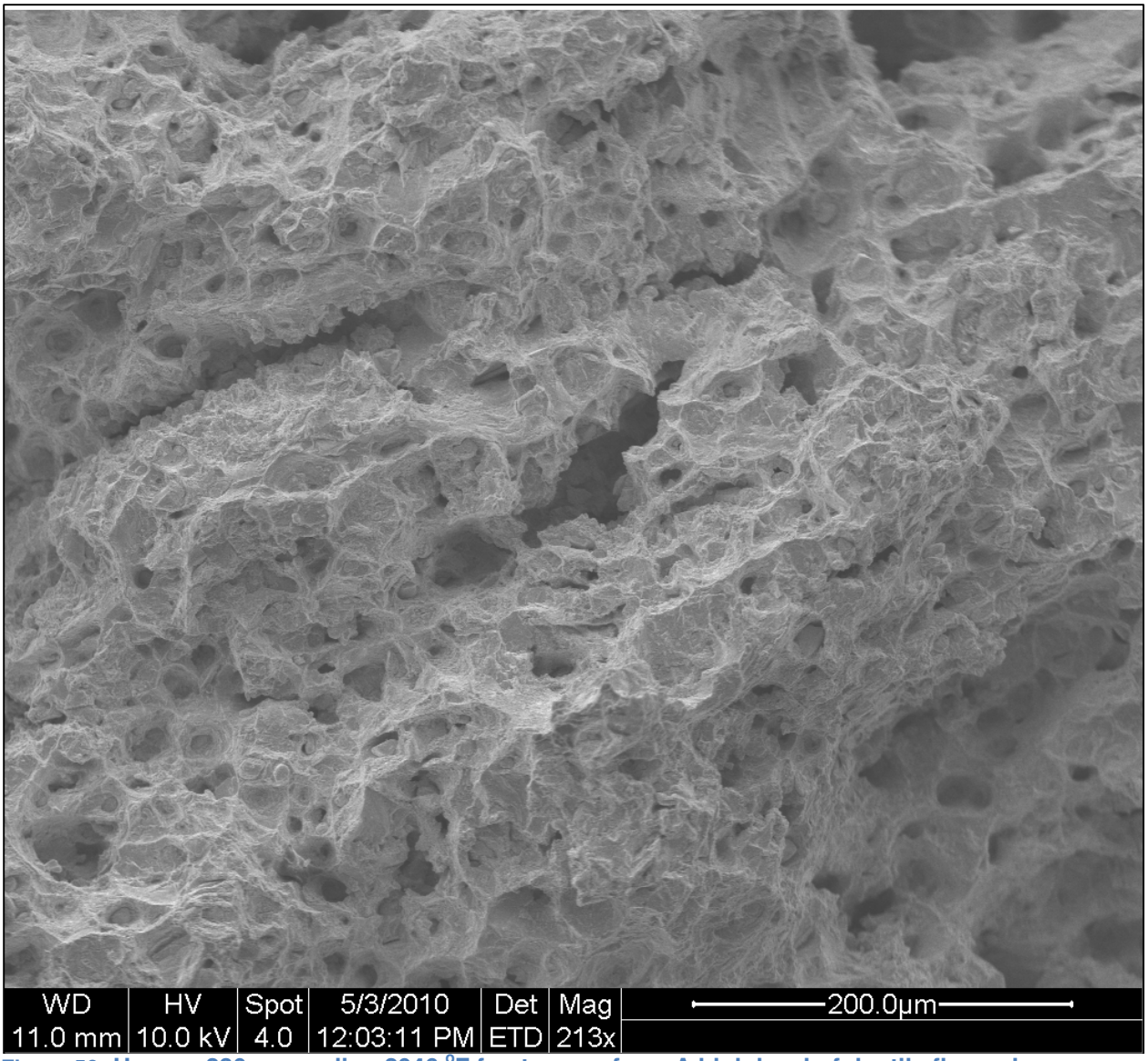

Figure 56: Haynes 230 on-cooling 2046 °F fracture surface. A high level of ductile flow prior to failure is evident. The cup-and-cone appearance of microvoid coalescence is clearly visible. Central to the image is a much larger void.

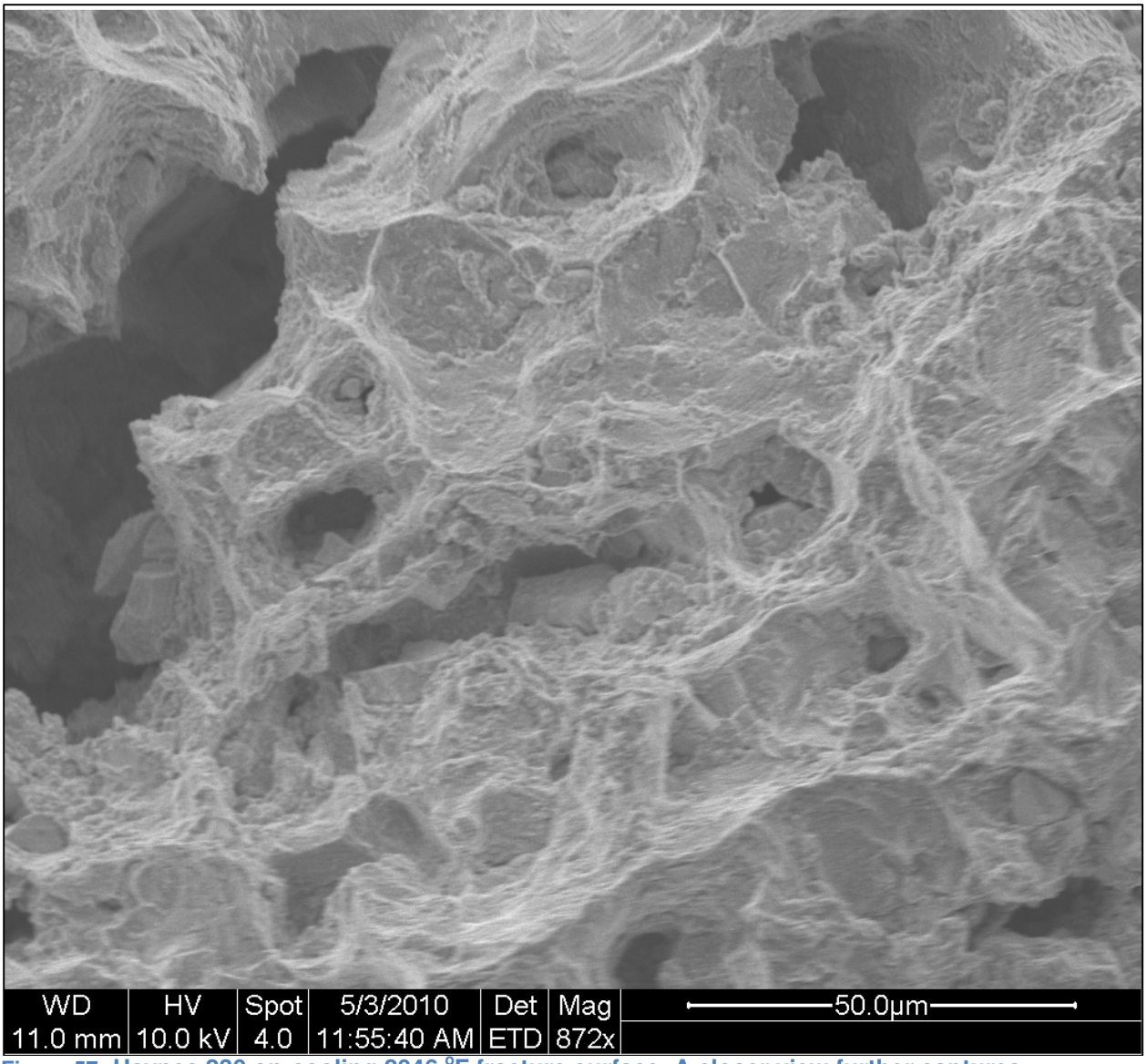

Figure 57: Haynes 230 on-cooling 2046 °F fracture surface. A closer view further captures the cup-and-cone appearance of ductile failure alongside the large void.

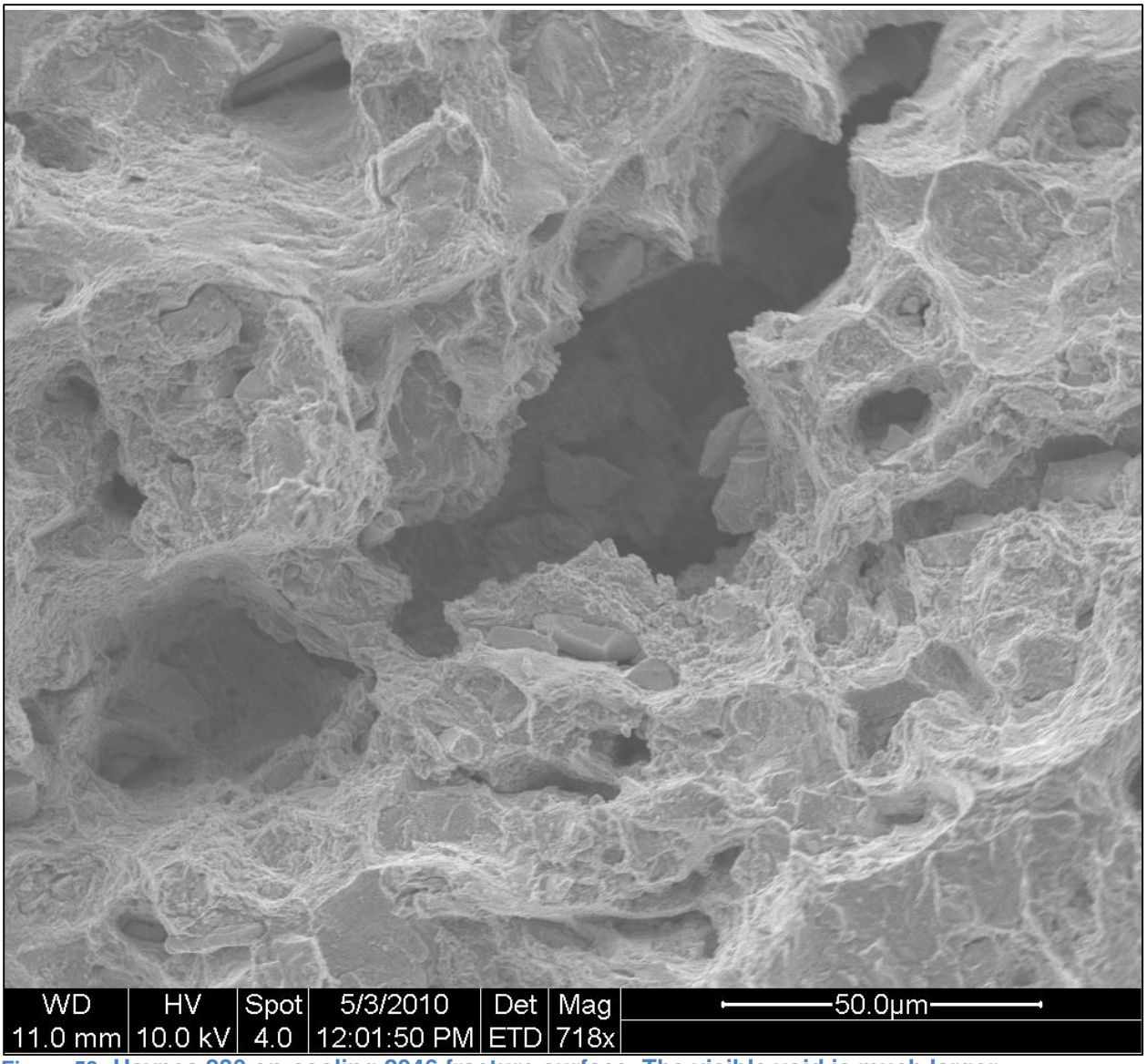

Figure 58: Haynes 230 on-cooling 2046 fracture surface. The visible void is much larger than the areas where cup and cone failure has occurred. Inward projections are seen at the image top right.

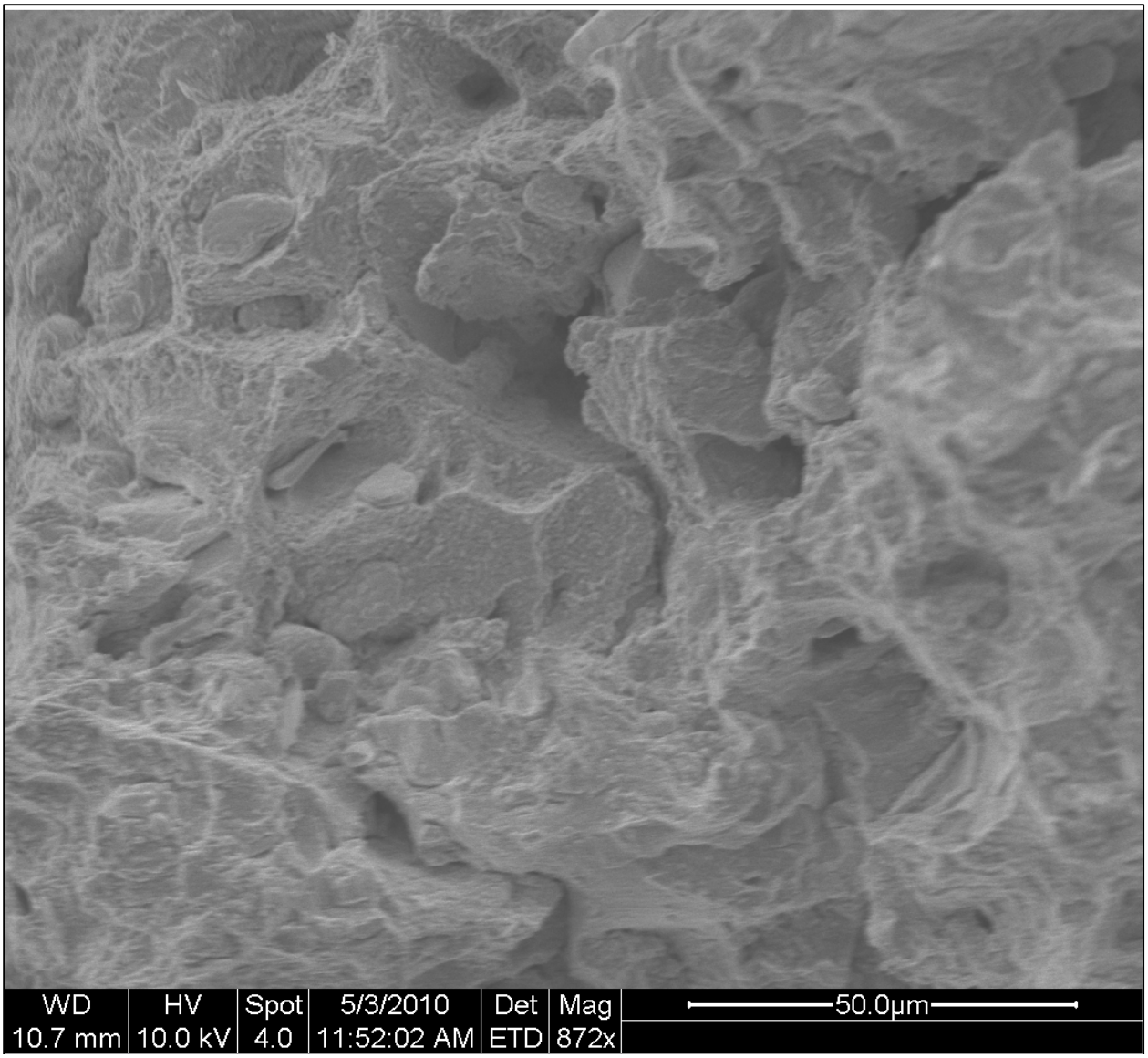

Figure 59: Haynes 230 on-cooling 2046 fracture surface. The surface appears jagged and deformed throughout the image.

3.4 Gleeble® Hot Ductility Sample Microstructure: Optical Microscopy Images

3.4.1 Inconel 718

Figure 63 is a photomicrograph of a longitudinal section of a nil-strength hot-ductility sample. It shows clear evidence that local melting is the cause of the failure. Constitutional liquation is clearly evident near the fracture surface. Grains at the fracture tip are larger than the base metal. They appear to peak in size in a region slightly removed from the fracture tip. Moving further from the fracture tip, grains return in size to that of the base metal, and no detectable grain refinement region is seen.

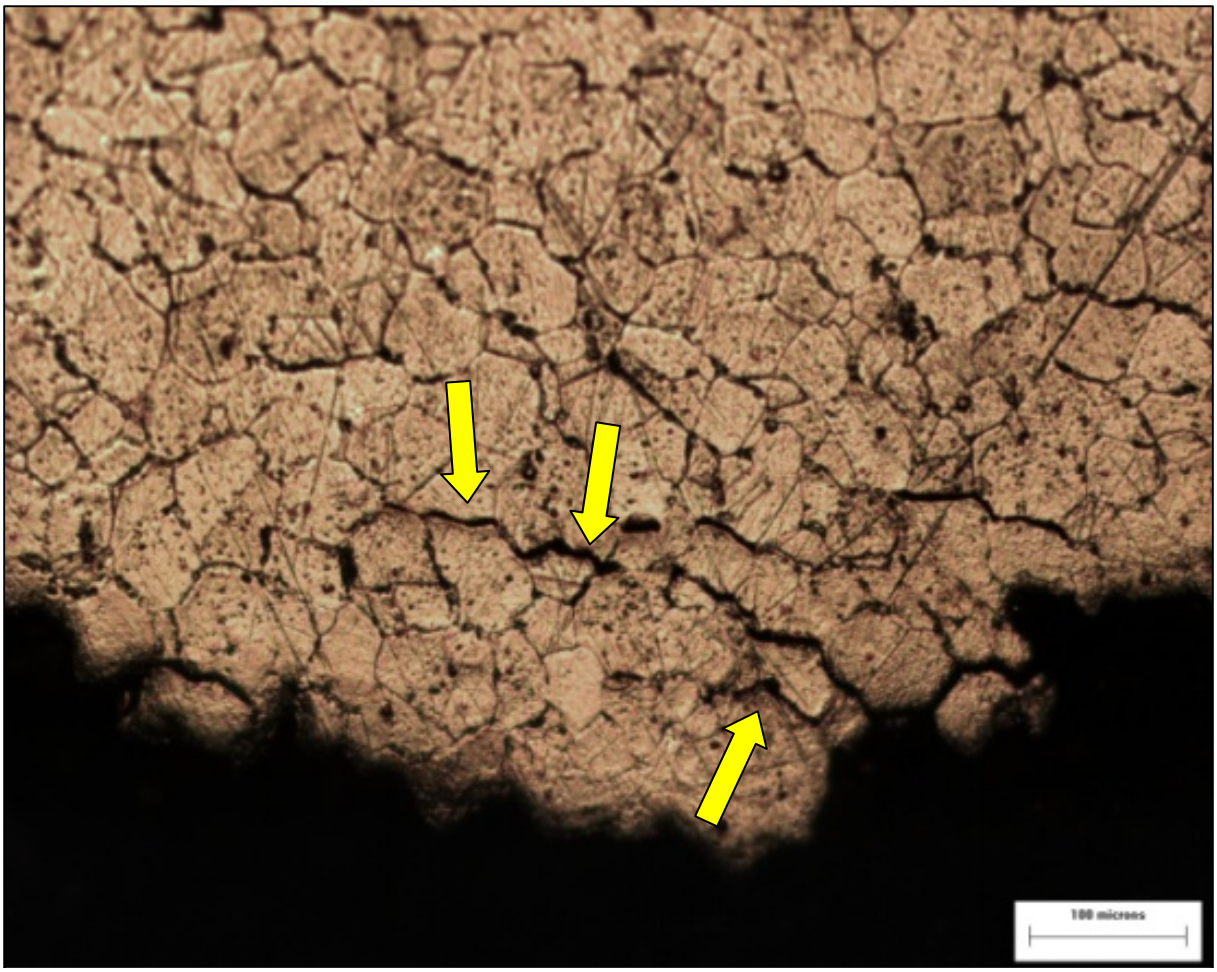

Figure 60: Micrographs of Nil strength sample. 100x image showing grain boundary melting and separation along the fracture surface.

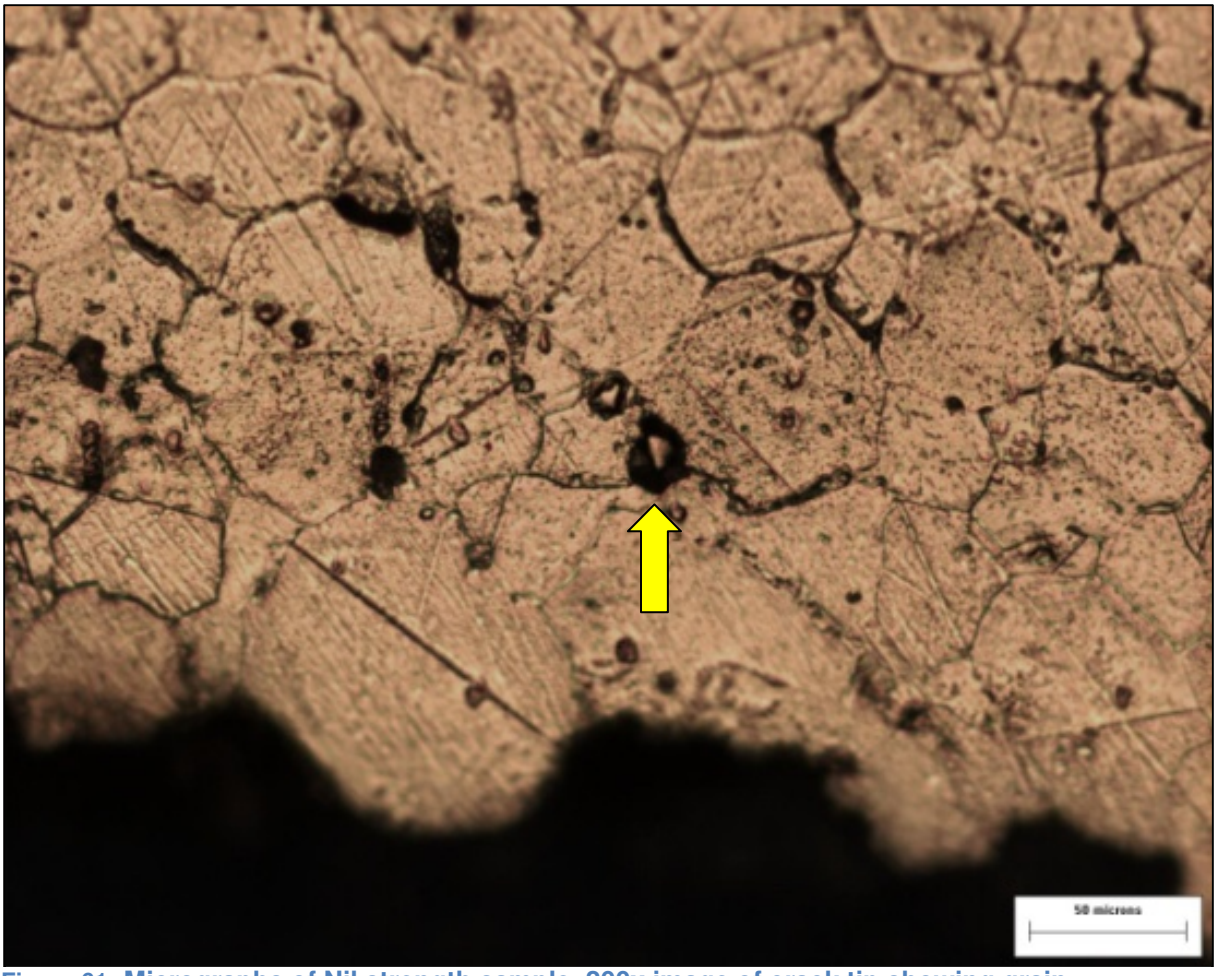

Figure 61: Micrographs of Nil strength sample. 200x image of crack tip showing grain boundary melting and constitutional liquation (arrow).

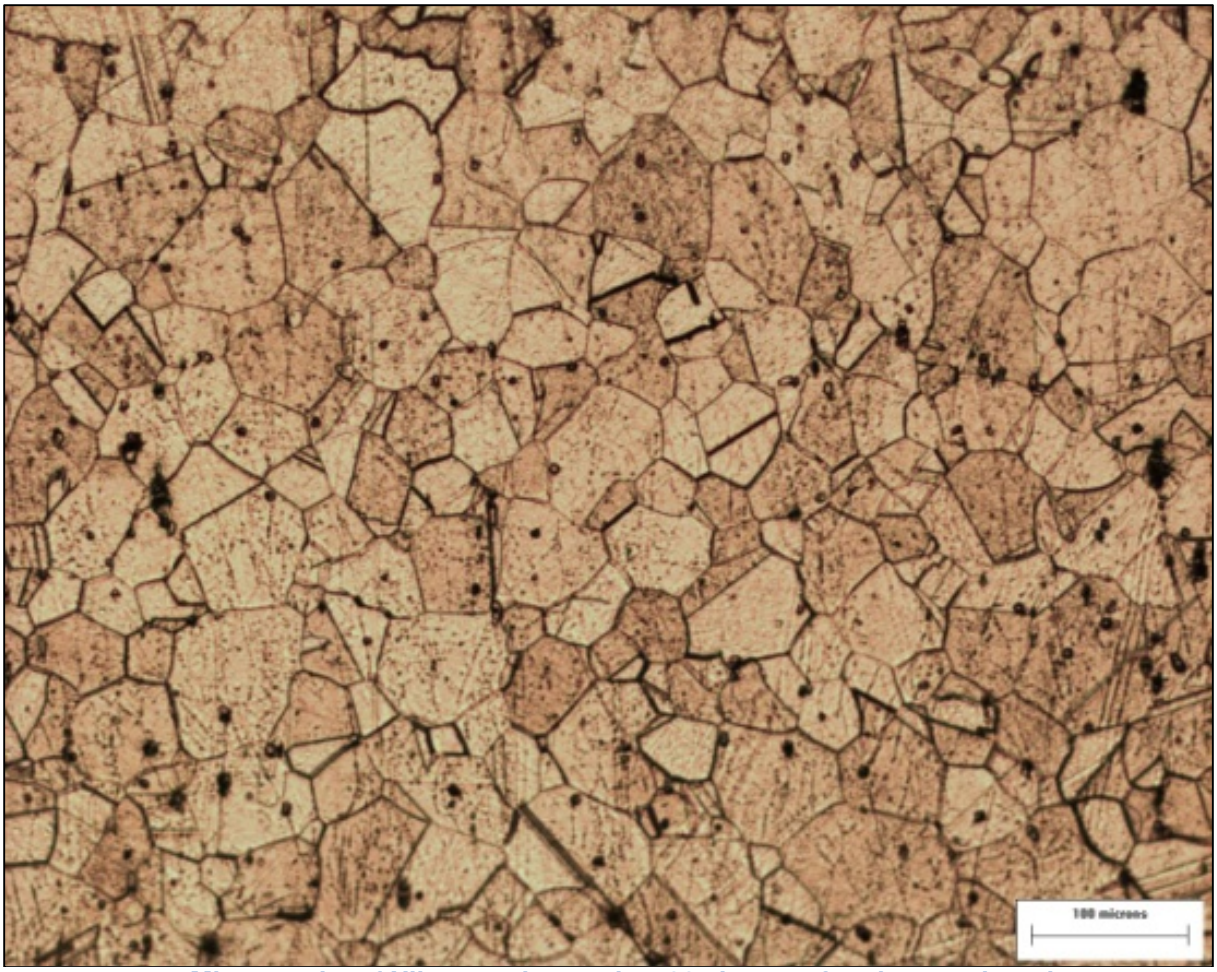

Figure 62: Micrographs of Nil strength sample. 100x image of grain growth region

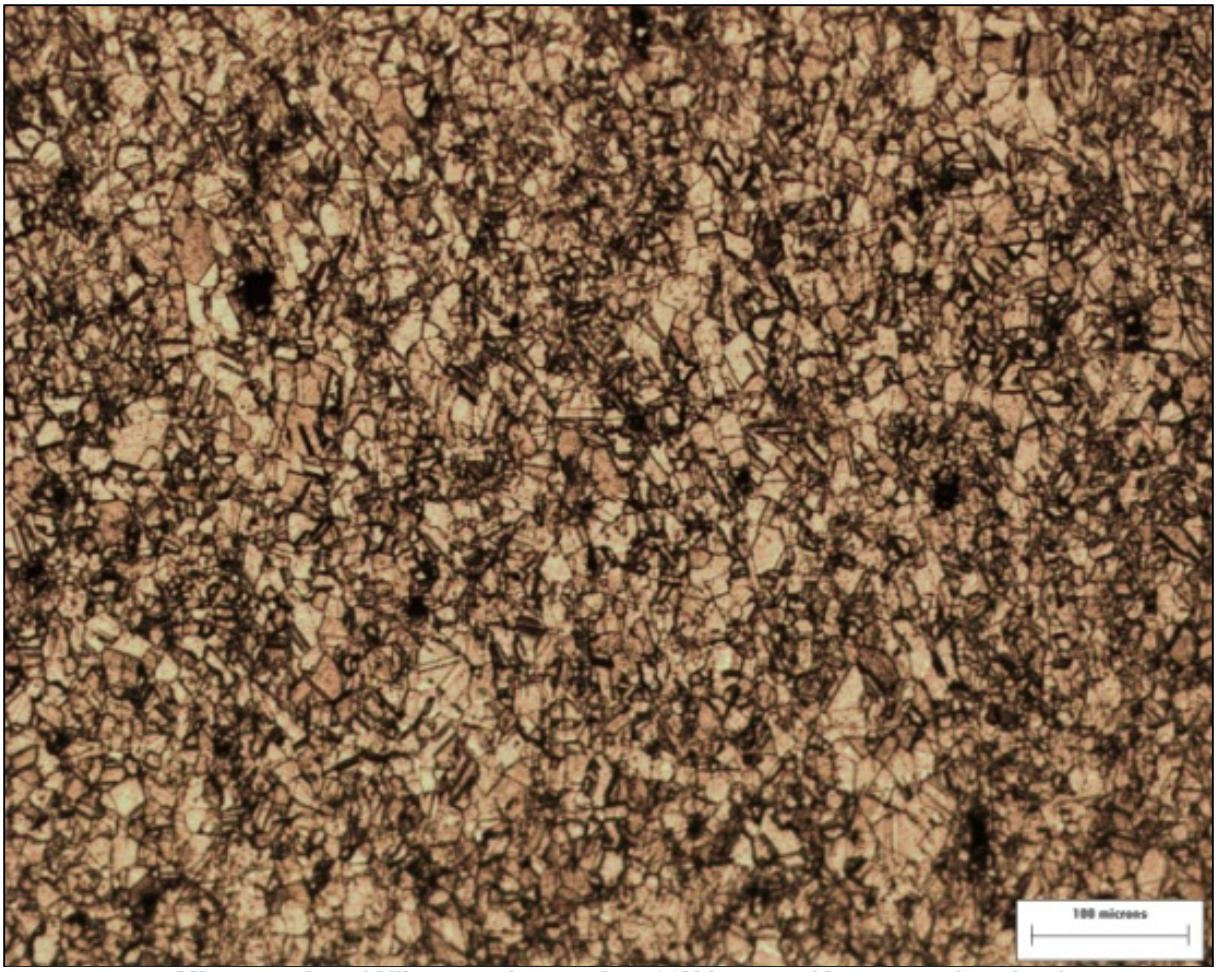

Figure 63: Micrographs of Nil strength sample. 100X image of base metal grain size.

The microstructure of the Gleeble® sample heated to 2188 ^{o}F and tested had a microstructural evolution similar to the nil strength sample, with grain growth at and near the crack trip, followed by a return to unaffected base metal grain size. Grain growth in this sample was expected, as temperatures near the fracture surface exceeded 1950 ^{o}F, all precipitates were forced into solution, and grain boundaries were left unpinned. The sample lacked the grain boundary separation and meltback of the nil strength sample, though, at the fracture surface. Although the presence of liquid along grain boundaries at and near the fracture surface was less obvious, the micrograph still indicates a

intergranular failure mode. Grains along the fracture surface are not distorted, and ductility at this temperature was still low, with a %R/A of 2%.

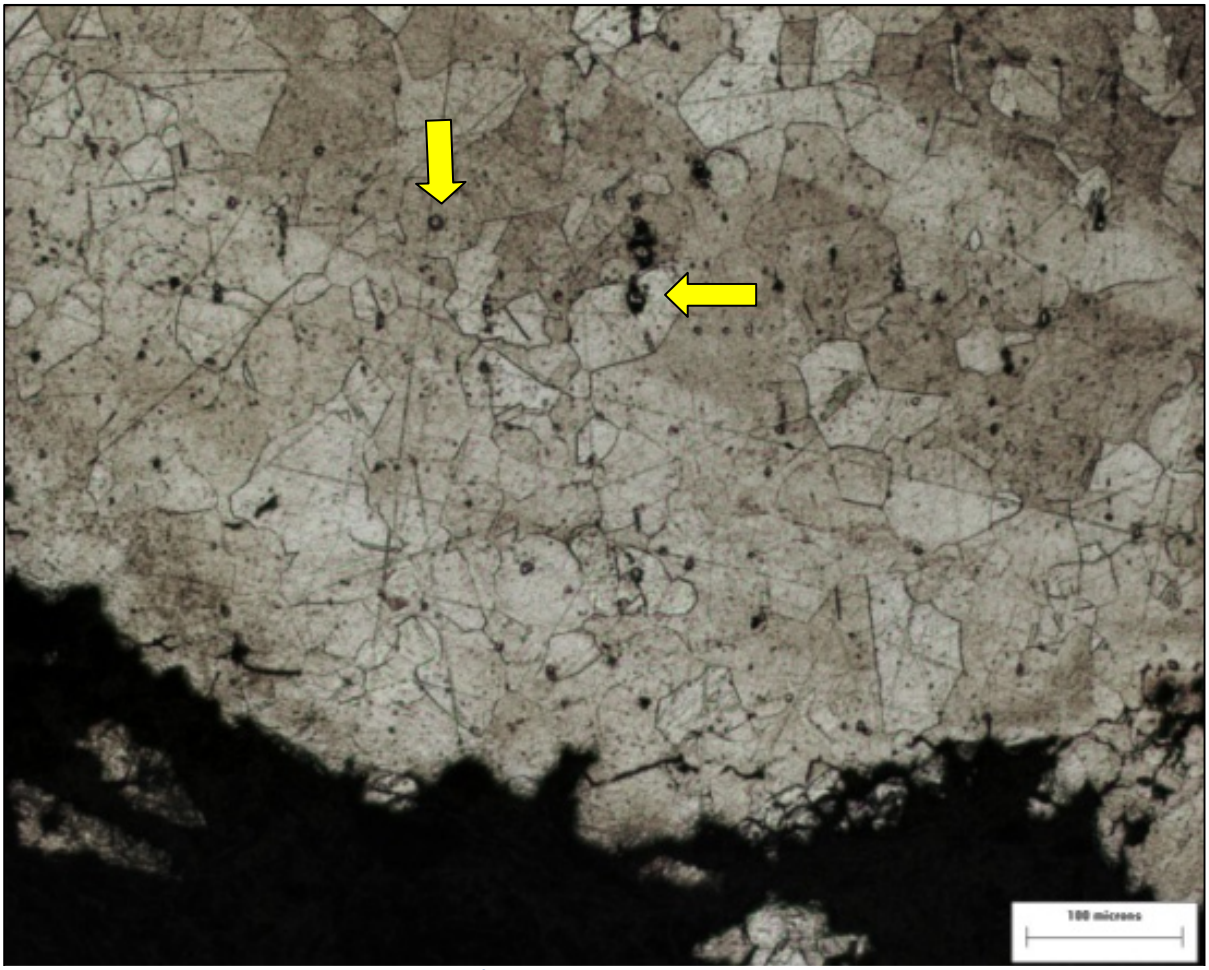

Figure 64: Inconel 718 on-heating 2188˚F micrographs. 100X fracture tip. The largest grains are on the scale of 100 microns in diameter. Arrows indicate locations of possible constitutional liquation.

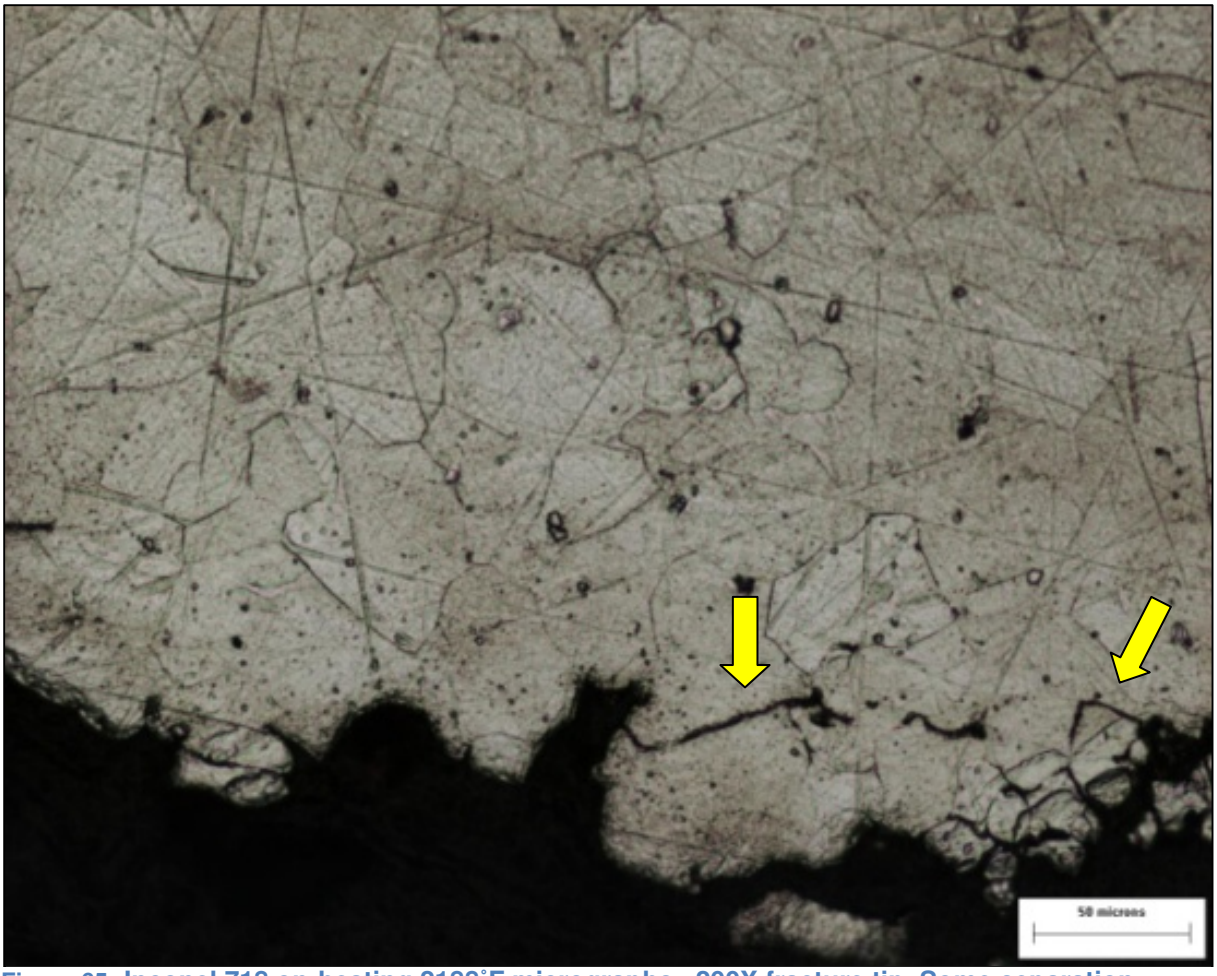

Figure 65: Inconel 718 on-heating 2188˚F micrographs. 200X fracture tip. Some separation along grain boundaries is visible.

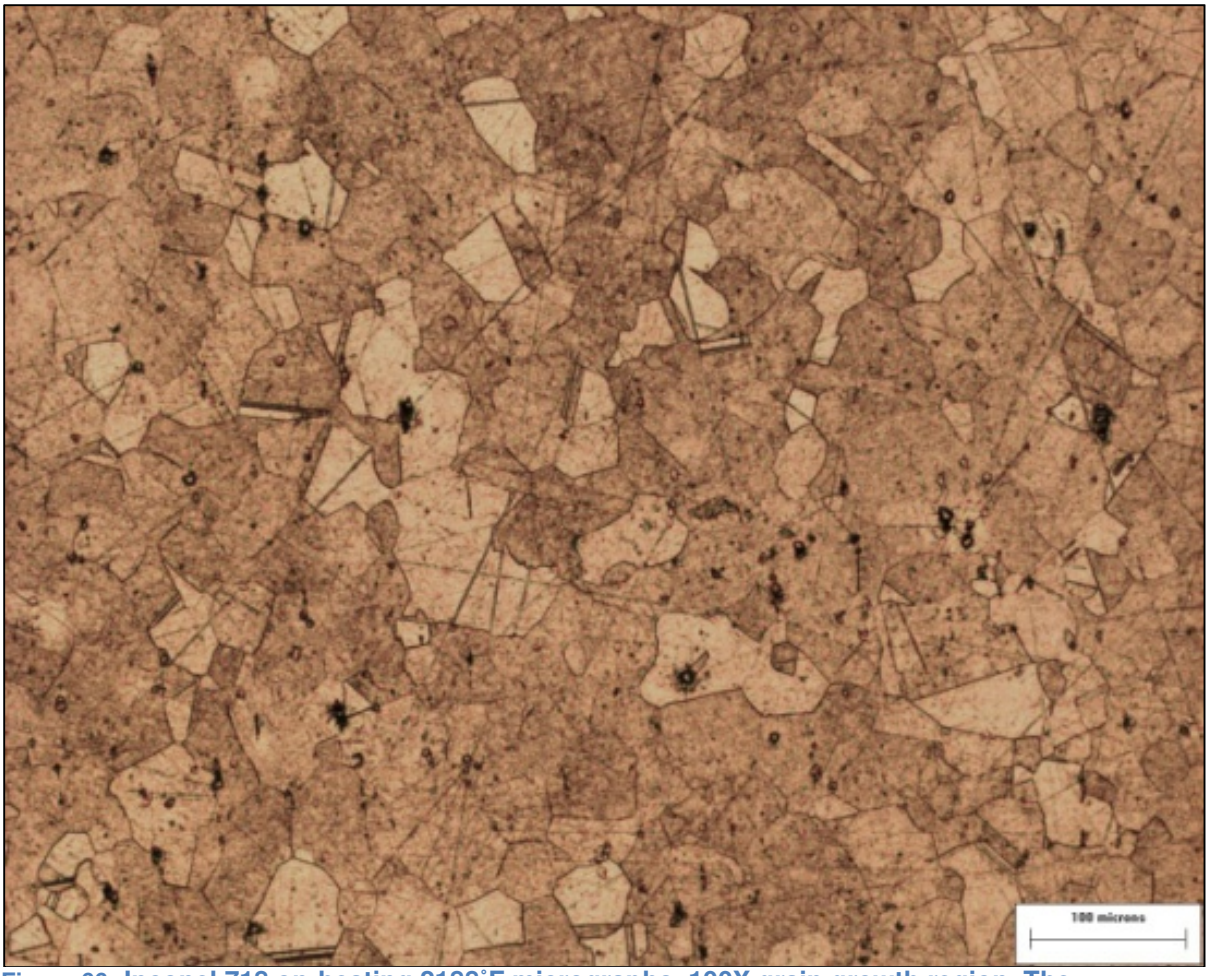

Figure 66: Inconel 718 on-heating 2188˚F micrographs. 100X grain growth region. The largest grains are similar in size as those near the fracture surface, with an approximate diameter of 100 microns.

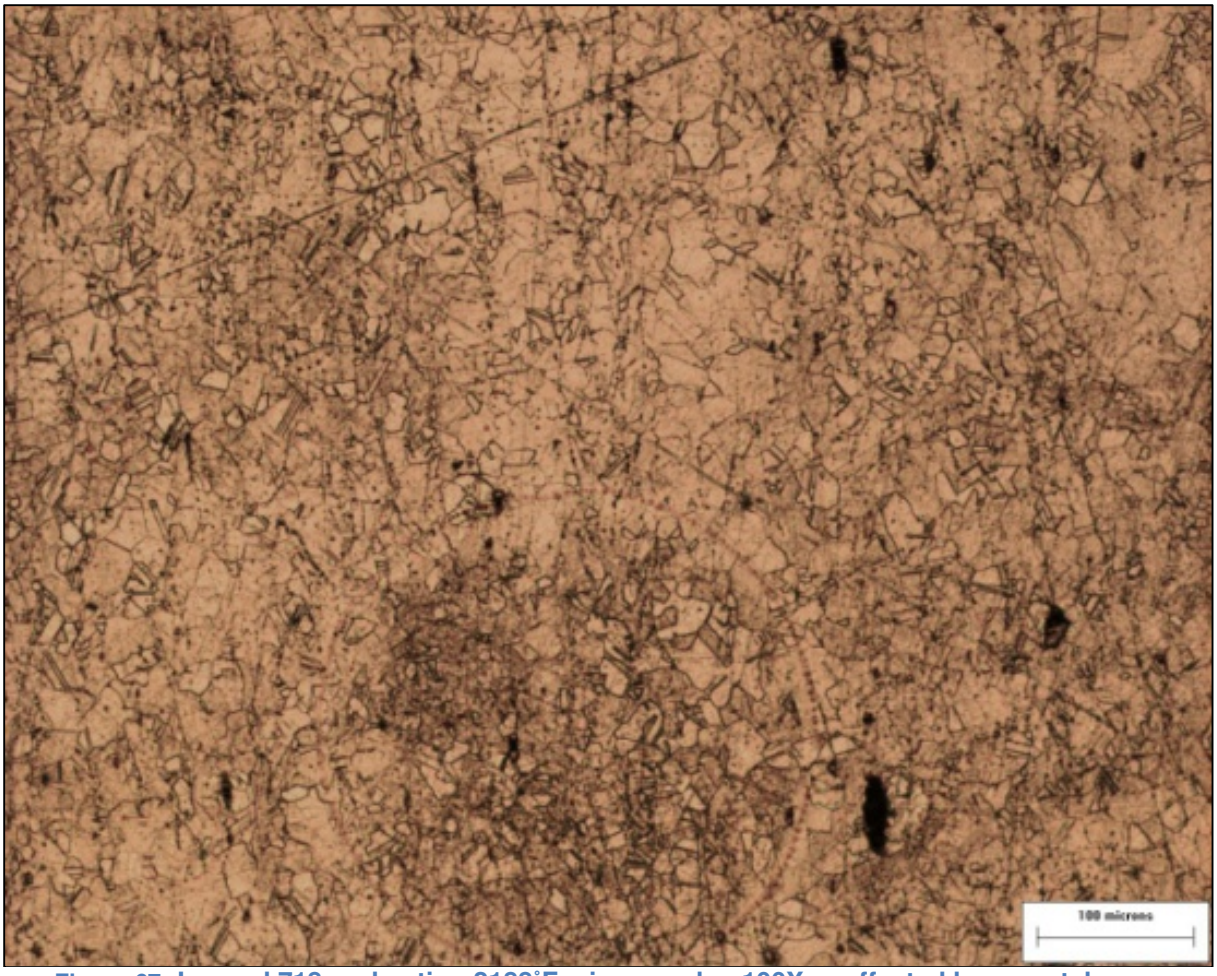

Figure 67: Inconel 718 on-heating 2188˚F micrographs. 100X unaffected base metal.

The microstructure of the on-heated sample heated and tested at 2073˚F completely lacks a visible region of grain growth at or near the crack tip, where temperatures were at a maximum. Temperatures at the tip have surpassed 1950°F, where grain growth is expected to begin. The lack of visible grain growth at the fracture tip can be attributed to the level of ductility at this temperature. The %R/A was 57 at this test temperature. As ductile failure occurs at the fracture surfaces, dynamic recrystallization reshapes and resizes grains that have already undergone grain growth. The result of this process is the lack of a visible region in which grain growth appears to have occurred. Some grain boundaries near the fracture tip show signs of liquation, appearing in the micrograph as

thicker and more pronounced than grain boundaries further removed. Signs of ductile flow can be seen along the edges of the sample, near the tip, where the sample deformed and reduced in cross sectional area. Grain boundaries can no longer be distinguished along the edge, having been drawn out and deformed in the process of ductile failure. Grain sizes at the tip, within the HAZ, and in the base metal, all appear relatively equal in size. Grains near the outer edge of the sample, where plastic flow has occurred, are distorted and difficult to identify individually.

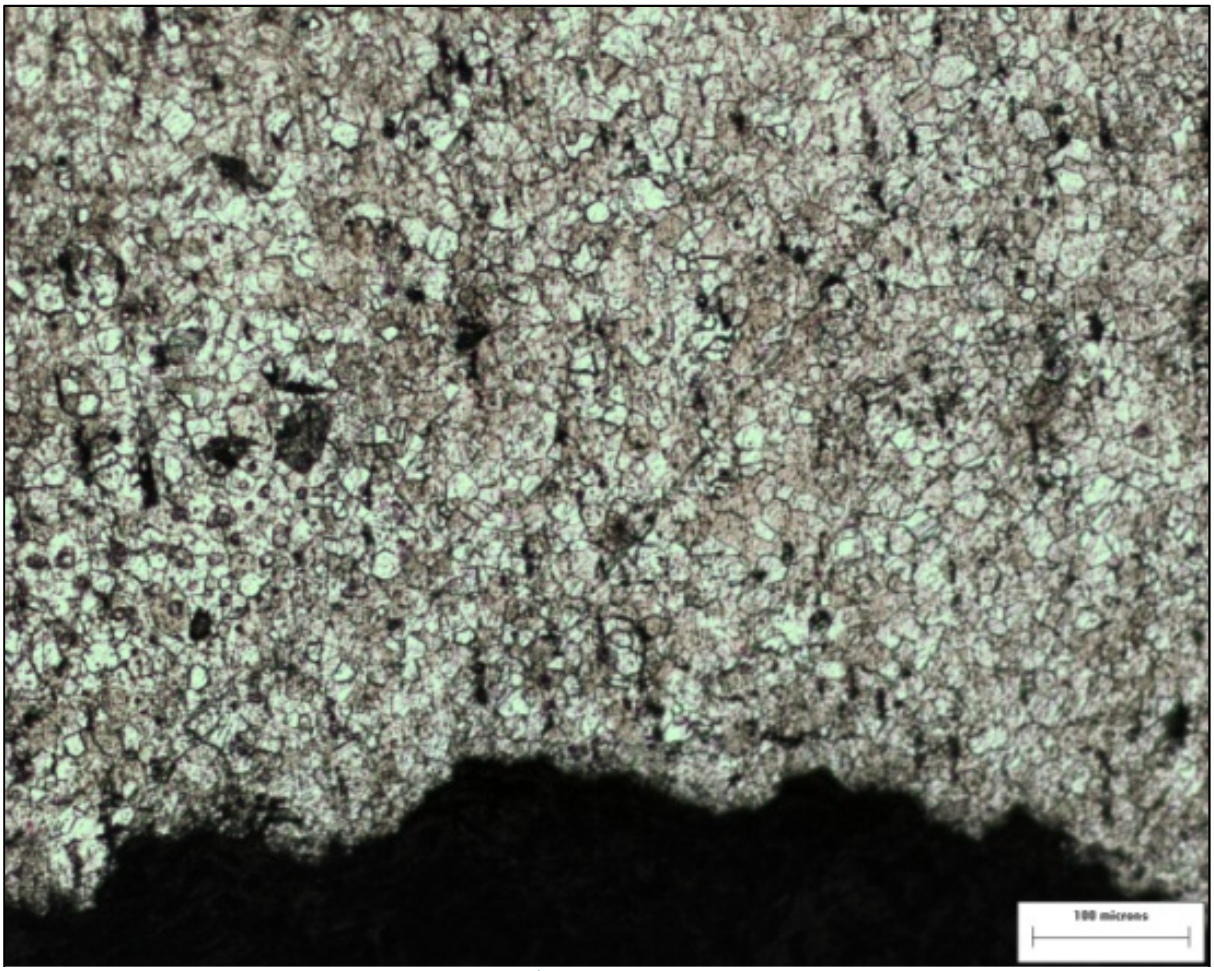

Figure 68: On-heating 2073˚F micrographs. 100x fracture tip

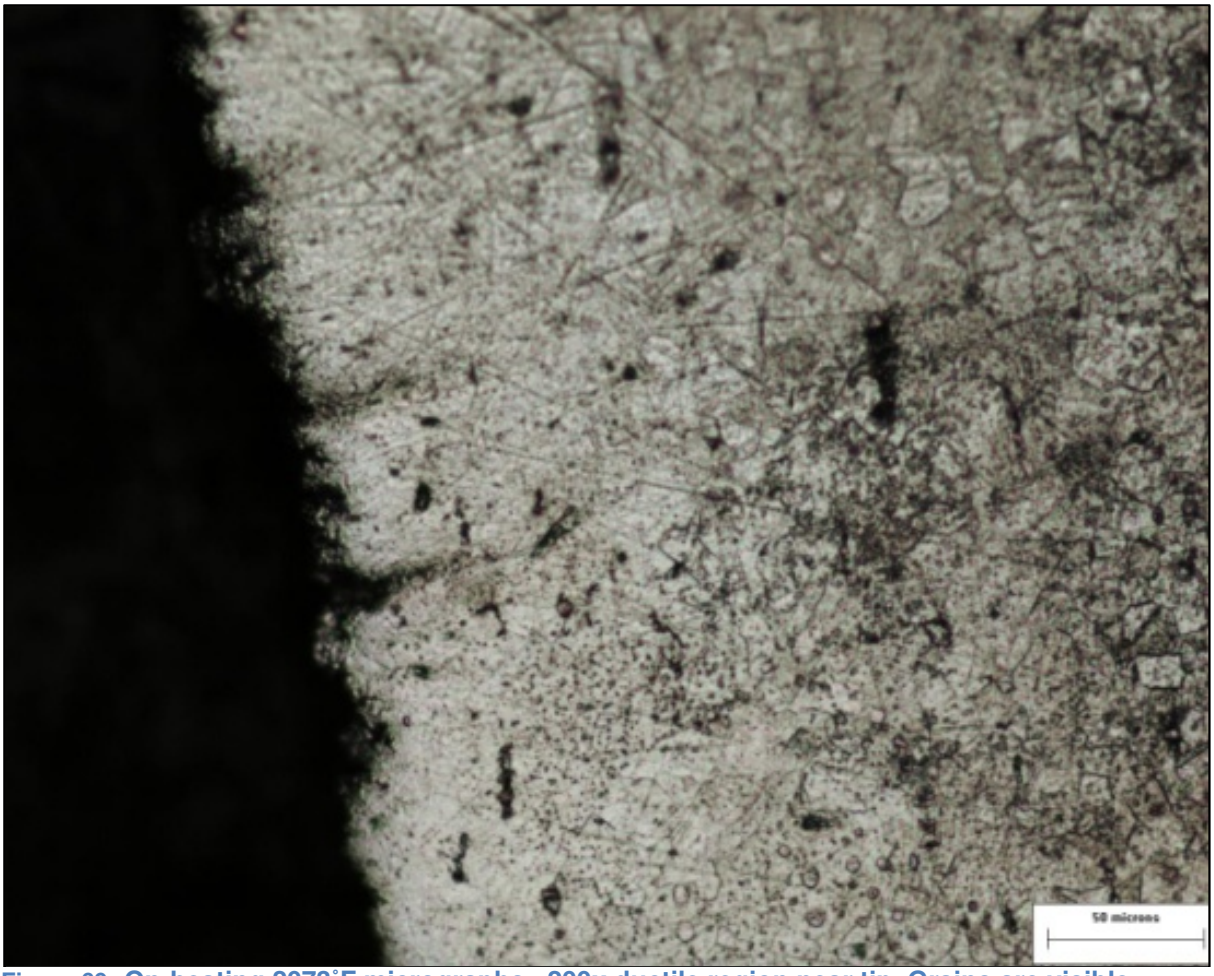

Figure 69: On-heating 2073˚F micrographs. 200x ductile region near tip. Grains are visible on the right edge of the image, but are distorted and indistinguishable at the sample edge.

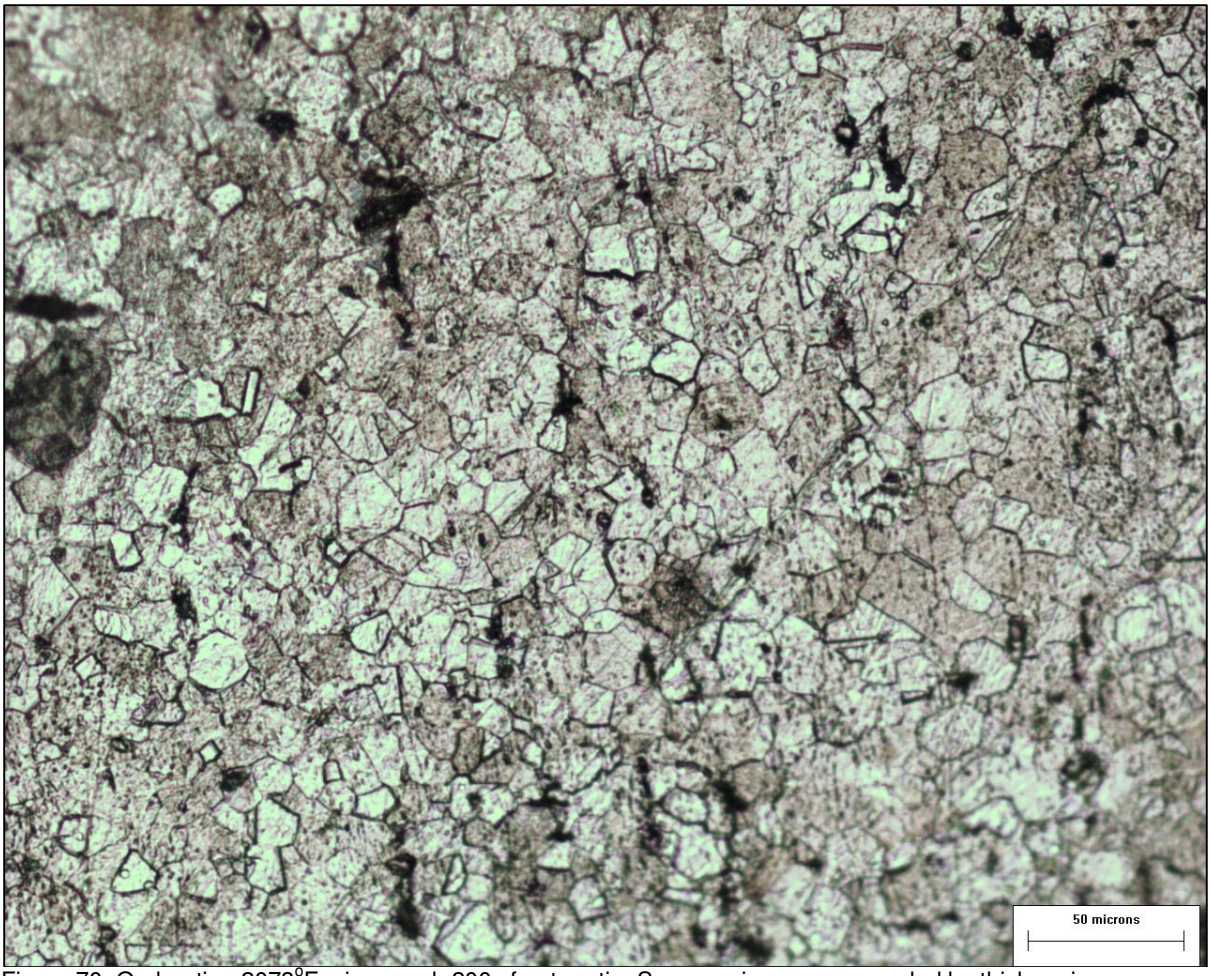

Figure 70: On-heating 2073°F micrograph 200x fracture tip. Some grains are surrounded by thick grain boundaries, a sign of grain boundary liquation having occurred prior to failure.

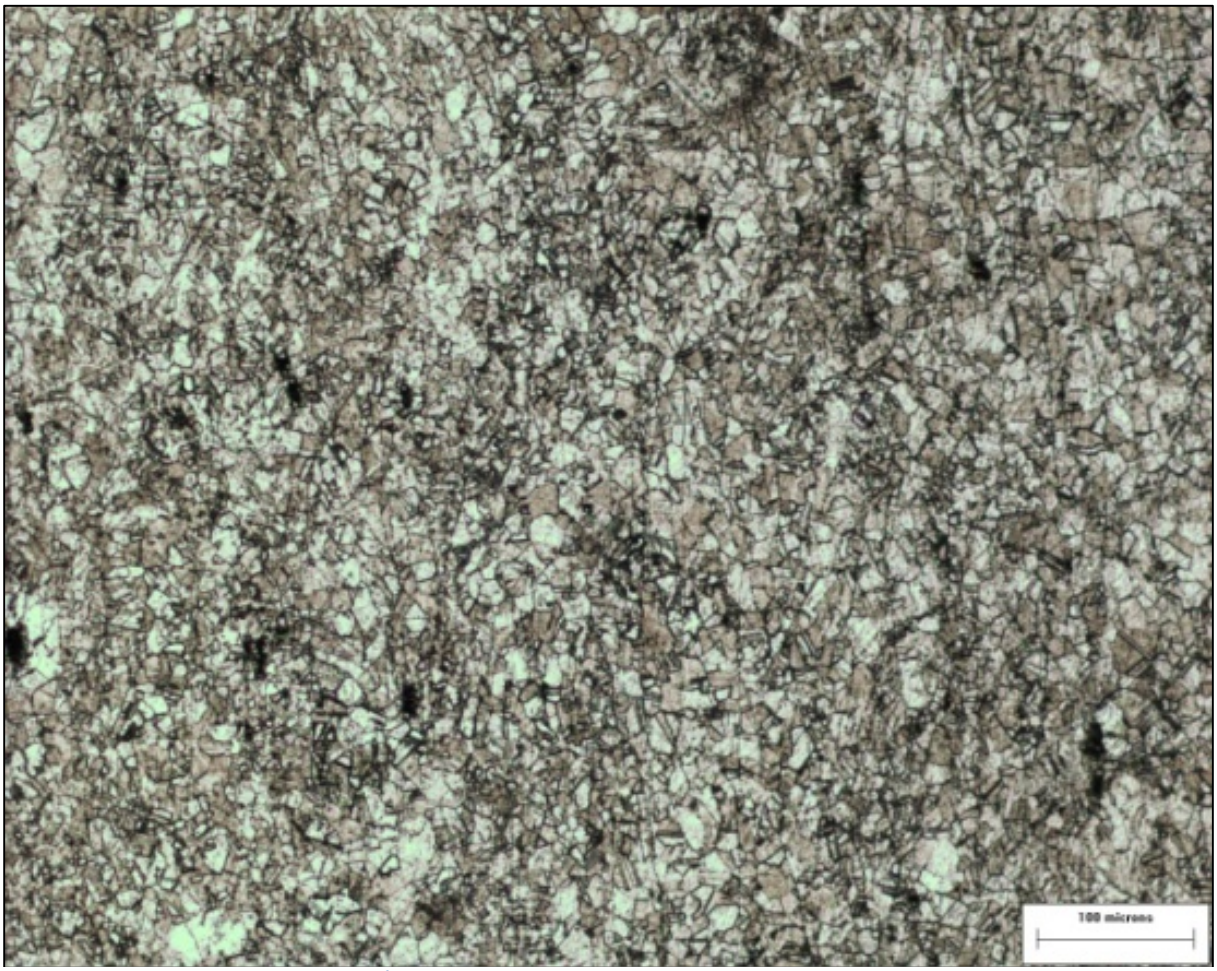

Figure 71: On-heating 2073˚F micrographs. 100x removed from the fracture surface.

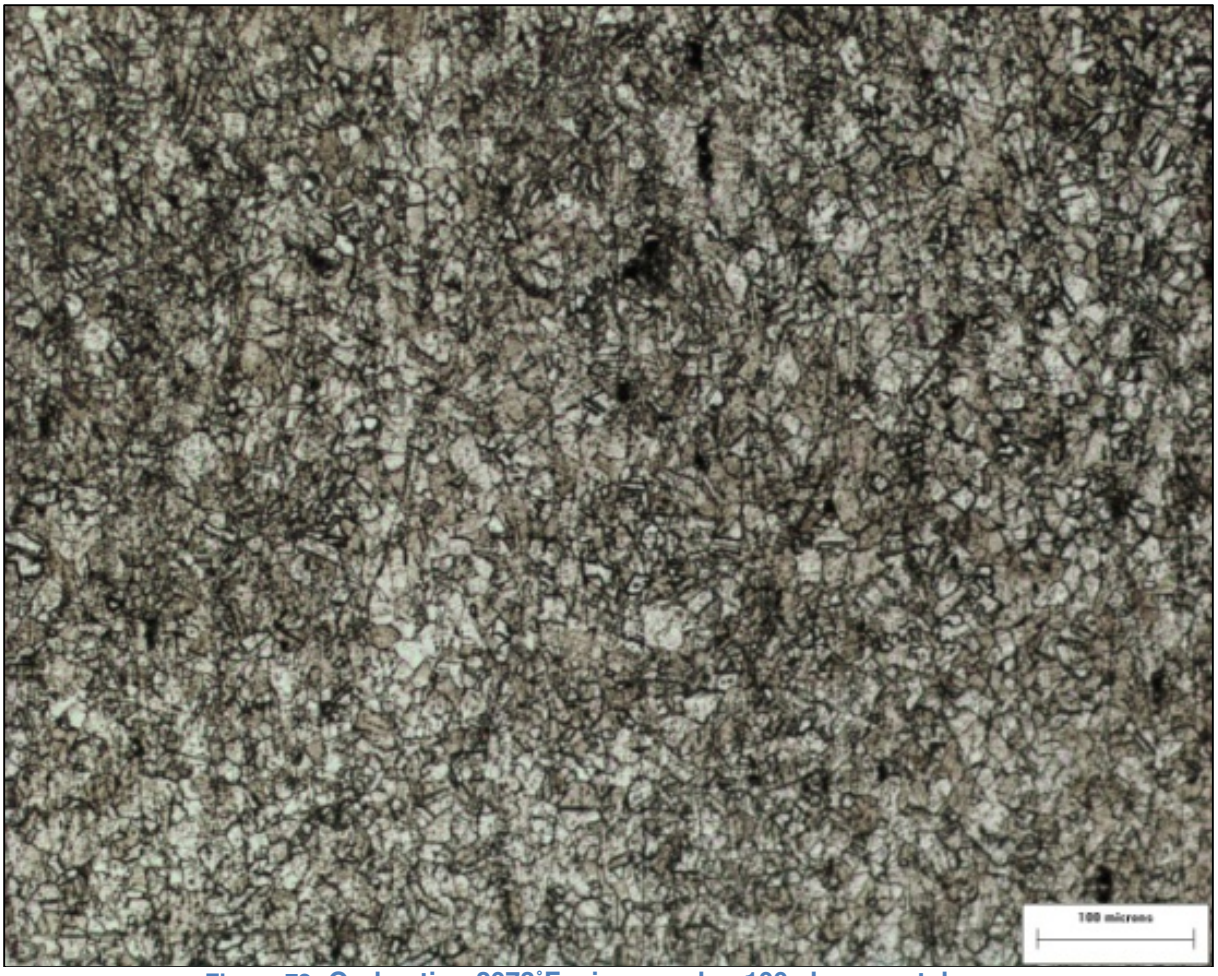

Figure 72: On-heating 2073˚F micrographs. 100x base metal

Micrographs of lower temperature Gleeble® samples showed similar features, as would be expected. No grain growth was visible at lower temperatures.

3.4.2 Haynes 230

The photomicrographs of the Haynes 230 samples showed some features similar to the INCO 718 samples. Figure 73 is a photomicrograph of a longitudinal section of a nil-strength hot-ductility sample. It shows clear evidence that local melting is the cause of failure. There is clear evidence of melting along grain boundaries near the crack tip, appearing in the micrographs as thick dark lines. Some areas near the crack tip showed extensive melting, exceeding the size of heavily liquated grain boundaries. Separations

between grains were visible at the fracture surface, as well. Large areas, parallel to and just beyond the fracture surface, have clearly experienced significant separation along a grain boundary. These large secondary cracks appear as dark regions in the micrographs. Although the static load of 20 lbs used in the nil strength test is low, it is significant enough to induce failure at the fracture surface, and cause wide separation of liquated grain boundaries nearby.

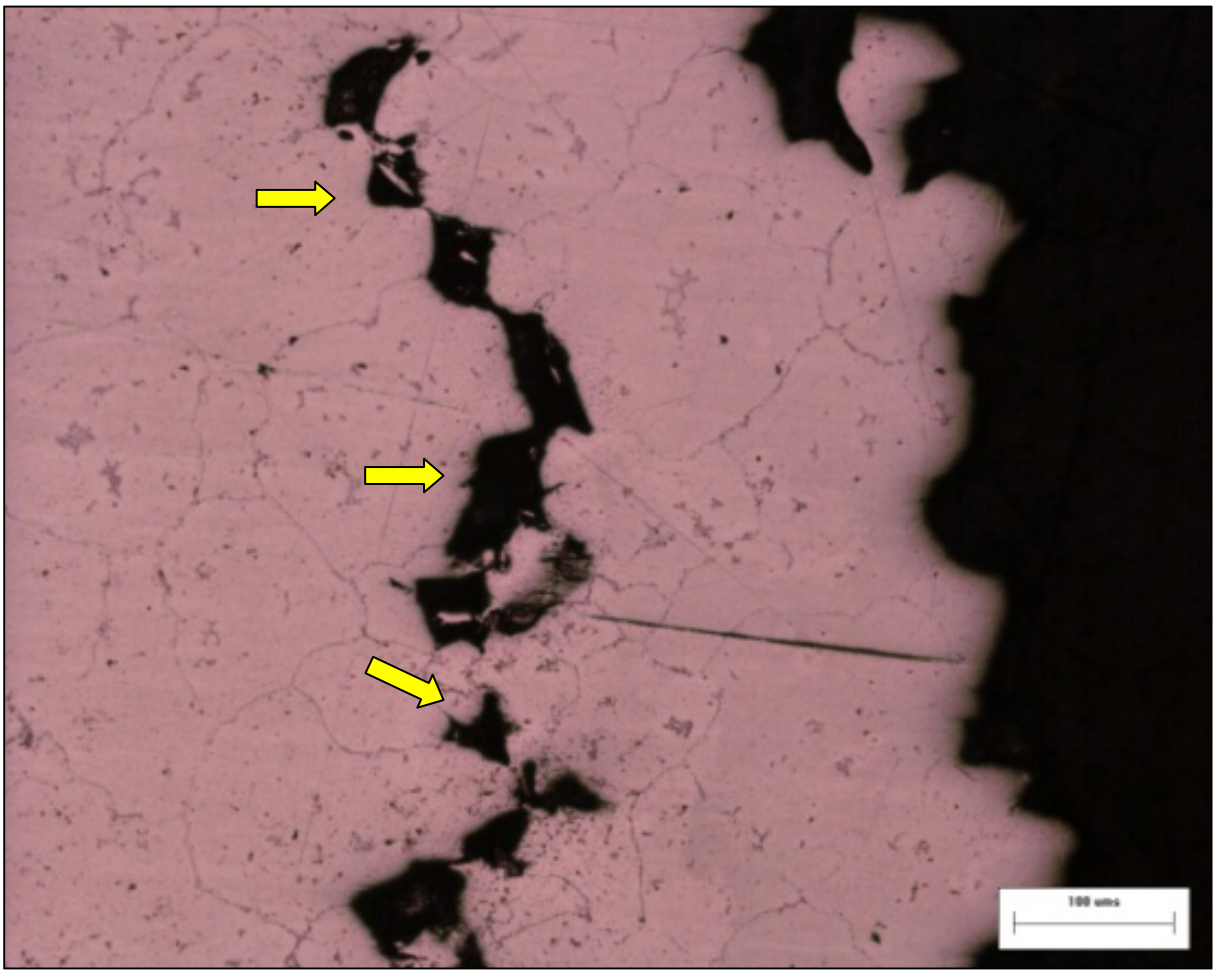

Figure 73: Nil-strength micrograph, 100x. Extensive melting is visible along grain boundaries (arrows).

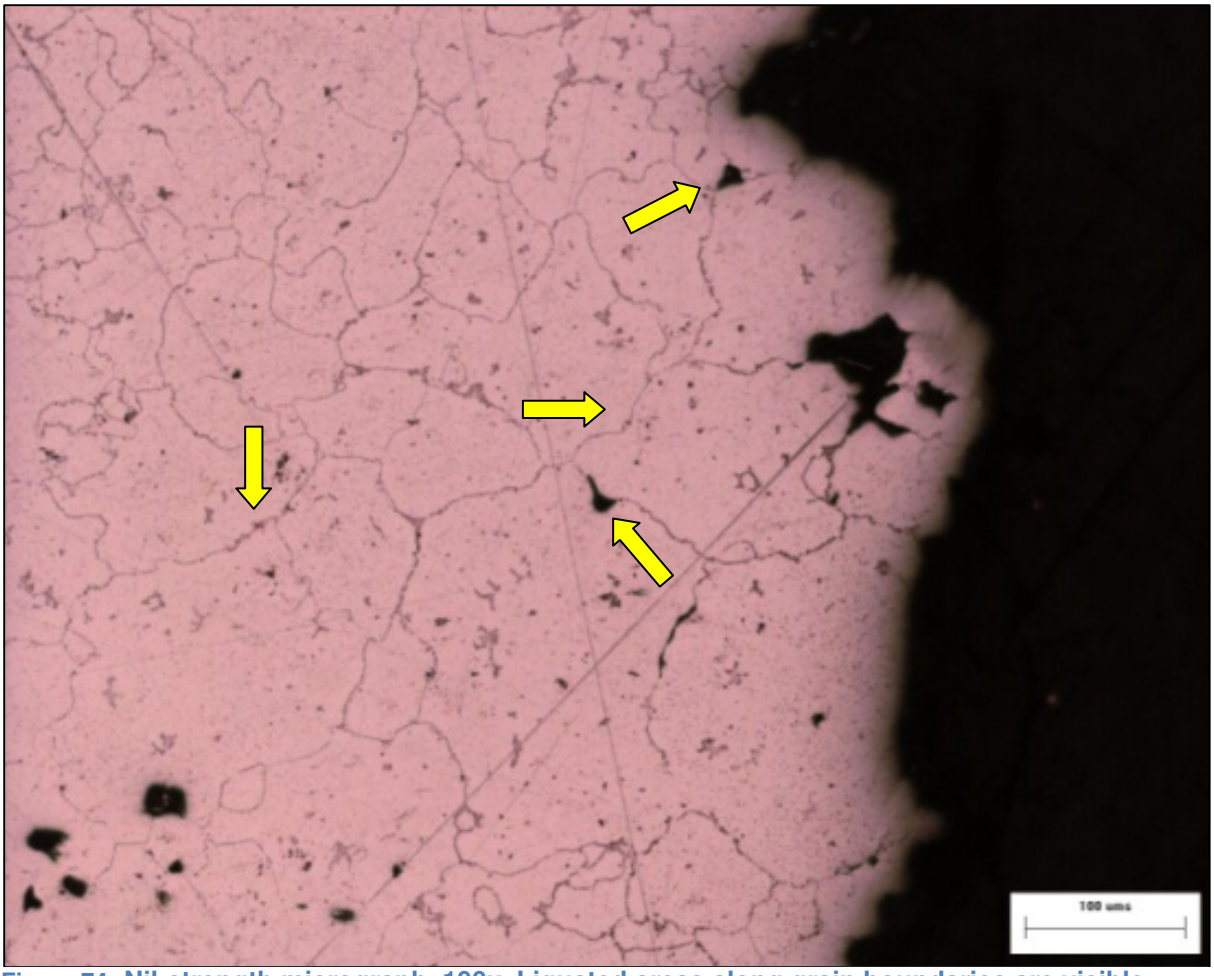

Figure 74: Nil-strength micrograph, 100x. Liquated areas along grain boundaries are visible (arrows).

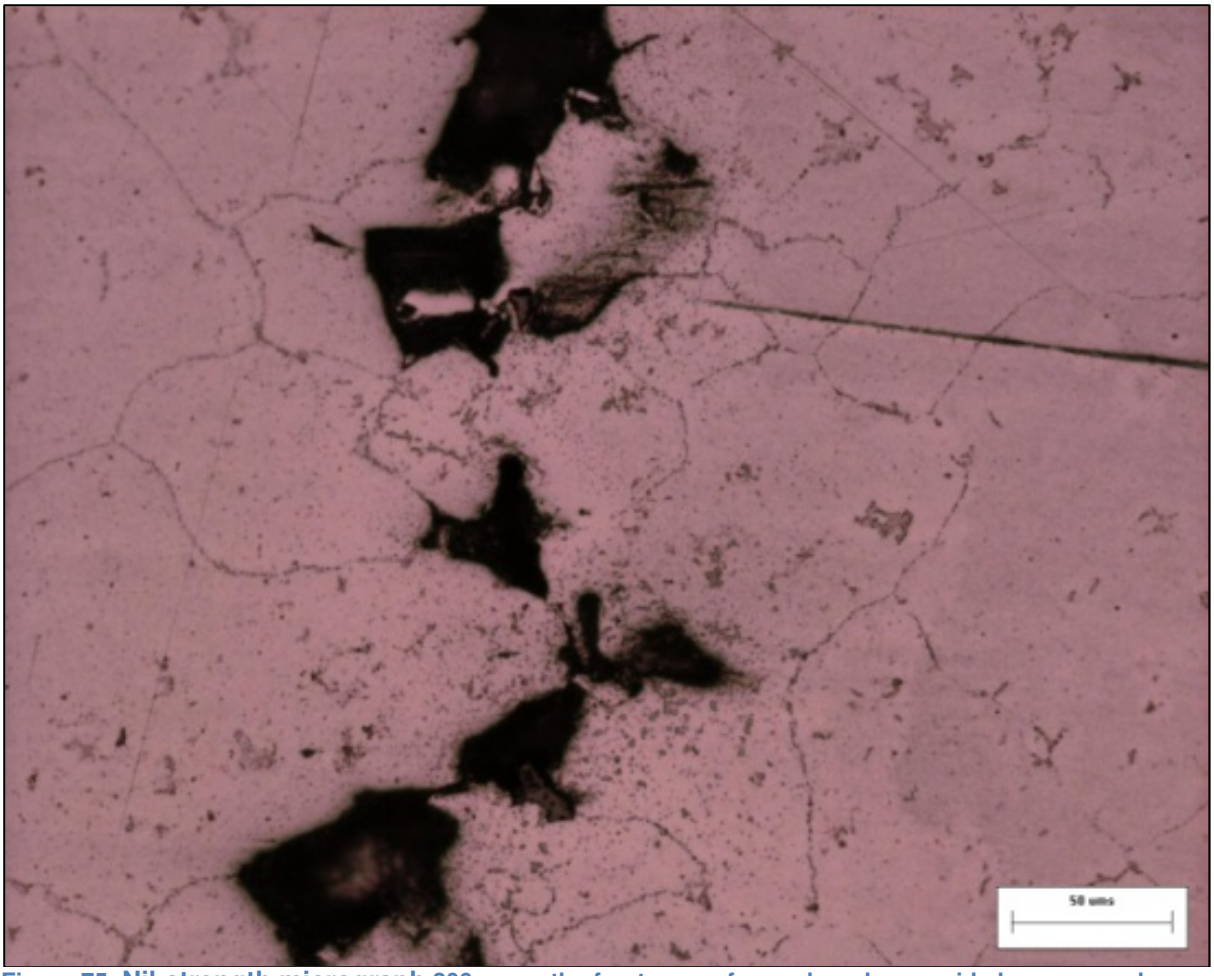

Figure 75: Nil-strength micrograph 200x near the fracture surface, where large voids have opened along liquated grain boundaries

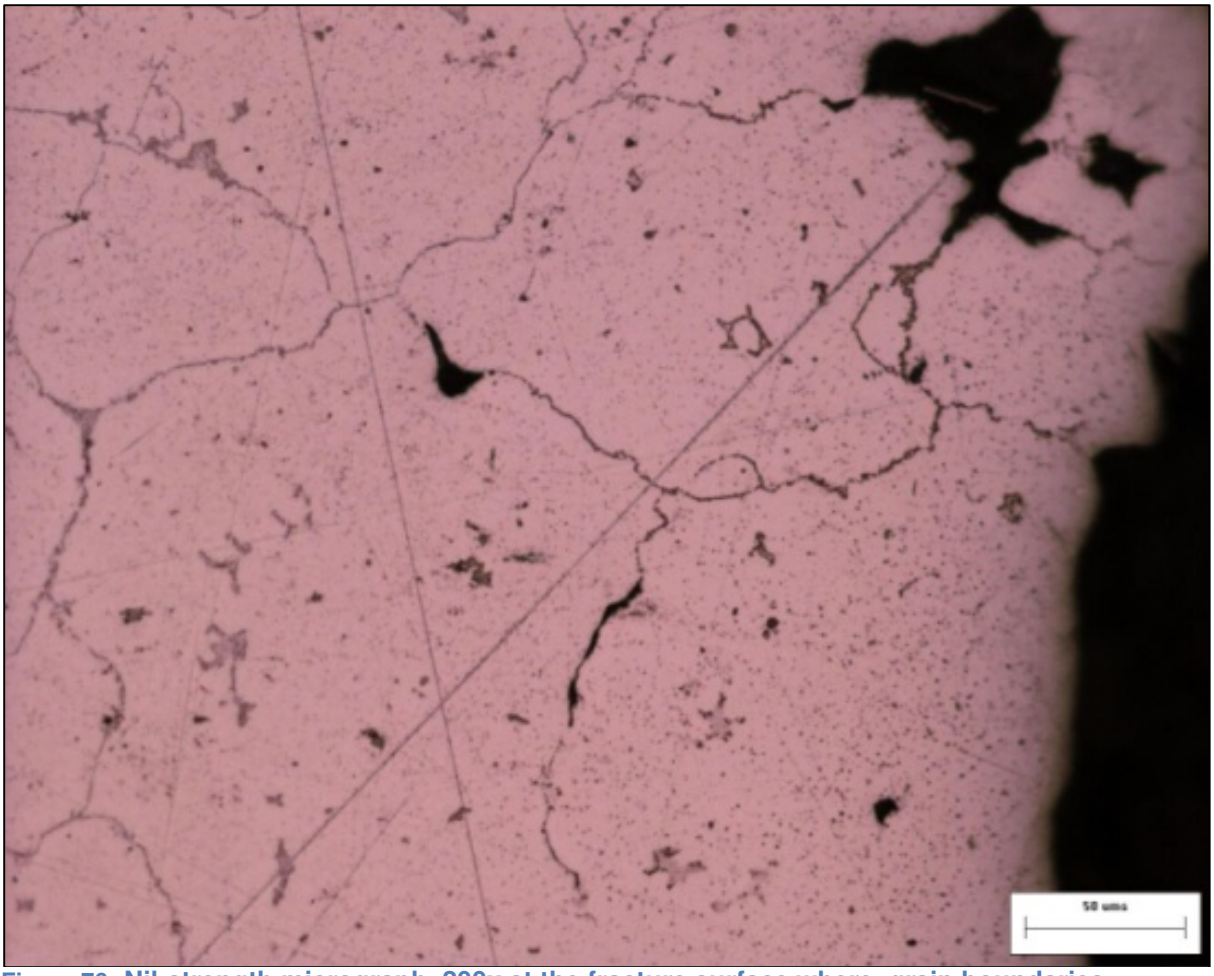

Figure 76: Nil-strength micrograph. 200x at the fracture surface where grain boundaries have liquated, and separated

Microstructures of the on-heating sample, tested at 2341 °F, are shown in Figure 77 Figure 80. These microstructures are similar to those seen in the nil-strength sample. Most notably, grain boundary melting and separation are evident at the fracture surface. Liquated grain boundaries appear dark and distinct. Seperation of grain boundaries is oriented perpendicular to the loading direction. In Figure 77, a single grain can be seen at the fracture surface, having experienced a large degree of liquation along its grain boundaries. Grain size appears to be in the range of 50-100 µm, as was observed in the corresponding SEM fracture surface images produced from this sample. Little deformation is evident at the fracture surface. Aside from the separation of liquated grain

boundaries, very little distortion to the grains can be detected in the micrographs. There are no indications of dynamic recrystallization having occurred during failure.

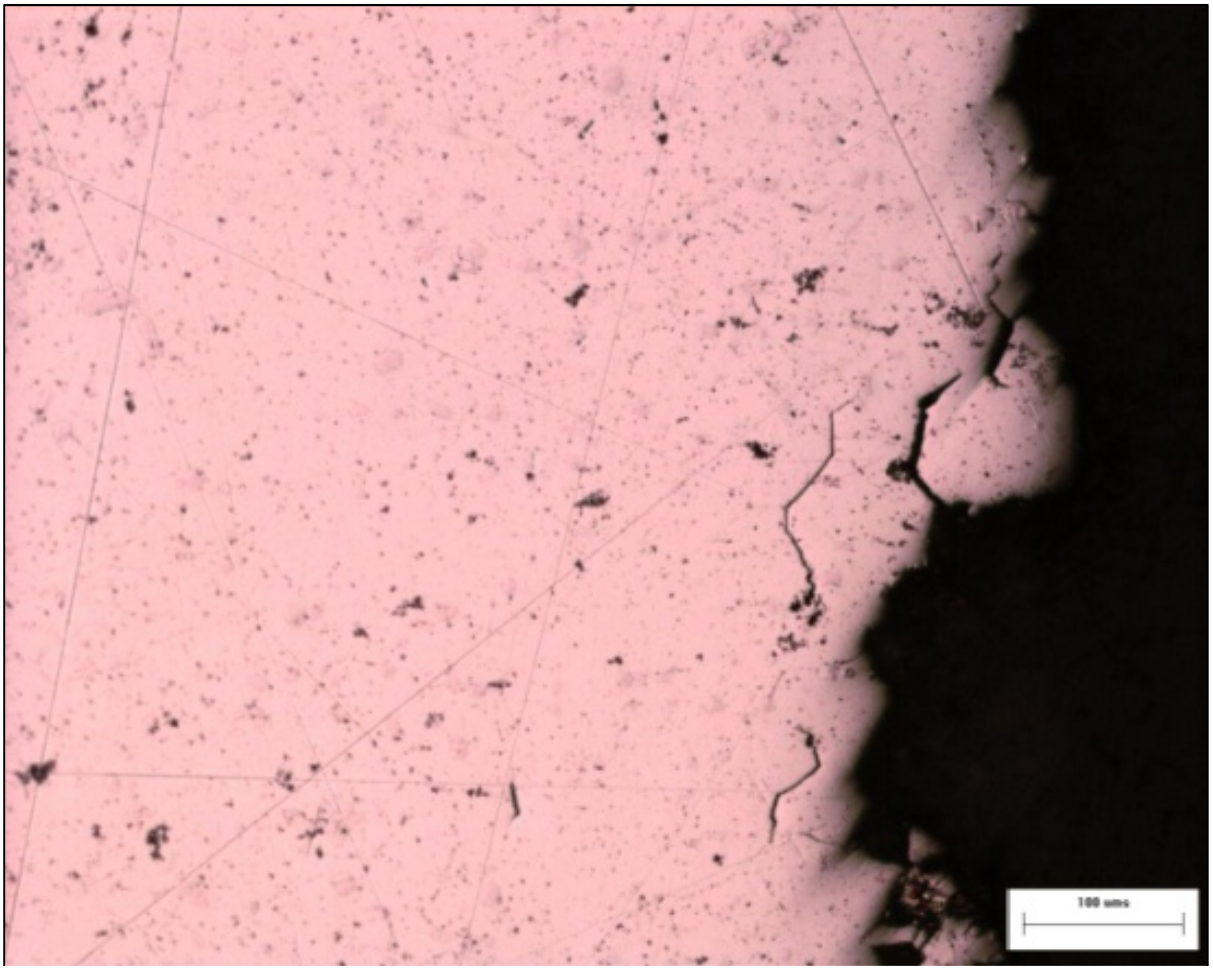

Figure 77: On-heating 2341 micrograph: 100x. Separation along grain boundaries is visible near the fracture surface.

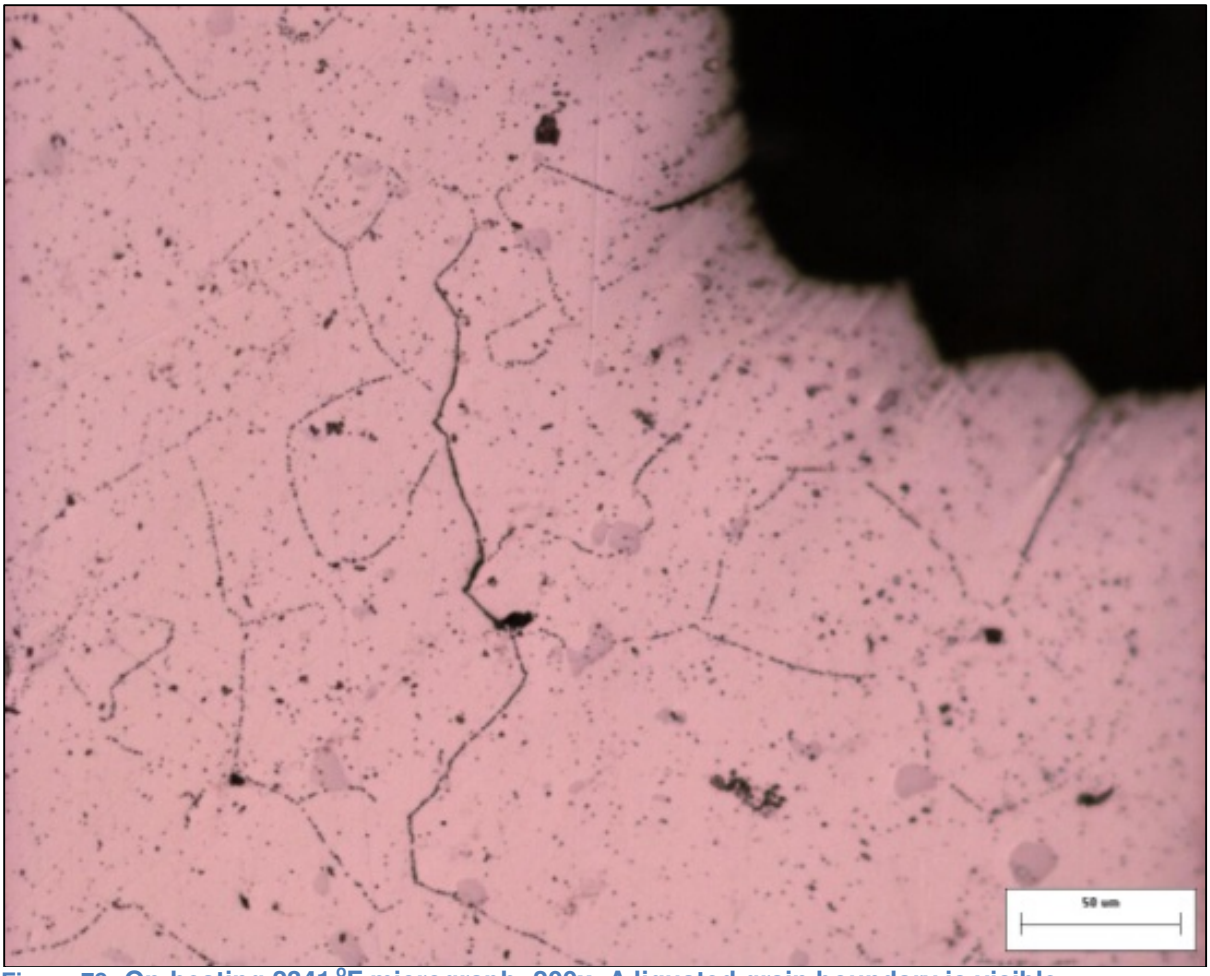

Figure 78: On-heating 2341 °F micrograph: 200x. A liquated grain boundary is visible running vertically in the middle of the image.

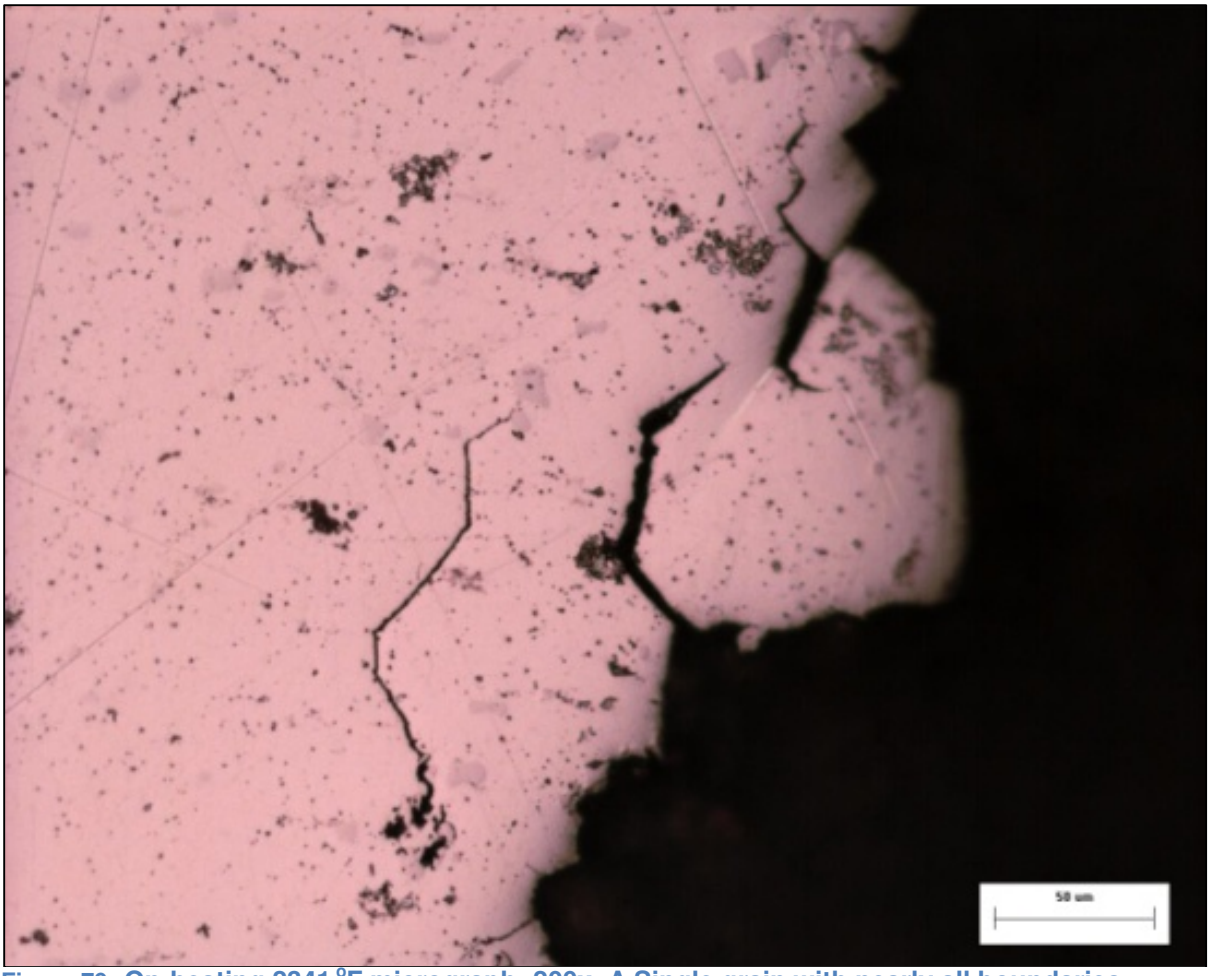

Figure 79: On-heating 2341 °F micrograph: 200x. A Single grain with nearly all boundaries liquated is visible

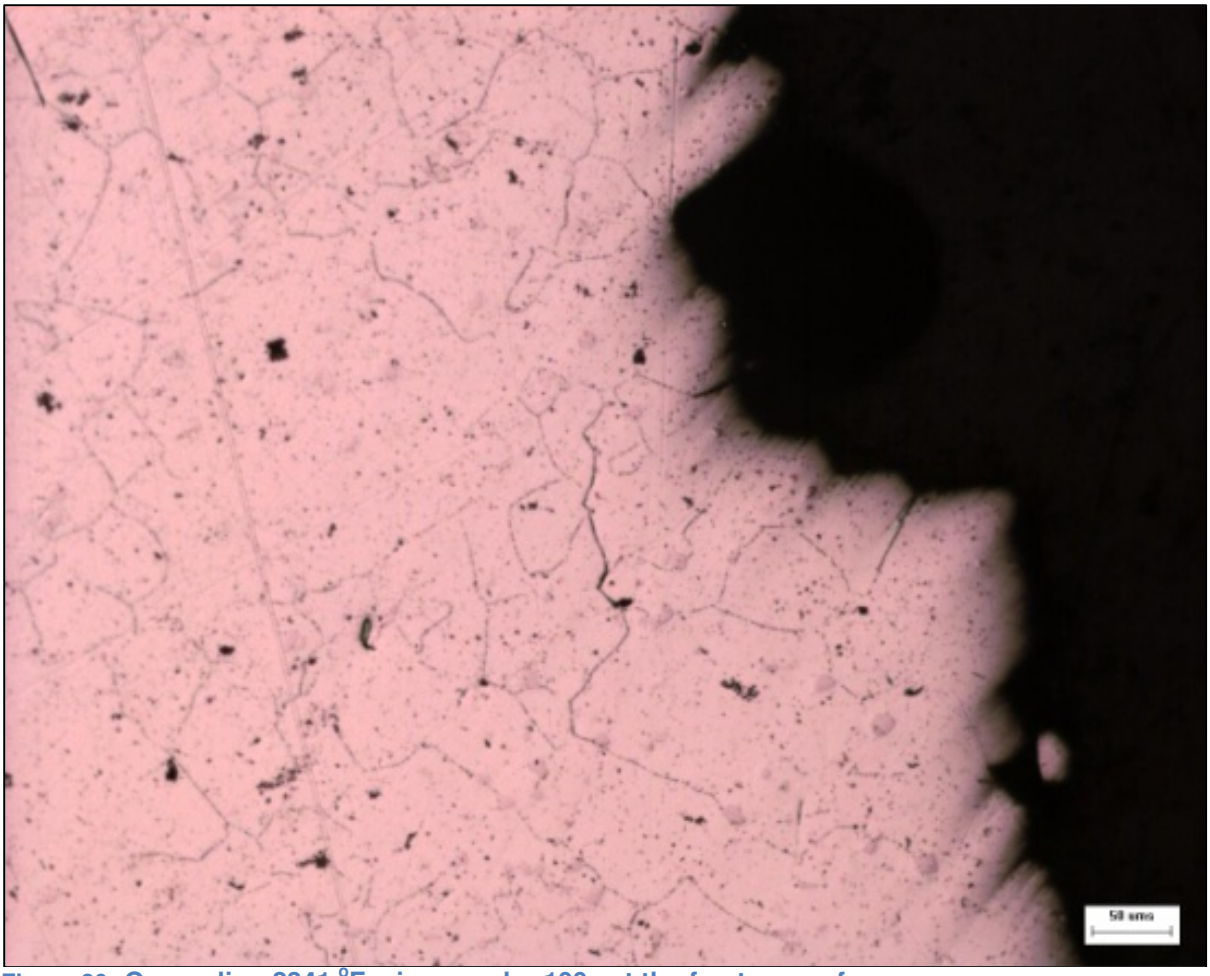

Figure 80: On-cooling 2341 °F micrograph: 100x at the fracture surface.

The on-cooling sample tested at 2202 °F exhibits less grain boundary liquation than the on-cooling sample tested at 2341°F. A number of voids near the fracture surface can be seen where grain boundaries have separated in the direction of loading. These can be seen in Figure 81-Figure 84, appearing as dark regions within the lighter metal sample surface. In Figure 83 andFigure 84 there are indications of dynamic recrystallization occurring near the fracture surface. Dynamic recrystallization has occurred through necklacing, where new grains initially form along existing grain boundaries. The micrographs showing areas where necklacing has occurred are congruent with features seen in the corresponding SEM images. The SEM images revealed a fracture surface exhibiting areas of intergranular cracking between existing grains, and solidified sections of grain boundaries that underwent plastic deformation. The micrographs

shown here are further evidence that dynamic recrystallization was occurring within the plastically deformed regions shown in the SEM images. The micrograph shown in Figure 84, was taken approximately one quarter of an inch back from the fracture surface. At this point in the sample there are no signs of dynamic recrystallization. Grains are distinguishable, and appear in the range of 50-100 µm. These sizes correlate to the grain sizes apparent in the SEM fracture surface images. There are no smaller grains visible in the micrograph.

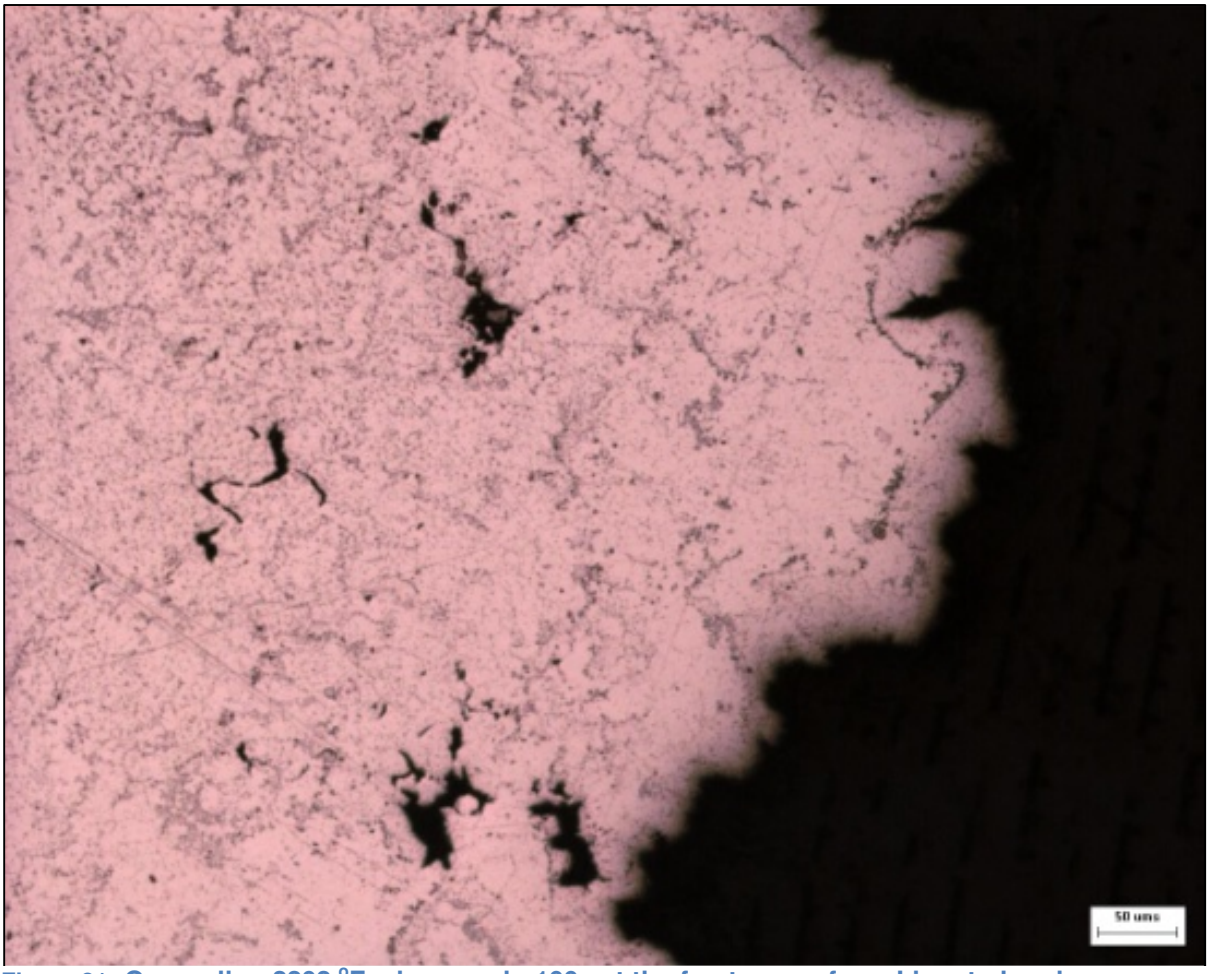

Figure 81: On-cooling 2202 °F micrograph. 100x at the fracture surface. Liquated grain boundaries have seperated in the direction of loading.

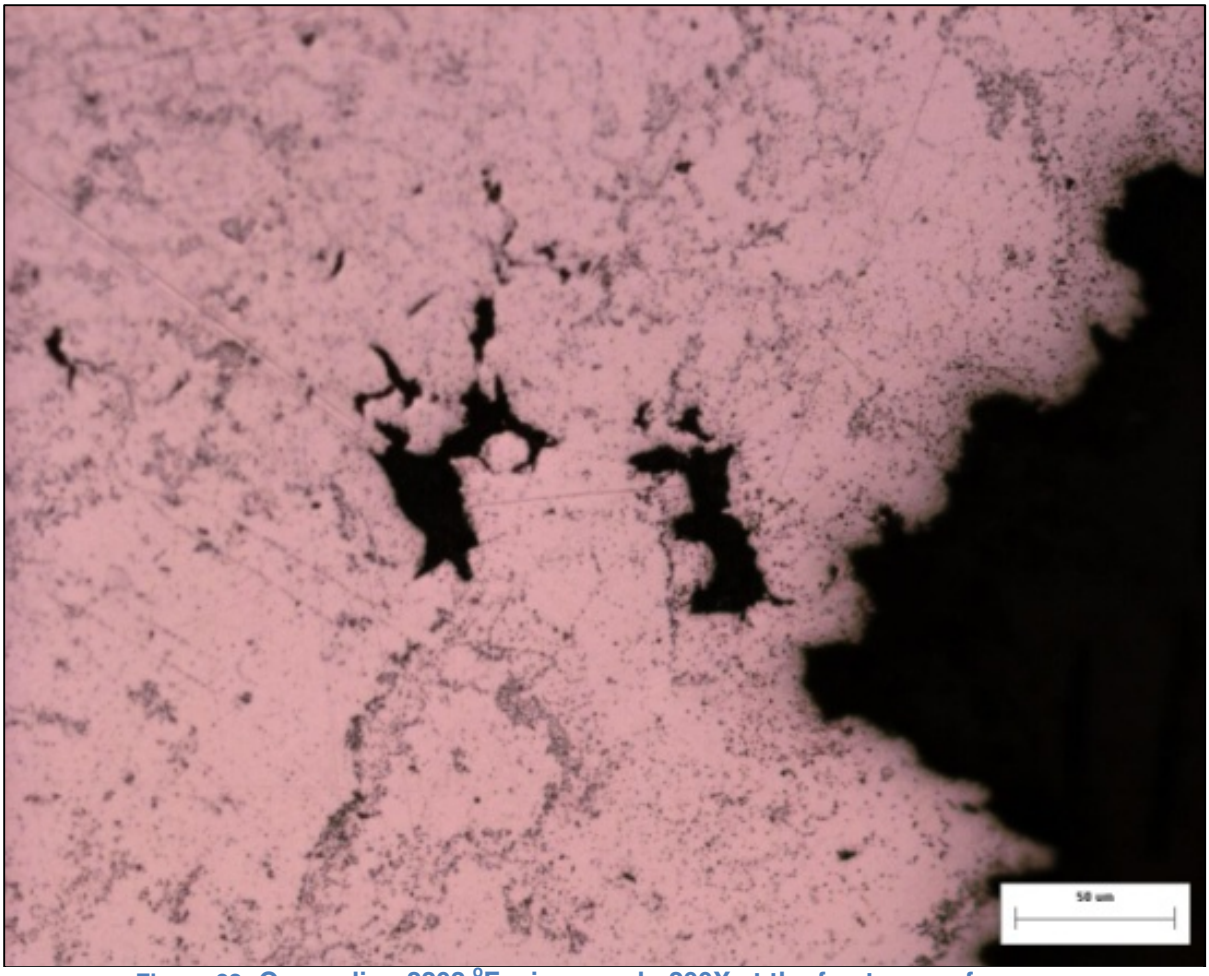

Figure 82: On-cooling 2202 °F micrograph. 200X at the fracture surface

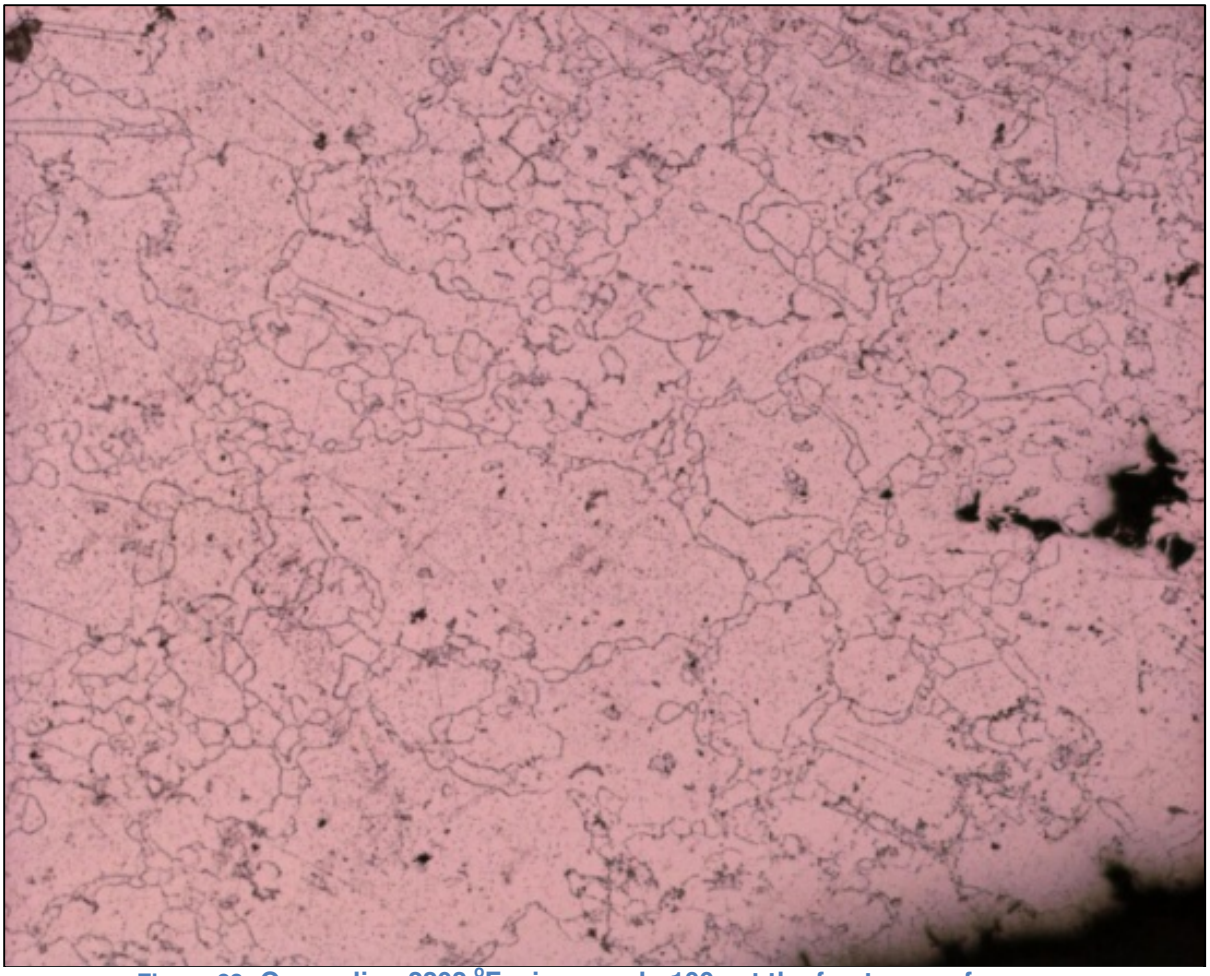

Figure 83: On-cooling 2202 °F micrograph. 100x at the fracture surface

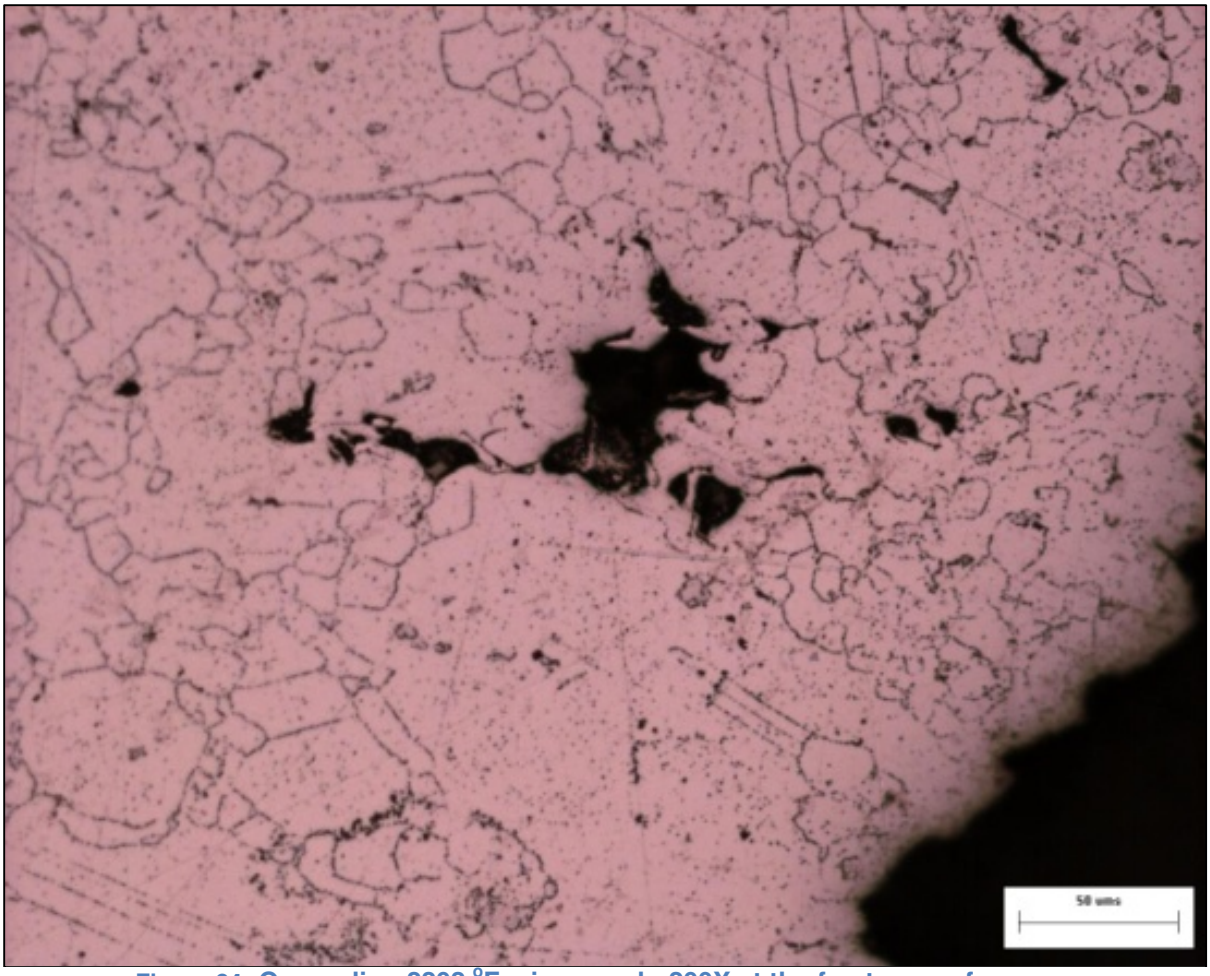

Figure 84: On-cooling 2202 °F micrograph. 200X at the fracture surface

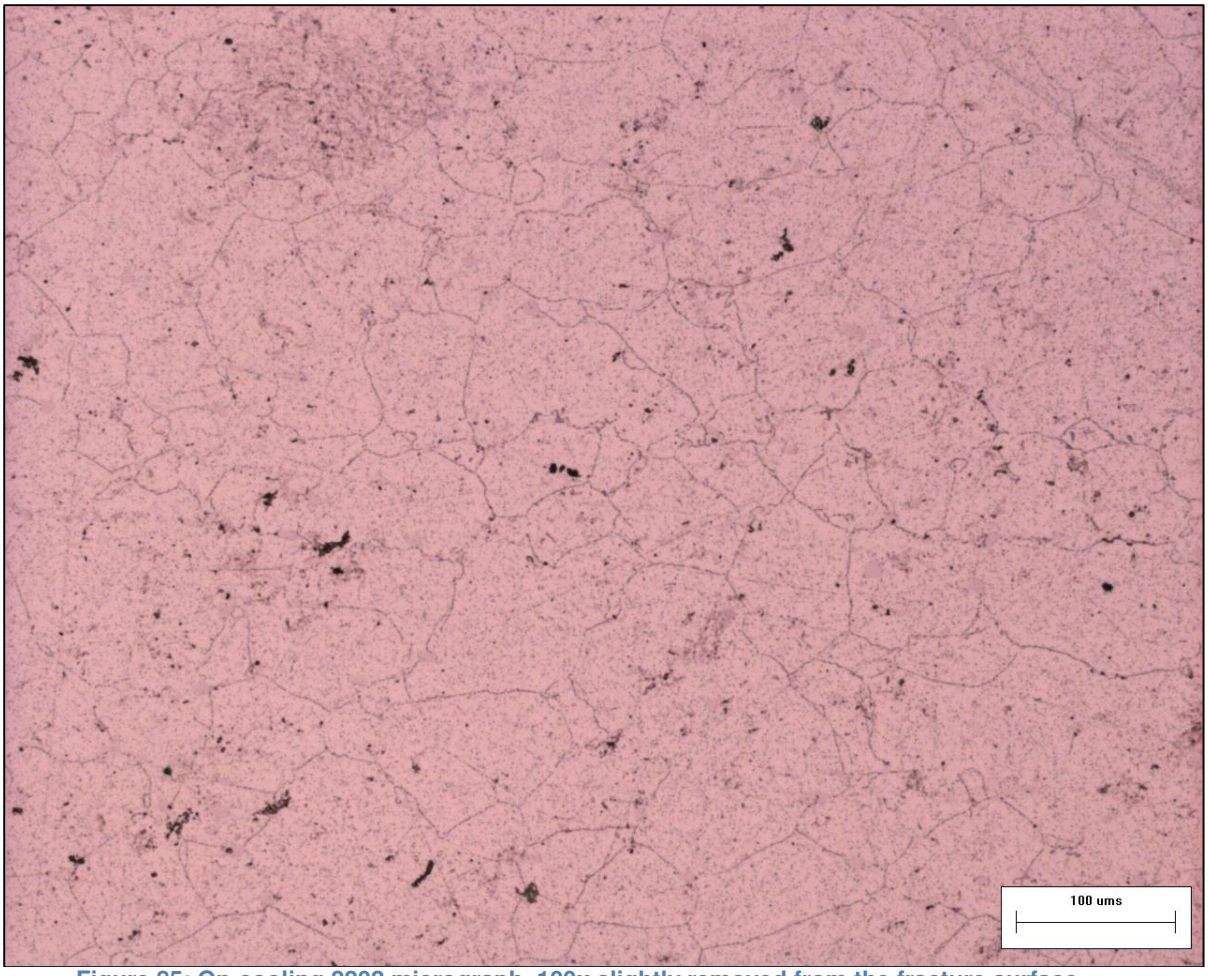

Figure 85: On-cooling 2202 micrograph. 100x slightly removed from the fracture surface

3.5 Varestraint SEM Images

Figure 86-Figure 96 are SEM images of Varestraint samples. SEM images were taken of the cracks produced in fusion zone and partially melted zone (PMZ) of the Varestraint test samples. Figure 86 shows a crack that extends from the PMZ into the rest of the HAZ. As the crack extends from the fusion zone into the PMZ, the crack profile changes in appearance. The portion within the PMZ appaers narrower, and more jagged than the portion within the PMZ. The crack travels along grain boundaries in the HAZ. The portion within the fusion zone is defined more by the shape of solidifying dendrites rather than pre-existing grain boundaries, as this region has fully liquated and

resolidified, producing a solidification substructure. Figure 87 and Figure 88 show the portion of the liquation crack that extends into the PMZ, with the crack edges revealing the shape of the grain boundaries. Solidification cracks within the weldpool follow boundarines in the substructure, along dendrites that form during solidification. They are observable at the surface of the weld pool, and along all boundaries within the crack.

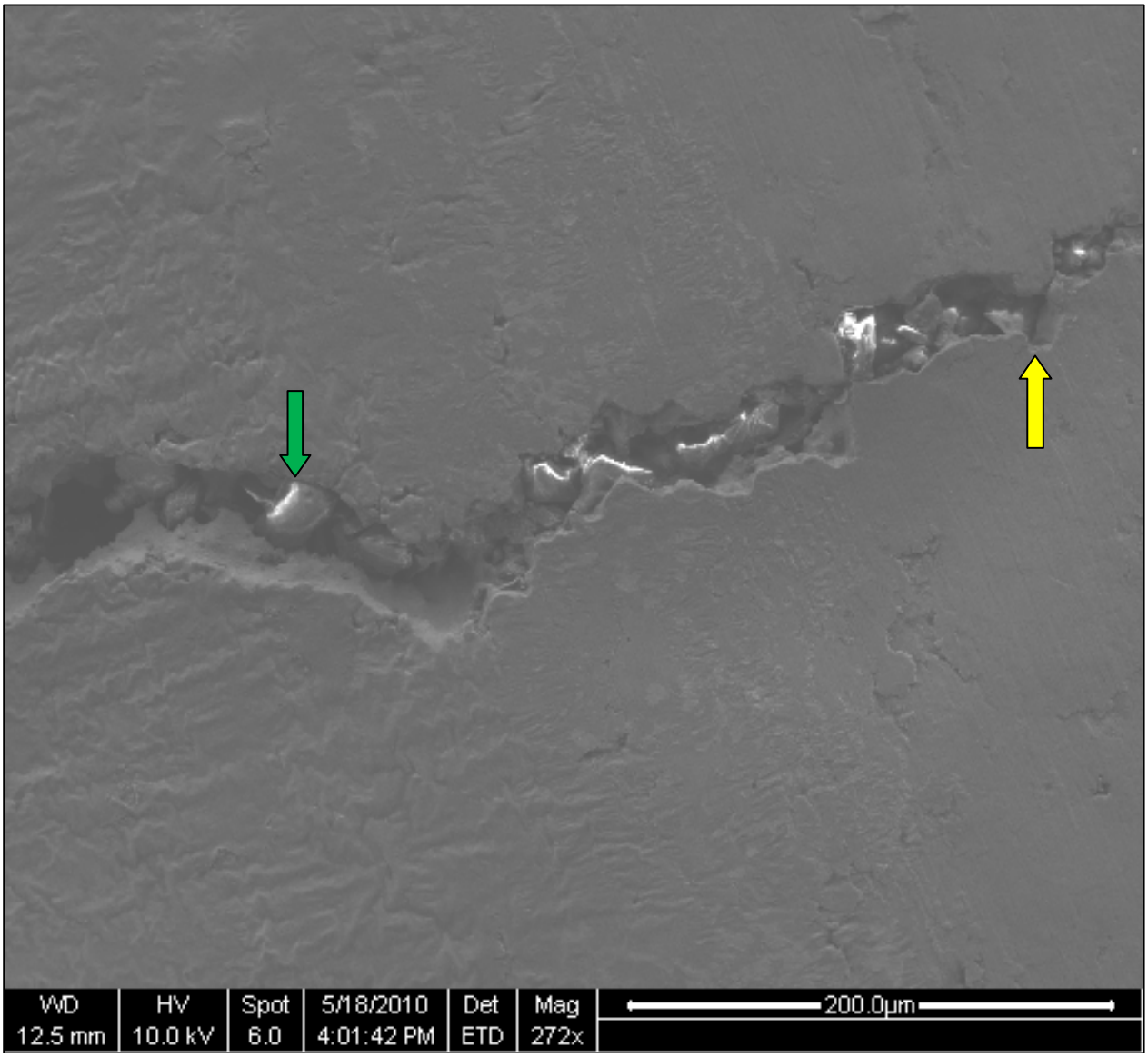

Figure 86: A crack extending from the fusion zone (green arrow) into the PMZ (yellow arrow), on an INCO 718 sample.

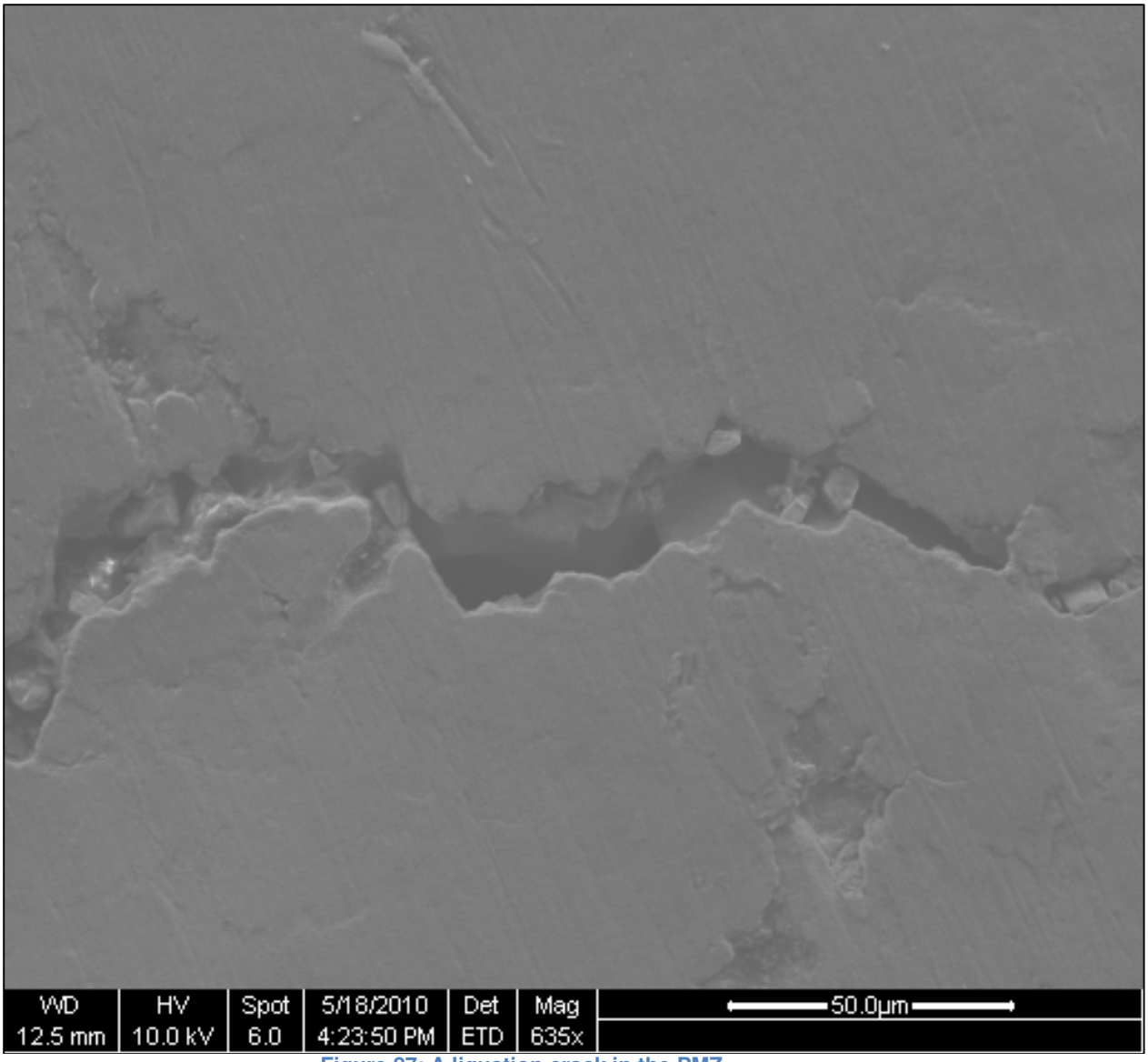

Figure 87: A liquation crack in the PMZ.

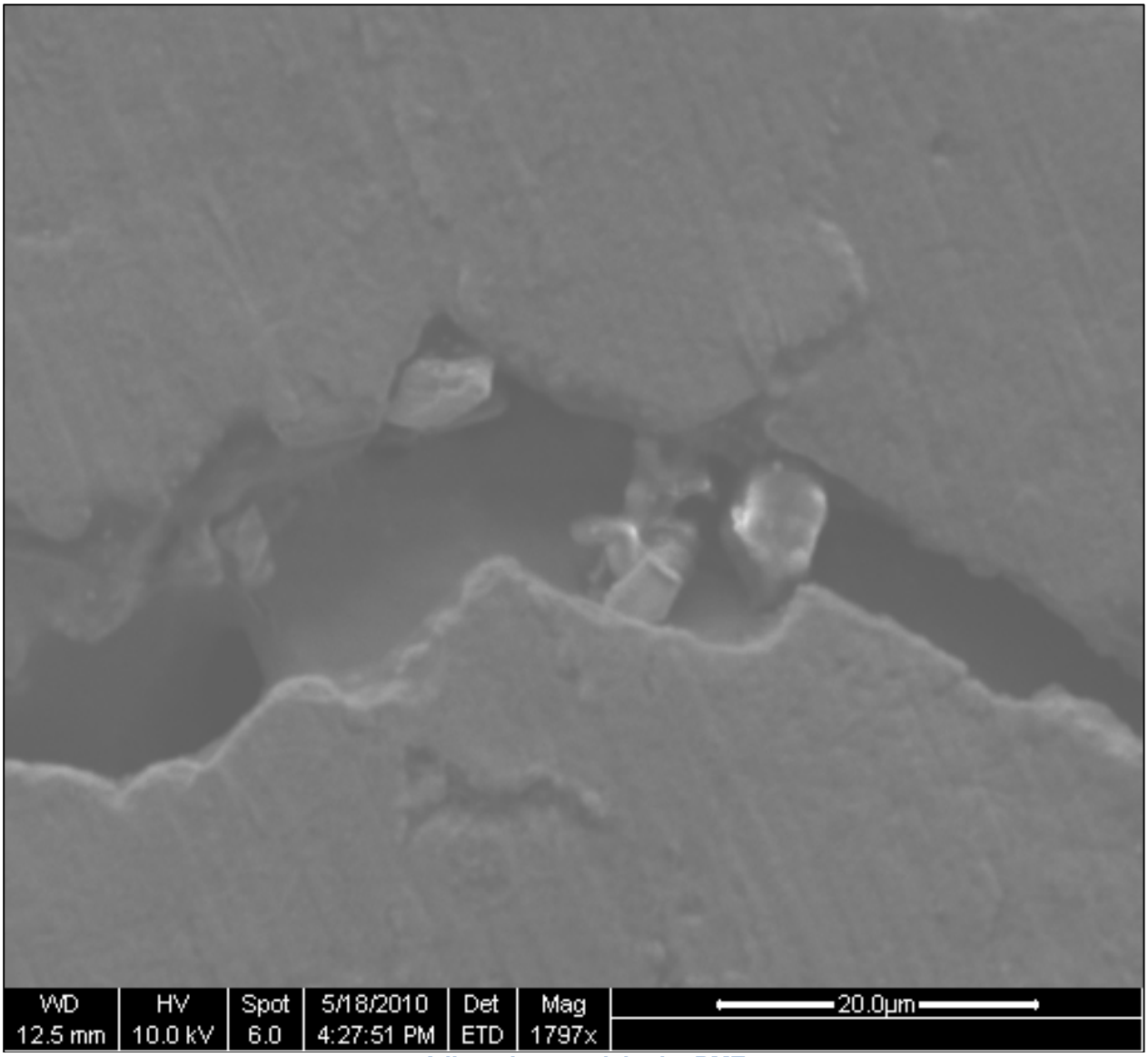

Figure 881: A liquation crack in the PMZ.

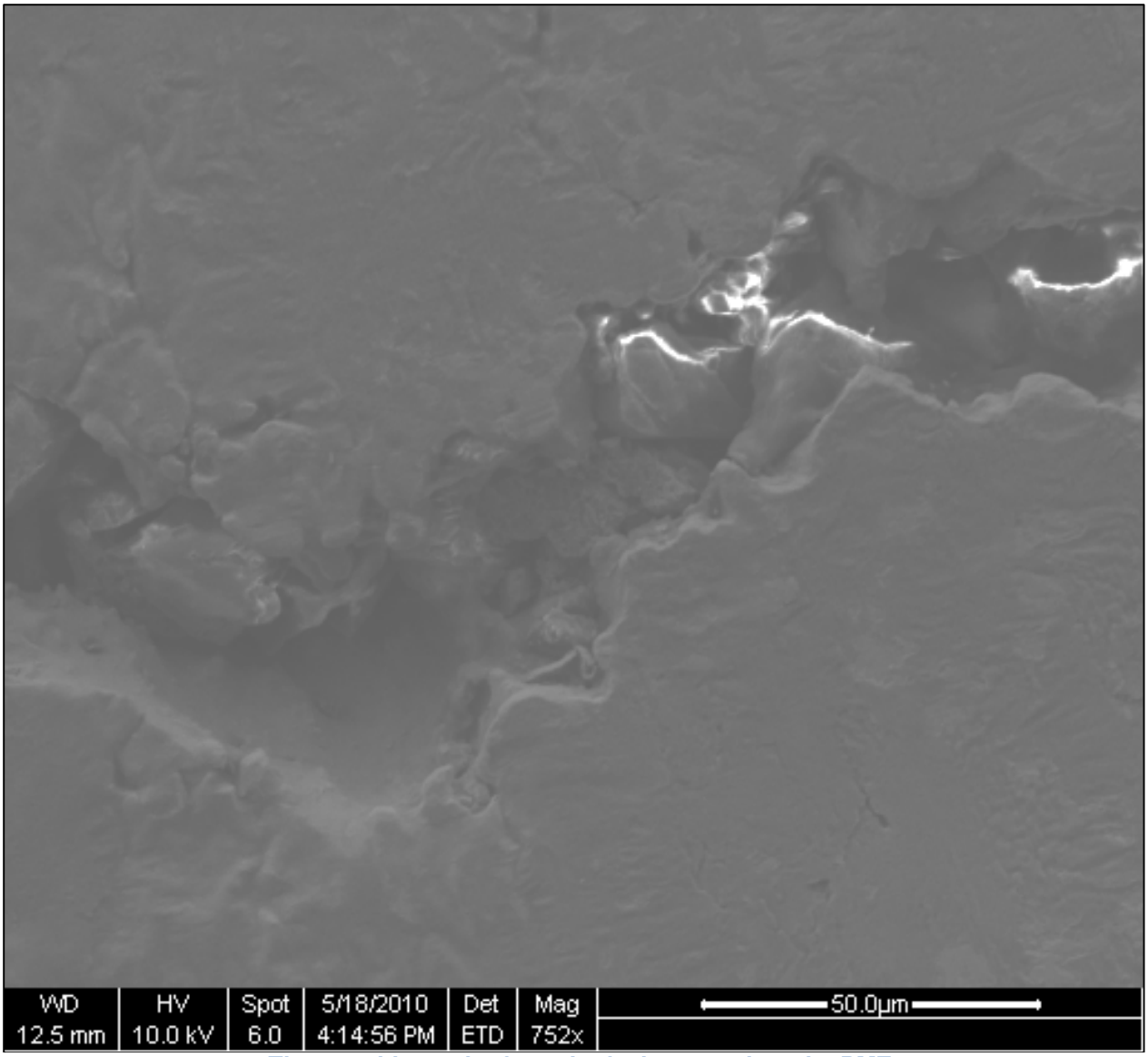

Figure 89: The transition point from the fusion zone into the PMZ

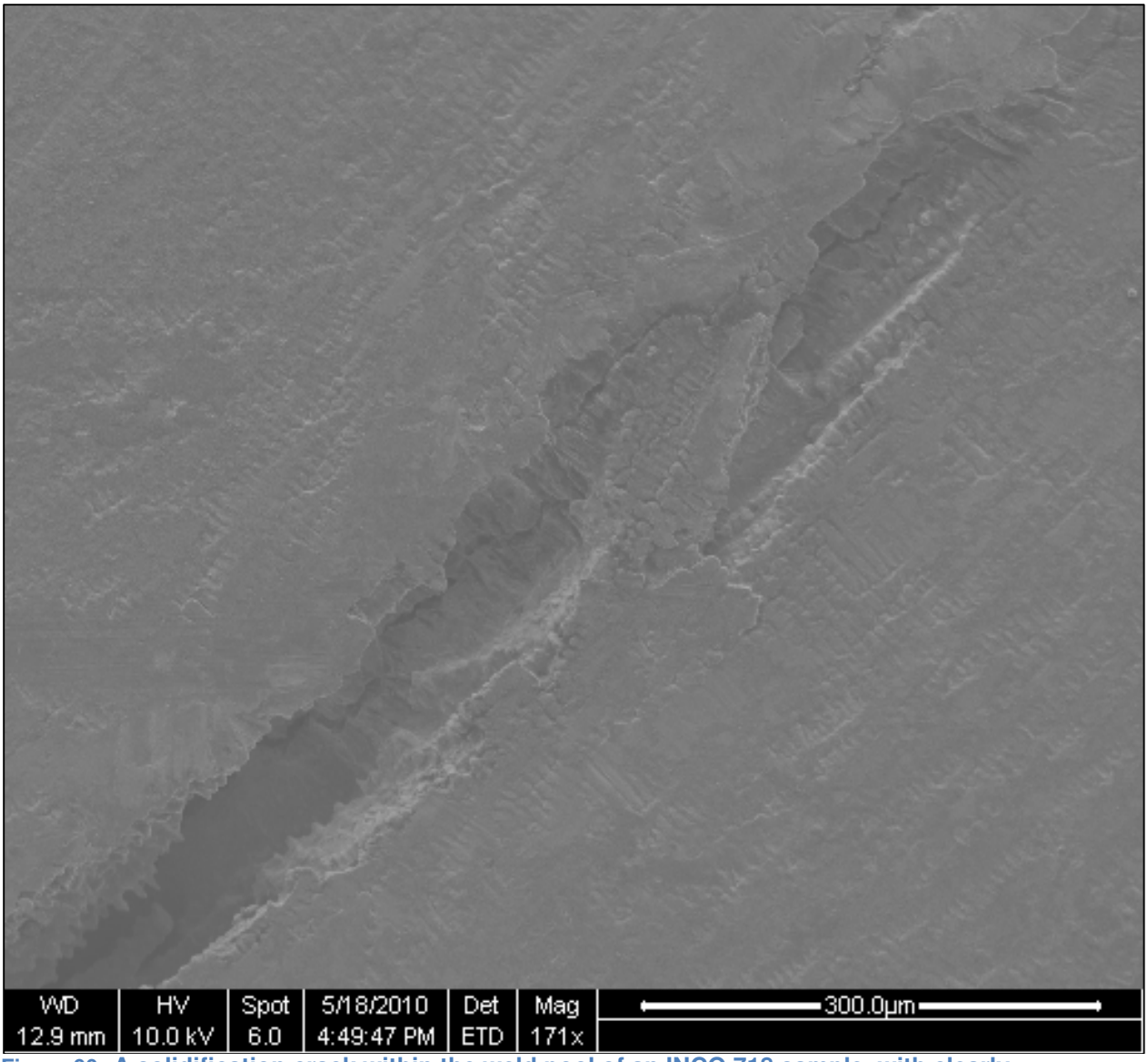

Figure 90: A solidification crack within the weld pool of an INCO 718 sample, with clearly visible dendrite formations.

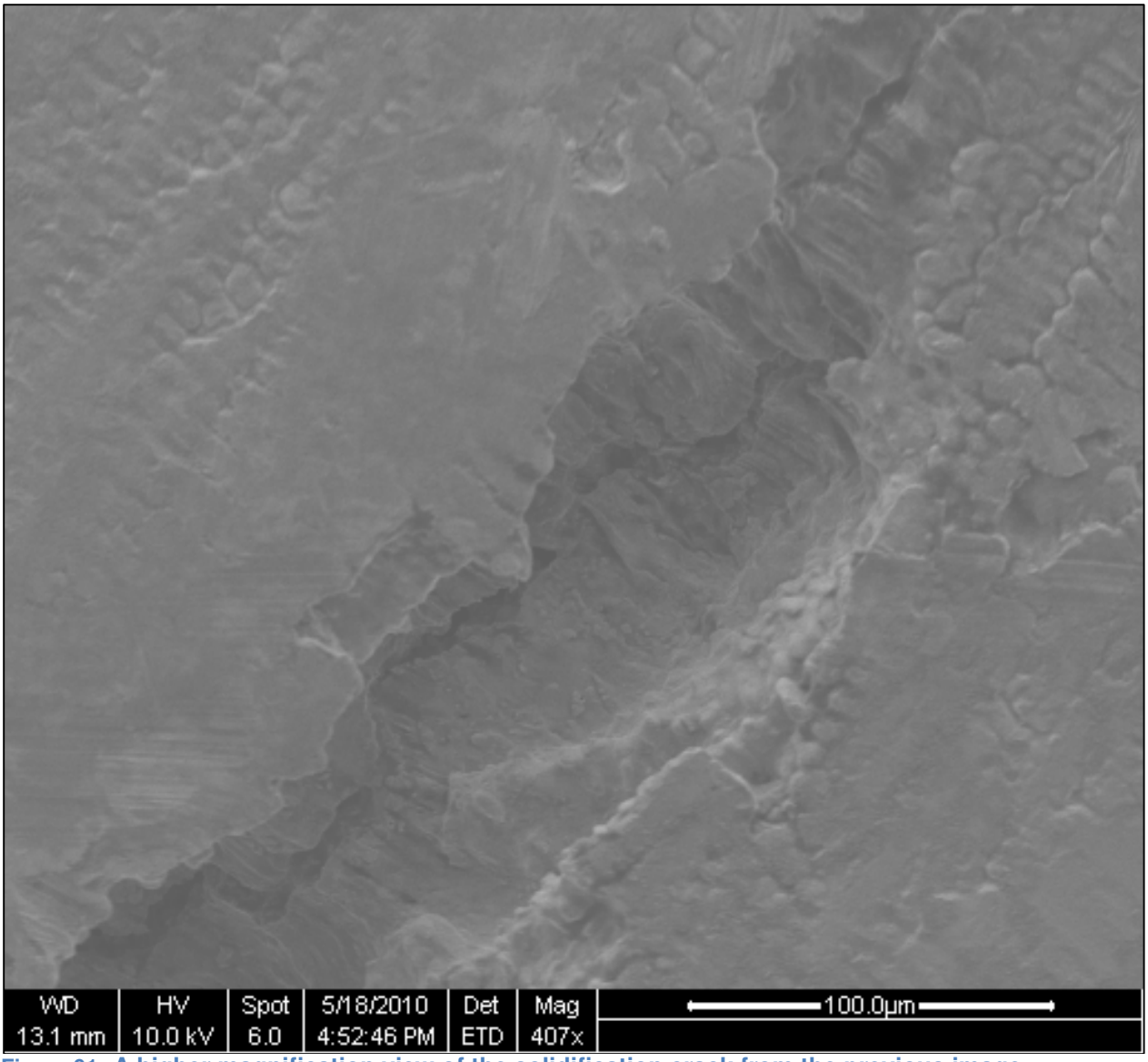

Figure 91: A higher magnification view of the solidification crack from the previous image. Cracking is occurring between dendrites, in the direction of growth.

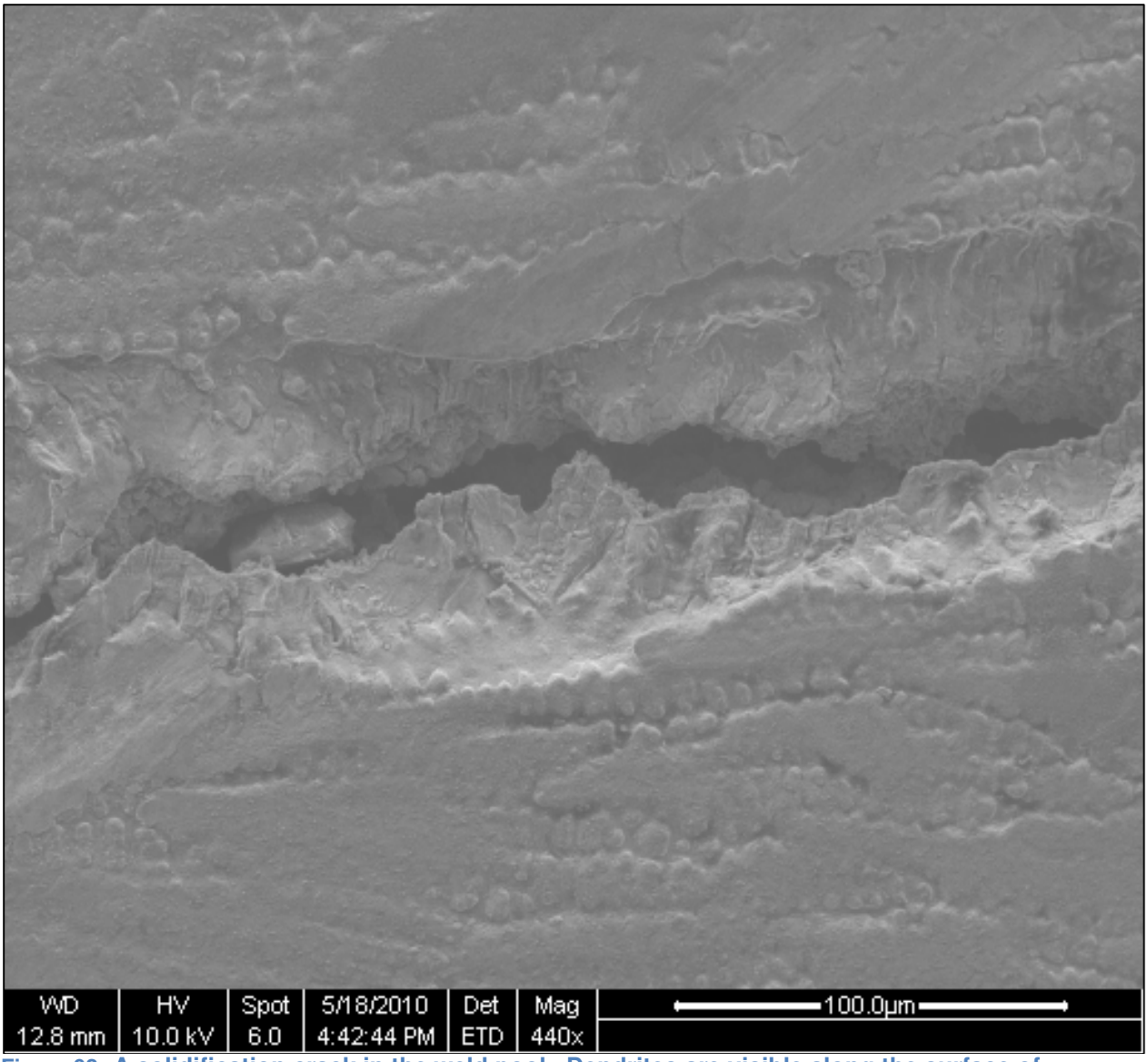

Figure 92: A solidification crack in the weld pool. Dendrites are visible along the surface of the weld pool, as well as within the crack.

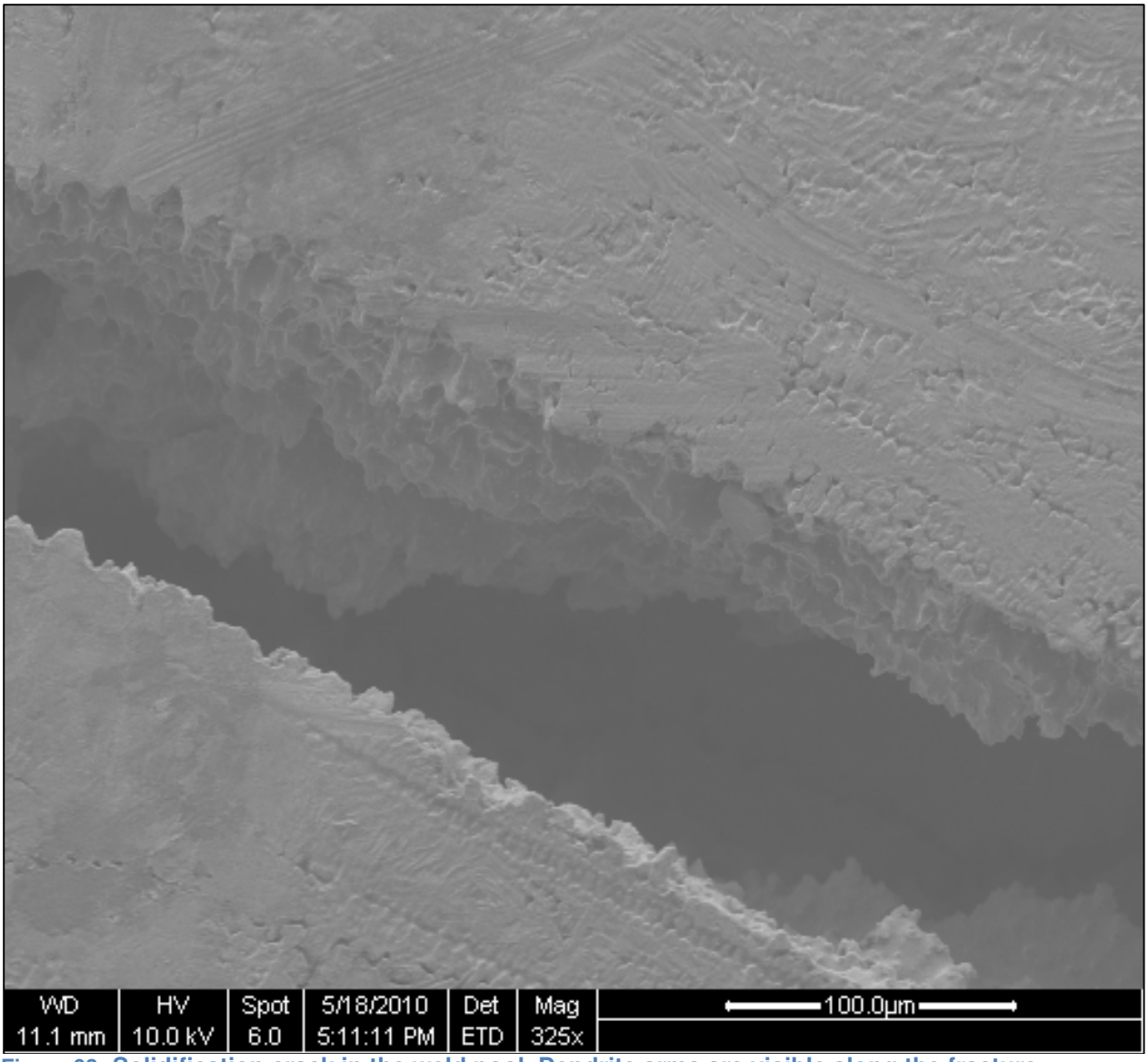

Figure 93: Solidification crack in the weld pool. Dendrite arms are visible along the fracture surface as well as the surface of the weld pool.

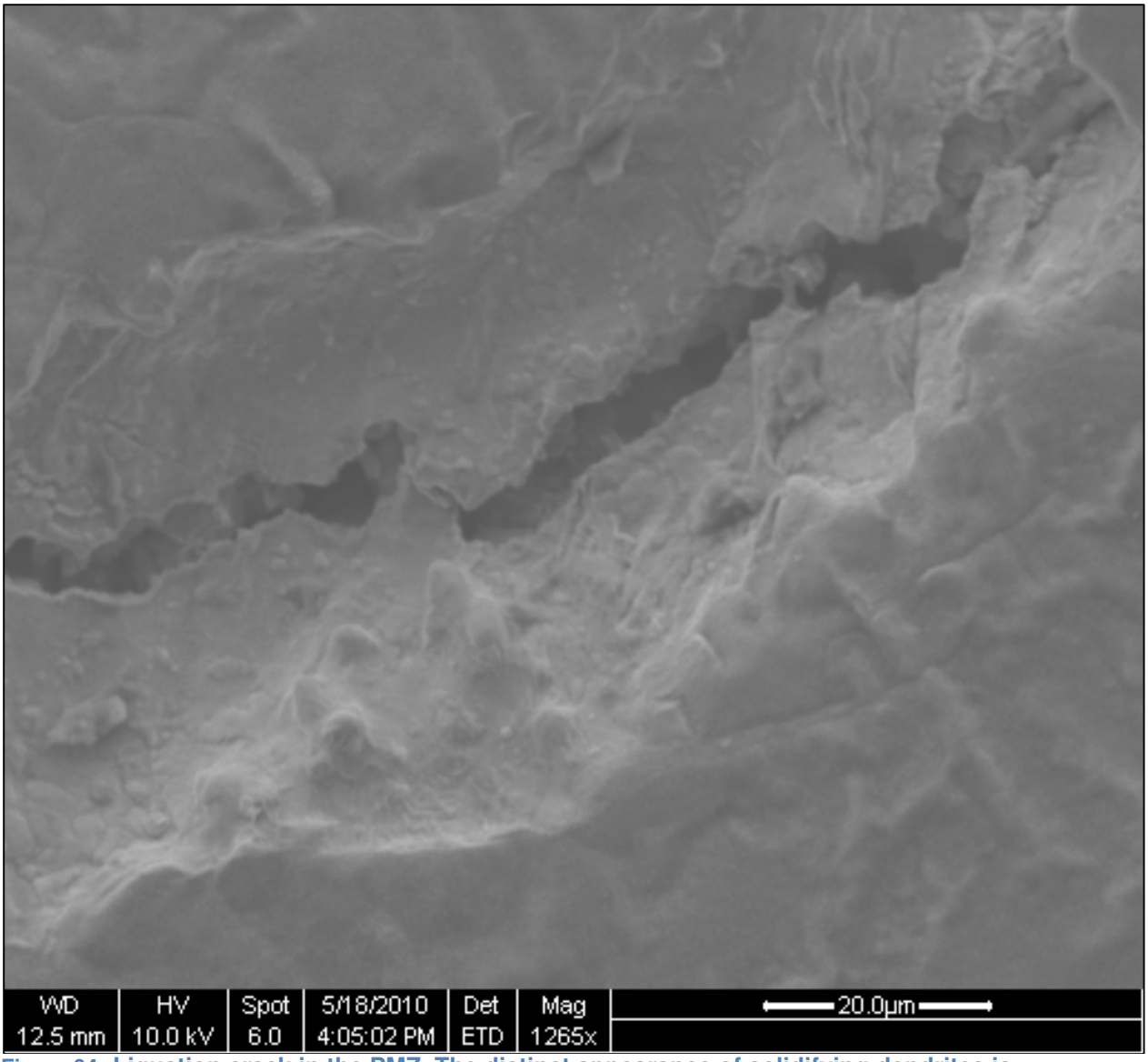

Figure 94: Liquation crack in the PMZ. The distinct appearance of solidifying dendrites is no longer as prevalent.

Figure 90-Figure 93 show cracking in the weld region of the imaged sample. Cracks follow inderdendritic paths, in accordance with all established solidification theories. As discussed previously, solute rich regions of persistent liquid become trapped between dendrites as solidification progresses. In the presence of tensile forces, fracture initiates in these regions, propagating between already formed dendrite arms. Figure 92Figure 93 show dendrites visible at the surface of the weld pool, having grown inward

from the fusion boundary towards the weld pool centerline during cooling. Cracks initiate in the direction of dendrite growth, at dendrites aligned with preferred growth directions at angles near perpendicular to the applied strain. These dendrites form through epitaxial growth of the existing grains in the PMZ. The competitive growth of dendrites in the weld pool leaves solute-rich regions of liquid between solidifying dendrites. Crack initiation begins in these locations, and propagates along the solidified dendrites. Cracks that extend into the PMZ and HAZ look notably different, with a more jagged shape, and textured fracture surface. Here, cracks follow the path of least resistance, propagating along liquated grain boundaries within the PMZ. Because grain boundaries are not subject to competitive growth like the dendrites in the weld region, they are not oriented in a continuous line, or arc, over distances greater than a single grain. Thus, a jagged crack path develops that follows connected liquated grain boundaries.

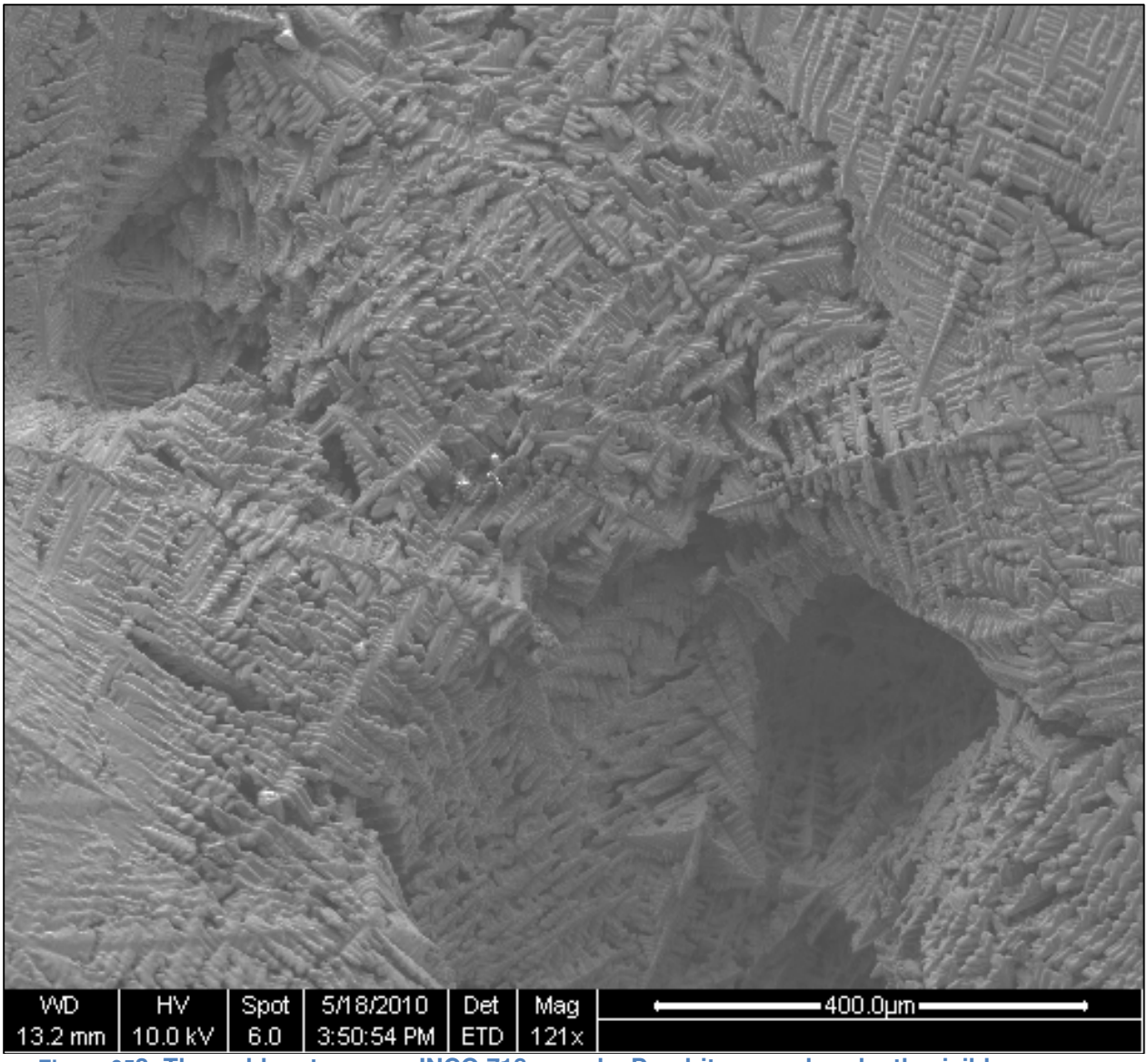

Figure 952: The weld crater on an INCO 718 sample. Dendrites are abundantly visible.

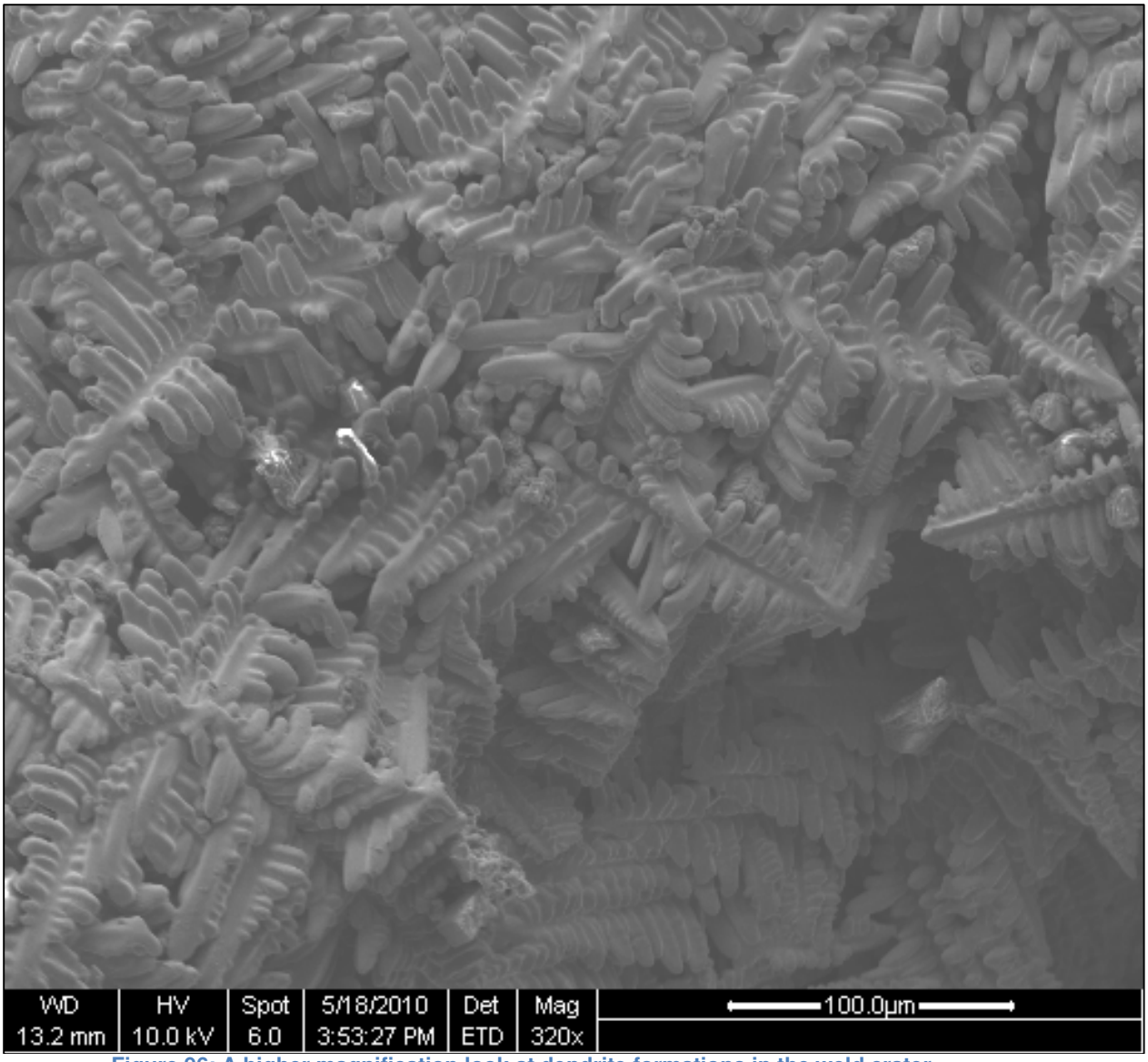

Figure 96: A higher magnification look at dendrite formations in the weld crater.

Figure 95 and Figure 96 further confirm the established weld pool solidification theories. Dendrites converge in the terminal weld crater, where solidification takes place last. The region also shows shrinkage and well defined secondary and tertiary dendrite arms. The substructure here shows less preferred orientation, as the magnitude of the thermal gradient during solidification becomes smaller and it also becomes less directionally defined.

4.0 Discussion

4.1 Gleeble® Results

The criteria established through the hot ductility testing are compared and summarized in

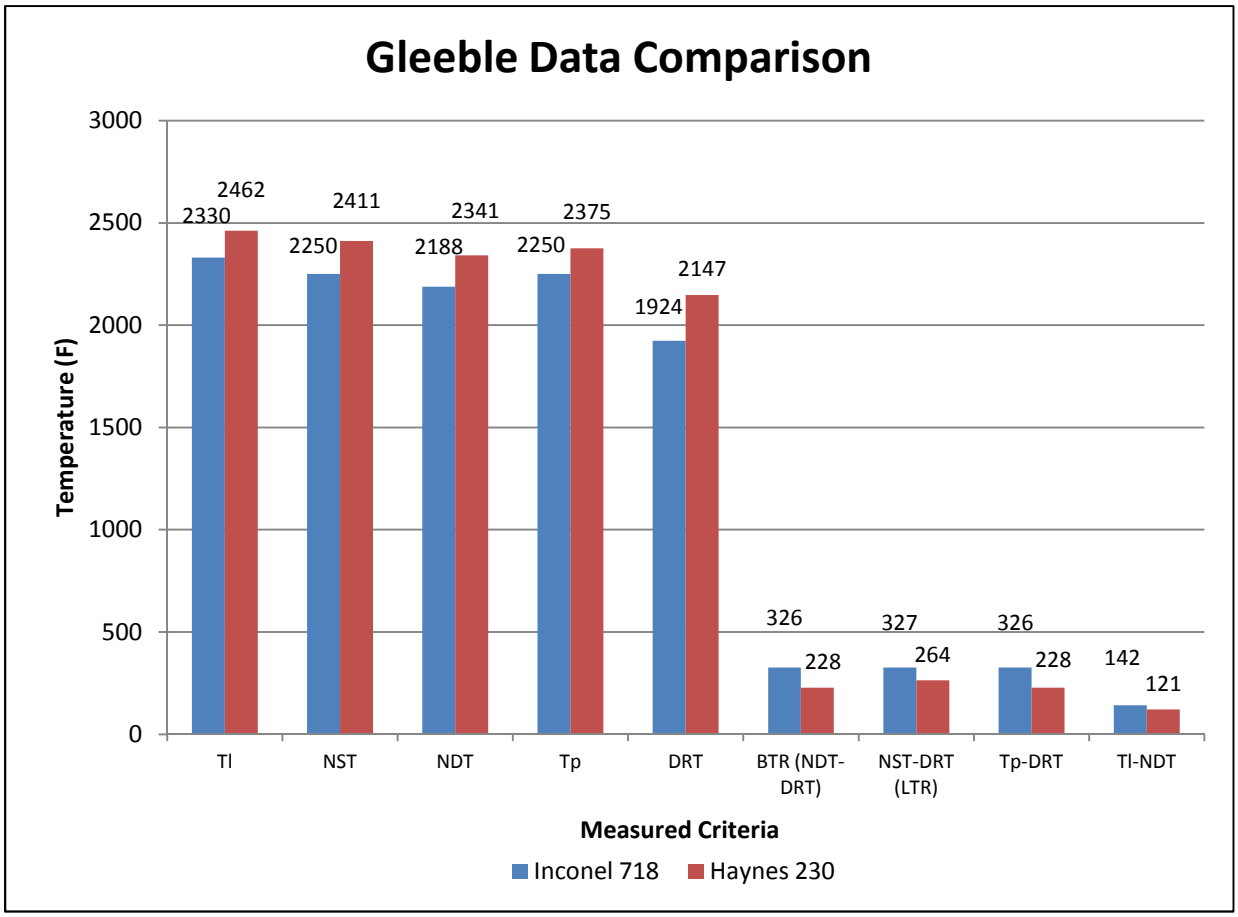

Figure 97 . The Haynes 230 had higher NST, NDT, T_p, and DRT. Given the higher T_L of Haynes 230, this result was not unexpected. Although the Haynes 230 undergoes the liquation, solidification, ductility loss and recovery processes at higher temperatures, it did so within a narrower temperature range than the INCO 718. The BTR, the NST-DRT, the T_p-DRT, and the T_L-NDT were all greater for the INCO 718 than for the Haynes 230. Because the INCO 718 and Haynes 230 have comparable thermal diffusivity values at test temperatures (<5% difference at 1800 ^{o}F), and thus, thermal gradients within the

HAZ are expected to be similar, these results are significant. The INCO 718 has not recovered ductility at a temperature further below its T_L than the Haynes 230. Upon cooling from the NST, it took a greater decrease in temperature for noticeable ductility to recover. The BTR, defined as the temperature between ductility loss on heating, and ductility recovery on cooling, was also larger in the INCO 718. The range between the NST, where complete wetting of grain boundaries occurs, and the DRT, where liquated boundaries have solidified during cooling, was larger in the INCO 718 as well. From this we can conclude that grain boundaries in the HAZ retain liquid at a lower temperature relative to the T_L in the INCO 718 than in the Haynes 230. Thus, grain boundary solidification occurs over a larger temperature range in the INCO 718 than in the Haynes 230. Ductility recovery also occurs at a lower temperature relative to the respective T_L in the INCO 718 than the Haynes 230. This means ductility recovery within the weldpool requires a greater level of cooling in the INCO 718 than the Haynes 230.

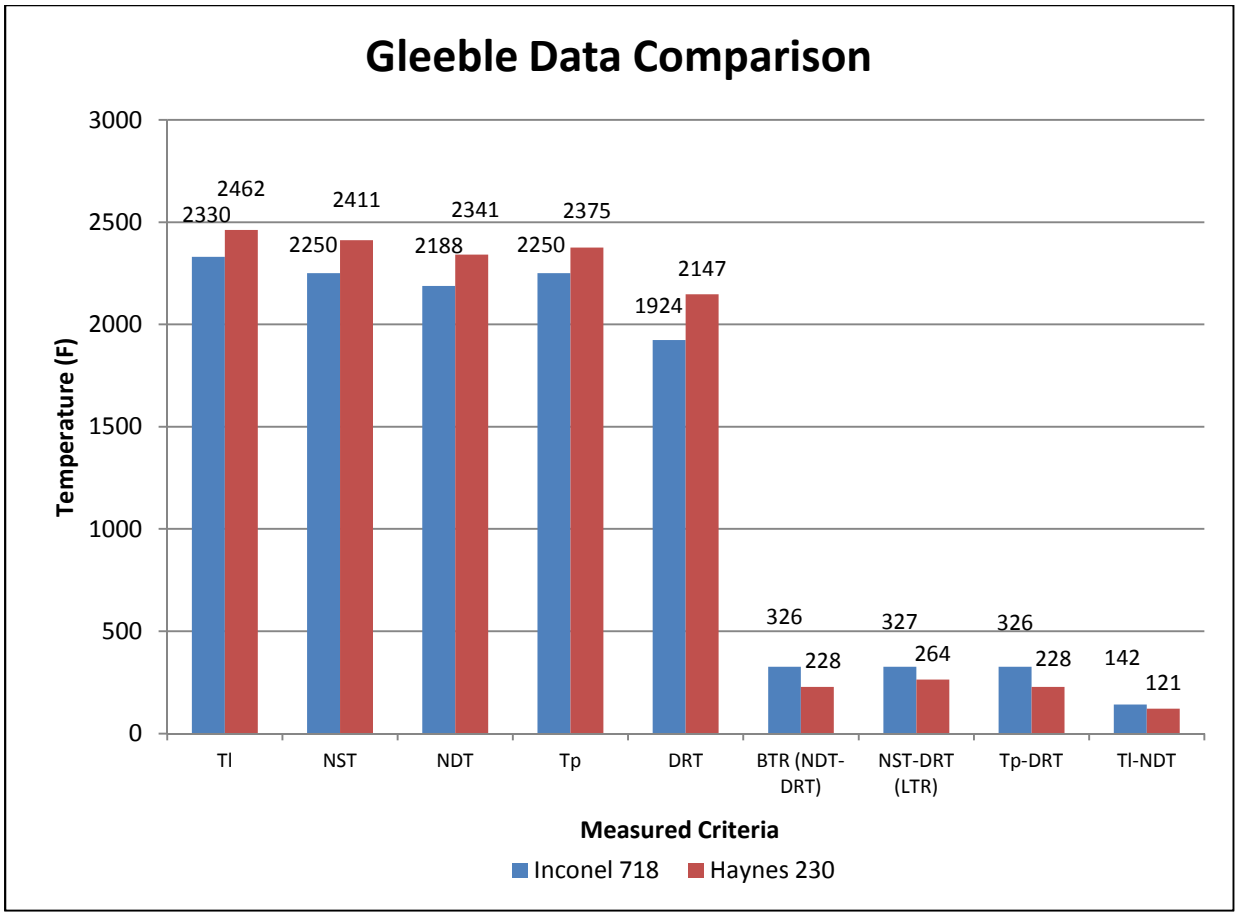

Figure 97: Comparison of hot ductility criteria temperatures for INCO 718 and Haynes 230

The SEM fracture surface analysis revealed similarities between the INCO 718 and the Haynes 230. Either alloy had signs of a transition from transgranular ductile failure to intergranular brittle failure as test temperatures increased. These transitions coincided with the ductility loss measured through reduction in area of the test samples. As ductility decreased, failure became increasingly intergranular. At tested temperatures where ductility was negligible, failure was entirely intergranular. At the nil-strength temperature, where strength was also negligible, failure was entirely intergranular, with obvious evidence of a high volume of liquid present along the grain boundaries at the time of failure (Figure 27-Figure 29). Figure 31Figure 32 clearly capture the

intergranular method of failure in the INCO 718 on-heating 2188 ^{o}F sample, where ductility was at 1% reduction-in-area. In Figure 33Figure 34, showing the fracture surface of the INCO 718 on-heating 2073 ^{o}F sample, failure has transitioned back to transgranular, coinciding with a restoration in ductility, with a 57% reduction-in-area. The highest temperature Haynes 230 on-heating sample (2341 ^{o}F, 2% reduction-in-area) failed intergranularly as well, confirmed through imaging of sample fracture surface (Figure 45). At the on-heating failure temperature of 2249 ^{o}F, ductility in the Haynes 230 has been restored to a 51% reduction-in-area, and failure is once again transgranular (Figure 45-Figure 47). The same transition from intergranular to transgranular failure is evident in the on-cooling samples of the INCO 718 and the Haynes 230. In Figure 35, the fracture surface of the highest temperature INCO 718 on-cooling sample (2130 ^{0}F, 0% reduction-in-area) has the same blocky appearance of undeformed and exposed grains as the low ductility on-heating samples. The next highest INCO 718 on-cooling sample, displayed in Figure 36 (1930 ^{o}F, 0% reduction-in-area), maintains the same intergranular failure appearance. At the on-cooling pull temperature of 1870 ^{0}F, ductility has been restored to 54% reduction-in-area, and the dominant failure mode has transitioned back to transgranular (Figure 37). In the Haynes 230, the two highest temperature on-cooling samples (2202 ^{o}F, 2153 ^{o}F) had low ductility, with less than a 3% reduction-in-area for either sample, and visual indications of intergranular failure (Figure 48-Figure 55). At the on-cooling pull temperature of 2046 ^{o}F, ductility was restored to a 45% reduction-in-area, with failure occurring transgranularly (Figure 56Figure 59).

In either alloy, as temperatures cooled further from the T_P, ductility levels increased, and fracture surfaces appeared progressively more dimpled, with a greater amount of “cup-and-cone” failure occurring through microvoid coalescence. Although

temperatures and temperature ranges differed between alloys, the process of ductility loss and recovery appears to be the same.

Optical microscopy of either alloy further contributed to the data collected through hot ductility testing, and SEM fracture surface analysis. Visible grain boundary liquation was identified near the fracture surface in the NST samples for both alloys. This resulted in grain boundary separation along the fracture surface. In the INCO 718 on-heating 2073 ^{o}F sample that experienced low levels of ductility, grain boundaries along the outer sample edge were distorted by the plastic flow resulting from the applied load. In the Haynes 230 on-cooling 2200 ^{o}F sample, where ductility was very low (2% reduction in area), dynamic recrystallization was observed along the outer edge of the sample, near the fracture surface.

4.2 Varestraint Results

Varestraint results illustrated a greater tendency of hot cracking in the INCO 718 than in the Haynes 230. The INCO 718 samples had a lower cracking threshold strain level as well as a greater number of cracks, greater MCL, and greater TCL at every strain level that induced cracking in either alloy. Although both alloys appeared to reach a MCL saturation strain at 4%, the average MCL value at 4% was 49% larger in the INCO 718 samples than in the Haynes 230 samples. At 2% strain, the INCO 718 average MCL value was still 40% larger than in the Haynes 230. As cracks form in the weldpool and extend into the HAZ and base metal, they travel along thermal gradients, starting at T_L at the fusion boundary, and propagating towards ambient temperatures existing at some distance away from the weld pool. Given the INCO 718 and the Haynes 230's comparable ability to diffuse heat, the equal energy inputs used during testing, and the uniform dimensions of all tests samples, the thermal gradients surrounding the weldpool of either alloy should be similar in size and shape. With similar thermal

gradients, but a significantly longer MCL for the INCO 718, results from the hot ductility testing are reaffirmed: the INCO 718 has a greater temperature range over which liquated grain boundaries exist and cracking remains possible and a temperature further from the T_L at which ductility is lost due to the initial formation of liquid films. The greater TCL at every strain level seen in the INCO 718 can be attributed to the greater MCL and the greater number of cracks. Cracking in the INCO 718 did not only occur over greater distances, but in larger quantities as well. Between 2 and 4% strain the average number of cracks in the INCO 718 increased by 57%, while the average MCL increased by only 9%. As strain levels were increased, an increasing number of cracks formed to alleviate internal stresses. The tendency to form more cracks was greater than the tendency to crack over longer distances. This trend was the same in the Haynes 230, although fewer cracks formed overall. Between 2 and 4% strain, the average number of cracks in the Haynes 230 increased by 45%, while the MCL increased by only 3.5%.

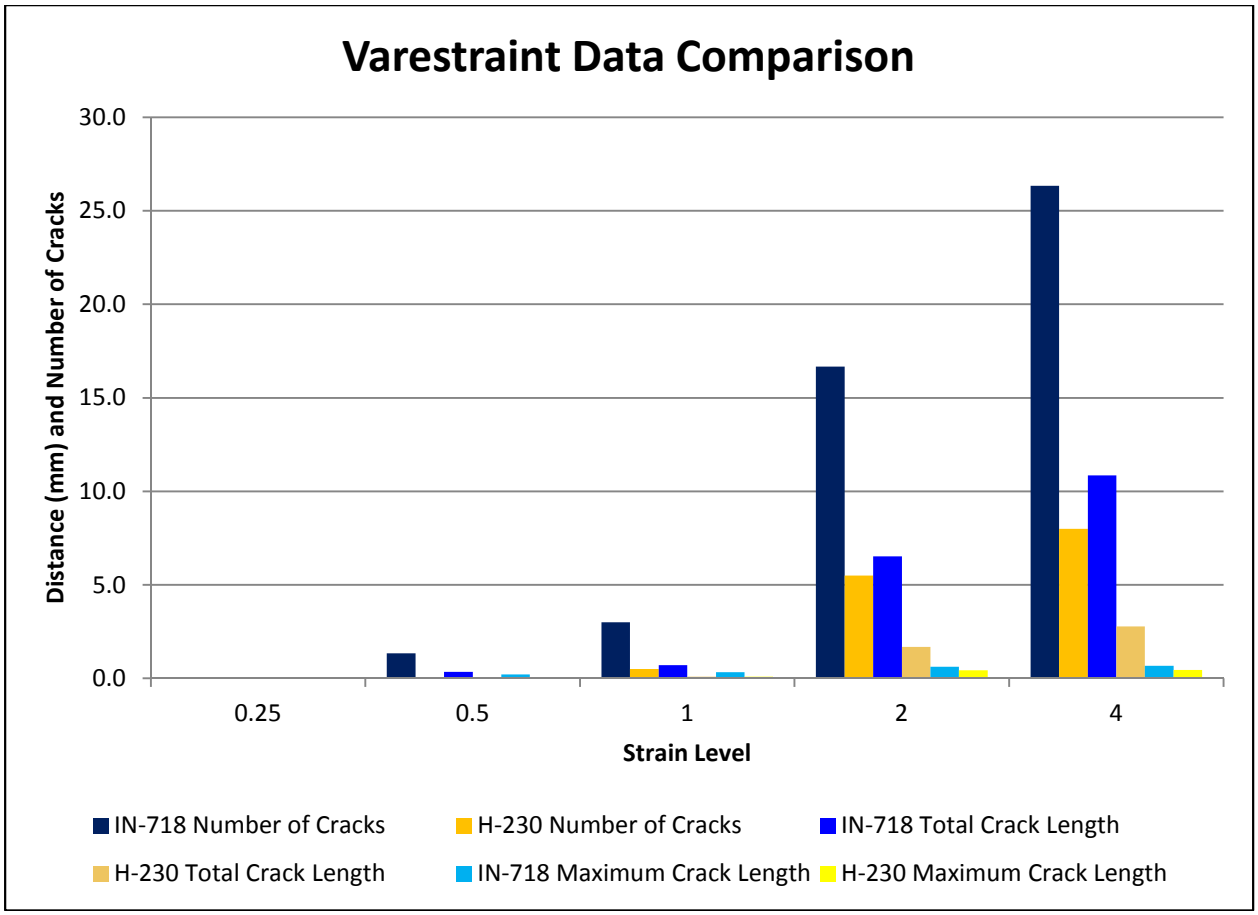

Figure 98 C: Comparison of the MCL, the TCL and the number of cracks between INCO 718 and Haynes 230

5.0 Conclusions

1. The hot ductility testing performed with the Gleeble®, the solidification and liquation cracking testing performed with the Varestraint, and the post-testing analysis done with optical micrography and SEM imaging produced valuable data from which several conclusions can be made.
2. The Gleeble® data revealed that the INCO 718 tested was more susceptible to the formation of intergranular liquid films than the Haynes 230 tested. Each alloy showed evidence of the formation of intergranular liquid films, but the liquid persisted over a greater temperature range in the INCO 718 than in the Haynes 230. The BTR, NST-DRT, the T_p-DRT and the T_L-NDT were all greater for INCO 718 than the Haynes 230. Relative to the T_L, grain boundary liquation begins to occur at a lower temperature in the INCO 718 than in the Haynes 230. Additionally, it takes a greater degree of cooling, from the T_L point, before grain boundaries resolidify in the INCO 718. What this results in is temperatures further below the T_L where ductility begins to decrease on heating and restore on cooling for the INCO 718. A broader temperature range over which ductility is low, and grain boundary liquation is present results in a greater susceptibility to liquation cracking in the HAZ during actual weld processes.
3. Results of the Gleeble® hot ductility tests supported the Varestraint data. While the data from the Gleeble® hot ductility testing showed that INCO 718 was likely to experience cracking issues over a broader range of temperatures during weld processes, the Varestraint testing demonstrated this with verisimilitude. The INCO 718 was shown to be

more prone to liquation cracking than the Haynes 230 samples. The INCO 718 samples had a lower cracking threshold strain level. In addition, it had a greater number of cracks, greater MCL, and a greater TCL than the Haynes 230 samples at every strain level tested. Cracks occurred at lower strain, propagated further into the base metal (and thus across a larger temperature gradient), and occurred in greater numbers in the INCO 718 samples. By these metrics of comparison, the INCO 718 was much more susceptible to hot cracking.

6.0 Future Work

Further work could be done to analyze grain orientation in both the Gleeble® and Varestraint test samples. Grain maps can be produced using an Electron Backscatter Defraction (EBSD) system in conjunction with an SEM system. Of interest is the grain orientation around cracks in the HAZ of the Varestraint samples, and grain orientation near the fracture surface of sectioned Gleeble® samples. Grain orientation maps would provide further information towards the microstructural evolution occurring during the Gleeble® tests, as well as information about preferred crack paths in the Varestraint testing. Furthermore the relationship between grain orientation and the preferred fracture path in Gleeble® samples should also be explored. Again, this was to be part of the effort in this work, but limitations in working with the department's EBSD system limited progress in this area of investigation.

This study could also benefit from the use of a surface analysis technique, such as an Energy Dispersive Spectroscopy (EDS), microprobe, or auger electron spectroscopy system to analyze fracture surfaces of Gleeble® samples, and crack surfaces on the Varestraint samples. Although EDS may lack the needed resolution, an electron beam microprobe or auger spectroscopy system analysis could provide data on which alloying elements are present at the fracture surface, helping to confirm existing cracking theories in either alloy.

References

[1] Willams, James. “Progress in structural materials for aerospace systems.” *Acta Materialia* 51.19 (2003): 5775-5779.
[2] “Nickel, Cobalt, Special, Superalloys, Inconel, Hastelloy.” *All Meteals & Forge*. 14 Oct 2008 <http://www.steelforge.com/nickelcobaltandspecialalloys.htm>.
[3] “Superalloys: A Primer and History.” TMS. 9 Apr 2009 <http://www.tms.org/Meetings/Specialty/Superalloys2000/SuperalloysHistory.html>.
[4] Nickel based superalloys. University of Cambridge. 10 Apr 2009. < http://www.msm.cam.ac.uk/phase-trans/2003/Superalloys/superalloys.html>
[5] “Superalloys: A Primer and History.” TMS. 9 Apr 2009 <http://www.tms.org/Meetings/Specialty/Superalloys2000/SuperalloysHistory.html>.
[6] M.D. Rowe, V.R. Ishwar, D.L.Klarstrom. “Properties, Weldability, and Applications of Modern Wrought Heat-Resistant Alloys for Aerospace and Power Generation Industries” Journal of Engineering for Gas Turbines and Power, April 2009. Vol 128. Pp 354-361.
[7]Nickel based superalloys. University of Cambridge. 10 Apr 2009. < http://www.msm.cam.ac.uk/phase-trans/2003/Superalloys/superalloys.html>
[8]Nickel based superalloys. University of Cambridge. 10 Apr 2009. < http://www.msm.cam.ac.uk/phase-trans/2003/Superalloys/superalloys.html>
9 Kayacan, Ramazan, Remzi Varol, and Olcay Kimilli. “The effects of pre- and post-weld heat treatment variables on the strain-age cracking in welded Rene 41 components.” Materials Research Bulletin 39.14-15 (2004): 2171-2186.
[10] Sims, Chester T., Norman S. Stoloff, and William C. Hagel, eds. *Superalloys II*. John Wiley & Sons, 1987. Pp 114-117
[11] Sims, Chester T., Norman S. Stoloff, and William C. Hagel, eds. *Superalloys II*. John Wiley & Sons, 1987. Pp 117, 221-223
[12]Nickel based superalloys. University of Cambridge. 10 Apr 2009. < http://www.msm.cam.ac.uk/phase-trans/2003/Superalloys/superalloys.html>
[13]Nickel based superalloys. University of Cambridge. 10 Apr 2009. < http://www.msm.cam.ac.uk/phase-trans/2003/Superalloys/superalloys.html>
[14] Nickel based superalloy: dislocation structure. University of Cambridge. 10 Apr 2009 <http://www.msm.cam.ac.uk/phase-trans/2002/Zhang.html>
[15] Nickel based superalloy: dislocation structure. University of Cambridge. 10 Apr 2009 <http://www.msm.cam.ac.uk/phase-trans/2002/Zhang.html>
[16] Nickel based superalloy: dislocation structure. University of Cambridge. 10 Apr 2009 <http://www.msm.cam.ac.uk/phase-trans/2002/Zhang.html>
[17] Sims, Chester T., Norman S. Stoloff, and William C. Hagel, eds. *Superalloys II*. John Wiley & Sons, 1987, pp 170-171.
[18]Nickel based superalloys. University of Cambridge. 10 Apr 2009. < http://www.msm.cam.ac.uk/phase-trans/2003/Superalloys/superalloys.html>
[19] Davis, J.R. *Corrosion of Weldments*. ASM International, 2006. Pg 1.
[20] Different Types of Corrosion – Recognition, Mechanisms, Prevention. 16 June, 2010. <http://www.corrosionclinic.com/types_of_corrosion/weld_decay_weldment_corrosion.htm>
[21] M.G.Collins, J.C. Lippold and J.M. Kikel, 2003. Quantifying Ductility-Dip Cracking Susceptibility in Nickel-base Weld Metals using the Strain-to-Fracture Test", Trends in Welding Research, Proc. of the 6th International Conference, ASM International, pp. 586-590.

[22] Sims, Chester T., Norman S. Stoloff, and William C. Hagel, eds. *Superalloys II*. John Wiley & Sons, 1987. Pp 502
[23] M.B. Henderson, D. Arrell, M. Heobel, R. Larsson, and G. Marchant. "Nickel-based Superalloy Welding Practices for Industrial Gas Turbine Applications." ALSTOM Power Technology Centre, Whetstone, UK.
[24] Ojo, O.A., N.L. Richards, and M.C. Chaturvedi. "Contribution of constitutional liquation of gamma prime precipitate to weld HAZ cracking of cast Inconel 738." *Scripta Materialia* 50 (2004): 641-646.
[25] G.A. Chadwick, W.A. Miller. "On the magnitude of the solid/liquid interfacial energy of pure metals and its relation to grain boundary melting" *Acta Metallurgica, 1967.* Vol 15, issue 4. Pg 607
[26] I.A. Aksay, C.E. Hoge, J.A. Pask. "Wetting under chemical equilibrium and nonequilibrium conditions" *The Journal of Physical Chemistry*, 1974. Vol 78, issue 12. Pp 1178-1183
[27] Ernst SC, Baeslack III WA, Lippold JC. Weld J 1989;68:145-s.
[28] Ojo, O.A., N.L. Richards, and M.C. Chaturvedi. "Contribution of constitutional liquation of gamma prime precipitate to weld HAZ cracking of cast Inconel 738." *Scripta Materialia* 50 (2004): 641-646.
[29] Owczarski WA, Duvall DS, Sullivan CP. Weld J 1966;44:145-s.
[30] A. Lingenfelter, "Welding of Inconel 718: A Historical Overview", Superalloy 718 – Metallurgy and Applications. The Minerals, Metals, & Materials Society, 1989
[31] M.B. Henderson, D. Arrell, M. Heobel, R. Larsson, and G. Marchant. "Nickel-based Superalloy Welding Practices for Industrial Gas Turbine Applications." ALSTOM Power Technology Centre, Whetstone, UK.
[32] P. Ravi Vishnu, "Nickel-based Superalloys", *ASM Handbooks Online, Vol 6, Welding, Brazing and Soldering.* 6 May 2010, <http://products.asminternational.org/hbk/index.jsp>
[33] Kuo, C.M. "Aging effects on the microstructure and creep behavior of Inconel 718 superalloy." *Materials Science and Engineering*, 2009:
[34] "Inconel alloy 718." *Special Metals*. 14 Apr 2009 <http://www.specialmetals.com/documents/Inconel%20alloy%20718.pdf>.
[35] "INCONEL® alloy 718 ." *HP Alloys*. 14 Apr 2009 <http://www.hpalloy.com/alloys/descriptions/INCONEL718.html>.
[36] A. Lingenfelter, "Welding of Inconel 718: A Historical Overview", Superalloy 718 – Metallurgy and Applications. The Minerals, Metals, & Materials Society, 1989
[37] P. Ravi Vishnu, "Nickel-based Superalloys", *ASM Handbooks Online, Vol 6, Welding, Brazing and Soldering.* 6 May 2010, <http://products.asminternational.org/hbk/index.jsp>
[38] A. Lingenfelter, "Welding of Inconel 718: A Historical Overview", Superalloy 718 – Metallurgy and Applications. The Minerals, Metals, & Materials Society, 1989
[39] Nishimoto, Kazutoshi. "Effects of Grain size and Homogenization Heat Treatment on HAZ cracking susceptibility of Cast Alloy 718" ISIJ International, Vol 40, 2000. 39-43.
[40] Nishimoto, Kazutoshi. "Effects of Grain size and Homogenization Heat Treatment on HAZ cracking susceptibility of Cast Alloy 718" ISIJ International, Vol 40, 2000. 39-43.
[41] CH. Radhakrishna, K. Prasad Rao. "The formation and control of Laves phase in superalloy 718 welds." *Journal of Material Science*. 1997
[42] CH. Radhakrishna, K. Prasad Rao. "The formation and control of Laves phase in superalloy 718 welds." *Journal of Material Science*. 1997
[43] R.G. Carlson, J.F. Radavich. In "Superalloy 718 Metallurgy and Applications." TMS, Warrendale, PA. 1989. Pp 79-85.

[44] A. Lingenfelter, “Welding of Inconel 718: A Historical Overview”, Superalloy 718 – Metallurgy and Applications. The Minerals, Metals, & Materials Society, 1989
[45] W. Chen, M.C. Chaturvedi, N.L. Richards. “Effect of Boron segregation at grain boundaries on Heat Affected Zone cracking in wrought INCONEL 718.” *Metallurgical and Materials Transactions A*, Volume 32A, April 2001. Pp 931-939
[46] T.J. Kelly. “Elemental Effects on the Cast 718 Weldability” *Welding Journal,* 68, 1989. Pp 44s-51s.
[47] R.G. Thomspon, D.E. Mayo, B. Radhadrishnan. “The relationship between carbon content, microstructure, and intergranular liquation cracking in cast nickel alloy 718” *Metallurgical Transactions A*, Volume 22A, February 1991. Pp 557-568
[48] J.X. Dong, X.S. Xie, R.G. Thompson. “The influence of sulfur on stress-rupture fracture in INCONEL 718 Superalloys” *Metallurgical and Materials Transactions A*. Volume 31A, September, 2000. Pp 2135-2144
[49] W.F. Savage, B.M. Krantz. *Welding Journal*, January, 1966. Pp 13s-25s
[50] V.P. Kujanpaa, S.A. David, C.L. White. *Welding Journal*. 1987. Vol 66 (8). Pp 221s-228s.
[51] J.C. Lippold. *Welding Journal*. 1983, vol 62 (1). Pp 1s-11s.
[52] A. Lingenfelter, “Welding of Inconel 718: A Historical Overview”, Superalloy 718 – Metallurgy and Applications. The Minerals, Metals, & Materials Society, 1989
[53] K. Nishimoto, I. Woo, M. Shirai. “Effects of grain size and homogenization heat treatment on the HAZ cracking susceptibility of Cast Alloy 718” *ISIJ International*, Vol 40, 2000. Pp S39-S43
[54]R.F. Decker, “Symposium: Steel Strengthening Mechanisms, Zurich, 1969” Climax Molybdenum, Greenwich CT, 1970. Pp 147-170.
[55] M.D. Rowe, V.R. Ishwar, D.L.Klarstrom. “Properties, Weldability, and Applications of Modern Wrought Heat-Resistant Alloys for Aerospace and Power Generation Industries” Journal of Engineering for Gas Turbines and Power, April 2009. Vol 128. Pp 354-361.
[56] “Haynes 230 alloy information” *Haynes International Inc. 21 May 2010*. <http://www.haynesintl.com/HAYNES230alloy/230HaynesAlloyWeld.htm>
[57] S.C. Ernst. “Weldability studies of Haynes 230 alloy” *Welding Journal* Vol 73, Issue 4, 1994. Pp 80s-89s.
[58] HAYNES Manuf. Info Sheet
[59] G. Pottlacher, H. Hosaeus, E. Kaschnitz, and A. Seifter. “Thermophysical Properties of solid and liquid Inconel 718 Alloy” *Scandinavian Journal of Metallurgy*, 2002. Vol 31, pp 161-168.
[60] “Company Background - Dynamic Systems Inc..” *Dynamic Systems, Inc.* 4 Jun 2009 <http://www.gleeble.com/background.htm>.
[61] J.C. Lippold, W.A. Baeslack, W. Lin. “An evolution of heat affected zone liquation cracking susceptibility, part I: development of a method for quantification” *Welding Journal, 1993.* Pp 135s-153s
[62] Sims, Chester T., Norman S. Stoloff, and William C. Hagel, eds. *Superalloys II*. John Wiley & Sons, 1987. Pp 504-507
[63] D.A. Krammer, E.C. Masuhachi, R.E. Monroe. “Cracking in high-strength steel weldments- a critical review” DMIC Report 197, February 7, 1964
[64] V. Shankar, T.P.S. Gill, S.L Mannan, S. Sundaresen. “Effect of nitrogen addition on microstructure and fusion zone cracking in type 316L stainless steel weld metals” *Materials Science and Engineering A*. Vol 343, Issue 1. Feb 2003. Pp 170-181

[65] Campbell, Richard D., and Daniel W. Walsh. “ASM Handbooks Online - Weldability Tests for Evaluating Cracking Susceptibility.” *ASM Handbooks Online*. 4 Jun 2009 <http://products.asminternational.org/hbk/index.jsp>.
[66] W.F. Savage, C.D. Lundin. “The Varestraint Test” Welding Journal,1965. Vol 44, issue 10. Pp 433s-442s
[67] "Standard Welding Terms and Definitions," ANSI/AWS A3.0-89, American Welding Society, 1989
[68] Cambell, Richard D., Walsh, Dan "Weldability Testing". ASM Handbook, Vol 6. ASM International, 2002.
[69] Walsh, Dan. Personal Interview (Advisor meeting). 3 Oct 2008
[70] R.E. Schafrik, D.D.Ward, J.R. Groh, in: E.A. Loria (Ed.),”Superalloys 718, 625, 706 and Various Derivatives”, TMS, 2001, pp. 1–11.
[71] Collier, J.P., Wong, S.H., Phillips, J.C., Tien, J.K. “The Effect of Varying Al, Ti, and Nb content on the Phase Stability of INCONEL 718” Metallurgical and Materials Transactions, Vol 19A, July 1988
[72] Dong, J.X., Fu, S.H., Zhang, M.C., Xie, X.S. “Alloy design and development of INCONEL718 type alloy” Materials Science and Engineering, 2009. Pg 215-220
[73] Williams, James C. “Progress in Structural Materials for aerospace systems.” *Acta Materialia* 51.19 (2003): 5775-5799.
[74] O.A. Ojo, M.C. Chaturvedi. “On the role of liquated γ’ precipitates in weld heat affected zone microfissuring of a nickel-based superalloy” *Materials Science and Engineering A 403*, 2005. Pp 77-86
[75]Khartchenko, Nikolai V. Advanced Energy Systems. Taylor & Francis, Inc. 1998. 95.
[76] Haglind, Fredrik. "A review on the use of gas and steam turbine combined cycles as prime movers for large ships. Part I: Background and Design." Energy Conversion Management (2008)
[77] "GE Energy to ramp up steam turbine engine production." Atlanta Business Chronicle 3 Dec 2007, 14 Oct 2008 <http://findarticles.com/p/articles/mi_qa3618/is_199903/ai_n8844369/pg_2?tag=artBody;col1>.
[78] Holcom, G.R., et al. “Steam turbine materials and corrosion”, Materials Science & Technology Division, Oak Ridge National Laboratory. Materials Science Forum, 2008.
[79]“ Konig, W. "Machining nickel-based superalloys." Manufacturing Engineering. Mar 1999. BNet. 14 Oct 2008 <http://findarticles.com/p/articles/mi_qa3618/is_199903/ai_n8844369/pg_2?tag=artBody;col1>.